BICARBONATE-RICH FLUID INCLUSIONS IN RELIC QUARTZ PHENOCRYSTS, ZINKGRUVAN BASIN, SWEDEN

Beverly A. Chomiak

Submitted in Partial Fulfillment of the Requirements for the Degree of Ph.D.

Department of Earth and Environmental Science

New Mexico Institute of Mining and Technology

Socorro, New Mexico

December 2001

Ackowledgements

There is a long list of people that need to be thanked for their assistance in my labors. At New Mexico Tech: Dave Norman, Kent Condie, Andy Campbell, Laurel Goodwin and David Johnson are the names that most often come to mind. Felix Barreras provided indispensible technical assistance. At Stockholm University: Sten Lindblom and Curt Broman supervised the initial work; Kurt Boström and Lennart Sjöberg facilitated my stay in Sweden. Access to material, the field, and the mines at Zinkgruvan and Garpenberg was provided by Annika Wasström at Gothenberg University and Per Hedström at Veielle Montagne.

Special thanks goes to the Scandinavian American Foundation for financial support during my stay in Sweden. Funding from Sigma Xi, the Geological Society of America and the NMIMT Graduate Student Research Project Scholarship program facilitated equipment acquisition for the fluid inclusion and mass spectrometer laboratories

Abstract

Fluid inclusions in relic quartz phenocrysts from metaporphyries of the Zinkgruvan basin in south-central Sweden were studied to identify the type of fluids present during metamorphism and constrain the retrograde metamorphic pressure-temperature-time path. Relationships between inclusions and host quartz microstructures were explored in order to refine the fluid inclusion paragenesis.

The rocks were extruded, metamorphosed and deformed during the Svecofennian orogen ca. 1.9-1.7 Ga ago. Previous workers estimated peak metamorphism to be about 550-700°C at 3-5 kbar, and identified four folding phases. The first two folding phases were responsible for the orientation of a basin-scale synform, and the second two were associated with peak metamorphism and granitoid intrusion. The samples studied originate from areas representing three metamorphic facies: lower, middle and upper amphibolite facies.

In the lower amphibolite facies, the phenocrysts exhibit core-and-mantle structures and rotation recrystallization was dominant. Initial deformation was accomodated by the (c)<a> slip system that created birefringent deformation bands in the cores. Subsequent deformation was mainly through {m}<a> slip. In the middle and upper amphibolite facies, the phenocrysts are completely recrystallized; grain boundary migration recrystallization was important. Distinctive blocky grains in the upper amphibolite facies phenocrysts are interpreted to indicate recrystallization of high quartz.

The fluid inclusion plane (FIP) orientations were measured using a strike-and-dip method and plotted on stereograms. FIP traces tend to intersect in "hubs" and exhibit preferred angles of intersection with other FIP. Hubs represent specific crystallographic directions in the quartz. They plot in great cricle girdles on a stereogram; the girdles coincide with a poorly developed preferred

orientation of FIP traces. Inclusions occupying FIP with a common hub have similar homogenization temperatures (Th), and inclusions occupying FIP that intersect different hubs have different Th. The range in Th along a single FIP is less than 60°C. FIP that intersect a single hub are, therefore, the same age. This is potentially a new tool for dating fluid inclusions. Preferred angles of FIP intersection correspond to quartz cleavage planes, therefore, the FIP likely formed along quartz cleavage cracks. The distribution of inter-FIP angles is different in upper and lower amphibolite facies samples. It is not known how the hub geometry might be used to relate the FIP to tectonic events.

Most fluid inclusions contain nahcolite crystals which do not completely dissolve upon heating. Type I inclusions are small (<8μm) and negative quartz-crystal shaped. Four subtypes that are identified by different cross cutting relations with grain boundaries exhibit different Th: IA at 400-550°C, IB at 300-400°C, IC at 200-300°C, and ID at 100-200°C. Type II inclusions are larger (<20μm) with complex rounded forms; mean Th is 170°C. Many type III inclusions are very large (>20 μm) with pinched shapes; mean Th is 130°C. All inclusions homogenize to liquid. Types IA and IB formed before quartz recrystallization and occur mainly in the lower amphibolite facies samples. Type IC formed during recrystallization. Types ID, II and III formed after recrystallization. Fluid compositions are similar: 83-88 mole% H_2O; 6-9 mole% CO_2; 2-8 mole% $NaHCO_3$; and 0.9-2.2 mole% NaCl with minor $CaCl_2$. Transposed fluid inclusions in the cores of lower amphibolite facies phenocrysts record an earlier metamorphic fluid that was richer in CO_2 (~20 mole%). Type C fluid inclusions occur adjacent to some type I FIP. Calcite precipitates as nahcolite dissolves upon heating type C inclusions, and the reverse occurs upon cooling. Calcite metastability creates unusual phenomena during microthermometry runs. Type C inclusions are interpreted to be type I inclusions with trapped calcite.

The metamorphic fluids probably came from devolatilization reactions involving skarn formation and were saturated with respect to calcite. Fluid evolution occurred in a more-or-less closed system. A CO_2-rich fluid was generated in the initial stages of devolatilization. Later production of Na^+ and HCO_3^- was from the breakdown of calcite and feldspar to produce zoisite, anorthite and quartz at near peak conditions. The alkaline fluids (pH 6-8) promoted stress corrosion cracking and the formation of FIP. Nahcolite precipitation in microcracks aided crack healing by lowering the fluid pH and quartz solubility. Isochores plotted on a PT grid occur on the high-pressure low-temperature side of peak metamorphism and record isobaric cooling on the retrograde metamorphic PT-time path. Future work should focus on correlating the fluid inclusions with the major fold phases.

The relic phenocrysts make good subjects for fluid inclusion study because they contain a long record of fluid entrapment. Strain partitioning into the fine grained matrix of a porphyry favors the preservation of phenocrysts from extensive recrystallization. The combined study fluid inclusions and quartz microstructures, however, is required to decipher the fluid inclusion paragenesis.

Ackowledgements

There is a long list of people that need to be thanked for their assistance in my labors. At New Mexico Tech: Dave Norman, Kent Condie, Andy Campbell, Laurel Goodwin and David Johnson are the names that most often come to mind. Felix Barreras provided indispensible technical assistance. At Stockholm University: Sten Lindblom and Curt Broman supervised the initial work; Kurt Boström and Lennart Sjöberg facilitated my stay in Sweden. Access to material, the field, and the mines at Zinkgruvan and Garpenberg was provided by Annika Wasström at Gothenberg University and Per Hedström at Veielle Montagne.

Special thanks goes to the Scandinavian American Foundation for financial support during my stay in Sweden. Funding from Sigma Xi, the Geological Society of America and the NMIMT Graduate Student Research Project Scholarship program facilitated equipment acquisition for the fluid inclusion and mass spectrometer laboratories

Table of Contents

Page

List of Tables

List of Figures

List of Abbreviations

a	neutral aqueous species (used as a superscript)
å	effective ionic radius of a hydrated aqueous species
Å	Ångstrom units
Aγ	empirical Debye-Huckel parameter in kg $^{0.5}$ /mole $^{0.5}$
ASW	air saturated water
atm	atmospheres
b	ion interaction factor in Debye-Hückel equation
Bγ	empirical Debye-Huckel parameter in kg $^{0.5}$ /mole $^{0.5}$ /cm
bub	bubble
C	degrees Celcius
clath	clathrate
cm	centimeter(s)
d	displacement of FIP between top and bottom of a section
eq. wt. %	equivalent weight percent
g	gram(s)
Ga	billion years
FIP	fluid inclusion plane(s) or trail(s)
hydro	hydrohalite
I	ionic strength
in	inch(es)
K	chemical equilibrium constant; Kelvin degrees
kbar	kilobar(s)

kg	kilogram(s)
K_H	Henry's Law constant
K_{SP}	solubility product
L	liquid phase
lb	pound(s)
lb/in^2	pounds per square inch pressure
leng	length
liq	liquid
logK	logarithm of an equilibrium constant
LPHT	low-pressure high-temperature
L=V	the liquid-vapor saturation curve
L+V→L	homogenization to the liquid phase
m	molality
mCO_2^T	"total" molality of CO_2 in solution
mCO_2^{TN}	"total nominal" molality of CO_2 in all phases
mNa^{+TN}	"total nominal" molality of Na^+ in all phases
$mSiO_2^T$	"total" molality of SiO_2 in solution
M	molar units (moles/ 1000 grams H_2O)
max	maximum
min	minute(s); minimum
mm	millimeter(s)
mol	mole(s)
m/e	mass/charge ratio
n	number of moles

nah	nahcolite
nCO_2^V	number of moles of CO_2 in the vapor phase
p	page(s)
P_{CO2}	partial pressure of CO_2
P_{H2O}	partial pressure of H_2O
Pmin	minimum trapping pressure
ppm	parts per million
PT-time	pressure-temperature-time path
QMS	quadrupole mass spectrometer
R	ideal gas constant (83.14241 bar • cm^3/K • mole)
samp	sample
SEM	secondary electron multiplier
t	temperature; thickness of a section
T	temperature
Td	temperature of mineral dissolution
Te	temperature of eutectic melting
Th	temperature of fluid phase homogenization
Th-CO_2	temperature of CO_2 homogenization
Tm	temperature of frozen phase final melting
Tm-clath	temperature of clathrate final melting
Tm-CO_2	temperature of solid CO_2 final melting
Tm-hydro	temperature of hydrohalite final melting
Tm-ice	temperature of ice final melting
Trxn	temperature of mineral-mineral reaction

V	vapor phase; total volume of a fluid inclusion
Vc	volume percent of calcite
V_{CO2}	volume of vapor phase CO_2
Vn	volume percent of nahcolite
Vn+c	volume percent of nahcolite and calcite combined
V%	volume percent
W%	weight percent
X_{CO2}	mole fraction of CO_2
X_{H2O}	mole fraction of H_2O
X_{NaHCO3}	mole fraction of $NaHCO_3$
X_{NaCl}	mole fraction of NaCl
Z	charge on an aqueous species
α	activity of an aqueous species
γ	activity coefficient of an aqueous species
μm	micrometers
ρ	density
ρ_{H2O}	density of an H_2O-rich fluid phase
ρ_{CO2}	density of a CO_2-rich fluid phase
σ_1, σ_2, σ_3	principal stress axes where $\sigma_1>\sigma_2>\sigma_3$
°C	degrees Celcius
°K	degrees Kelvin

Chapter I

Introduction

Objectives

The principal objective in studying fluid inclusions in metamorphic rocks is to obtain information about the fluids which were present at different times during metamorphism, and thus provide a more comprehensive picture of the metamorphic process. The information gained usually concerns the type of fluids involved, and the temperature and depth of the system when the fluids were trapped. It can be used for something as simple as obtaining isochores that constrain the pressure-temperature-time (PT-time) path of metamorphism, or for something as sophisticated as reconstructing fluid movements through the crust.

The early Proterozoic metavolcanic rocks in Bergslagen, Sweden, are an interesting place to do fluid inclusion research for several reasons. Studies addressing the fluids present in low-pressure high-temperature (LPHT) terranes are sparse. Quartz veins are rare here, but inclusion-rich quartz phenocrysts are abundant. The metavolcanic rocks host metamorphosed ore deposits that contain diverse suites of fluid inclusions, but the metavolcanic rocks themselves have never been examined for fluid inclusions.

The goals of this study are to evaluate the usefulness of quartz phenocrysts as subjects for fluid inclusion study and to locate points on a PT-time path for a particular basin in Bergslagen. The Zinkgruvan basin was chosen for study because the massive metavolcanic rock unit there has been metamorphosed to different facies within a relatively small area. The information gained will be particularly useful for future studies of fluid inclusions in the ore deposits of Bergslagen. This study also contributes to the general knowledge of metamorphic fluids in LPHT terranes.

Organization of Topics

A summary of the geology of Bergslagen is presented in the remaining sections of this chapter. Most of the information can be found in English language publications, but Swedish geologists commonly use Swedish terms when discussing the geology of this classic region. The Swedish geological terms are introduced for the benefit of the reader who may wish to reference original material, and because some are simply more convenient to use than their awkward English translations. In Chapter II the various methods of investigation used in this study are briefly described.

This study is subdivided into three parts. A retrograde PT-time path for the Zinkgruvan basin is presented in Chapter III, unusual phenomena encountered in the secondary fluid inclusions are reported in Chapter IV and observations on how fluid inclusions in relic quartz phenocrysts can be dated are addressed in Chapter V. The chapters are papers submitted for publication in *Geofluids* and *Journal of Structural Geology.*

Background

Geologic Setting

The lower Proterozoic crust of the Baltic shield outcrops in a triangular area across most of central Sweden and southwestern Finland (Figure 1). It is also known as the Svecofennian domain. It is considered to be a package of 1.9-1.7 Ga old island arcs accreted obliquely onto the Archean craton, which lies to the north and east (Gaal and Gorbatschev, 1987; Gorbatschev and Gaal, 1987). Two major districts of volcanic associated mineralization are recognized in Sweden, Skellefte in the north and Bergslagen in the south. Both have counterparts in western Finland, and the mineral belts are thought to be continuous across the Baltic Sea.

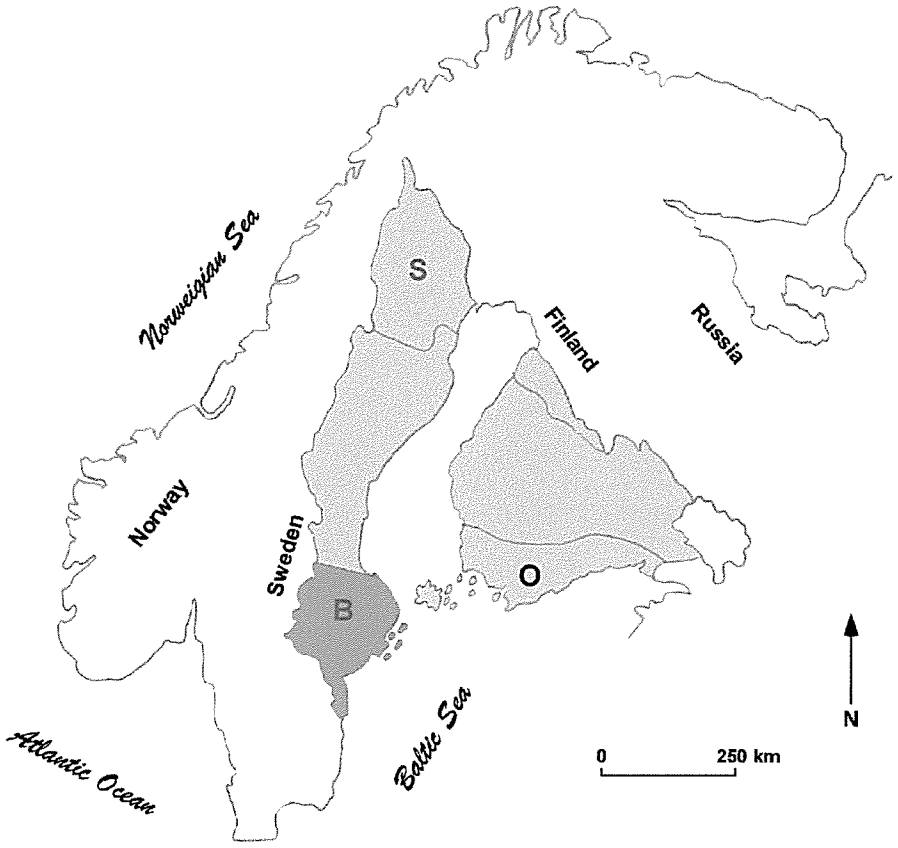

Figure 1. The early Proterozoic crust of the Baltic Shield covers areas of Sweden and southern Finland (colored areas). The mineralized regions of Bergslagen (B) and Skellefte (S) are separated by the thick metasedimentary rock sequences of the Bothnian Basin. A major shear zone separates Bergslagen from the basin. Bergslagen and the Orijarvi (O) belt of southwestern Finland are continuous beneath the Bothnian Bay.

Large regions of Bergslagen (Figure 2) are occupied by deformed and foliated granitoids, which traditional Swedish geologists call *urgranit*. They are bounded by enclaves of metavolcanic and metasedimentary rocks which are folded into synclines. The contacts between the granitoids and the enclave rocks are intrusive in some places and tectonic in others. There is a regional trend of increasing grain size in enclave rocks towards the margins of the granitoids (Magnusson, 1936). The urgranites or "early" granitoids have zircon U-Pb and whole rock Rb-Sr radiometric dates of 1.89-1.85 Ga (Welin, 1992). They are mostly granodiorites and tonalites, with subordinate gabbros and granites. They are geochemically similar to the metavolcanic rocks, and many have been interpreted as synvolcanic intrusions (e.g. Allen et al., 1996). The early granitoids have been called "synorogenic" granitoids because they are thoroughly deformed, more intensely closer to their contacts with the enclaves. Foliations and lineations in the granitoids follow the regional tectonic grain. Both the early granitoids and the enclave rocks have been intruded by a few "late" granitoids, which are smaller isolated granite plutons clustered around 1.80-1.78 Ga in age (Welin, 1992). These granites have been called "serorogenic" granitoids because they are deformed only on their margins. Geologists commonly characterize the early granitoids as I-types and the late granitoids as S-types (e.g. Wilson, 1980; Armands and Xefteris, 1987), but there are many exceptions. The subdivision generally does not apply well to the Bergslagen granitoids (Rickard, 1988).

The enclave regions of Bergslagen are mostly composed of repetitious quartz-feldspar-biotite gneisses of volcanic origin, which traditional Swedish geologists call *leptit*. Formerly, geologists dealt with the monotonous 8-10 km thick sequence by subdividing the leptites into an upper, commonly grey, K-rich unit and a lower, generally red, Na-rich unit (Magnusson, 1936). The compositional differences between the "upper leptite" and the "lower leptite" are now attributed to subseafloor alterations, with the more common sodic alteration characteristic of deeper seawater circulation (Frietsch, 1982; Lagerblad and Gorbatschev, 1985). In the least metamorphosed

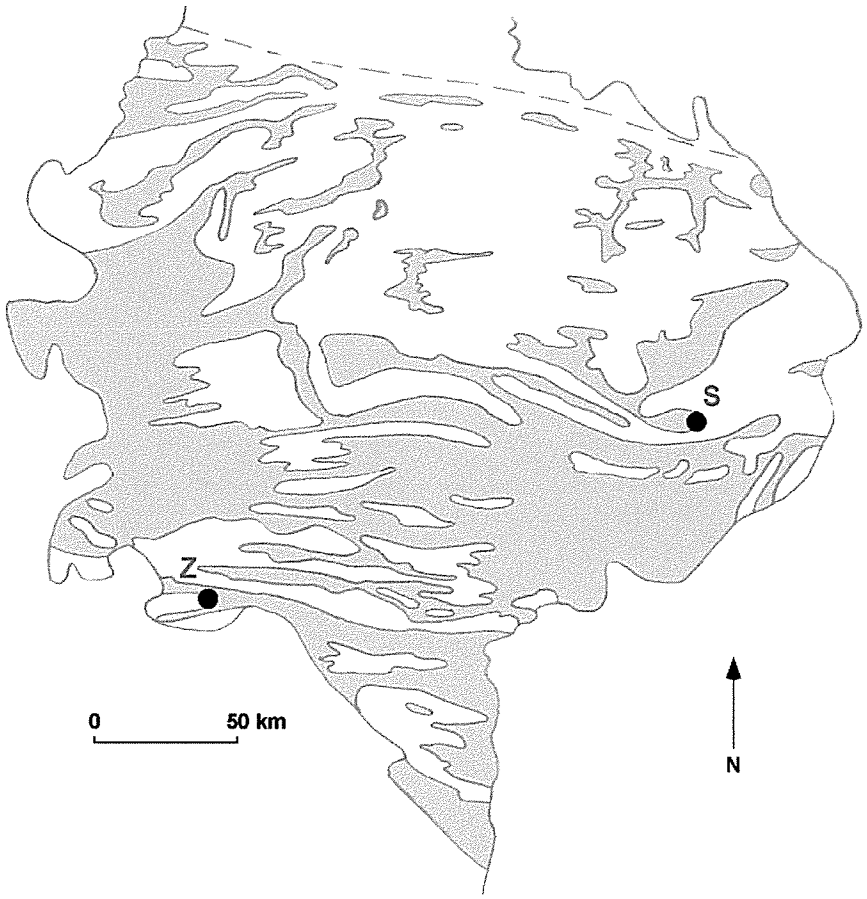

Figure 2. A sketch of the distribution of early orogenic granitoids (white) and metavolcanic and metasedimentary rocks (colored) in Bergslagen, modified after Rickard (1988). S= Stockholm. Z= Zinkgruvan. Metamorphic grade generally increases toward the southeast.

enclaves the leptite correlates are subaerial to subaqueous, rhyolitic pyroclastic falls and fallout units, and their resedimented equivalents. Traditional Swedish geologists call them *hälleflinta*. The volcanic textures preserved in the hälleflintas are now also recognized in the leptites (Allen et al., 1996). There is a greater proportion of resedimented material in the upper leptites than in the lower leptites. A metasedimentary unit is usually found above the upper leptite, and it is prominent in the cores of synclines. The metasediments are dominantly argillaceous and sandy turbidites of volcanic provenance (Allen et al., 1996). Most of the radiometric dates for the volcanic rocks and their associated metasediments fall between 1.90 and 1.87 Ga (Welin, 1992).

The tectonic setting of Bergslagen is controversial because of the volumetric importance of subalkaline rhyolitic rocks and the lack of internal stratigraphy for the leptite units. In the late 1970s, the leptites were considered to be a calcalkaline volcanic suite from an island arc whose character was masked by alkali metasomatism (e.g. Löfgren, 1979; Wilson, 1980; Loberg, 1980). In the 1980s competing arguments, based mainly on immobile element analyses, included a continental margin arc (e.g. Vivallo and Rickard, 1984; Lagerblad, 1988) and a rifted continental margin (e.g. van der Velden et al., 1982; Oen, 1987). The most recent argument, based on volcanic facies analysis, is for an extensional, back-arc, active continental margin (Allen et al., 1996). Features of both extensional and compressional tectonic regimes are generally recognized by geologists today.

The Bergslagen rocks were metamorphosed during the Svecofennian orogeny. Rickard (1988) provides a comprehensive review of the distribution of metamorphic facies in Bergslagen, summarized here. The westernmost enclave at Grythyttan is the least metamorphosed, at greenschist facies. The transition from greenschist to amphibolite facies, especially between *hälleflinta* and *leptit*, can be seen in the Saxå, Nora and Ställdalen enclaves. Most of the northern-central enclaves attained lower amphibolite facies, whereas the southern and eastern enclaves are

commonly at upper amphibolite grade (Figure 3). The andalusite-sillimanite isograd distinguishes upper from lower amphibolite facies regions. The occurrence of veined gneisses, which traditional Swedish geologists call *ådergnejs*, in the upper amphibolite facies regions tends to be spotty in the south and widespread in the east of Bergslagen. The veined gneisses have quartz-feldspar segregations which are conformable with the foliation and were produced in place by partial melting. Veined gneisses with much coarser grained segregations are distinguished as *pegmatitgnejs*, or pegmatite gneisses. Current thinking is that the hälleflintas, leptites, and veined and pegmatite gneisses represent a continuum of increasingly metamorphosed rhyolitic rocks.

The lack of kyanite is indicative of LPHT peak metamorphism, estimated to have been in the general range of 3-5 kbar pressure and 550-700°C temperature in the amphibolite facies (Rickard, 1988). Pressure and temperature estimates for peak metamorphism in various regions are presented in Table 1. A retrograde greenschist facies metamorphism overprinted the amphibolite grade rocks of pelitic composition in some enclaves. The age of peak metamorphism is in dispute. The earliest suggested interval is 1.87-1.85 Ga (Rickard, 1988). Retrograde greenschist metamorphism was prolonged after 1.70 Ga. The veined and pegmatite gneisses have never been dated. There is only one study addressing the ages of metamorphic skarn minerals (Moorman et al., 1982). K-Ar radiometric dates of hornblendes, with a closure temperature of about 500°C, cluster at 1.83 Ga. K-Ar dates of biotites, with a closure temperature around 280°C, cluster at 1.69 Ga.

Two major Svecofennian deformation phases were recognized in Bergslagen by traditional Swedish geologists (e.g. Magnusson, 1936; Magnusson et al., 1962; Stålhös, 1976): an early phase of westward-verging isoclinal folding and thrusting that created the north and northeast trending enclaves in northern and western Bergslagen, and a later phase of north-south shortening that formed the east-west trending synclines of southern Bergslagen. Both north-south and east-west trending synclines tend to wrap around adjacent early granitoids. It is not clear whether the

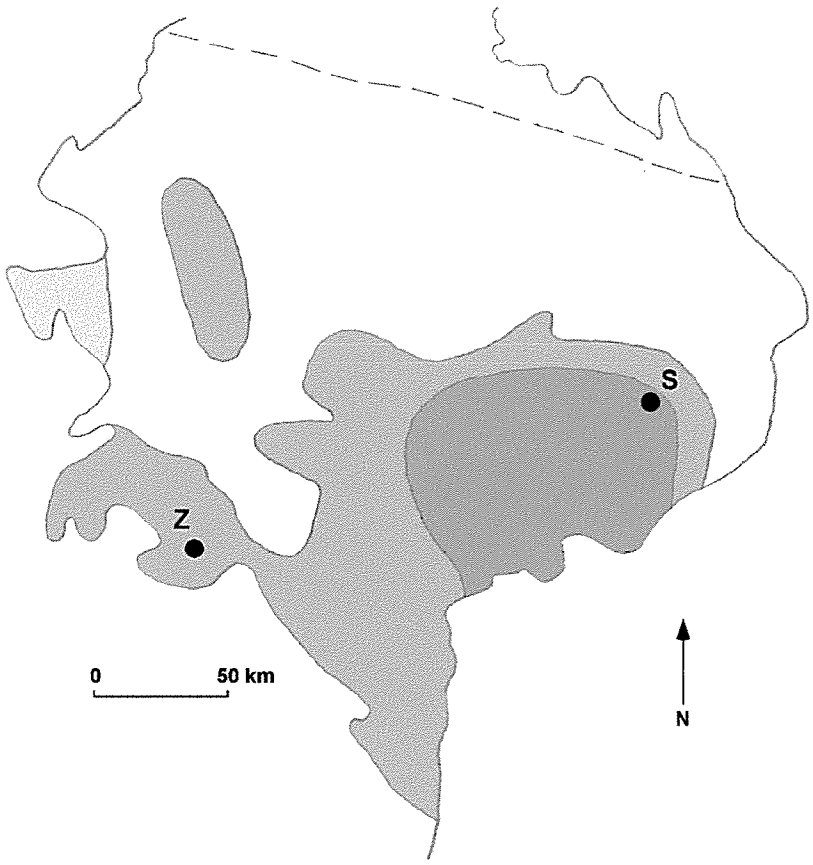

Figure 3. The distribution of metamorphic facies in Bergslagen according to Rickard (1988). Light grey= greenschist facies. White= lower amphibolite facies (andalusite). Medium grey= upper amphibolite facies (sillimanite). Dark grey= the region where veined gneisses are prevalent. Z= Zinkgruvan. S= Stockholm.

Table 1. Peak metamorphic conditions in Bergslagen and SW Finland.

Location	Temperature Min (°C)	Temperature Max (°C)	Pressure Min (bars)	Pressure Max (bars)	Reference	
Garpenberg		550		3.5	1990	Vivallo & Rickard[1]
Gasborn	500	550		(4)	1990	Dammen & Kieft[1]
Stollberg	560	600	2	3.5	1992	Beetsma[1]
Harmsarvet	500	600	1.5	3.5	1984	Wolter & Seifert[1]
Orijarvi	550	650	3	5	1985	Schreuers & Westra[2]
Kemio	550	680	3	4	1982	Dietvorst[2]
Saxberget	550	700	2.5	5	1988	Lindblom & Burke[2]
Zinkgruvan	700				1964	Henriques[3]
Uusimaa	710	810	3	5	1985	Schreuers & Westra[2]

[1]based on skarn mineral equilibria
[2]based on pelitic mineral equilibria
[3]based on sulfide exsolution textures

early granitoids behaved more like massifs (e.g. Stålhös, 1981) or more like diapirs (e.g. Stephansson, 1975) during the deformation. The timing between the two folding phases is thought to be very close. In fact, Stålhös (1981, 1984) suggests that the east-west synclines in the south of Bergslagen are due to accommodation of the enclave rocks between early granitoid massifs during the final stages of the first folding phase. In his view, only east-west shortening is required to explain both fold phases.

The major structures in northern and western Bergslagen are early isoclinal folds (F_1) and an associated well-developed axial planar foliation (S_1) that strikes north or northeast, and later cross folds (F_2) and an associated axial planar foliation (S_2) that strikes northeast to northwest. In southern and eastern Bergslagen, the later cross folds (F_2) are associated with an axial planar foliation that strikes mainly east-west (Allen et al., 1996). The dating of deformed and undeformed pegmatites indicates that the major folding occurred some time between 1.85 and 1.79 Ga (Welin and

Stålhös, 1986). In the south, however, the situation is more complex than can be explained by just two phases of folding, since many of the east-west synclines have been folded again. The younger folds are interpreted to be related to the emplacement of late and post-orogenic granitoids (e.g. Wikström, 1984; Wikström and Karis, 1991).

There is a pervasive subhorizontal to subvertical east or west trending lineation in the rocks of Bergslagen. The lineation in the leptites was first interpreted as an intersection lineation, produced by the intersection between S_1 and S_2 foliations (e.g. Stålhös, 1984). Recent work suggests that it is a stretching lineation associated with the second folding phase (Allen et al., 1996). A lineation in the late granitoids may reflect their diapiric motions (e.g. Stephansson, 1975). Clearly the lineations are not well understood and may well have multiple origins.

The timing and nature of the deformation, metamorphism, and emplacement of the granitoids are controversial subjects. There are two perspectives which are impossible to reconcile. In one school of thought (e.g. Oen et al., 1982; Oen, 1987; Rickard, 1988), intrusion of the early granitoids in combination with extensional tectonics and deep burial was responsible for the distribution of metamorphic facies in a "thermal sag basin". Partial melting of the bottom of the volcanic pile produced the early granitoids. The pervasive alteration of the leptites is one aspect of the regional metamorphism that was driven by both deep burial and heat from the upper level intrusions. The metamorphism in the basin was short lived and occurred sometime between 1.89 and 1.84 Ga (Rickard, 1988). Folding due to compressional tectonics followed peak metamorphism. The intrusion of late granitoids is loosely linked with regional retrograde metamorphism that followed the folding (Oen et al., 1982).

In the other school of thought, preferred by traditional Swedish geologists (e.g. Magnusson, 1936; Magnusson et al., 1962; Stålhös, 1976), the onset of regional metamorphism is associated with compressional tectonics which deformed the early granitoids. There is some disagreement

about the timing of the metamorphism. Peak metamorphism was once associated with intrusion of the late granitoids (e.g. Magnusson, 1936) which were thought to be anatectites. Since the late orogenic granitoids have not been folded, it follows that metamorphism must have outlasted deformation. The late granitoids are mainly 1.80 to 1.78 Ga in age (Welin, 1992) which allows for the possibility that peak metamorphism and the late granitoids are coeval. However, Stålhös (1976, 1981) associates peak metamorphism with the major folding phases that predate emplacement of the late granitoids. Allen et al. (1996) argue that annealing recrystallization that overprints fabrics developed during the major fold phases in amphibolite facies areas clearly demonstrate that metamorphism outlasted deformation.

The differences in opinion between the two schools have been attributed to research conducted in different enclaves. Geologists who work in the greenschist facies areas, most of them Dutch, emphasize the importance of extensional tectonics. Geologists who work in the amphibolite grade areas, most of them Swedish, believe that compressional tectonics better explains the features observed there. The more traditional view of the Swedish school is adopted in this study.

Post-Svecofennian events in Bergslagen are not clearcut. The Trans-Scandinavian porphyry belt, a batholith approximately 1.73 Ga in age (e.g. Nyström, 1992), truncates Bergslagen on its southwestern margin. The boundary is mapped as a series of faults. Metamorphism and folding related to the batholithic intrusions are not generally recognized in Bergslagen. However, it has been suggested that intrusion of post-orogenic granitoids and related folding in southern Bergslagen may be linked to development of the porphyry belt (e.g. Wikström, 1984, 1991).

Dolerite dike swarms trending ESE and NNE intruded in the middle Proterozoic, as early as 1.53 Ga (Welin, 1992). ESE striking ductile shear zones, one of which truncates Bergslagen to the north, postdate the dike swarms (Stephens and Wahlgren, 1993). The final regional feature is a set

of NNE striking, east-side-down brittle faults that are probably related to the late Proterozoic Vättern Rift Zone (e.g. Wikström and Karis, 1991).

The Zinkgruvan Basin

The Zinkgruvan Basin, named after Zinkgruvan ('the zinc mine"), is located in the southwestern region of Bergslagen, in the vicinity of Askersund, in the Finspång SV quadrant of the Swedish geological mapping system (Wikström and Karis, 1991). Major English language references for Zinkgruvan and its environs include papers by Johansson (1910), Kautsky (1955), Henriques (1964) and Hedström et al. (1989). Henriques provides a very detailed description of the rocks and geochemistry, and Hedström et al. point out features demonstrating the sedimentary-exhalative nature of the ore deposit.

The Zinkgruvan basin is an east-west trending, overturned syncline (Figure 4) outlined by an older leptite unit and a younger metasedimentary unit. The probable location of the axis of the syncline is marked by a major east-west striking dike. The axial plane of the syncline generally dips to the north. The Zinkgruvan ores occur on the northern flank of the syncline, in a 500 meter thick metatuff unit occurring between the leptite and metasediments. The metatuff is interbedded with a variety of marbles and skarns, quartzites, and disseminated and massive ores. The metatuff has not been assigned to either the leptite or the metasedimentary units. It is a distal volcanic ash-siltstone (Hedström et al., 1989; Allen et al., 1996). A discontinuous limestone marker horizon lies between the older leptite and younger metasedimentary units on the southern flank of the syncline. Its relationship to the ore-bearing skarns on the northern flank of the syncline is uncertain.

The syncline formed during the Svecofennian orogeny, but the age of the cross folds which control the outcrop patterns are in doubt. They may be related to the intrusion of late or

Figure 4. The geological map of the Zinkgruvan area taken from the Finspång SV quadrant map from the Swedish Geological Survey (Wikström and Karis, 1991). The width of the map is 9.5 km. The dike in the center of the map view approximately marks out the hinge of the E-W oriented synform. Metamorphic grade increases to the west of the Zinkgruvan mine (to uppermost amphibolite facies), and decreases to the south of the mine (to lower amphibolite facies).

Brown= synorogenic granitoid or *urgranit*.

Yellow= metavolcanic rock or *leptit*.

Light blue= metasedimentary rock.

Dark blue= marble.

Green= early orogenic basic intrusive.

Red= late orogenic granitoid.

Purple= postorogenic basic dike.

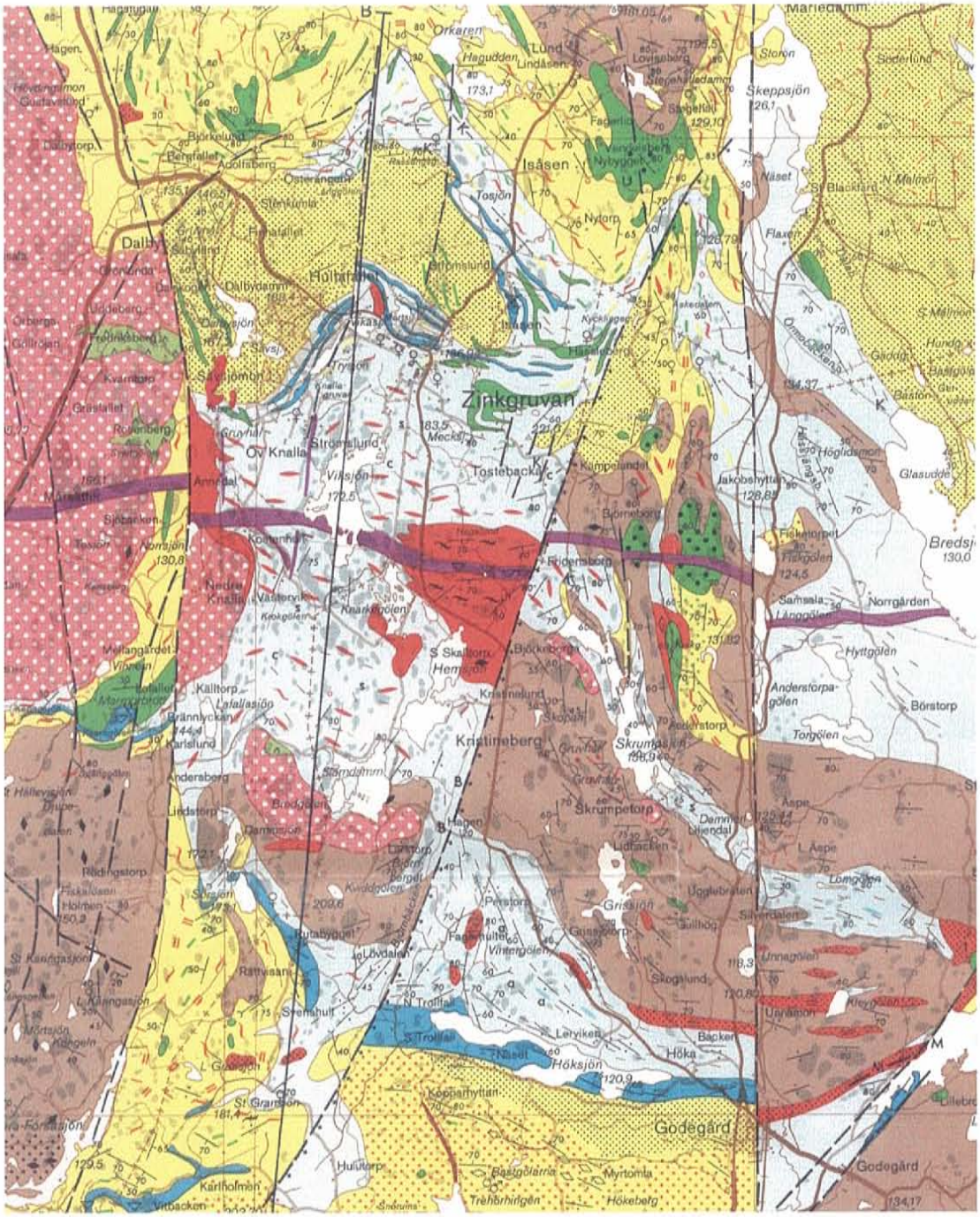
Zinkgruvan
Kristineberg
Godegård
Isåsen
Hulbarden
Dallhyttan
Ov Knalla
Tostebacka
Skrumpetorp
Skrumasjön
Grisasjön
Höksjön
Lerviken
Kopparhyttan
Orkaren
Lund
Skeppsjön
Tosjön
Nytorn
Strömslund
Viksjön
Kristineberg
Godegård

post-orogenic granites. Up to four fold phases are recognized in the mine area (Hedström and Wikström, 1986; Hedstrom et al., 1989): two early generations of isoclinal folds plunging shallowly to the east or west, and two later generations of open folds. One set of open folds plunges steeply to the north or northeast, and the other set plunges shallowly to the east. The isoclinal folds presumably represent the first and second folding phases of the Svecofennian orogeny described elsewhere in Bergslagen as discussed in the previous section. The later folds seem to be related to the intrusion of late or post-orogenic granitoids. Later folding in adjacent basins to the east of Zinkgruvan has been attributed to emplacement of the Finspång gneiss (Wikström and Aaro, 1986; Wikström and Karis, 1991). The Finspång gneiss formed as arms of a late or post-orogneic granite which were deformed by the episodic introduction of more magma.

Hedström et al. (1989) refer to both isoclinal folding phases as F_1, and both open folding phases as F_2, in keeping with the convention used in Bergslagen for labelling early isoclinal folds and later cross folds. However, this is confusing since the age of the later cross folds in the Zinkgruvan basin is probably not the same as elsewhere in Bergslagen. In this study the two isoclinal fold phases are called F_1 and F_2 and the two open fold phases are called F_3 and F_4.

The region was metamorphosed to the low pressure amphibolite facies, with temperatures possibly as high as 700°C at Zinkgruvan (Henriques, 1964). The southern flank of the syncline is not as metamorphosed as the northern flank, with andalusite rather than sillimanite present as an accessory mineral. The northeastern areas are more metamorphosed, with spotty occurrences of veined gneisses and migmatites. The basin, therefore, is subdivided into low, medium and high amphibolite facies regions (Wasström, 1995).

Fluid Inclusion Studies in Bergslagen

Several fluid inclusion studies on ore deposits within the Bergslagen region of south-central Sweden have led to different conclusions about fluid characteristics during peak and retrograde metamorphism. On one hand, van den Kerkhof (1987) and Beetsma (1992) propose that immiscible CO_2-CH_4-rich and saline H_2O-rich fluids characterize peak metamorphism at the Harmsarvet and Stollberg deposits. In each case, fluid immiscibility was sustained during retrograde metamorphism, with the H_2O-rich fluids becoming less saline by influence of meteoric waters, and the CO_2-rich fluids losing CO_2 content through carbonate precipitation over time. On the other hand, Lindblom and Burke (1988) and Åberg and Fallick (1993) attribute mixed CO_2-rich and H_2O-rich fluid inclusions to heterogeneous trapping at the Saxberget and Falun deposits. The H_2O-rich fluids at Saxberget are not sufficiently saline to coexist with immiscible CO_2-rich fluids. Immiscibility cannot explain the highly variable degree-of-fill and Th data obtained from Falun. Åberg and Fallick propose that pulses of fluid, alternately CO_2-rich and H_2O-rich, were recorded in complex fluid inclusion chronologies.

The question of fluid immiscibility is not the only point of difference between the studies. Isochores for the CO_2-rich inclusions at Harmsarvet and Stollberg intersect peak metamorphic conditions, whereas isochores for the CO_2-rich inclusions at Saxberget and Falun intersect the retrograde metamorphic PT-time path at pressures significantly lower than that of peak metamorphism. Either there are major differences in fluid evolution among the deposits of Bergslagen, or features of the fluid inclusions which enable workers to date them and assess their possible re-equilibration have been seriously neglected.

Some of the granitoids are mushroom shaped structures whose caps are deformed conformably with the enclosing rocks (e.g. Wikström, 1984, 1991). There is a gradual transition from gneiss in the caps to undeformed granite in the stems or cores, which is interpreted to be the result of multiple intrusion of similar magmas along particular conduits. Migmatization in the enclosing rocks is adjacent to the gneisses that represent initial intrusions; deformation in the gneisses is attributed to later intrusions.

Chapter II

Methods of Investigation

Microthermometry

Fluid inclusions were examined using doubly polished, 200 μm thick petrographic sections. Microthermometric results were obtained on a Linkam THM600 heating and freezing stage. Temperatures attained with this stage range between -180 and +600°C. The stage was calibrated for temperature using pure potassium dichromate (melting point 398°C) and triple distilled water (melting point 0.0°C) as standards. A synthetic H_2O-CO_2 fluid inclusion standard was used for calibration on the melting point (-56.6°C) of CO_2. Freezing cycle temperature determinations on standards typically have an error of about 0.2° C on this apparatus; heating cycle temperatures have an error of less than 5°C (MacDonald and Spooner, 1981).

Phase volume ratios in fluid inclusions were determined by measuring the dimensions of the inclusions and the phases within them with an optical micrometer. The shapes of regular inclusions were assumed to be doubly terminated negative quartz crystals, and irregular inclusions were approximated as clusters of spheres and six-sided prisms. Bubbles were assumed to be spherical. Daughter minerals were assumed to be parallelepipeds. Mineral identifications were made using laser Raman microspectrometry at the University of Stockholm.

Initial salinity estimates were made in equivalent weight percent NaCl using the freezing point depression curves of Bodnar (1993) for ice melting, and Collins (1979) for clathrate melting. Ratios between NaCl and $CaCl_2$ were estimated, and the total salinity revised, using hydrohalite final melting temperatures (Oakes et al., 1990) whenever hydrohalite final melting could be observed. It was assumed that the $NaHCO_3$ component behaves more like NaCl than $CaCl_2$, therefore,

hydrohalite melting reflects the relative amounts of $CaCl_2$ and $NaCl+NaHCO_3$. In nahcolite-bearing inclusions, ratios between NaCl and $NaHCO_3$ and the total salinity were estimated from ice final melting temperatures (Borisenko, 1974), provided that ice melting occurred at or below -2.3°C (the ice-nahcolite eutectic).

Densities for the H_2O-rich phase were approximated using the equation of Potter and Brown (1977) for NaCl solutions. It was assumed that substitutions of other salts for NaCl in the fluids do not significantly change the density calculation. Densities of 2.21 and 2.71 g/cm^3 were used where needed for nahcolite and calcite, respectively (Palache et al., 1951). Densities for the CO_2-rich phase were estimated using the approach of Burruss (1981) and the diagrams of Thiery et al. (1994).

Minimum pressure determinations and isochore calculations were made on an electronic spread-sheet using the equations of Bowers and Helgeson (1983). It was assumed that substitution of other salts for NaCl does not significantly alter the isochores in the system H_2O-CO_2-NaCl.

Microstructural Analysis

Doubly polished petrographic sections 200 μm thick were used in this study. The sections were oriented with the principal foliation perpendicular to the section; the orientation relative to lineation could not be determined. The quartz subjects were examined for distinctive petrographic features, such as deformation bands and lamellae, and obvious patterns of recrystallization, such as core-and-mantle structures. The term *deformation lamellae* is reserved for thin, parallel sided, planar microstructures which are best observed in plane light with the substage diaphragm nearly closed. *Deformation bands* are thicker, birefringent, planar domains which are obvious under crossed nichols; exsolution inclusions decorating the band boundaries may highlight them in normal light. *Exsolution inclusions* are micron-sized or smaller, monophase, presumably aqueous

inclusions which form by mobilization and coagulation of structural water in quartz as a result of ductile deformation (Wilkins and Barkas, 1978). Deformation lamellae are significantly thinner (<5 μm in width) than deformation bands (tens of μm in width).

In the study of phenocrysts, an attempt was made to characterize fabric elements such as grain size and orientation. The aspect ratio, an indicator of phenocryst shape in the plane of the section, was obtained from the ratio between length and width. The length of each phenocryst was measured as its single longest dimension and the width was measured as the widest dimension perpendicular to the length. The angle between the long direction of a phenocryst and the trace of the foliation was used to describe the orientation of the phenocryst.

Relative fluid inclusion chronology was obtained by careful observation of the relationships between the fluid inclusion planes (FIP) and other microstructures in the host quartz. The following criteria and assumptions were applied: 1) transposed FIP are older than FIP that are not transposed; 2) older FIP tend to have fewer, smaller, more nearly negative-crystal-shaped fluid inclusions than do younger FIP; 3) FIP that are crosscut by new grain boundaries are older than FIP which crosscut the same grain boundaries; 4) FIP in identical orientations within the same phenocryst resulted from the same resolved stress and are approximately the same age; 5) FIP whose orientation is uniform in all phenocrysts in one thin section are the same age and can be related to a final stage of deformation; 6) FIP that are deflected toward other FIP are younger than the straighter FIP; and 7) FIP that postdate recrystallization may be refracted between grains or along grain boundaries. Further elaboration on these points can be found in discussions by Crawford (1981), Touret (1981) and Roedder (1984, p. 344).

FIP orientations were found using the method of Boullier and Robert (1992). Orientations of FIP in the phenocrysts in each section were measured relative to a single reference direction, i.e. one edge of the petrographic section. Horizontal displacement of a FIP between the upper and

lower surfaces of the section was measured with an optical micrometer. The "dip" of the FIP was found from the ratio between section thickness (t) and displacement (d); t/d is the tangent of the "dip". Most of the error in measurement is associated with shallow dips since the edges of FIP are more difficult to see in nearly flat planes. The "strike" was determined in a straightforward manner by rotating the microscope stage. A few phenocrysts were examined on the universal stage to determine the orientation of the quartz c axis with respect to the FIP and other microstructures. The shareware computer program StereoNett 2.20 (Duyster, 1998) was used to plot the orientation data in stereographic projection. The microstructural data were plotted on lower hemisphere equal-angle stereograms.

The terminology used for FIP geometry is similar to that proposed by Simmons and Richter (1976) and Kranz (1983) for microcracks. An *intragranular* FIP does not intersect grain boundaries. A *transgranular* FIP extends across one grain, from grain boundary to grain boundary. An *intergranular* FIP crosses one or more grain boundaries and extends across more than one grain. The fluid inclusion planes are assumed to be mode I, stress induced cracks which were healed.

Parallel linear clusters of fluid inclusions which are arrayed along a common trend are *transposed* FIP. Transposed FIP are intragranular or transgranular FIP whose original fluid inclusions have been stretched and necked down in one direction (Swanenberg, 1980). The degree of dispersion of the fluid inclusion plane is in part a function of the angle between the original FIP and the stretch direction.

A number of interesting fluid inclusion types encountered in this study do not occur on typical FIP. Since they are not addressed in other fluid inclusion studies and have no descriptive names, some names are introduced here. Micron-sized monophase inclusions that congregate around grain boundaries are *migration inclusions*. They are assumed to be mobilized exsolution inclusions. *Satellite inclusions* are small inclusions (<6 μm) that decorate mineral inclusions in the quartz.

They tend to be prominent in strain shadows on one side of the mineral inclusions. *Ghost trails* are poorly defined intragranular FIP which appear to remnants of former intergranular FIP. Two or more ghost trails may lie along the same plane in a single large quartz grain.

Quadrupole Mass Spectrometry

Volatile analyses were made on a Balzers® QMS 420 model quadrupole mass spectrometer (QMS) in crush-fast-scan mode as described by Ruff (1993) and Norman et al. (1997). A QMS differs from a conventional mass spectrometer in using an oscillating electric field, rather than a magnetic field, to filter out ionized particles of a given mass/charge (m/e) ratio. In the crush-fast-scan technique the QMS continually records a time-intensity spectrum for a finite number of m/e peaks. A mineral grain is gently crushed in the vacuum and its fluids are analyzed by the QMS as they are pumped away, resulting in a pulse on the time-intensity spectrum. The contents of an aqueous inclusion 40 μm in diameter (on the order of $1x10^{-7}$ μmoles of fluid) can be analyzed with 10% or better precision given the sensitivity of the QMS. The grain is crushed in small increments so that only the fluids from one or two inclusion trails are liberated, and so that the QMS is not overwhelmed with fluids. Each sample yields 5 to 15 gas analyses depending upon the density of the fluid inclusion population within the grains. The relative proportions of the fluid species are determined from the m/e peaks which make up the pulse, and the results are reported as normalized molar compositions. Details of the procedure followed in this study are described below.

Information on the QMS is not easily located, therefore, the interested reader is directed to papers by Barker and Smith (1986), Norman and Sawkins (1987), Garney and Kesler (1995) and Williams (1996) for discussions of other QMS systems and extraction methods used for analyzing gases in fluid inclusions. The crush-fast-scan method used here is unique.

The Spectrometer

The QMS consists of a rhenium ionizing filament, a quadrupole mass filter and a secondary electron multiplier (SEM) with one Faraday cup detector. Operating parameters and data aquisition on 16 channels are controlled with QuadStar® software run on a personal computer. A Balzers® model QMI 420 multi-channel analyzer serves as the interface between the computer and the QMS. The filament is operated at about 100 eV. The electronics are designed in such a way that ions are separated out in the order of increasing atomic weight, for a total m/e range of 1 to 200. The resolution of the N_2 (28) peak is about 0.25 at half peak height (or 0.40 at 0.1 peak height) for normal operations. Detection limits are on the order of 1×10^{-10} Torr (Balzers, 1983) or about 5 ppm molar (Ruff, 1993).

Calibration of the QMS is done with Scott's® standard gas mixtures introduced into the QMS at an inlet pressure of 1×10^{-6} Torr. Air is used as a standard for N_2, O_2 and Ar. Triple distilled water is used as an H_2O standard. A cracking outline, or pattern of ion current intensities, is obtained for each species. The sensitivities of the individual gases are calculated against N_2. An in-house standard, Hansonburg fluorite, is run periodically to check for drift in the calibration values.

Analytical Procedure

Hand-picked mineral separates were washed in a 90°C 10% NaOH solution, dried in an oven at temperatures less than 100°C to prevent excessive He loss, and stored in air-tight containers to prevent water adsorption. An analytical sample consisted of 5 to 7 grains 1-3 mm in size. Prior to loading into the crushing chambers, the samples were reheated briefly to about 100°C to speed up water desorption and the pump down process. The crushing chambers (which are modified MDC® vacuum valves fitted with two steel grinding plates) and the loaded samples were heated to

nearly 200°C for 8-24 hours until a vacuum of $2x10^{-7}$ Torr was attained in the system. Each sample provided between 5 and 15 analyses. Analyses were made at room temperature.

The 16 channel QMS was set up to detect twelve m/e peaks at 2 (H_2), 4 (He), 14 (N_2), 15 (CH_4 fragments), 18 (H_2O), 28 (N_2), 32 (O_2), 34 (H_2S), 40 (Ar), 41 (organic fragments), 44 (CO_2) and 48 (SO_2 fragments). The spare channels recorded background spectra at 1.5 and 2.5, and 3.5 and 4.5 in order to obtain more accurate results for the H_2 and He signals. Two peaks, 14 and 28, were needed to resolve the N_2 signal since the CO_2 spectrum overlaps on 28 and the CH_4 spectrum overlaps on 14. The QMS was configured to cycle through the 16 channels in about 250 milliseconds. The sensitivity of each channel was adjusted using the secondary electron multiplier (SEM) to best fit the size of the peak. For example, Ar, H_2S and SO_2 peaks were measured at 1000 times the sensitivity used on the H_2O peak.

The QMS output was recorded both graphically and numerically. The numerical output was read by an unpublished data reduction program written in QBasic by David Norman which calculates 1) peak areas over background, 2) a water adsorption correction, 3) corrections for QMS sensitivities and 4) a normalized molar fluid analysis. A peak-stripping algorithm is used, i.e. peaks with no interference are used to resolve peaks with interference from multiple species. A precision of a few percent is typical for the major fluid species (H_2O, CO_2, CH_4, N_2); precision for the minor species is an order of magnitude worse. The accuracy of analyses are not known because fluid inclusion standards are not available.

O_2 was detected in many of the fluid analyses. It is attributed to air adsorbed onto intergranular surfaces and inside naturally decrepitated fluid inclusions. An air correction was made to each fluid analysis in order to remove O_2. The N_2/O_2 and Ar/O_2 ratios of modern air (3.728 and 0.04459, respectively) were used to reduce the number of N_2 and Ar moles attributed to air

contamination. The final analysis, without O_2, was renormalized to 100%. All air correction factors were made on a spreadsheet.

Geochemical Modeling

The equilibrium constants for geochemical reactions were calculated using the FORTRAN77 computer program and database supplied with SUPCRT92 (Johnson et al., 1992). Copies of SUPCRT92 can be obtained from James W. Johnson at *johnson@s05.es.llnl.gov*. The SUPCRT92 program was compiled using Microsoft® Fortran Power Station 1.0 in DOS mode. The only modification required to make the program run was to reset the variable NBACK=12.

Thermodynamic data for nahcolite, hydrophylite, kalicinite, natrite and portlandite were listed in Kelley (1960) or Knacke et al. (1991). Thermodynamic parameters for some aqueous species ($CaOH^+$, $Ca(OH)_2^a$, $NaHCO_3^a$, $Na_2CO_3^a$, $NaCO_3^-$) were predicted using the correlation method of Shock and Helgeson (1988) and the parameters for correlative species listed in Tanger and Helgeson (1988). Parameters for the unlisted mineral and aqueous species were calculated for the purpose of finding out whether log K values warranted consideration of a given species in the thermodynamic modeling of the H_2O-CO_2-NaCl-$NaHCO_3$-$CaCl_2$ system.

Chapter III

Fluid Inclusion Evidence for Sodium Bicarbonate Fluids, Low-Pressure High-Temperature Metamorphism and Isobaric Cooling of the Zinkgruvan Basin, Bergslagen, Sweden

Introduction

Few studies of fluid inclusions in metamorphic rocks have addressed low-pressure high-temperature (LPHT) terranes, particularly those of Proterozoic age (e.g. Phillips, 1980; Schreurs, 1984; Olsen, 1987; Blom, 1988). In this paper, the results of a fluid inclusion study in an early Proterozoic LPHT terrane, the Zinkgruvan basin in Bergslagen, south-central Sweden, are reported. The Bergslagen region is distinctive in being composed of extremely thick felsic metavolcanic rock sequences that host numerous base-metal ore deposits. Previous fluid inclusion studies are limited to the ore deposits. In contrast, this study addresses fluid inclusions in relic quartz phenocrysts in the felsic metavolcanic rocks in order to characterize metamorphic fluid evolution in the basin hosting the Zinkgruvan ore deposit.

Fluid inclusion studies on the Bergslagen ore deposits have led to different conclusions about fluid characteristics during peak and retrograde metamorphism. On one hand, van den Kerkhof (1987) and Beetsma (1992) propose that immiscible CO_2-CH_4-rich and saline H_2O-rich fluids characterize peak metamorphism at the Harmsarvet and Stollberg deposits respectively. Each maintains that fluid immiscibility was sustained during retrograde metamorphism, with the H_2O-rich fluids becoming less saline by influence of meteoric waters, and the CO_2-rich fluids losing CO_2 content through carbonate precipitation over time. On the other hand, Lindblom and Burke (1988) and Åberg and Fallick (1993) attribute the assemblage of carbonic and aqueous fluid inclusions to heterogeneous trapping at the Saxberget and Falun deposits. Åberg and Fallick

propose that pulses of fluid, alternately CO_2-rich and H_2O-rich, were recorded in complex fluid inclusion chronologies.

This study is a significant departure from the previous ones in that secondary fluid inclusions in quartz from the footwall rocks of an ore deposit are targeted. Samples were examined from locations in the Zinkgruvan basin metamorphosed to different grades as indicated by an andalusite-sillimanite isograd and localized migmatization. The goal is to characterize fluids associated with regional metamorphism and not influenced by the presence of ore bodies.

Local and Regional Geology

The Zinkgruvan basin consists of a deformed east-west trending synform developed in a sequence of early Proterozoic volcanic and clastic strata within the Svecofennian domain of southern Sweden (Wikström and Karis, 1991). The sequence is divided into a lower formation of metamorphosed felsic pyroclastic rocks and an upper formation of metagreywackes, although the rock types are mixed in with one another in subordinate amounts. Numerous interlayered skarn bands, marbles and metapelites are present throughout the sequence. Exhalative strata and mineralized horizons, including the Zinkgruvan massive sulfide deposit, occur in the top of the metavolcanic unit and in the metasedimentary rocks above.

The basin rocks were metamorphosed to low pressure amphibolite grade during Svecofennian events, approximately 1.85 to 1.79 Ga (Stålhös and Welin, 1986). The andalusite-sillimanite isograd is used to divide the region into lower and upper amphibolite areas. The upper amphibolite area is subdivided further on the basis of localized migmatitization and pegmatite veining that occur in the east (Figure 5). Rickard (1988) suggests minimal conditions of 650°C at 3.5 kbar for the onset of migmatitization in Bergslagen since sillimanite-muscovite assemblages are prevalent in the

Figure 5. Geology of the Zinkgruvan basin after Wikström and Karis (1991). Outcrop locations for samples HÖK and 103 are indicated with a ■. The eastern shaft of Zinkgruvan is located with a ◪. Samples 4Z and DBH are from sites underground in the mine.

The Zinkgruvan basin is an early Proterozoic, E-W trending synform with younger metasedimentary rocks (white) forming the core and older metavolcanic rocks (light grey) forming the flanks. A middle Proterozoic aged basic dike (black) approximately marks the hinge of the synform. Synorogenic granitoids (medium grey) intruded both metavolcanic and metasedimentary rocks prior to formation of the synform. Late and post-orogenic granitoids are shown in dark grey. The N- to NE-striking faults are late Proterozoic in age.

The andalusite-sillimanite isograd (dotted line) outlines the area of lower amphibolite facies metamorphism. Upper amphibolite facies rocks are limited to the northern end of the northeast fault block, in the region of sample 103. The remaining areas were generally metamorphosed to middle amphibolite facies.

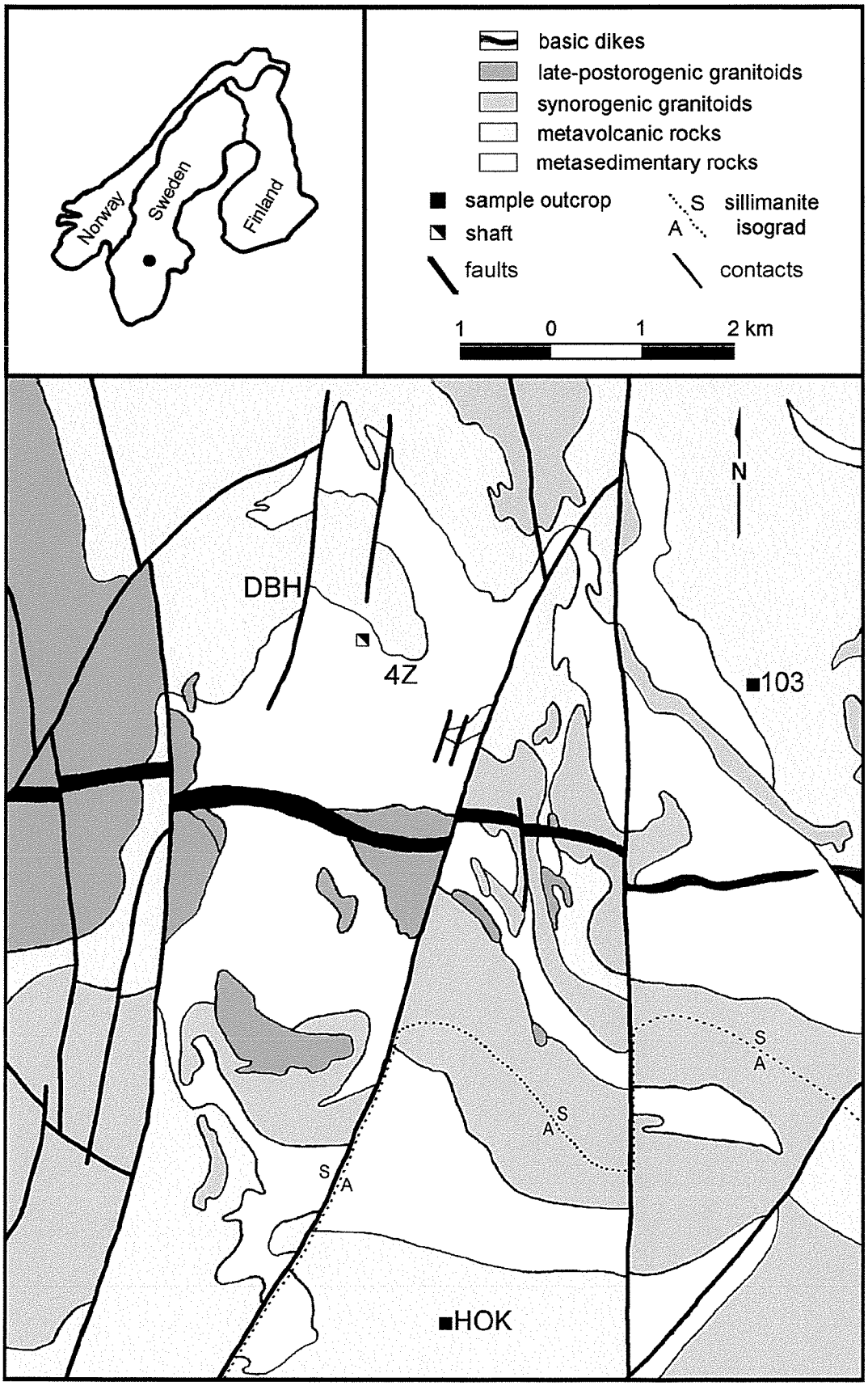
Norway
Sweden
Finland
basic dikes
late-postorogenic granitoids
synorogenic granitoids
metavolcanic rocks
metasedimentary rocks
sample outcrop
shaft
faults
S
A
sillimanite isograd
contacts
1 0 1 2 km
N
DBH
4Z
103
HOK

migmatites. A lack of kyanite in the metapelites suggests an upper pressure limit of about 5 kbar. The skarn mineral assemblage anorthite-diopside at Zinkgruvan is consistent with temperatures over 520°C at 3.5 kbar (Ferry, 1976).

Several phases of deformation are apparent in the Zinkgruvan basin. Two early phases of isoclinal folding, which are associated with the formation of the basin, are overprinted by two phases of open crossfolds, which control local outcrop patterns (Hedström and Wikström, 1986). Late deformation is characterized by prominent north-striking faults. There are several granitoids within and surrounding the basin that are synorogenic to postorogenic in age (Wikström and Karis, 1991). The open folding phases and peak metamorphism are attributed to emplacement of the late granitoids (Hedström and Wikström, 1986) at about 1.80 to 1.78 Ga (Welin, 1992).

The most recent tectonic setting proposed for Bergslagen, on the basis of volcanic facies analysis, is a back-arc rift developed on a continental margin (Allen et al., 1996). Most of the massive sulfide ore deposits in Bergslagen, including Zinkgruvan, occur at a transition in rock types representing extensive subaqueous volcanism followed by rapid subsidence. The regional geothermal gradient is thought to have been very high, on the order of 50°C/km or more (Rickard, 1988).

Metamorphism in Bergslagen ranges from greenschist facies to the amphibolite-granulite transition. Granulites are rare in Bergslagen but are common in southwest Finland. The Svecofennian domains of Bergslagen and southwest Finland are thought to be continuous beneath the Baltic Sea, so here Bergslagen is considered to be part of a larger granulite-bearing terrane. Furthermore, metamorphism at the Zinkgruvan mine may have exceeded 700°C (Henriques, 1964), thus the peak metamorphic conditons are higher than those for the Orijarvi amphibolites and closer to the West Uusimaa granulites of Finland (Schreurs and Westra, 1985). Bergslagen has tectonic features that are typical of LPHT granulite-bearing terranes for which isobaric cooling, or anticlockwise PT-time paths, have been proposed, specifically early isoclinal and late open styles of folding, and late S-type orogenic

granitoids associated with the highest metamorphic facies. In the model of Harley (1989), these features can be attributed to specific processes in the development of granulite-bearing terranes. Isoclinal folds are associated with thickening of relatively hot extended crust by thrusting. Rocks of low metamorphic grade are preserved in the upper crust. In the lower crust, melting of tectonically buried rock leads to the formation of S-type granitoids. Diapiric rise of the granitoids to mid-crustal levels results in open folds. Rocks of high metamorphic grade occur in the middle crust. The high temperatures attained at peak metamorphism are due both to "preheating" in an extensional basin and heating from the mid-crustal intrusions. The Harley (1989) model seems to fit the geologic setting of Bergslagen rather well, except that granulites *per se* have not been identified in Bergslagen.

Methods

Fluid inclusions were examined in relic quartz phenocrysts using doubly polished, 200 μm thick petrographic sections. Microthermometric results were obtained on a Linkam THM600 heating and freezing stage, properly calibrated for temperature using pure standards. Freezing cycle temperature determinations on standards typically have an error of about 0.2° C on this apparatus; heating cycle temperatures have an error of less than 5°C.

Liquid degree of fill was estimated using the diagrams of Shepherd et al. (1985) in solid-free fluid inclusions. Phase volume ratios in solid-bearing inclusions were determined by measuring the dimensions of the inclusions, and the phases within them, with an optical micrometer. The shapes of regular inclusions were assumed to be doubly terminated, negative quartz crystals, and irregular inclusions were approximated as clusters of spheres and six-sided prisms. Bubbles were assumed to be spherical. Included minerals were assumed to be parallelepipeds.

Initial salinity estimates were made in equivalent weight percent NaCl using the freezing point depression curves of Bodnar (1993) for ice melting, and Collins (1979) for clathrate melting. Salinity estimates in $NaHCO_3$-bearing inclusions were refined using the diagrams of Borisenko (1974), provided that ice melting temperatures were less than -2.3°C (the ice-nahcolite eutectic). Salinity estimates for $CaCl_2$-bearing inclusions were refined using the diagrams of Oakes et al. (1990), only if hydrohalite temperatures were less than -21.8°C (the hydrohalite-nahcolite eutectic). Densities for the H_2O-rich phase were approximated using the equation of Potter and Brown (1977) for NaCl solutions. It was assumed that Potter and Brown's density equation can also be used to find the density of NaCl-$NaHCO_3$-$CaCl_2$ solutions. Densities for the CO_2-rich phase were estimated using the approach of Burruss (1981). A density of 2.21 g/cm^3 was used for solid $NaHCO_3$ (Palache et al., 1951). Minimum pressure determinations and isochore calculations were made using the equations of Bowers and Helgeson (1983).

Fluid inclusion plane (FIP) orientations were determined using the method of Boullier and Robert (1992). Fluid inclusion chronology was obtained by careful observation of the relationships between the FIP and other microstructures in the host quartz. The following criteria and assumptions were employed: 1) transposed FIP are older than FIP that are not transposed; 2) older FIP tend to have fewer, smaller, more nearly negative-crystal-shaped fluid inclusions than do younger FIP; 3) FIP which are crosscut by new grain boundaries are older than FIP that crosscut the same grain boundaries; 4) FIP in identical orientations within the same phenocryst resulted from the same resolved stress and are the same age; 5) FIP whose orientation is uniform in all phenocrysts in one thin section are the same age and can be related to a final stage of deformation; 6) FIP that are deflected toward other FIP are younger than the straighter FIP; 7) FIP that postdate recrystallization may be refracted between grains or along grain boundaries.

Quantitative volatile analyses were made on a quadrupole mass spectrometer (QMS) in crush-fast-scan mode as described by Norman et al. (1997). Phenocryst samples 1 to 2 grams in weight were cleaned in NaOH and distilled water, then heated to 180°C prior to crushing at room temperatures to remove adsorbed volatiles. Phenocrysts were crushed in vacuum and the liberated fluids were analyzed as they were pumped from the system. Multiple crushes were performed on the same sample. The sensitivity of the analysis is such that only about $1x10^{-7}$ moles of vapor, comparable to the volume contained in an inclusion 40 μm in diameter, are measured. Each analysis represents the opening of smaller inclusions on only one or two trails. The relative proportions of H_2O, CO_2, CH_4 N_2, Ar, H_2S and C_3H_8 are measured. Precision for gaseous species varies from 5 to 20%, and depends upon the species, the size of the volatile sample, the amount of the species in the sample and the water/gas ratio. The precision of the water/gas ratio is about 1%.

Samples

Samples for fluid inclusion study were obtained from three different regions of the Zinkgruvan basin (Figure 5). Sample HÖK originates from the southern limb of the synform and was metamorphosed to lower amphibolite (andalusite) facies. Samples DBH and 4Z were collected on the northern limb of the synform, in the vicinity of the Zinkgruvan massive sulfide deposit, and are middle amphibolite (sillimanite) facies rocks. Sample 103 comes from a partially migmatitized outcrop of upper amphibolite grade on the northern limb of the synform, to the east of all the other samples. The sample protoliths are potassically altered quartz-crystal tuff, and the principal metamorphic minerals are quartz, chlorite-altered biotite and sericite-altered potassium feldspar (Wasström, 1995).

Relic phenocrysts in HÖK are principally mantled quartz porphyroclasts with 10 to 90 percent recrystallized material. The regular hexagonal outlines and resorption embayments can still be seen

on many phenocrysts in spite of recrystallization. Unrecrystallized or "igneous" quartz is readily identified by the presence of deformation bands and plentiful exsolution fluid inclusions. Exsolution inclusions result from the mobilization of structural water within the deformed quartz (Wilkins and Barkas, 1978). Recrystallization removed deformation bands and exsolution inclusions. Recrystallized or "metamorphic" quartz is clear, and some grains exhibit fine deformation lamellae.

In the higher grade rocks the phenocrysts are totally recrystallized and sharp phenocryst faces are preserved in only a few individuals in samples DBH and 4Z. Symmetrical quartz porphyroclast tails, although weakly developed, may be seen on some sample 103 relic phenocrysts. Recrystallized grains in sample 103 are commonly rectilinear in outline, suggesting recrystallization in the high quartz field.

Quartz recrystallization was continuous with protracted deformation. A crude division between two generations of recrystallized quartz grains can be made where both older and younger recrystallized grains occur in the same phenocryst. These are called simply "younger quartz" and "older quartz" for lack of any better terms. Younger quartz grains are relatively strain free, or exhibit undulatory extinction only, and have few if any fluid inclusion trails. Older quartz grains commonly have one or two intersecting plastic deformation structures and many fluid inclusion trails.

Fluid Inclusions

Fluid inclusions in the relic quartz phenocrysts occur in many microstructural settings. Inclusions are, hence, classified according to their microstructural environment and overall form and not by their composition. This greatly aids in assigning relative ages to the various fluid inclusion types. Cartoons of the various fluid inclusions are shown in Figure 6. Fluid inclusion characteristics and microthermometry results are provided in Table 2.

Figure 6. Cartoons of various fluid inclusion types discussed in the text are shown for the lower amphibolite facies sample (a) and the upper amphibolite facies sample (b).

In (a) the fluid inclusion types include transposed fluid inclusions (T) and exsolution inclusions (E). Type IA fluid inclusions occur along deformation band boundaries (horizontal), which are decorated with exsolution inclusions. The older quartz has birefringent deformation bands whereas the younger quartz has neither deformation bands nor exsolution inclusions.

The relationships between quartz grain boundaries and fluid inclusion planes for type I fluid inclusions are shown in (b). The upper left grain is interpreted to be growing at the expense of its neighbors. Type IB and IC fluid inclusions are removed in the process. Rootless fluid inclusion planes, and those radiating out from the biotite inclusion (colored grey) in the upper left grain, are interpreted to be relic type IB inclusions. Type III inclusions are deflected along grain boundaries, but otherwise exhibit a preferred orientation in thin section.

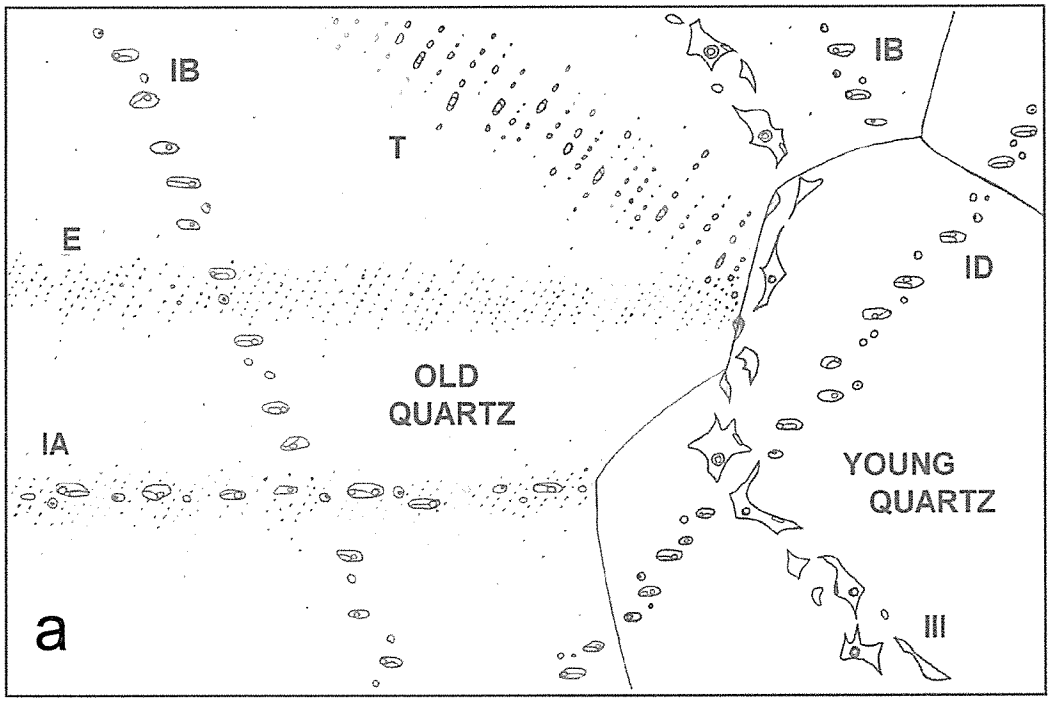
IB
T
IB
E
ID
OLD
QUARTZ
IA
YOUNG
QUARTZ
a
III

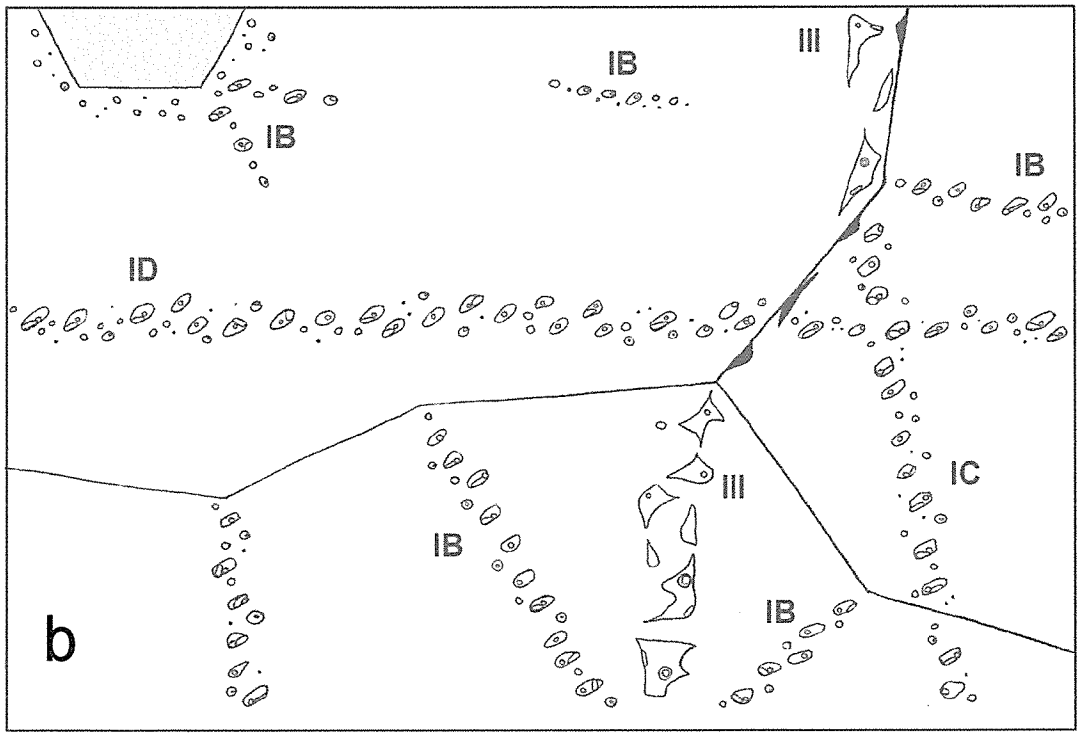
III
IB
IB
IB
ID
IC
III
IB
IB
b

Table 2. Fluid inclusion characteristics and microthermometry. L = length, V = volume, Bub = vapor bubble, Liq = liquid phase, Nah = nahcolite daughter mineral, Th = homogenization temperature, Tm = melting temperature, Te = first melting temperature, clath = clathrate, hydro = hydrohalite, TDS = total dissolved solids.

Type	Sample	L (μ)	V (μ^3)	Volume percents			Th (°C)	Tm ice (°C)	Tm clath (°C)	Tm hydro (°C)	Te (°C)	Salinity (eq. wt. % NaCl)	Molality (moles/ kg H_2O)	Density (cm^3)	Weight percents			Molar volume (cm^3)	TDS (wt. %)
				Bub	Liq	Nah									NaCl	$CaCl_2$	$NaHCO_3$		
IA	HÖK	5	16	5	95	0	555	-2.3				3.87	0.688	1.024				18.40	0.81
IA	HÖK	5	17	10	84	6	546	-0.9				1.57	0.272	1.008	100	0	0	20.48	1.77
IA	HÖK	3	4	2	98	0	491	-5.1				8.00	1.487	1.054	100	0	0	15.76	1.61
IA	HÖK	3	4	30	70	0	471	-5.6		-23.0		9.3	1.753	1.064	91	9	0	21.16	1.63
IA	HÖK	4	4	30	57	13	459	-0.9				1.57	0.272	1.008	100	0	0	24.42	4.68
IA	HÖK	4	9	20	73	7	458	-0.8				1.40	0.242	1.007	100	0	0	22.71	2.23
IA	HÖK	7	25	15	85	0	457			-23.0	-61.6								
IA	HÖK	4	17	5	87	8	447			-25.0									
IA	HÖK	4	8	5	89	6	441												
IA	HÖK	5	16	10	86	4	440												
IA	HÖK	4	10	2	58	40	437	-1.0				1.74	0.302	1.009	100	0	0	15.75	11.62
IA	HÖK	4	10	2	98	0	435												
IA	HÖK	7	4	10	63	27	433												
IA	HÖK	3	3	2	89	9	423												
IA	HÖK	7	65	2	87	11	406												
IB	103	6	44	2	81	17	357	-6.5	8.8	-22.6		12.52	2.446	1.088	80	0	20	17.44	4.36
IB	103	5	7	2	84	14	336	-5.1				11.75	2.276	1.082	70	0	30	14.16	4.45
IB	103	3	3	2	87	11	322	-4.1				10.17	1.935	1.070	56	0	44	14.73	3.64
IB	103	4	19	12	75	13	301	-6.9		-22.6		12.74	2.496	1.089	81	0	19	15.40	4.71
IB	4Z	5	31	2	98	0	368	-0.3				0.53	0.091	1.001	100	0	0	20.55	0.12
IB	4Z	8	43	2	53	35	358	-0.1				0.18	0.030	0.998	100	0	0	18.64	11.65
IB	4Z	6	36	8	92	0	350	-0.6				1.05	0.182	1.004	100	0	0	21.21	0.23
IB	4Z	6	68	2	91	7	321	-5.2				11.81	2.289	1.082	70	0	30	14.36	3.22
IB	4Z	6	8	2	98	0	320	-6.0				9.21	1.734	1.063	100	0	0	15.29	1.83
IB	4Z	12	85	10	68	22	318	-3.0	5.0			5.00	0.900	1.032	31	0	69	15.87	6.19
IB	4Z	4	14	2	98	0	313	-3.3				5.41	0.978	1.035	100	0	0	16.98	1.11

Table 2. (Continued.)

Type	Sample	L (μ)	V (μ³)	Volume percents Bub	Liq	Nah	Th (°C)	Tm ice (°C)	Tm clath (°C)	Tm hydro (°C)	Te (°C)	Salinity (eq. wt. % NaCl)	Molality (moles/ kg H_2O)	Density (cm^3)	Weight percents NaCl	$CaCl_2$	$NaHCO_3$	Molar volume (cm^3)	TDS (wt. %)
IB	4Z	8	22	2	82	16	310												
IB	DBH	13	49	5	79	16	383	-0.3		-22.7	-69.5	0.53	0.091	1.001	76	24	0	19.24	4.20
IB	DBH	17	317	2	66	32	335	-3.7		-23.6		9.52	1.799	1.065	52	20	28	14.92	8.39
IB	HÖK	5	51	10	90	0	390		7.1			5.59	1.012	1.037				18.24	1.15
IB	HÖK	4	7	10	73	17	388												
IB	HÖK	10	18	35	65	0	385												
IB	HÖK	6	52	5	76	19	385		6.6			6.46	1.181	1.043				17.77	1.31
IB	HÖK	4	11	5	95	0	373	-0.2				0.35	0.061	1.000	100	0	0	21.31	0.08
IB	HÖK	5	27	10	87	3	349			-24.0		1.57	0.272	1.008	70	30	0	20.84	1.01
IB	HÖK	3	5	8	92	0	335					1.57	0.272	1.008	100	0	0	20.73	0.34
IB	HÖK	5	4	5	95	0	335	-0.4		-23.3	-63.4	0.9	0.155	1.003	99	1	0	20.87	0.16
IB	HÖK	4	126	10	85	5	305												
IB	HÖK	10	7	2	95	3	305	-2.1				3.55	0.629	1.022	100	0	0	20.59	1.52
IB	HÖK	8	13	2	86	12	299	-1.7	8.2			3.57	0.634	1.022	100	0	0	17.17	3.26
IB	HÖK	5	9	2	98	0	284	-1.3				2.24	0.392	1.013	100	0	0	19.04	0.48
IC	103	4	3	7	78	15	273	-2.7				7.59	1.404	1.051	18	0	82	16.24	4.22
IC	103	8	56	5	85	10	263	-3.7				9.52	1.799	1.065	47	0	53	15.43	3.40
IC	103	9	66	5	85	10	262	-15.8		-22.8		19.29	4.085	1.140	94	0	6	13.12	4.97
IC	103	3	3	5	95	0	262	-0.4				0.70	0.121	1.002	100	0	0	20.95	0.15
IC	103	4	4	2	87	11	257	-4.7				11.19	2.154	1.078	65	0	35	14.41	3.80
IC	103	5	18	17	71	12	253	-7.2				12.92	2.536	1.091	78	0	22	16.25	4.66
IC	103	5	14	5	86	9	252	-0.3			-55.3	0.53	0.091	1.001	100	0	0	20.04	2.31
IC	103	5	23	2	89	9	240	-16.0				19.02	4.015	1.138	94	0	6	12.79	4.73
IC	103	10	69	2	90	8	239	-5.8				12.13	2.360	1.085	73	0	27	14.23	3.45
IC	103	5	41	20	65	15	237	-3.6				9.36	1.765	1.064	45	0	55	17.89	4.99
IC	103	5	5	5	95	0	237	-0.3				0.53	0.091	1.001	100	0	0	21.13	0.12
IC	103	5	7	2	89	9	232	-0.4				0.70	0.121	1.002	100	0	0	19.36	2.25
IC	103	9	168	2	88	10	230	-5.8				12.13	2.360	1.085	73	0	27	14.17	3.79

Table 2. (Continued.)

Type	Sample	L (μ)	V (μ^3)	Volume percents			Th (°C)	Tm ice (°C)	Tm clath (°C)	Tm hydro (°C)	Te (°C)	Salinity (eq. wt. % NaCl)	Molality (moles/ kg H_2O)	Density (cm^3)	Weight percents			Molar volume (cm^3)	TDS (wt. %)
				Bub	Liq	Nah									NaCl	$CaCl_2$	$NaHCO_3$		
IC	103	8	59	2	80	18	227	-0.3				0.53	0.091	1.001	100	0	0	18.51	4.62
IC	103	4	6	2	98	0	225	-0.3				0.53	0.091	1.001	100	0	0	20.55	0.12
IC	103	7	28	5	61	34	207	-0.5				0.88	0.152	1.003	100	0	0	17.10	10.00
IC	4Z	8	124	8	81	11	277	-1.1		-22.0		1.91	0.332	1.011	79	21	0	19.32	3.03
IC	4Z	4	19	2	87	11	275	-0.3				0.53	0.091	1.001	100	0	0	19.28	2.74
IC	4Z	5	25	12	63	25	271	-2.2				3.71	0.658	1.023	100	0	0	17.75	7.32
IC	4Z	5	36	8	92	0	268	-0.3				0.53	0.091	1.001	100	0	0	21.74	0.12
IC	4Z	5	38	10	76	14	265												
IC	4Z	5	15	8	92	0	265	-0.2				0.35	0.061	1.000	100	0	0	21.92	0.08
IC	4Z	6	20	2	98	0	260		3.7			11.01	2.115	1.076	100	0	0	14.69	2.16
IC	4Z	5	14	10	90	0	254	-2.1				3.55	0.629	1.022	100	0	0	19.54	0.74
IC	4Z	4	2	4	96	0	248		3.2			11.70	2.266	1.082	100	0	0	14.76	2.28
IC	4Z	4	9	10	90	0	245	-7.6				11.22	2.160	1.078	100	0	0	15.82	2.19
IC	4Z	5	36	5	82	13	244												
IC	4Z	10	192	5	86	9	243	-17.9				20.50	4.408	1.149	95	0	5	12.96	5.00
IC	4Z	4	6	5	95	0	241	-7.9				11.58	2.238	1.081	100	0	0	14.94	2.26
IC	4Z	8	22	10	52	38	241	-18.1				20.66	4.451	1.150	95	0	5	13.30	11.47
IC	4Z	7	25	3	97	0	240	-2.7	7.4			5.05	0.910	1.033	100	0	0	17.34	1.04
IC	4Z	8	20	10	74	16	240	-17.8				20.82	4.495	1.152	100	0	0	13.67	3.83
IC	4Z	12	42	10	90	0	238	-0.5				0.88	0.152	1.003	100	0	0	21.80	0.19
IC	4Z	5	11	2	79	19	238	-18.0				20.58	4.430	1.150	95	0	5	12.45	6.57
IC	4Z	5	11	5	75	20	235												
IC	4Z	7	16	2	90	8	232	-2.4	6.3			7.00	1.287	1.047	5	0	95	16.11	2.52
IC	4Z	5	17	5	95	0	230	-0.4				0.70	0.121	1.002	100	0	0	20.95	0.15
IC	4Z	6	8	3	97	0	227	-6.0				9.21	1.734	1.063	100	0	0	15.44	1.83
IC	4Z	4	9	3	97	0	224	-0.6				1.05	0.182	1.004	100	0	0	20.24	0.23
IC	4Z	10	177	10	55	35	222	-1.2	5.4			8.45	1.578	1.057	100	0	0	15.24	10.19
IC	4Z	5	14	6	94	0	218	-8.6		-22.8	-69.5	13.5	2.668	1.095	87	14	0	15.04	2.20

Table 2. (Continued.)

Type	Sample	L (μ)	V (μ³)	Volume percents Bub	Liq	Nah	Th (°C)	Tm ice (°C)	Tm clath (°C)	Tm hydro (°C)	Te (°C)	Salinity (eq. wt. % NaCl)	Molality (moles/ kg H_2O)	Density (cm^3)	Weight percents NaCl	$CaCl_2$	$NaHCO_3$	Molar volume (cm^3)	TDS (wt. %)
IC	4Z	8	27	8	92	0	217	-0.7	6.2			7.14	1.315	1.048	100	0	0	17.09	1.44
IC	4Z	5	11	2	98	0	206	-7.3				10.86	2.082	1.075	100	0	0	14.74	2.13
IC	DBH	5	23	2	89	9	247	-2.4				6.77	1.241	1.045	5	0	95	16.14	2.70
IC	DBH	12	274	5	74	21	246	-4.4	8.9			2.20	0.385	1.013	60	0	40	17.69	5.59
IC	DBH	4	9	15	63	22	235	-0.9				1.57	0.272	1.008	100	0	0	19.70	6.71
IC	DBH	5	11	10	54	36	226	-3.0				8.40	1.568	1.057	31	0	69	15.36	10.41
IC	DBH	5	16	10	74	16	222	-0.6				1.05	0.182	1.004	100	0	0	19.75	4.46
IC	DBH	3	2	2	81	17	222	-2.1				3.55	0.629	1.022	100	0	0	16.81	4.44
IC	DBH	6	35	5	69	26	217	-0.4				0.70	0.121	1.002	100	0	0	18.01	7.25
IC	DBH	5	16	4	76	20	215	-1.8		-23.0		3.06	0.540	1.019	74	26	0	17.16	5.26
IC	DBH	4	6	2	74	24	214	-0.3				0.53	0.091	1.001	100	0	0	17.86	6.39
IC	DBH	4	8	5	95	0	212	-1.7				2.90	0.511	1.018	100	0	0	19.07	0.61
IC	DBH	4	6	2	90	8	200	-0.5				0.88	0.152	1.003	100	0	0	19.33	2.03
IC	HÖK	10	45	5	76	19	253	-0.3				0.53	0.091	1.001	100	0	0	18.89	5.08
IC	HÖK	10	62	10	78	12	240	-0.7				1.22	0.212	1.006	100	0	0	20.08	3.32
ID	103	6	40	5	79	16	193	-1.3				2.24	0.392	1.013	100	0	0	18.09	4.25
ID	103	7	43	10	86	4	188	-13.8		-22.6	-52.8	18.9	3.984	1.137	72	23	5	14.00	3.94
ID	103	4	9	2	93	5	184	-0.3				0.53	0.091	1.001	100	0	0	19.96	1.26
ID	103	4	7	2	74	24	167	-4.0				10.00	1.899	1.069	54	0	46	14.28	6.32
ID	103	5	25	5	74	21	144	0.0				0.00	0.000	0.997	100	0	0	19.03	5.72
ID	103	6	33	3	90	7	139	-12.3		-25.4		17.8	3.702	1.128	62	33	6	13.74	3.57
ID	103	7	13	3	77	20	102	-5.2				11.81	2.289	1.082	70	0	30	14.09	5.68
ID	4Z	6	10	5	77	22	196	-1.3				2.24	0.392	1.013	100	0	0	16.86	5.65
ID	4Z	10	9	5	95	0	190	-0.9	8.6	-22.9	-69.8	2.81	0.494	1.017	98	2	0	19.18	0.56
ID	4Z	10	53	5	95	0	187	-3.9				6.30	1.150	1.042	100	0	0	17.00	1.28
ID	4Z	8	7	2	98	0	187	-5.3				8.28	1.542	1.056	100	0	0	15.65	1.66
ID	4Z	10	32	2	98	0	184	-6.9				10.36	1.976	1.072	100	0	0	14.90	2.04
ID	4Z	9	108	5	95	0	183	0.0		-23.3	-53.6	0.00	0.000	0.997	100	0	0	21.69	0.00

Table 2. (Continued.)

Type	Sample	L (μ)	V (μ^3)	Volume percents Bub	Liq	Nah	Th (°C)	Tm ice (°C)	Tm clath (°C)	Tm hydro (°C)	Te (°C)	Salinity (eq. wt. % NaCl)	Molality (moles/ kg H_2O)	Density (cm^3)	Weight percents NaCl	$CaCl_2$	$NaHCO_3$	Molar volume (cm^3)	TDS (wt. %)
ID	4Z	7	33	2	88	10	183	-0.4		-21.5	-69.7	0.70	0.121	1.002	81	19	0	19.25	2.50
ID	4Z	12	27	2	98	0	177	-0.3				0.53	0.091	1.001	100	0	0	20.55	0.12
ID	4Z	6	70	5	95	0	177	-0.6		-24.9		1.1	0.190	1.005	99	1	0	20.61	0.20
ID	4Z	6	18	4	96	0	177		1.2			14.22	2.833	1.100	100	0	0	14.09	2.72
ID	4Z	10	58	5	86	9	176	-0.6			-69.7	1.05	0.182	1.004	100	0	0	19.61	2.36
ID	4Z	4	5	2	98	0	172	-7.0				10.49	2.002	1.072	100	0	0	14.86	2.06
ID	4Z	4	21	2	98	0	172	0.0				0.00	0.000	0.997	100	0	0	21.10	0.00
ID	4Z	4	25	9	91	0	170	-0.2				0.35	0.061	1.000	100	0	0	22.14	0.08
ID	4Z	9	34	4	95	1	170	-0.1				0.18	0.030	0.998	100	0	0	21.17	0.27
ID	4Z	4	9	2	80	18	167	-0.5				0.88	0.152	1.003	100	0	0	18.27	4.62
ID	4Z	4	13	1	94	5	159	-0.4				0.70	0.121	1.002	100	0	0	19.63	1.28
ID	4Z	6	6	2	98	0	158	-1.7				2.90	0.511	1.018	100	0	0	18.55	0.61
ID	4Z	5	15	2	76	22	155	-0.8				1.40	0.242	1.007	100	0	0	17.55	5.74
ID	4Z	10	271	6	94	0	153	-0.3				0.53	0.091	1.001	100	0	0	21.33	0.12
ID	4Z	4	18	1	82	17	153	-0.8				1.40	0.242	1.007	100	0	0	17.87	4.31
ID	4Z	6	22	2	80	18	153	-0.8				1.40	0.242	1.007	100	0	0	17.93	4.62
ID	4Z	6	22	4	96	0	151	0.0		-23.3	-54.6	0.00	0.000	0.997	100	0	0	21.49	0.00
ID	4Z	8	108	2	88	10	149	-0.2				0.35	0.061	1.000	100	0	0	19.54	2.47
ID	4Z	6	27	5	78	17	146	-0.4			-52.4	0.70	0.121	1.002	100	0	0	18.99	4.49
ID	4Z	4	19	2	98	0	139		5.1			8.93	1.675	1.061	100	0	0	15.40	1.78
ID	4Z	5	30	5	84	11	135		3.6			2.57	0.451	1.015	100	0	0	14.72	4.05
ID	4Z	6	68	4	92	4	133	-7.8				13.32	2.627	1.094	80	0	20	14.30	3.03
ID	4Z	5	10	2	98	0	132	-0.6				1.05	0.182	1.004	100	0	0	20.05	0.23
ID	4Z	6	68	4	87	9	130	-0.5				0.88	0.152	1.003	100	0	0	19.57	2.32
ID	4Z	6	37	5	72	23	126	-0.8				1.40	0.242	1.007	100	0	0	17.92	6.24
ID	4Z	10	19	4	96	0	124		5.4			8.45	1.578	1.057	100	0	0	15.88	1.69
ID	4Z	4	18	2	98	0	107	0.0				0.00	0.000	0.997	100	0	0	21.10	0.00
ID	DBH	8	31	5	71	24	192	-0.7				1.22	0.212	1.006	100	0	0	17.92	6.56

Table 2. (Continued.)

Type	Sample	L (μ)	V (μ^3)	Volume percents			Th (°C)	Tm ice (°C)	Tm clath (°C)	Tm hydro (°C)	Te (°C)	Salinity (eq. wt. % NaCl)	Molality (moles/ kg H_2O)	Density (cm^3)	Weight percents			Molar volume (cm^3)	TDS (wt. %)
				Bub	Liq	Nah									NaCl	$CaCl_2$	$NaHCO_3$		
ID	DBH	4	8	7	93	0	191	-0.6				1.05	0.182	1.004	100	0	0	21.01	0.23
ID	DBH	6	13	2	80	18	186	-1.2				2.07	0.362	1.012	100	0	0	17.52	4.63
ID	DBH	4	18	5	74	21	186	-1.7				2.90	0.511	1.018	100	0	0	17.29	5.62
ID	DBH	4	11	2	78	20	183	-3.9		-24.3		9.84	1.866	1.068	52	23	25	15.59	5.21
ID	DBH	6	21	5	89	6	171	-0.9				1.57	0.272	1.008	100	0	0	19.52	1.69
ID	DBH	4	15	2	80	18	168	-2.3				6.50	1.188	1.043	0	0	100	15.74	4.61
ID	DBH	4	11	5	76	19	166	-2.8		-22.3		7.86	1.458	1.053	56	0	44	15.51	5.20
ID	DBH	9	41	5	95	0	160	0.0				0.00	0.000	0.997	100	0	0	21.69	0.00
ID	DBH	4	21	5	81	14	152	-3.5				9.20	1.732	1.063	43	0	57	15.37	4.15
ID	DBH	8	100	5	83	12	146	-0.5				0.88	0.152	1.003	100	0	0	19.42	3.12
ID	DBH	8	37	5	95	0	145	-0.9				1.57	0.272	1.008	100	0	0	20.15	0.34
ID	DBH	7	47	5	77	18	137		4.3			2.74	0.481	1.016	100	0	0	14.75	5.32
ID	HÖK	8	45	1	79	20	205	-0.3				0.53	0.091	1.001	100	0	0	18.13	5.13
ID	HÖK	8	34	5	89	6	192	-1.1				1.91	0.332	1.011	100	0	0	19.26	1.74
ID	HÖK	5	11	7	93	0	189	-0.3				0.53	0.091	1.001	100	0	0	21.53	0.12
ID	HÖK	8	18	8	92	0	183	-0.5				0.88	0.152	1.003	100	0	0	21.38	0.19
ID	HÖK	7	17	11	89	0	180	-2.9				4.80	0.863	1.031	100	0	0	18.90	0.99
ID	HÖK	8	33	5	89	6	170	-1.4				2.41	0.422	1.014	100	0	0	18.89	1.82
ID	HÖK	10	75	4	89	7	167	-0.1				0.18	0.030	0.998	100	0	0	20.41	1.73
ID	HÖK	6	41	2	89	9	165	-3.6	9.7	-24.3		9.36	1.765	1.064	50	22	28	16.35	2.77
ID	HÖK	6	18	2	87	11	162	-3.8	7.7	-22.8	-66.4	9.68	1.832	1.067	54	18	28	16.79	3.09
ID	HÖK	5	32	9	91	0	157	0.0				0.00	0.000	0.997	100	0	0	22.53	0.00
ID	HÖK	5	8	5	95	0	155	-1.5				2.57	0.451	1.015	100	0	0	19.32	0.54
ID	HÖK	5	19	5	95	0	151	-1.3				2.24	0.392	1.013	100	0	0	19.58	0.48
ID	HÖK	7	67	5	95	0	150	-0.1				0.18	0.030	0.998	100	0	0	21.50	0.04
ID	HÖK	8	27	5	95	0	149	-13.4				17.26	3.565	1.124	100	0	0	13.58	3.24
ID	HÖK	8	30	4	91	5	145	-1.2				2.07	0.362	1.012	100	0	0	19.05	1.53
ID	HÖK	6	24	2	87	11	133	-2.1				3.55	0.629	1.022	100	0	0	17.26	3.03

Table 2. (Continued.)

Type	Sample	L (μ)	V (μ³)	Volume percents Bub	Liq	Nah	Th (°C)	Tm ice (°C)	Tm clath (°C)	Tm hydro (°C)	Te (°C)	Salinity (eq. wt. % NaCl)	Molality (moles/ kg H_2O)	Density (cm^3)	Weight percents NaCl	$CaCl_2$	$NaHCO_3$	Molar volume (cm^3)	TDS (wt. %)
ID	HÖK	8	62	5	95	0	131	-0.2				0.35	0.061	1.000	100	0	0	21.31	0.08
II	103	12	243	5	91	4	198	-4.9	9.6	-22.3	-54.2	11.53	2.228	1.080	59	22	19	14.88	2.80
II	103	8	26	1	90	9	177	-0.4		-23.2	-69.4	0.70	0.121	1.002	73	27	0	19.20	2.22
II	103	8	72	5	74	21	173	-2.3	9.9	-22.7		6.50	1.188	1.043	50	0	50	15.88	5.60
II	103	8	89	5	88	7	162	-0.5		-23.2		0.88	0.152	1.003	73	27	0	19.99	1.83
II	103	5	14	2	95	3	161	-2.9		-23.6	-70.2	8.13	1.513	1.055	47	18	34	17.19	1.47
II	103	10	22	2	73	25	131	-4.1	5.3			0.00	0.000	0.997	56	0	44	14.58	6.50
II	4Z	10	59	5	88	7	177	-2.2				3.71	0.658	1.023	100	0	0	17.96	2.23
II	4Z	12	231	15	82	3	162	-0.5				0.88	0.152	1.003	100	0	0	22.53	0.96
II	4Z	12	74	2	84	14	157	-0.6			-69.4	1.05	0.182	1.004	100	0	0	18.56	3.55
II	4Z	18	295	2	80	18	154	-1.4	3.5			11.29	2.176	1.078	100	0	0	14.04	5.32
II	4Z	13	94	2	87	11	136		5.1			8.93	1.675	1.061	33	0	67	15.18	3.40
II	4Z	10	37	2	92	6	134	-7.4				13.05	2.566	1.092	79	0	21	14.04	3.29
II	4Z	12	62	2	71	27	122		4.6			9.69	1.835	1.067	33	0	67	14.29	6.95
II	4Z	15	85	4	90	6	121		4.5			9.84	1.867	1.068	33	0	67	15.40	2.61
II	DBH	12	106	5	75	20	190	-3.6	4.4	-26.3	-64.4	9.99	1.898	1.069	47	28	26	14.89	5.49
II	DBH	15	603	5	70	25	189	-8.8	8.0	-23.3		13.89	2.757	1.098	65	24	11	16.53	6.70
II	DBH	8	79	10	71	19	186	-3.9	8.6	-22.9		9.84	1.866	1.068	55	19	26	18.38	5.33
II	DBH	10	206	8	89	3	182	-1.8	5.7			7.97	1.480	1.054	100	0	0	16.57	2.14
II	DBH	8	22	8	76	16	178	-4.0				10.00	1.899	1.069	54	0	46	15.47	4.80
II	DBH	7	45	5	75	20	167	-3.9		-23.1		9.84	1.866	1.068	55	19	26	16.01	5.40
III	HÖK	8	130	5	93	2	155	-4.4	12.2			10.68	2.044	1.074	60	0	40	15.32	2.19
III	HÖK	20	533	5	84	11	154	-1.4	10.8			2.41	0.422	1.014	100	0	0	18.44	2.99
III	HÖK	13	88	5	89	6	152	-1.5		-25.5	-68.0	2.57	0.451	1.015	83	17	0	18.85	1.77
III	HÖK	12	18	10	90	0	152												
III	HÖK	12	287	8	81	11	146	-0.8	6.1			7.31	1.348	1.049	100	0	0	16.45	3.62
III	HÖK	20	328	5	94	1	146	-1.2				2.07	0.362	1.012	100	0	0	19.62	0.66
III	HÖK	5	32	10	90	0	146												

Table 2. (Continued.)

Type	Sample	L (μ)	V (μ³)	Volume percents Bub	Liq	Nah	Th (°C)	Tm ice (°C)	Tm clath (°C)	Tm hydro (°C)	Te (°C)	Salinity (eq. wt. % NaCl)	Molality (moles/ kg H_2O)	Density (cm^3)	Weight percents NaCl	$CaCl_2$	$NaHCO_3$	Molar volume (cm^3)	TDS (wt. %)
III	HÖK	7	71	2	98	0	142												
III	HÖK	8	109	5	87	8	135	-0.6				1.05	0.182	1.004	100	0	0	19.72	2.11
III	HÖK	12	225	3	93	4	133												
III	HÖK	4	8	5	80	15	131	-1.1	5.6			8.13	1.513	1.055	100	0	0	15.49	4.47
III	HÖK	10	147	3	93	4	130												
III	HÖK	56	741	2	98	0	123												
III	HÖK	8	26	10	90	0	117	-0.1				0.18	0.030	0.998	100	0	0	22.55	0.04
III	HÖK	12	36	2	98	0	114												
III	HÖK	8	74	4	87	9	114	0.0				0.00	0.000	0.997	100	0	0	20.33	2.23
III	HÖK	10	113	2	90	8	109												
III	HÖK	20	258	2	96	2	104	-1.2	6.5			6.63	1.215	1.044	100	0	0	16.26	1.70
III	HÖK	45	554	2	96	2	94	-1.2	6.5			6.63	1.215	1.044	100	0	0	16.26	1.70

Not all of the fluid inclusions are large enough for microthermometry study. However, small inclusions are volumetrically important and contribute to the gas analyses of the bulk quartz. Furthermore, they are clues to a fluid history that has been mostly lost to deformation and recrystallization.

Fluid Inclusions Studied by Microthermometry

A long, slender, transparent mineral was present in about 2/3 of the fluid inclusions listed below. The mineral was very difficult to analyze by Raman spectroscopy because it is typically 1x3 μm in dimension and it moves under the laser beam. However, a small peak for nahcolite ($NaHCO_3$) was obtained in one analysis. The mineral has low or moderate relief lengthwise and high relief on its end. Lying on its side the crystal changes relief upon rotation of the microscope stage. These phenomena suggest a biaxial negative crystal with high birefringence, consistent with nahcolite (Palache et al., 1951).

Fluid inclusions are described below in chronological order (older to younger) on the basis of the criteria established above.

Type I fluid inclusions range in size up to 10 μm in length and are most numerous along straight planar trails in phenocrysts in the lower and middle amphibolite facies samples. Larger inclusions are subangular and generally irregular in shape, with a few negative crystal faces. Smaller inclusions are oblong; some are negative quartz crystals and others are well rounded. Type I inclusions suitable for microthermometry consist of a liquid and a vapor phase, with a consistent degree of fill of about 90 to 95%. The vapor bubbles generally are very active. Nahcolite is present in about half of the fluid inclusions. Where present, the solid volume is commonly 10 to 15% of the inclusion. Type I fluid inclusion trails occur in all phenocrysts, in quartz of every generation. The distribution of inclusions

along a given trail is fairly uniform, but some trails are more densely populated than others. By using this criterion and the microstructural setting of the trails, four subtypes can be identified:

Type IA fluid inclusions occur in sparsely populated trails that extend along deformation band boundaries in "igneous" quartz grains.

Type IB fluid inclusions occur in sparsely populated trails that crosscut deformation textures in "igneous" quartz grains, and generally are truncated by quartz grain boundaries; also included in this group are inclusions occurring in short rootless FIP in the older quartz grains.

Type IC fluid inclusions occur in densely populated trails in older quartz grains, they cross-cut older quartz grain boundaries, and are truncated by younger quartz grain boundaries.

Type ID fluid inclusions occur in densely populated trails in both olderquartz and younger quartz grains and crosscut younger quartz grain boundaries.

No more than three subtypes have been encountered in any one phenocryst or thin section, and only one or two subtypes are volumetrically important in a given phenocryst. Trails of type I fluid inclusions do not exhibit any preferred orientation.

Type II fluid inclusions are distinguished by having many large individuals ranging up to 20 μm in size and commonly having two liquid phases at room temperature. Most of these have complex shapes and internal architecture but outwardly display rounded forms. Some shapes resemble popcorn. Large individuals contain two or three fluid phases and commonly a nahcolite crystal. The degree of fill varies mostly between 90 and 95%. Where three fluid phases can be seen, the inner liquid typically is less than 35% of the bubble volume. The majority of vapor bubbles are sluggish or inactive. The solid volume varies between 10 and 20%. Small individuals of this group resemble type I fluid inclusions but most are readily identified by their association with larger distinctive neighbors. Type II fluid inclusions are plentiful in planar trails in the upper amphibolite sample 103 and

crosscut younger quartz grain boundaries. Trails of type II fluid inclusions do not exhibit any preferred orientation.

Type III fluid inclusion trails exhibit a preferred orientation on the scale of a thin section. The inclusions are also distinguished by having thin, delicate pinched forms that can be up to 40 μm in overall length. They occupy poorly healed, curviplanar microfractures, and can be found along new grain boundaries and amidst trails of older fluid inclusions as well. Type III fluid inclusion trails are easily distinguished by naturally decrepitated individual inclusions and trails that are deflected into older fluid inclusion planes. Large inclusions contain two or three fluid phases and rarely a nahcolite crystal. Generally their degree of fill is about 95%, and two-phase bubbles contain about 65% vapor phase and 35% liquid phase by volume. The bubbles are active only in smaller rounder inclusions in which the second liquid is difficult to see. Where present the nahcolite volume is less than 5%. Corresponding fingers between adjacent fluid inclusions indicate necking down pairs; the smaller inclusion generally is monophase liquid.

Fluid Inclusions not Studied by Microthermometry

Transposed fluid inclusions occur in linear clusters 20 to 40 μm in length, with individual inclusions up to 5 μm in size. They are preserved in "igneous" quartz grains and are found only in the lower amphibolite grade sample HÖK. The larger inclusions commonly are subangular and elongate, oriented with their longest dimension parallel to the group axis. Inclusions under 2 μm are spherical or oblong, and dark. At moderate magnification (40x objective) some appear monophase and others consist of a liquid and a vapor phase. The degree of fill in two phase inclusions is variable, but greater than 80%. The transposed fluid inclusion clusters are arranged into parallel arrays that form distinctive bands, which may crosscut one another with no apparent offset. The axes of the parallel

clusters correspond with the intersection of deformation bands wherever two well defined sets of bands can be seen.

Exsolution fluid inclusions decorate deformation band boundaries developed only in "igneous" quartz in sample HÖK. At high magnification (80x objective) they appear monophase and spherical, and tend to occur in short linear groups of several individuals whose sizes vary up to diameters of 1 μm. The orientation of linear groupings coincides with the intersection of two sets of deformation bands, in a fashion similar to transposed fluid inclusions. Exsolution fluid inclusions are easily distinguished from the latter, however, by the small size of both individual inclusions and clusters. Furthermore, arrays of exsolution fluid inclusions are aligned with deformation bands, whereas arrays of transposed fluid inclusions are intersected by deformation bands.

Grain boundary fluid inclusions occupy the new grain boundaries in many of the quartz phenocrysts examined. The inclusions generally are too small to study, and they leak or decrepitate before homogenization occurs, generally at temperatures in excess of 150°C. Grain boundary fluid inclusions are commonly replaced by type III fluid inclusions that form within intergranular microcracks developed along the new quartz grain boundaries. Grain boundary inclusions are prevalent in highly recrystallized relic phenocrysts.

Calcite-bearing (type C) fluid inclusions, or inclusions which exhibit calcite precipitation at high temperatures, are loosely associated with type I and type II FIP. They are also found in strain shadows encircling mineral inclusions in the quartz. The calcite was probably trapped at high temperatures by the same fluids that formed the type I and II fluid inclusions. Reaction between nahcolite and calcite that is discussed in Chapter IV produces some very unusual behavior during heating and freezing cycles.

Microthermometry Results

Homogenization Phenomena

Final liquid-vapor homogenization in all the fluid inclusions proceeds as L+V→L and, in solid-bearing inclusions, invariably occurs before complete dissolution of the nahcolite. Final dissolution of nahcolite is never seen in any fluid inclusions before decrepitation occurs. Vapor bubbles disappear in solid-bearing inclusions at about the same temperatures as in solid-free inclusions along the same trail, and this temperature is reported as Th without any indication of whether nahcolite was or was not present at homogenization. The justification for doing this will become apparent below.

The Th measurements have a temperature range of more than 400 degrees and exhibit several modes on a histogram (Figure 7). Measurements divided by inclusion types, however, have a more limited range. Fluid inclusions on a single trail yield similar Th values, generally within a range of less than 60 degrees. Inclusions of a given type show fewer than ten degrees difference between average Th values measured in lower, middle and upper amphibolite facies samples. The Th distributions at high temperature (type IA, IB and IC inclusions) are slightly skewed toward higher temperatures (skewness = +1.51, +0.30 and +0.11 respectively), whereas Th distributions at lower temperatures (type ID, II and III inclusions) are slightly skewed toward lower temperatures (skewness = -0.43, -0.49 and -0.76 respectively).

Liquid-vapor homogenization of the second inner liquid with the vapor bubble can be observed only in the larger and flatter type II and III fluid inclusions. Freezing measurements and gas analyses discussed below indicate that the second liquid is mostly CO_2. Homogenization proceeds as L+V→V which involves large errors in homogenization temperature determinations (Sterner, 1992). Homogenization temperatures (Th-CO_2) range between 20°C and 31°C, with an average value of 24°C. A very large number of the inclusions from which Th-CO_2 could be obtained also contain nahcolite.

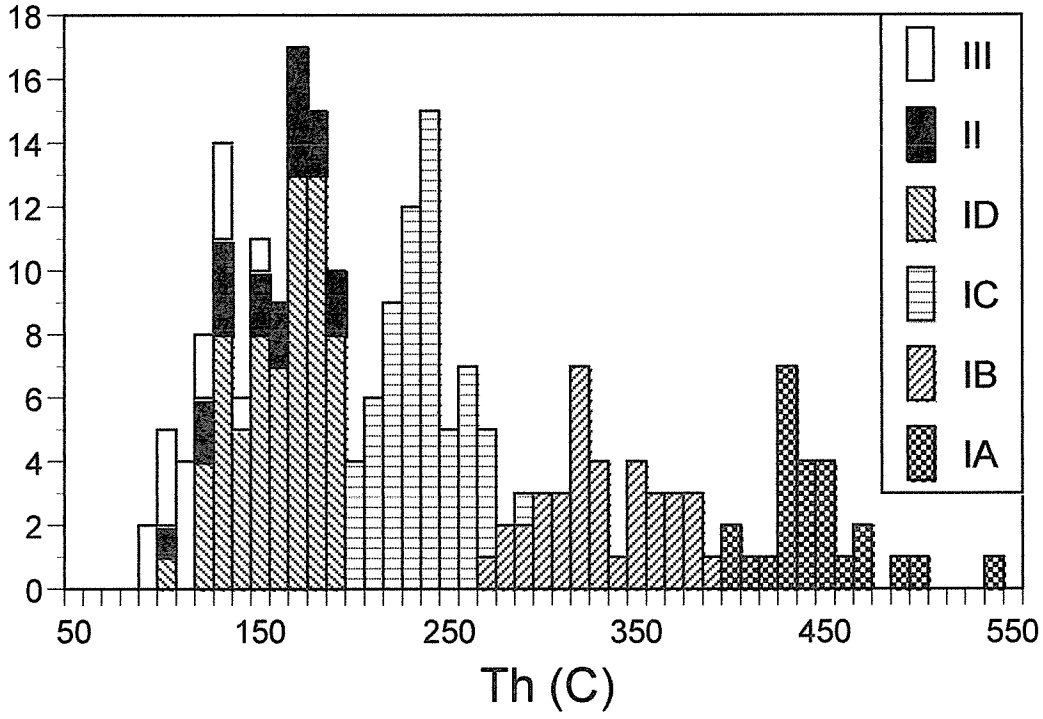

Figure 7. A histogram of all the liquid phase homogenization temperature data. Data from different fluid inclusion generations are indicated by different patterns.

Final Melting Phenomena

In solid-free fluid inclusions, salinity determinations were made from ice or clathrate final melting temperatures (Tm-ice or Tm-clathrate). Nahcolite does not completely dissolve before decrepitation occurs, thus, the salinity of the solid-bearing inclusions was estimated by using the size and density of the nahcolite crystal and the liquid phase at ice or clathrate final melting temperatures. Tm-ice and Tm-clathrate values were collected for solid-bearing inclusions for this purpose.

The final melting phase generally is ice for type I fluid inclusions, and clathrate for type II and III fluid inclusions. Many of the vapor bubbles in smaller inclusions disappear upon freezing and reform at Tm-ice. Both ice and clathrate final melting temperatures are multimodal in distribution and skewed toward lower temperatures. There is no correlation between various modal temperatures and fluid inclusion types. Both solid-free and solid-bearing fluid inclusions exhibit a modal Tm-ice of about -0.2 to -0.4°C (Figure 8a). The solid-bearing inclusions exhibit secondary modal values at -2.3°C and -3.6°C.

The distribution of Tm-clathrate is weakly bimodal and covers a wide temperature range (Figure 8b). The fluids in solid-free inclusions tend to melt at lower temperatures than do the fluids in solid-bearing inclusions. The data suggest an average salinity for the liquid phase of about 8.7 eq. wt. % NaCl for solid-free inclusions and about 5.0 eq. wt. % NaCl for solid-bearing inclusion fluids at temperatures in the 0 to 10°C range.

Only rarely do the bubbles in type II and III fluid inclusions contain an obvious liquid CO_2 phase in which solid CO_2 final melting (Tm-CO_2) can be observed. The range in Tm-CO_2 is between -57.4 and -56.6°C with an average value of -57.0°C. This indicates that some CH_4 and/or N_2 is present in the CO_2-rich phase, in agreement with maximum Tm-clathrate measurements in the 10 to 11°C range.

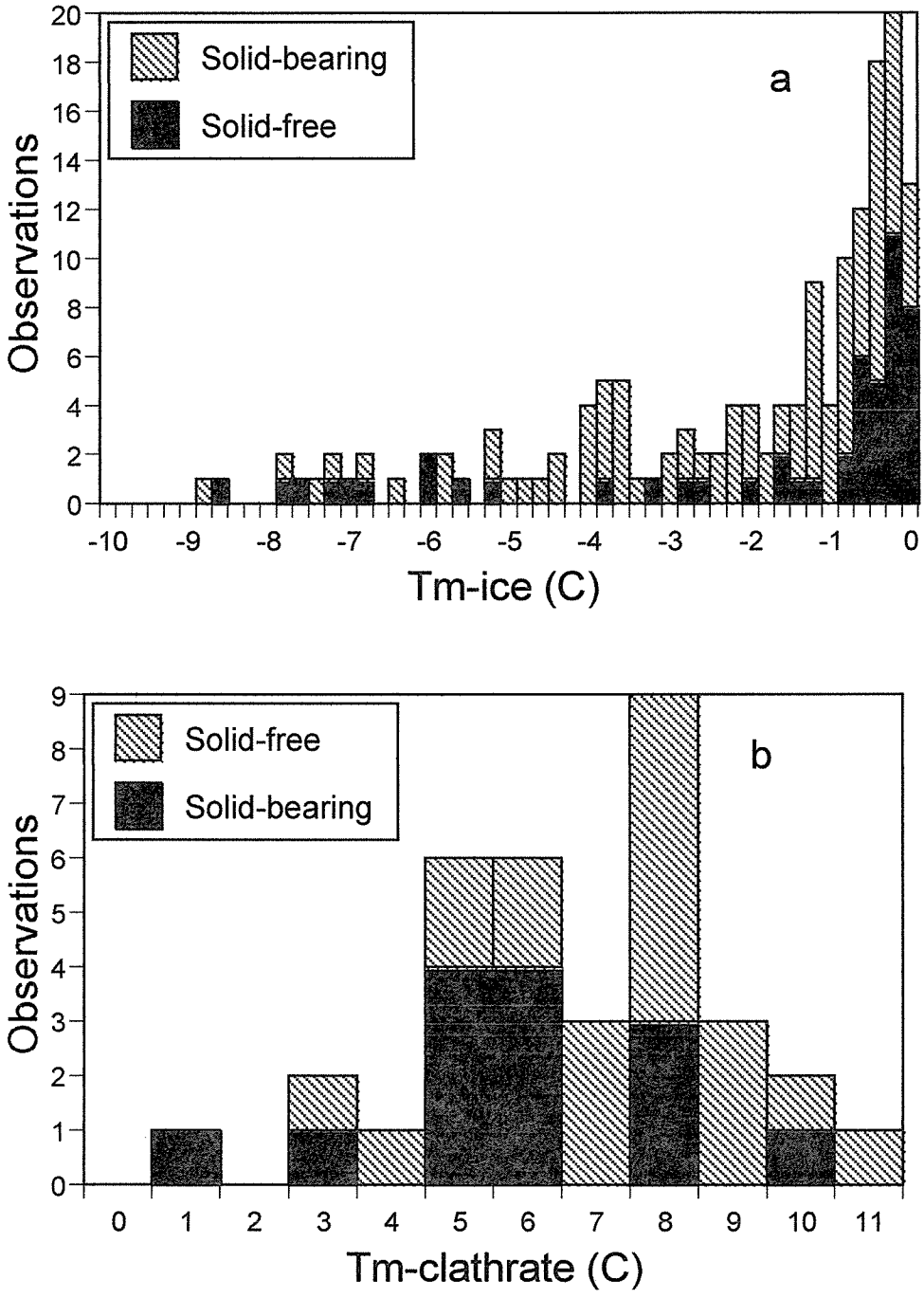

Figure 8. Final melting temperature data for a) ice and b) clathrate. Solid pattern= solid-bearing fluid inclusions. Striped pattern= solid-free fluid inclusions.

Eutectic Phenomena

Very low temperature eutectic melting is seen in some solid-bearing fluid inclusions. Some of the inclusions exhibit first melting between -55.3 and -51.6°C, with an average value of -53.3°C. Others exhibit first melting between -70.2 and -61.6°C, with an average value of -67.4°C. The ternary system H_2O-NaCl-$CaCl_2$ exhibits a normal eutectic around -55°C and a metastable eutectic around -70°C (Davis et al., 1990), thus, $CaCl_2$ may be an important component of the fluid inclusions.

Hydrohalite final melting temperatures (Tm-hydrohalite) have a modal value at -22.8°C. Because the ternary eutectic for the H_2O-NaCl-$NaHCO_3$ system is located at -21.8°C, another component, probably $CaCl_2$, must be present in the fluid inclusions. The depression of Tm-hydrohalite could be due to the presence of a 1:4 molar ratio of $CaCl_2$ to NaCl (Oakes et al., 1990).

Fluid Analyses by QMS

Quartz phenocrysts from the lower amphibolite sample, HÖK, were analyzed for gases by quadrupole mass spectrometer (QMS) and the results are shown in Table 3. Analyses for H_2O, CO_2 and combined CH_4+N_2 are presented on a ternary diagram (Figure 9). The analyses separate into two populations, one relatively water-rich and the other relatively CO_2-rich. Most of the water-rich analyses have more than 90% water whereas the CO_2-rich analyses have less than 80% water. Fewer than 20% of the water-rich analyses have more than 2 mole% CH_4+N_2 whereas more than 60% of the CO_2-rich analyses have higher CH_4+N_2 compositions. Methane and N_2 contents are correlated; the average CH_4/N_2 ratio is 8 in both sets of analyses.

Other gaseous species analyzed include H_2, He, H_2S, C_3H_8, Ar and SO_2. The only species that demonstrate a very strong correlation are H_2, CH_4 and C_3H_8. The He concentration is very high

Table 3. Gas analyses of crushed quartz phenocrysts by quadrupole mass spectrometer. All measurements are in percent.

Run #	H_2	He	CH_4	H_2O	N_2	H_2S	Ar	C_nH_n	CO_2	SO_2	CH_4/N_2	N_2/Ar	CO_2/CH_4
5296D	0.052	0.0049	0.22	88.6	0.013	0.00054	0.0205	0.0115	11.0	0.00126	16.4	0.66	50.0
5510D	0.219	0.0103	2.33	89.2	0.317	0.00097	0.0324	0.0102	7.9	0.00170	7.36	9.78	3.4
5296C	0.054	0.0054	0.14	89.2	0.142	0.00021	0.0190	0.0117	10.5	0.00191	0.96	7.48	76.8
5510C	0.075	0.0061	0.31	91.3	0.133	0.00052	0.0220	0.0092	8.1	0.00084	2.34	6.05	26.2
5296B	0.058	0.0000	0.14	91.3	0.248	0.00081	0.0216	0.0134	8.2	0.00252	0.57	11.5	58.2
5496A	0.988	0.0000	1.50	92.3	1.69	0.00000	0.0479	0.0301	3.4	0.0324	0.89	35.4	2.3
5497A	0.171	0.0000	0.82	92.3	0.292	0.0171	0.0041	0.0205	6.4	0.0131	2.79	71.5	7.8
5296F	0.062	0.0052	1.04	94.0	0.070	0.00312	0.0150	0.0029	4.8	0.00325	14.7	4.70	4.7
5510A	0.137	0.0000	0.31	94.4	0.249	0.00009	0.0229	0.0056	4.9	0.00081	1.25	10.9	15.9
5510E	0.077	0.0038	0.54	95.7	0.024	0.00081	0.0135	0.0032	3.7	0.00137	22.2	1.81	6.8
5510F	0.044	0.0000	0.51	98.1	0.248	0.00077	0.0091	0.0026	1.1	0.00114	2.08	27.3	2.1

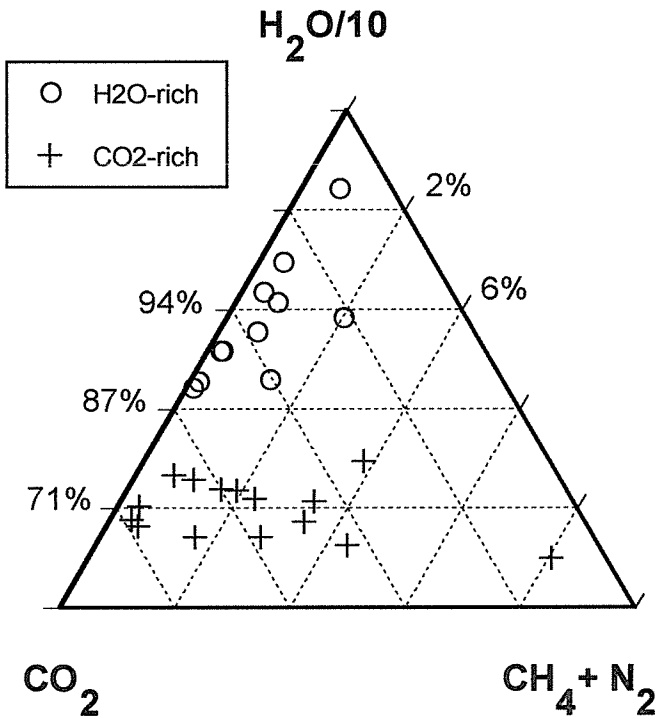

Figure 9. The composition of fluid inclusions in mole percent, plotted on a ternary diagram. About half of the CO_2-rich analyses (+) have more than 2% combined CH_4 and N_2. Only one H_2O-rich analysis (O) has more than 2% CH_4 and N_2.

in cases where He is detected. Heat treatment of the samples prior to analysis to remove water adsorbed onto grain boundaries may be responsible for He loss by diffusion.

N_2/Ar and CO_2/CH_4 ratios are plotted in Figure 10. The N_2/Ar ratios are less than the ratios in modern air or air saturated water (ASW), with an average N_2/Ar ratio of 17 in both sets of analyses. Highly variable N_2 content controls the N_2/Ar ratio. The CO_2/CH_4 ratios vary over two orders of magnitude. Highly variable CH_4 content controls the CO_2/CH_4 ratios that are similar for both water-rich and CO_2-rich analyses.

Discussion

Origin of Nahcolite

Nahcolite is present in a significant percentage of the fluid inclusions, but not in all of them. This raises the question of whether nahcolite is an accidentally trapped mineral or a daughter mineral. Trapped minerals generally are not numerous and may occur as mineral inclusions in the host mineral. The reverse is true for daughter minerals, suggesting that nahcolite is a daughter mineral. The definitive evidence for daughter minerals is a constant phase ratio between fluid and solid (Roedder, 1984, p. 27). In Figure 11 the volumes of inclusions of various types are plotted against the volumes of included nahcolite crystals. Since fluid inclusions in metamorphic rocks are prone to fluid leakage, the inclusion volume is used here in place of fluid volume. Type I and II fluid inclusions exhibit a more constant volume ratio whereas type III inclusions show more scatter. Correlation coefficients for inclusion and nahcolite volumes are 0.87 (type IA inclusions), 0.93 (IB), 0.86 (IC), 0.72 (ID), 0.88 (II) and 0.63 (III). The high correlation suggests that nahcolite is indeed a daughter mineral in type I and II inclusions. There is a lower correlation between volumes in type III inclu-

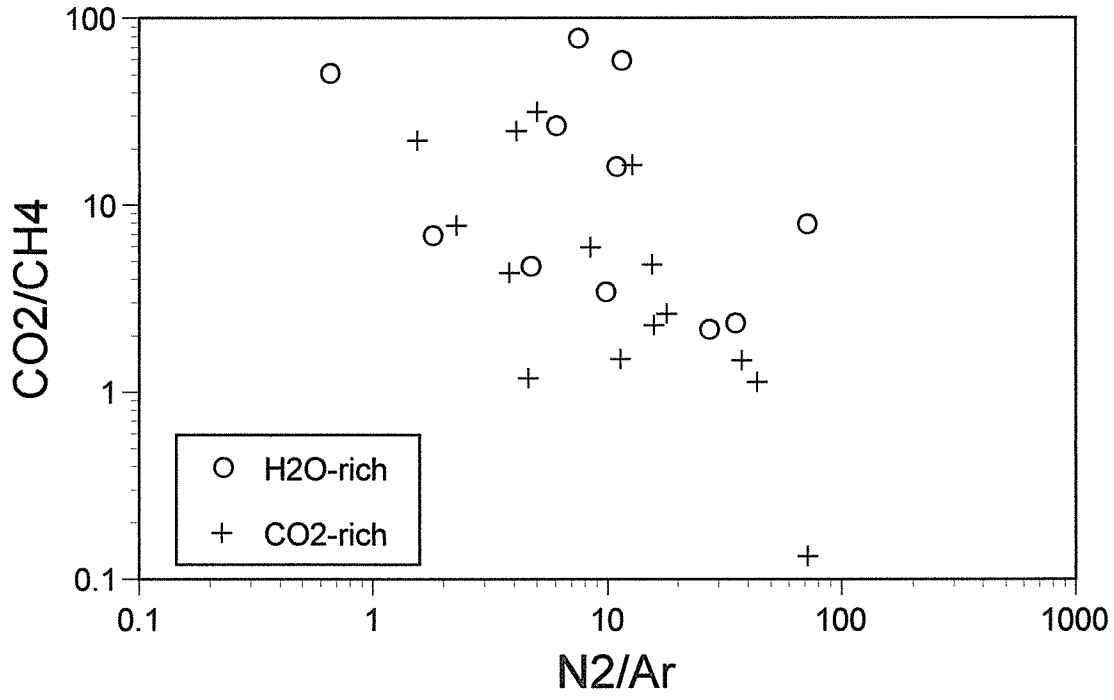

Figure 10. Semi-bulk gas analyses of fluid inclusions in the lower amphibolite facies sample HÖK. H_2O-rich analyses (O) have a compositional range similar to CO_2-rich analyses (+).

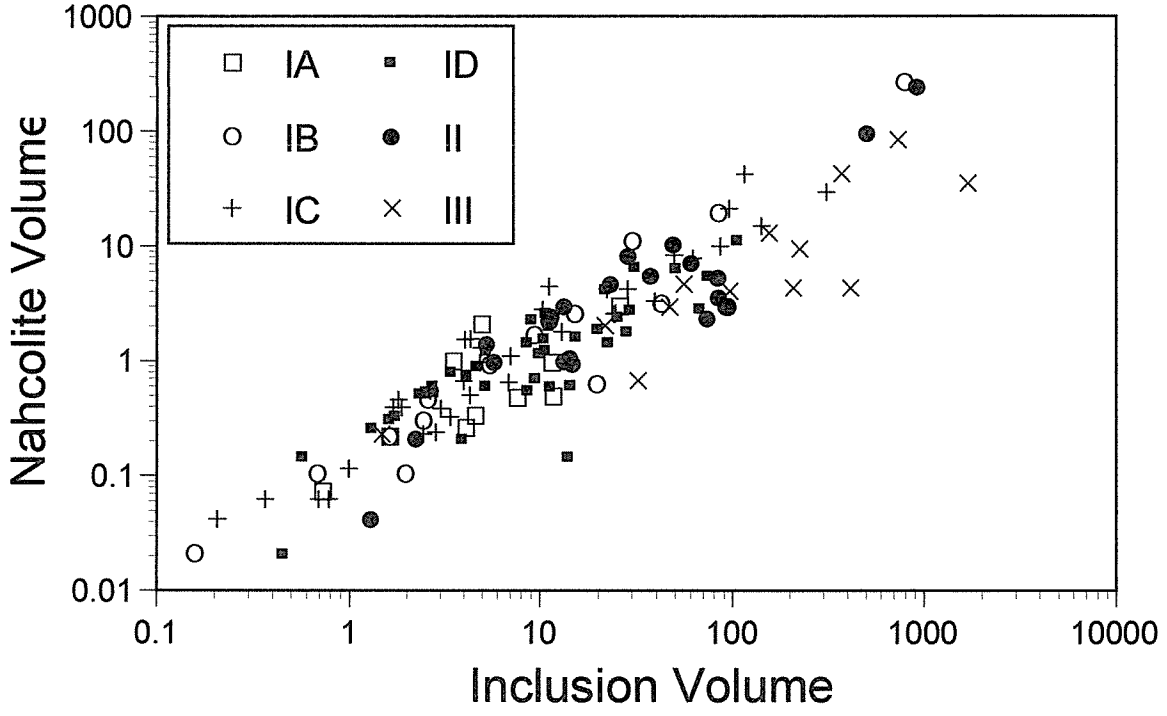

Figure 11. Volume ratios of fluid inclusions and nahcolite for various fluid inclusion generations. Volume units are μm^3. There is a fairly constant volume ratio for type I and II fluid inclusions. Type III fluid inclusions ehxibit more scatter in the volume data.

sions. This suggests that nahcolite may have been captured by type III inclusions where microcracks propagated along the older type I and II fluid inclusion trails.

The observation that nahcolite never completely dissolves upon heating before the inclusions decrepitate, however, is explained by nahcolite entrapment. Since the fluid inclusions occur in trails, necking down along a fluid-filled fracture is required to explain the inclusions. Early precipitation of nahcolite in the microfractures from a homogeneous fluid, followed by necking down prior to the separation of liquid and vapor phases produces the observed features. In this view, nahcolite is neither a typical daughter mineral nor an accidentally trapped mineral. On the one hand, this interpretation explains why there is a basic similarity in degree-of-fill, and Th and Tm data, in solid-free and solid-bearing inclusions on a single trail. On the other hand, it is difficult to explain why the volume ratios in type I and II inclusions are constant. Solid-free and solid-bearing inclusions of similar size on individual trails suggest that pockets of fluid uniform in size were pinched off to become fluid inclusions, and that single nahcolite crystals were simply trapped in some pockets and not in others. Precipitation of additional nahcolite upon cooling could explain larger nahcolite crystals in larger inclusions, and the constant volume ratio.

Why there is no evidence for nahcolite precipitation in the solid-free inclusions is an unresolved problem. The average salinity of the fluids present at clathrate final melting in solid-free inclusions (8.7 eq. wt. % NaCl) is higher than that in solid-bearing inclusions (5.0 eq. wt. % NaCl). This is consistent with the possibility that solid-free inclusions are supersaturated with respect to nahcolite.

Fluid Composition

A majority of the type I, II and III fluid inclusions do not exhibit Tm-ice at or below -2.3°C as required with nahcolite saturation in the ternary H_2O-NaCl-$NaHCO_3$ system. The problematic Tm-ice data may be due to ice metastabilty. Metastable ice has been observed at temperatures as

high as six degrees above the stable melting point of ice in low-salinity fluid inclusions (Roedder, 1967). Ice metastability occurs when small vapor bubbles, like those in this study, disappear upon freezing due to the expansion of ice, and upon heating fail to nucleate at the stable melting temperature. Ice melting temperatures in this study are only two or three degrees above the temperatures produced by ice melting in the presence of nahcolite, consistent with a low chloride, high bicarbonate solution.

An alternative explanation is that elevated CO_2 partial pressure (P_{CO2}) affects the H_2O-NaCl-$NaHCO_3$ system. Gas analyses of the inclusions in sample HÖK by QMS confirm the presence of significant amounts of CO_2. Analyses from the H_2O-rich cluster have an average CO_2 composition of 6 mole %, with values ranging between 1 and 11%. The mole fraction of CO_2 (X_{CO2}) in the fluid inclusions can be estimated from the mean Th-CO_2 of 24°C. Using a CO_2 density of 0.23 g/cm^3 the P_{CO2} is roughly 130 bars. Using Henry's Law (Drummond, 1981), X_{CO2} in just the liquid fraction is found to be about 0.045. Using an average bubble volume fraction of 0.075, X_{CO2} in the combined liquid and bubble fractions should be roughly 0.053 (or 5.3 mole % CO_2). This is within the compositional range of CO_2 in the H_2O-rich gas analyses, hence the H_2O-rich analyses are attributed to type I, II and III fluid inclusions.

Experimental data for the solubility of nahcolite at elevated P_{CO2} are available only at 1.2 atm P_{CO2} (Linke, 1965), and they indicate that nahcolite solubility *increases* with a rise in P_{CO2}. This is due to higher solution pH in higher P_{CO2} systems. The solubility of nahcolite at 25°C and 130 bars P_{CO2} was calculated to be 7.3 weight% or 0.92 M using the thermodynamic data from Knacke et al. (1991) and from the computer program SUPCRT92 (Johnson et al., 1992) as outlined in Appendix A. According to this calculation, nahcolite solubility in the fluid inclusions is significant, even when the salting out effect of NaCl on $NaHCO_3$ is considered. For example, at 3.7 weight% or 1.0 M NaCl the solubility of nahcolite at 130 bars CO_2 partial pressure is 4.2 weight% or 0.54 M. In light

of this, Tm-ice data at temperatures above the $NaHCO_3$-H_2O eutectic at -2.3°C in nahcolite-bearing fluid inclusions cannot be attributed to elevated P_{CO2} and are, therefore, attributed to ice metastability.

The salinity of the fluid inclusions is difficult to constrain, not only because of the effects of ice metastability, but also because the nahcolite never completely dissolves. There are two ways of estimating the salinity or total dissolved salts (TDS) in individual inclusions. First, the TDS at Th could be calculated using a model for nahcolite solubility, but the dependence of the solubility on P_{CO2}, which cannot be estimated in a reliable manner, makes this impossible. A second method is to add some portion of the solid nahcolite in to the fluid salinity obtained from Tm-ice data to account for nahcolite dissolution at homogenization temperatures. Since an estimated 2/3 of the inclusions in any given trail contain nahcolite, 2/3 of the nahcolite crystal is assumed to be dissolved in nahcolite-bearing inclusions at trapping temperatures. A total molality for each inclusion was calculated from combined NaCl and $CaCl_2$ obtained from Tm measurements, plus $NaHCO_3$ from 2/3 of the nahcolite crystal in each inclusion. The results are shown in Figure 12 for both solid-bearing (+) and solid-free (•) inclusions exhibiting various Th. The error in salinity estimates due to ice metastability creates a range of salinities skewed toward lower values and an overlap between the solid-bearing and solid-free inclusions.

The solubility of nahcolite in water and in a 6.0 molal NaCl solution (solid lines) are illustrated in Figure 12 for reference. The CO_2-saturated nahcolite solubility was extrapolated from the data in Linke (1965). A second order polynomial curve for the solubility data as a function of temperature in the 0 to 45°C range was extrapolated to higher temperatures (dotted lines). Most of the inclusion data occur to the right or below the nahcolite saturation curves; this indicates that most of the nahcolite could have precipitated from the inclusion fluids after a nahcolite crystal was initially trapped.

The bulk composition of inclusion fluids was calculated using the weighted average properties of all the inclusions of a given type (Table 4). It is assumed that all the nahcolite trapped in the fluid

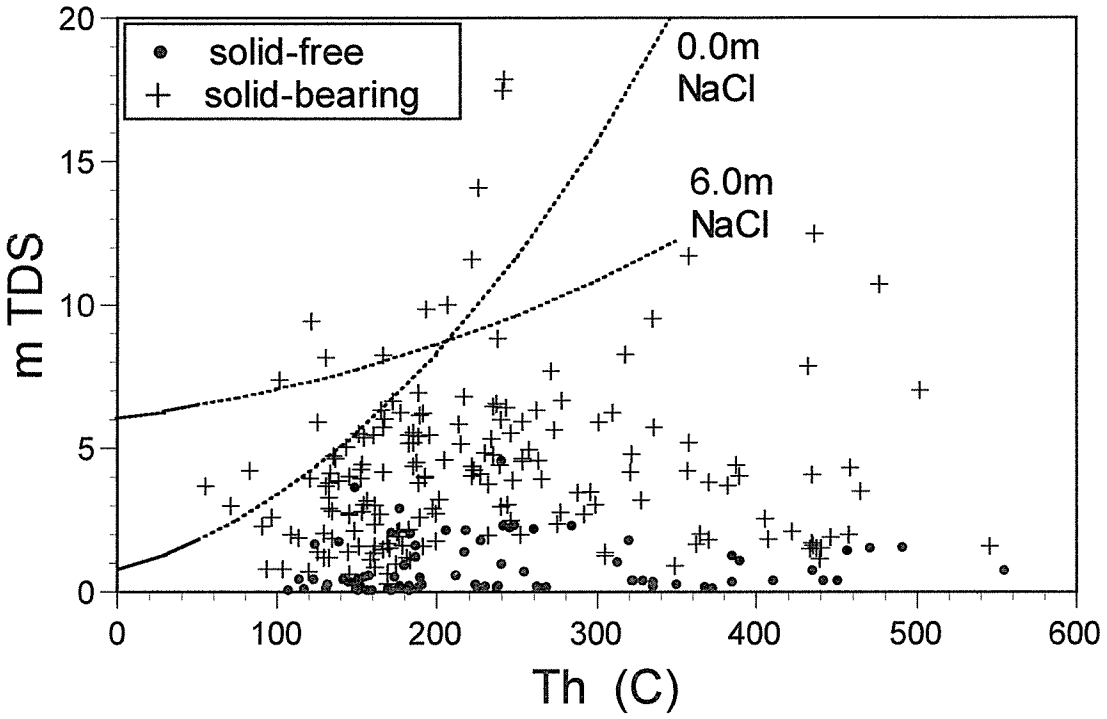

Figure 12. The variability of molality versus homogenization temperatures. Molality is combined NaCl, $CaCl_2$ and $NaHCO_3$. Nahcolite solubility in CO_2-saturated 6.0 and 0.0 molal NaCl solutions are shown for comparison. Solubility data are available in Linke (1965). The solubility curves are extrapolated beyond the limits of the available data at 45°C (dotted line) using a second order polynomial best fit curve of the available data.

Table 4. Bulk composition of inclusion fluids based on weighted averages of fluid inclusion properties. TDS = total dissolved salts, X = mole fraction, eq. wt. $\%_w$ = equivalent weight percent with respect to water, X_w = mole fraction with respect to water, Th = homogenization temperature, Pmin = minimum trapping pressure.

Type	TDS (moles/kg)	Bulk density (g/cm^3)	Molar volume (cm^3)	X					NaCl (eq. wt. $\%_w$)	X_w CO_2	Th (°C)	Pmin (bars)
				H_2O	CO_2	NaCl	$NaHCO_3$	$CaCl_2$				
IA	3.425	1.151	20.51	0.857	0.0899	0.0095	0.0432	0.00024	21.41	0.0949	451	5162
IB	6.550	1.328	19.65	0.827	0.0755	0.0131	0.0840	0.00049	34.58	0.0837	339	3069
IC	6.344	1.364	18.71	0.837	0.0678	0.0223	0.0733	0.00004	33.12	0.0750	242	2465
ID	2.863	1.155	19.89	0.868	0.0870	0.0104	0.0340	0.00032	18.30	0.0911	160	610
II	6.036	1.353	18.82	0.837	0.0716	0.0172	0.0731	0.00076	32.40	0.0788	171	1759
III	2.103	1.175	18.81	0.883	0.0840	0.0123	0.0211	0.00003	13.57	0.0870	129	1033

inclusions can be dissolved in the bulk composition at temperatures higher than Th. The bulk compositions are plotted on a ternary diagram in Figure 13 for comparison. There are no significant compositional trends with respect to the age of the inclusions, and all the bulk compositions are fairly similar. Type III fluid inclusions have the lowest chlorinity and percentage of $NaHCO_3$.

Isochores

The Th data for the bicarbonate-rich fluid inclusions range over more than 400 degrees and show a regular decrease in average Th through inclusion types, except for types ID and II which have very similar Th distributions. Isochores were calculated for each fluid inclusion type with the Bowers and Helgeson (1983) equation of state, using average inclusion properties. It was assumed that the H_2O-CO_2-NaCl system adequately represents bicarbonate-rich fluids. The isochores are shown in Figure 14. The tips of the isochores indicate the minimum trapping conditions for the fluid inclusions.

Isochores for all the inclusion types occur on the high pressure, low temperature side of peak metamorphic conditions at 3-5 kbar and 500-750°C. Isochores for type IA and IB inclusions overlap; isochores for type IC, ID and II inclusions are fairly close. The location of the isochores for younger inclusion types shifts toward the left of the figure in a crude way. It is difficult to explain these data unless the retrograde PT-time path involved isobaric cooling following peak metamorphism. The inclusions have minimum trapping conditions in the kyanite field. The aluminum silicate phase diagram of Holdaway (1971) has been added to the figure for reference. Kyanite does not occur in Bergslagen (Rickard, 1988), however, this does not preclude fluid inclusion trapping in the kyanite field, since retrograde metamorphism may have been more rapid than the rate of aluminum silicate conversion.

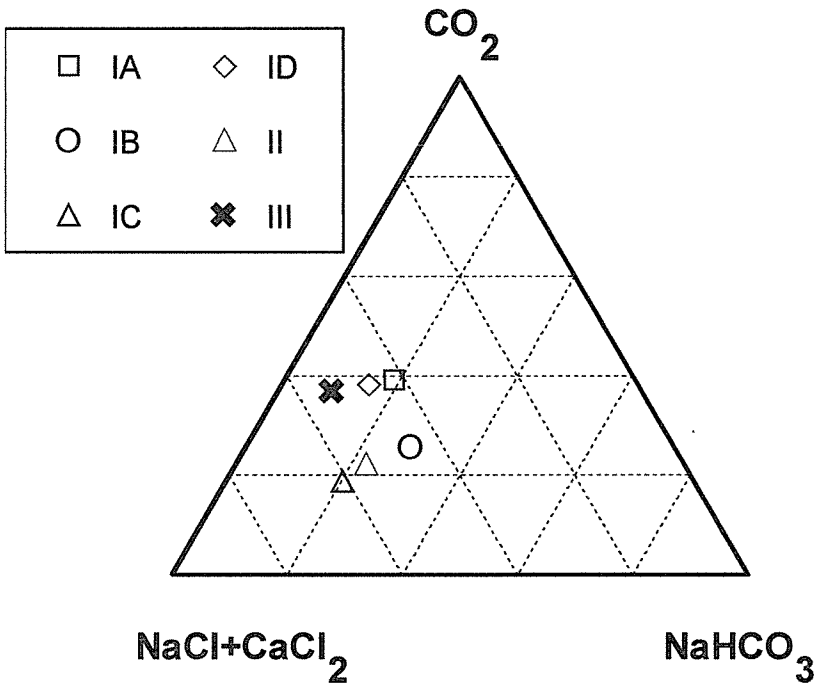

Figure 13. The bulk composition of inclusion fluids in terms of H_2O, $NaCl+CaCl_2$ and $NaHCO_3$. There are no significant trends in composition with respect to the age of the inclusions. The bulk compositions are fairly similar.

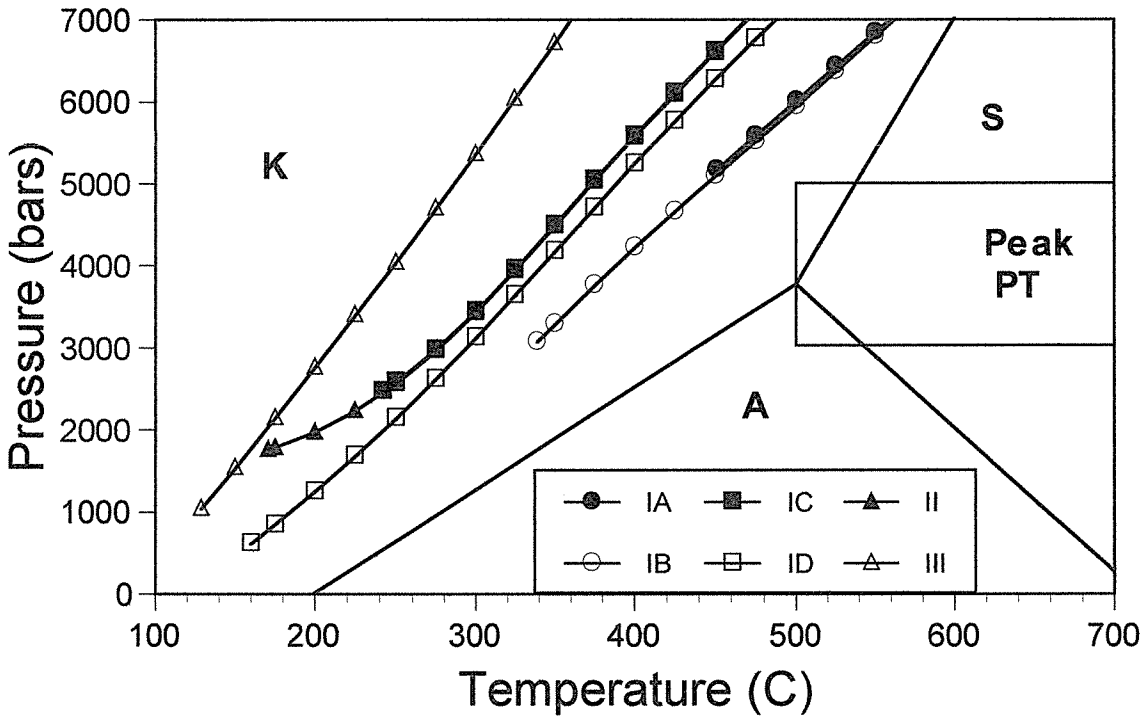

Figure 14. Isochores for fluid inclusion types based on the weighted average bulk compositions listed in Table 4. The isochores occur on the high-pressure low-temperature side of peak metamorphic PT conditions, in the kyanite field. The aluminum silicate phase diagram of Holdaway (1971) is shown. K= kyanite. S= sillimanite. A= andalusite.

Inclusion Fluid pH

The trapped fluids must have had a very high pH in order to precipitate nahcolite. In order to find the pH of the fluid inclusions at trapping conditions, and to examine the effects of nahcolite precipitation and bubble formation on pH and the solubility of SiO_2, calculations were made on an electronic spreadsheet. More details of the calculations can be found in Appendix A. The general procedures are summarized here.

The calculations involve simultaneous solution of mass and charge balance equations, and equations involving mass action constants. The nominal composition of each fluid inclusion type was taken from Table 4. Four different algorithms were used for the four different phase assemblages:

1) To find pH in an inclusion with only a liquid phase (L), an initial guess for pH is made and the concentrations of H^+ and OH^- are calculated. The concentration of the three carbon dioxide species (aqueous CO_2 or CO_2^a, HCO_3^- and CO_3^{-2}) can be found since the amount of total CO_2 available in the fluid is already provided in the nominal composition. The charges on cations and anions are added up, and if the totals are not equal, another pH is chosen until one is found that satisfies the charge balance requirement.

2) To find pH in an inclusion with liquid and a nahcolite crystal (L+S), initial guesses of both pH and the concentration of Na remaining in the liquid (mNa+) must be made. The concentrations of all species can be calculated as outlined above. Successive guesses for pH at a given mNa$^+$ are made until the charge balance requirement is satisfied. Because nahcolite is present, the concentration of HCO_3^- can be calculated an alternative way using the mass action constant for:

(3.1) $\quad NaHCO_3 = Na^+ + HCO_3^-$.

If the concentrations of HCO_3^- calculated each way are not equal, then another guess for mNa$^+$ must be made, and pH found all over again.

3) To find pH in an inclusion with liquid and a vapor bubble (L+V), initial guesses of both pH and P_{CO2} must be made. The concentration of CO_2^a is found from P_{CO2} using Henry's Law. The concentrations of HCO_3^- and CO_3^{-2} are found using the assumed pH. If the charge balance requirement is not satisfied, another pH is found for the given P_{CO2} until the requirement is satisfied. Thereafter, the concentration of CO_2 sequestered in the vapor bubble is found by subtracting the concentrations of CO_2^a, HCO_3^- and CO_3^{-2} from the total CO_2 in the nominal composition. Assuming that an inclusion has a volume of 1 cm^3 expedites the next calculation: finding the partial pressure of H_2O in the liquid phase (P_{H2O}), which must equal P_{CO2}. The volume of the bubble is calculated from P_{CO2} and the concentration of CO_2 in the bubble. The volume of the liquid, obtained from the bubble volume, is then used to calculate P_{H2O}. If P_{CO2} and P_{H2O} are not equal, another P_{CO2} is chosen and the whole procedure is repeated until the two quantities are equal.

4) To find pH in an inclusion with liquid, a vapor bubble and a nahcolite crystal (L+V+S), initial guesses of pH, P_{CO2} and mNa$^+$ must be made. The initial estimate for P_{CO2} is obtained from procedure 3 outlined above. Next, mNa$^+$ is chosen and a pH is found such that the charge balance requirement is satisfied. The concentrations of species are calculated using P_{CO2} with Henry's Law and the pH. A new mNa$^+$ is calculated using the mass balance equation for reaction (3.1). If the assumed and calculated values for mNa$^+$ do not agree, then another mNa$^+$ is chosen and a new pH is found. When the charge balance requirement is satisfied, and the assumed and calculated values of mNa$^+$ agree, P_{H2O} is calculated to make sure that P_{CO2} and P_{H2O} are still equal.

No activity coefficients were used. Henry's Law constants were obtained using the equation of Drummond (1981). Thermodynamic data for nahcolite were obtained from Knacke et al. (1991). Mass action constants were calculated using the computer program SUPCRT92 (Johnson et al., 1992). The results of the pH calculations are summarized in Table 5.

Precipitation of nahcolite at trapping conditions generally involves a significant drop in fluid alkalinity as predicted by:

(3.2) $Na^+ + H_2O + CO_2 = H^+ + NaHCO_3$ (solid).

The nucleation of a bubble changes pH very little unless nahcolite is present in the inclusion. Silica solubility in alkaline fluids is high due to the dissociation of H_4SiO_4 to $H_3SiO_4^-$. A drop in solution pH is likely to promote quartz precipitation through:

(3.3) $H_3SiO_4^- + H^+ = 2H_2O + SiO_2$ (solid).

Thus, the necking down of the fluid inclusions by quartz precipitation can be related to the pH drop associated with nahcolite precipitation. The solubility of quartz is also included in the pH calculations outlined in Table 5. There is a sufficient drop in quartz solubility to account for rapid necking down on type IB, IC, ID and II fluid inclusion trails.

Transposed and Exsolution Inclusions

The purpose of the QMS gas analysis was to determine the composition of the transposed and exsolution inclusions. Since the water-rich analyses are attributed to the bicarbonate-rich fluid inclusions, the CO_2-rich analyses must represent the transposed and exsolution inclusions. Due to the small size of the inclusions there are no microthermometry data that would confirm this interpretation. The average composition indicated for the transposed and exsolution inclusion fluids is 8% CH_4, 20% CO_2 and 68% H_2O.

Table 5. Estimated pH and SiO_2 solubility for fluid inclusions with average composition and different phase assemblages at selected isochoric PT conditions. T = temperature, P = pressure, m = molality, L = liquid, S = solid nahcolite, V = vapor bubble, ns = no solution.

Type	T (°C)	P (bars)	Phases present	pH	$mSiO_2$	PCO_2
IA	501	6022	L	8.11	0.47	
	451	5162	L	7.86	0.38	
	451	5162	L+S	ns	ns	
	451	5162	L+V	ns	ns	ns
	451	5162	L+S+V	ns	ns	ns
IB	389	4015	L	7.91	0.45	
	339	3069	L	7.64	0.18	
	339	3069	L+S	7.41	0.083	
	339	3069	L+V	7.60	0.16	2337
	339	3069	L+S+V	7.33	0.079	2337
IC	292	3280	L	7.09	0.074	
	242	2465	L	6.79	0.027	
	242	2465	L+S	6.50	0.016	
	242	2465	L+V	6.81	0.028	2070
	242	2465	L+S+V	6.60	0.016	2070
ID	210	1413	L	6.35	0.0073	
	160	610	L	6.16	0.0029	
	160	610	L+S	6.10	0.0028	
	160	610	L+V	6.12	0.0029	1730
	160	610	L+S+V	5.96	0.0028	1730
II	221	2182	L	6.64	0.0167	
	171	1759	L	6.30	0.0064	
	171	1759	L+S	5.78	0.0046	
	171	1759	L+V	6.37	0.0067	1783
	171	1759	L+S+V	6.06	0.0047	1783

Fluid Sources and Evolution

The fluid evolution recorded in the quartz phenocrysts in the metavolcanic rocks of the Zinkgruvan basin is considered in three stages that are based upon the compositional differences in the fluids (CO_2-rich versus water-rich), and the crosscutting relations between the FIP and recrystallized quartz:

Stage 1: The oldest fluid is found in the transposed and exsolution inclusions. The QMS gas analyses demonstrate that it is richest in CO_2, at about 20 mole%. The nature and amount of salts in the aqueous phase is unknown because no microthermometry is possible on the tiny inclusions.

Stage 2: The second fluid is found in the unoriented fluid inclusion trails (types I and II). It is a bicarbonate-rich aqueous fluid, with about 6 mole% CO_2. It has a salinity possibly as high as 35 eq. wt. % NaCl. Nahcolite precipitated from the fluid both before and after the fluid was trapped as inclusions under a range of PT conditions.

Stage 3: The youngest fluid is found in the incompletely healed fluid inclusion trails with preferred orientation (type III). The maximum salinity is only 14 eq. wt % NaCl. Nahcolite is a captured mineral phase.

There are no isochores for the stage 1 (CO_2-rich) fluids, hence it is difficult to locate where on the PT grid these fluids belong. Two lines of evidence suggest that the transposed fluid inclusion trails predate peak metamorphism. First, the fluid inclusions are removed by recrystallization. Second, CO_2-rich fluids originate in calcareous layers and, therefore, should be related to the development of skarn bands in the metaporphyries. H_2O-rich fluids are associated with high grade zoisite- and diopside-bearing mineral assemblages, whereas CO_2-rich fluids are more characteristic of intermediate grade skarns (Ferry, 1976). Thus, the CO_2-rich fluids may record prograde metamorphic fluid evolution.

Nahcolite-precipitating fluids can be associated with skarnification of the carbonate layers in the metavolcanic rocks. Henriques (1964) described the general sequence of banding associated with the

skarns at Zinkgruvan as progressing outward from calcite, to diopside-wollastonite, to anorthite, and lastly zoisite at the interface with the least altered metavolcanic rock. In order to account for these mineral assemblages the following reactions could be written:

(3.4) calcite + quartz = wollastonite + CO_2

(3.5) calcite + 2 albite + H_2O + CO_2 = anorthite + 4 quartz + 2 Na^+ + 2 HCO_3^-

(3.6) anorthite + albite + calcite + H_2O = zoisite + 2 quartz + Na^+ + HCO_3^-

(3.7) dolomite + 2 quartz = diopside + 2 CO_2

(3.8) 6 calcite + chlorite + 8 quartz = 6 diopside + 4 H_2O + 6 CO_2.

It is not clear whether the Mg required for the formation of diopside comes from magnesian calcite or an aluminous mineral such as chlorite. An important feature of this set of reactions is that Na^+ and HCO_3^- can be generated by the formation of anorthite and zoisite from calcite and the albite component in plagioclase. The bicarbonate-rich fluids trapped in the Zinkgruvan quartz phenocrysts, therefore, are viewed as having evolved during metamorphism.

The compositional differences between the second and third stage fluids are subtle: the stage 2 fluids (type I and II inclusions) precipitated nahcolite before and after entrapment and had in general higher total dissolved solids than the stage 3 fluid (type III inclusions). Whether this is due to continuous precipitation of nahcolite in the fluid inclusions or to mixing with an infiltrating fluid with significantly lower TDS is not known. However, the deformation that caused the microfracturing associated with type III fluid inclusions could have introduced more dilute meteoric waters. Isochore calculations agree with this idea because they suggest that stage III fluids were trapped during retrograde metamorphism.

There is no textural evidence for fluid immiscibility at any stage in the fluid evolution, i.e. CO_2-rich and H_2O-rich fluid inclusions do not coexist in the same domains or microstructural settings. The compositional range of the H_2O-rich inclusions occurs well outside the immiscibility

field for both the H_2O-CO_2-NaCl and H_2O-CO_2-$CaCl_2$ systems at 500°C and 5 kbar located by Shmulovich and Plyasunova (1993). The addition of $CaCl_2$ tends to expand the immiscibility field. However, there are no experimental data defining the immiscibility field at conditions along the isochores shown in Figure 14.

Plots of the fluid inclusion gas analyses on a N_2/Ar versus CO_2/CH_4 diagram (Figure 10) suggest that there was a common fluid for all the stages of entrapment. It also suggests that the fluid had two sources, but was mainly crustal in origin. N_2/Ar ratios less than 100 suggest, by analogy with present day groundwaters, that they are meteoric in origin (Norman and Musgrave, 1994; Giggenbach, 1997). Ratios less than 38, the ratio in modern air saturated water at 20°C, are measured in water and fluid inclusions in active geothermal systems (Giggenbach, 1986; Moore et al., 2000; Norman et al., 1997). Such low ratios are explained by the loss of N_2 by ammonia substitution into phyllosilicate minerals and by the release of radiogenic Ar from potassium-rich wall rocks. The latter explanation is applicable to Zinkgruvan. Waters with CO_2/CH_4 ratios of about 1 are common in modern basins and geothermal systems (Moore et al., 2001). Methane can originate from pyrolysis of organic material and reaction of CO_2-bearing fluids with Fe^{+2} in the wall rock minerals (Giggenbach, 1997). A simple explanation for the analyses plotted on Figure 10 is that they represent an initial methane-rich evolved or crustal fluid to which CO_2 and Ar were added during metamorphism. Remarkably, fluids from stage 1 and 2 have the same distribution of gas species. This suggests that the Zinkgruvan rocks remained a closed system to fluids throughout retrograde metamorphism, which agrees with the occurrence of nahcolite throughout the stage 2 and 3 fluid inclusion paragenesis.

Tectonic Model

The data in this study agree with the model for mid-crustal tectonism, magmatism and metamorphism proposed by Harley (1989) for LPHT granulite-bearing terranes. The slope of a typical

isobaric cooling PT-time path in a LPHT granulite-bearing terrane is 0.3 to 0.5 kbar/100°C; the P interval over which isobaric cooling paths have been documented is less than 2 kbar from peak metamorphic conditions (Harley, 1989). These constraints fit most of the fluid inclusion data from the Zinkgruvan basin. In Figure 15 possible cooling paths with an average slope of 0.4 kbar/100°C and isochores for various fluid inclusion generations are presented. The cooling paths are slightly curved toward higher pressures in order to intersect all the isochores. It is possible that previous estimates for peak metamorphic pressures in Zinkgruvan may be about 1 kbar too low.

Only type IA isochores, with minimum trapping pressures of about 5 kbar, are problematic. Type IA inclusions are found in the lower amphibolite facies sample, which is not likely to have been metamorphosed near 5 kbar. Because type IA inclusions occur on deformation band boundaries, they are more likely to have leaked fluids than the other inclusions. The Th results for type IA inclusions may be shifted to higher temperatures because aqueous fluid leaked out along the deformation band boundaries during microthermometric analysis.

Deformation, Metamorphism and Fluid Inclusions

The CO_2-rich fluid inclusions represent prograde metamorphic fluids that developed during anorthite- to zoisite-grade metamorphism of the skarn bands. The shift toward more H_2O-rich fluids is associated with diopside-grade metamorphism of the skarn bands at near peak metamorphic conditions. Because peak metamorphism is associated with the intrusion of late orogenic granitoids, which are responsible for the later open fold phases (Hedström and Wikström, 1986), the H_2O-rich fluids can be roughly correlated with late granitoid intrusion and the open fold phases. Consequently, the CO_2-rich fluids are loosely correlated with the early isoclinal fold phases.

Type IA and IB inclusions have overlapping isochores that are located close to peak metamorphic conditions on the PT grid. Type IC, ID and II inclusions have isochores that are fairly close on the

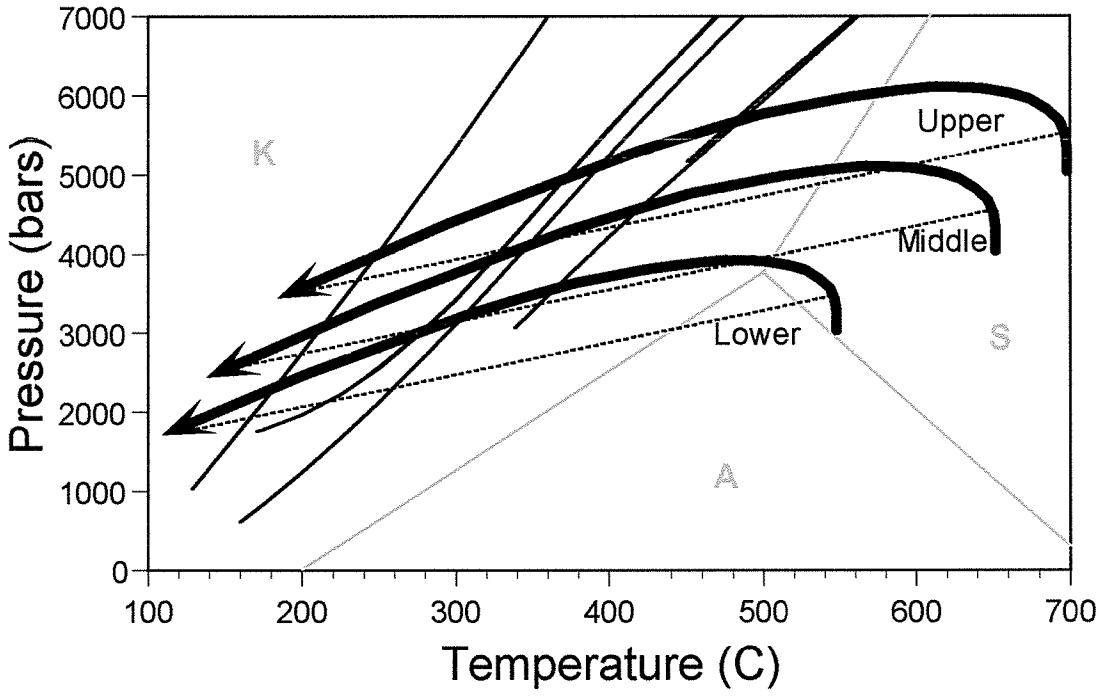

Figure 15. The possible isobaric cooling paths (thick black lines) shown have an average slope of 0.4 kbar/100°C (dotted lines). Thin solid lines are isochores. The aluminum silicate diagram of Holdaway (1971) is shown in grey lines. K= kyanite. S= sillimanite. A= andalusite.

PT grid. A possible explanation for these observations is that two major deformation phases occurred, in which multiple sets of fluid inclusions were trapped under slightly different conditions. A correlation between the two open folding phases and entrapment of the two groups of inclusions is suggested, but further work is needed to establish the relationships between folds and fluid inclusions.

The style of late orogenic granitoid emplacement could be responsible for multiple deformations along the isobaric cooling path. Some of the late granitoids in the areas around the Zinkgruvan basin are complex diapir-like structures formed by multiple intrusions of similar magma (e.g. Wikström, 1984, 1991). Peak metamorphism in the enclosing rocks is associated only with the initial intrusion. Later intrusions at retrograde metamorphic conditions could explain multiple deformation phases in the enclosing rocks at successively lower temperatures suggested by the fluid inclusion isochores.

Type IA and IB inclusions predate recrystallization of quartz in the relic phenocrysts. Type ID and II inclusions postdate recrystallization, thus, recrystallization mainly occurred in the time interval between entrapment of type IB and ID fluid inclusions. Recrystallization occurred along the retrograde PT path rather than at peak metamorphic temperatures. This suggests that deformation rather than heat was the principal driving force for recrystallization.

Type III inclusion fluids are distinguished from type I and II inclusion fluids by lower salinity. Because type III inclusion trails are not well healed and many inclusions are naturally decrepitated, it is likely that they formed at temperatures and pressures not much greater than Th and Pmin, about 130°C and 1 kbar. The observation that type III inclusion trails have a preferred orientation suggests that type III trails formed as a result of a regional stress field (e.g. Lespinasse and Pêcher, 1986), in contrast to type I and II trails which formed in relation to local intrusions. These features suggest that type III inclusions were trapped when the rocks were uplifted to higher levels in the crust where meteoric waters probably mixed in with the metamorphic fluids.

Comparison to Other Studies

The abundance of aqueous bicarbonate-rich fluid inclusions in this study is an obvious contrast to the fluid inclusions described in other studies of Bergslagen (van den Kerkhof, 1987; Beetsma, 1992; Lindblom and Burke, 1988; Åberg and Fallick, 1993). In these studies, fluid inclusions from the immediate vicinity of ore deposits were examined, and complex histories of aqueous and carbonic fluid inclusion parageneses were proposed. In this study, fluid inclusions in the host rocks were examined, and they entrapped fluid originating from only one major source: the skarn banded metaporphyries. The ubiquitous skarn and marble layers in the metavolcanic rocks of the Zinkgruvan basin are a unique feature that are responsible for the unusual bicarbonate-rich fluid inclusions.

The complexity in fluid inclusion parageneses in the ore deposits may be attributed to the relatively incompetent behavior of the ore rocks during deformation. Ore rocks that behave less competently than their host rocks are well documented (e.g. Vokes, 1969; Plimer, 1987; Vokes and Craig, 1993; Marshall and Gilligan, 1993). The ore deposits, therefore, were probably much more permeable than the metavolcanic rocks. The Zinkgruvan metaporphyries metamorphosed in a closed system and the fluids trapped by inclusions are all similar. On the other hand, the ore deposits were subject to the passage of many different fluids from diverse sources which were trapped as fluid inclusions.

Conclusions

Most fluid inclusions in metamorphosed phenocrysts in the Zinkgruvan Basin are bicarbonate-rich. Nahcolite precipitated both before and after fluid-filled microfractures healed and is a common mineral in the fluid inclusions. Estimates of salinity are as high as 35 eq. wt. % NaCl, but the salinity is difficult to constrain because the nahcolite does not completely dissolve. Nahcolite precipitation

produces a drop in pH sufficient to cause rapid quartz precipitation and microfracture healing. The pH at trapping conditions was between 6 and 8.

An older, more CO_2-rich fluid is recorded in transposed fluid inclusions. The older fluid records the generation of large amounts of CO_2 early on during skarn formation. The bicarbonate-rich fluid was generated by the conversion of calcite and albite to zoisite and anorthite later in the skarnification process. A younger fluid, less saturated with $NaHCO_3$, is recorded in partially healed fluid inclusion planes. Lower salinity of the younger fluid was probably due to meteoric water mixing in with the metamorphic fluid. Gas analyses indicate that all the inclusion fluids are related, and came from one crustal source. The fluids were generated and trapped in a nearly closed system. The gas analyses also point to a minor influx of meteoric water.

Isochores for the bicarbonate-rich inclusions are consistent with fluid entrapment on an isobaric cooling PT-time path. The quartz phenocrysts continued to be deformed and recrystallized along the retrograde path, trapping successively younger, less $NaHCO_3$-saturated fluids at lower temperatures.

Chapter IV

Nahcolite-Calcite Dissolution-Precipitation Phenomena inside Fluid Inclusions in Quartz

Introduction

The daughter mineral nahcolite ($NaHCO_3$) was first identified in CO_2-rich, aqueous fluid inclusions in carbonatites (Rankin and LeBas, 1974). It also occurs in the aqueous and carbonic fluid inclusions of high-grade metamorphic rocks (e.g. Coolen, 1982; Olsen, 1987; Anderson et al. 1989, 1990) and is reported in a few studies of mesothermal lode gold deposits (e.g. Robert and Kelly, 1987; Guilhaumou et al., 1990; Ansdell and Kyser, 1991). In the majority of studies, the nahcolite readily dissolves upon heating; rarely, the nahcolite daughter mineral fails to dissolve completely before fluid inclusion decrepitation occurs. In aqueous inclusions of the Waikari carbonatite apatites, high temperature precipitation of an unidentified carbonate mineral in place of nahcolite was reported by Rankin (1975). It is the only previously reported occurrence of nahcolite dissolution in combination with retrograde precipitation of a carbonate mineral. In this study, fluid inclusions in which nahcolite dissolves on heating in combination with the precipitation of calcite are reported.

Samples and Related Work

The samples are metamorphosed quartz-crystal tuffs of early Proterozoic age from the Zinkgruvan region of Bergslagen, south-central Sweden. The inclusion hosts are relic quartz phenocrysts up to several millimeters in size. Some quartz eyes are relatively unrecrystallized and

show deformation bands; others exhibit a variety of new grains and deformation lamellae. Peak metamorphic conditions in the Zinkgruvan area are estimated to range between 500 and 750°C at 3 to 5 kbar (Rickard, 1988). Some samples were metamorphosed to a higher temperature (sillimanite grade) than others (andalusite grade). The rocks have three essential matrix minerals: quartz, sericite-altered feldspar, and chlorite-altered biotite.

Many of the fluid inclusions in the quartz phenocrysts are described in detail in Chapter III. This study is a continuation of that work; therefore, the fluid inclusion types identified in that study are summarized here. On the basis of microstructural criteria, three common types of bicarbonate-rich, chloride-poor aqueous fluid inclusions were identified and dated relative to one another. They are, in chronological order, type I, II and III fluid inclusions. Type I inclusions are less than 12 μm in length and have negative crystal shapes. Type II inclusions range up to 20 μm in size and have complex rounded forms. Type III inclusions range up to 50 μm in size and exhibit a variety of flat digitate forms. Up to two thirds of the inclusions on any given trail of type I and II inclusions possess nahcolite daughter minerals. Solid-free and solid-bearing inclusions have similar microthermometry results. The explanation for this is that nahcolite precipitated before necking down of the fluid inclusions occurred. Homogenization temperatures (Th) for the inclusions vary between 555 and 94°C with a general decrease in temperature in younger inclusion types. Inclusions on individual trails, however, exhibit a maximum range in Th of about 60 degrees.

Methods

Microthermometric results were obtained on a Linkam THM600 heating/freezing stage calibrated for temperature using the melting point of potassium dichromate (398°C) and pure water (0.0°C), and the melting point of CO_2 (-56.6°C) in a synthetic H_2O-CO_2 fluid inclusion standard.

Phase volume ratios were determined by measuring the dimensions of the inclusions, and the phases within them, with an optical micrometer. The shapes of regular inclusions were assumed to be doubly terminated negative quartz crystals, and irregular inclusions were approximated as clusters of spheres and six-sided prisms. Bubbles were assumed to be spherical. Daughter minerals were assumed to be parallelepipeds. Mineral identifications were made by laser Raman microspectrometry.

Salinity of the liquid phase at room temperature in the presence of solids was estimated from the final melting of clathrate (Collins, 1979) or ice (Bodnar, 1993). Ratios of NaCl to $CaCl_2$ were estimated using hydrohalite final melting temperatures (Oakes et al., 1990) whenever final melting could be observed. The bubble phase was assumed to be pure CO_2 and the CO_2 density was assumed to be uniform in all the fluid inclusions. The density of CO_2 was determined from liquid-vapor homogenization of the CO_2-rich phases in several of the larger inclusions.

Calculations of minimum trapping pressures were made using the equation of state of Bowers and Helgeson (1983). The substitution of NaCl for $NaHCO_3$ and $CaCl_2$ was assumed to have very little effect on the estimate of minimum trapping pressures.

Results

Fluid Inclusions and Daughter Minerals

The fluid inclusions in this study occur in the same samples reported in Chapter III. The ones described here are called type C fluid inclusions in order to avoid confusion between the nomenclature used in this and the other study.

Type C fluid inclusions are aqueous inclusions that occur mainly in close proximity to type I or II inclusion trails. They do not form trails of their own; however, they may be common along a

given type I or II trail. Type C inclusions are typically offset about 10 μm from the plane of the type I or II trails. In addition, type C inclusions occur in strain shadows adjacent to mineral inclusions and on the convex side of angular bulges in the new grain boundaries. The inclusions are more common in unrecrystallized quartz than in recrystallized quartz. Most range between 6 and 20 μm in length and are irregular in shape. The vapor bubble in most type C fluid inclusions is 2-5% of the volume, but can represent up to 20% of the inclusion volume. All type C fluid inclusions contain at least one daughter mineral. Three subtypes are recognized on the basis of the included mineral assemblage at room temperatures: type C_1 inclusions contain one rod-like mineral, type C_2 inclusions contain one rhomb-shaped mineral, and type C_3 fluid inclusions contain both a smaller rod-shaped mineral and a larger rhomb-shaped mineral. Both forms of included mineral are colorless.

The rod-shaped crystal has the optical properties of a biaxial negative mineral. The morphology and optical properties are consistent with nahcolite, however, the twinning common in nahcolite is not seen. The second mineral has a rhombohedral form, is highly birefringent and has a low refractive index. These properties are consistent with calcite. Both nahcolite and calcite were identified with laser Raman spectroscopy. The phase volume ratios of nahcolite and calcite in the fluid inclusions are listed in Table 6.

Microthermometry

Type C fluid inclusions exhibit L+V→L homogenization over a large range in temperature (Figure 16). Calcite is always present at fluid homogenization and inclusion decrepitation. The vapor bubble generally is attached to one of the daughter minerals, and shrinks away at fluid homogenization without Brownian motion. Homogenization temperatures for type C fluid inclusions generally are not similar to Th in neighboring type I or II fluid inclusions. Eutectic melting is

Table 6. Fluid inclusion characteristics, microthermometry results and liquid phase salinity. V = volume, Bub = vapor bubble, Nah = nahcolite, Cal = calcite, Tm = final melting temperature, Clath = clathrate, Hydro = hydrohalite, Te = first melting temperature, TDS = total dissolved solids.

Type	Inclusion	Size (μm)	V (μm³)	Volume percent			Tm			Te (°C)	Th (°C)	%Ca	NaCl (eq. wt. %)	Molality TDS
				Bub	Nah	Cal	Ice (°C)	Clath (°C)	Hydro (°C)					
C_1	4Z-55	8	60	1	16	0	-0.8				55	0	1.4	0.234
C_1	HÖK-175	8	15	5	4	0	-0.4				175	0	0.7	0.121
C_1	HÖK-183	5	29	1	21	0	-1.4		-22.6		183	11	2.4	0.379
C_1	HÖK-189	4	15	1	22	0		4.3			189	0	10.1	1.735
C_1	103-194	5	16	2	25	0	-13.7				194	0	17.5	2.998
C_1	DBH-223	7	43	5	16	0	-2.1				223	0	3.5	0.607
C_1	DBH-234	6	38	5	8	0	-12.8		-22.1		234	7	15.8	2.548
C_1	103-242	4	4	2	45	0	-7.2				242	0	10.7	1.836
C_1	4Z-246	5	25	2	9	0	-2.1				246	0	3.5	0.607
C_1	4Z-253	8	58	5	18	0	-4.0	8.4	-23.8	-69.8	253	21	3.2	0.460
C_1	DBH-278	8	90	2	18	0	-3.6	3.6	-21.7		278	4	11.2	1.842
C_1	HÖK-292	5	15	3	11	0	-1.3				292	0	2.2	0.383
C_1	4Z-296	8	20	1	15	0	-0.9			-70.4	296	0	1.6	0.268
C_1	103-465	4	2	5	15	0	-0.6			-70.8	465	0	1.1	0.180
C_1	4Z-477	4	9	15	29	0	-5.5	6.2			477	0	7.1	1.222
C_2	4Z-174	6	49	7	0	20	-1.5				174	0	2.6	0.440
C_2	HÖK-322	4	10	8	0	9					322			
C_2	HÖK-323	6	38	1	0	14					323			
C_2	HÖK-329	5	10	8	0	13					329			
C_2	HÖK-411	5	3	8	0	11					411			
C_2	HÖK-442	4	21	1	0	7					442			
C_2	HÖK-451	5	9	1	0	14					451			
C_3	103-71	10	140	1	12	14	-0.2	10.1	-24.4		71	26	0.4	0.049

Table 6. (continued)

Type	Inclusion	Size (μm)	V (μm³)	Volume percent			Tm			Te (°C)	Th (°C)	%Ca	NaCl (eq. wt. %)	Molality TDS
				Bub	Nah	Cal	Ice (°C)	Clath (°C)	Hydro (°C)					
C_3	103-83	8	33	2	6	9	-13.9		-23.8	-67.8	83	21	16.8	2.423
C_3	103-91	8	89	2	9	7	-1.0		-22.3		91	9	1.8	0.281
C_3	103-97	9	129	2	9	8	-0.8	8.2	-22.6		97	11	3.5	0.541
C_3	HÖK-120	9	128	2	2	19	-0.6	2.0			120	0	13.3	2.269
C_3	DBH-126	17	188	5	5	19	-0.3	1.5			126	0	13.9	2.373
C_3	103-133	8	61	1	11	6	-3.5		-23.8		133	21	5.6	0.811
C_3	103-161	9	34	5	9	6	-15.8	10.0	-22.9	-69.9	161	14	0.0	0.000
C_3	DBH-162	6	43	2	5	6	-0.3	5.2	-25.4		162	33	8.8	1.157
C_3	103-170	6	53	5	1	9	-1.2				170	0	2.1	0.355
C_3	103-179	10	36	2	7	2	-0.7		-26.1		179	37	1.4	0.176
C_3	103-189	15	62	1	16	6	-0.3		-22.5		189	10	0.5	0.086
C_3	HÖK-190	6	41	1	9	20	-0.9				190	0	1.6	0.268
C_3	4Z-193	8	179	2	12	16	-2.9	8.3			193	0	3.4	0.579
C_3	DBH-200	5	6	2	11	12	-0.3				200	0	0.5	0.091
C_3	DBH-202	8	64	2	12	8	-1.5				202	0	2.6	0.440
C_3	DBH-288	12	156	2	9	9	-6.8		-26.2	-69.8	288	37	10.0	1.284
C_3	DBH-328	5	14	2	12	10	-1.2				328	0	2.1	0.355
C_3	4Z-358	5	15	2	14	35	-0.4				358	0	0.7	0.121
C_3	4Z-363	13	126	5	4	17	-4.0	7.8	-23.8	-70.7	363	21	4.3	0.622
C_3	HÖK-365	8	20	1	7	16					365			
C_3	HÖK-371a	12	63	2	6	4	-1.8				371	0	3.1	0.524
C_3	HÖK-371b	5	15	1	14	13		7.6			371	0	4.7	0.802
C_3	DBH-390	9	243	8	7	9	-7.8		-22.8	-70.3	390	13	11.5	1.756
C_3	HÖK-408	7	46	2	7	7					408			
C_3	4Z-434	10	45	1	4	26	-1.6		-23.4	-72.2	434	18.0	2.7	0.403

Table 6. (continued)

Type	Inclusion	Size (μm)	V (μm³)	Volume percent			Tm			Te (°C)	Th (°C)	%Ca	NaCl (eq. wt. %)	Molality TDS
				Bub	Nah	Cal	Ice (°C)	Clath (°C)	Hydro (°C)					
C_3	HÖK-435a	5	22	5	15	10			-25.0		435			
C_3	HÖK-435b	4	10	1	6	12					435			
C_3	HÖK-436	5	11	1	6	12	-0.8	7.7		-68.9	436	0.0	4.5	0.771
C_3	HÖK-438	10	173	2	5	15					438			
C_3	HÖK-502	7	14	5	23	11					502			

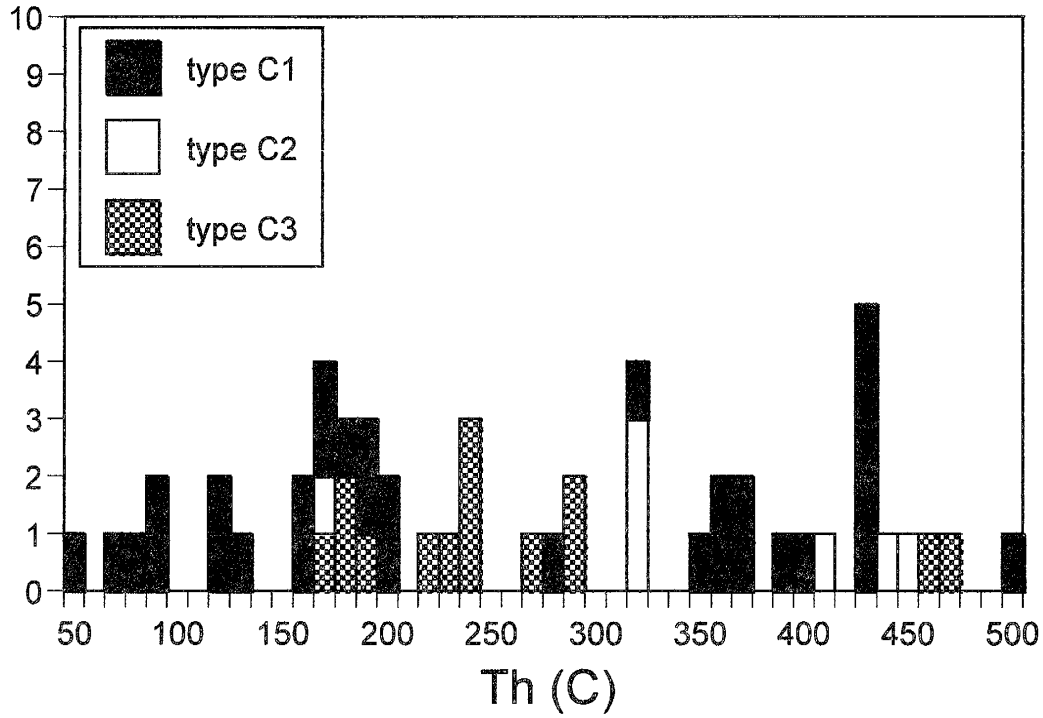

Figure 16. Homogenization temperatures (L+V→L) of the three different type C fluid inclusions. Fluid phases homogenize to the liquid phase after nahcolite has dissolved (in type C_1 and C_3) and calcite has precipitated (in type C_1).

observed in a few inclusions at a mean temperature of -70.1°C; it is manifest as the sudden rearrangement of solid phases. Hydrohalite is seen to form in some inclusions and exhibits final melting at an average temperature of -23.7°C. Ice or clathrate may be the final frozen phase to melt in any given inclusion. The average temperature for ice melting (Tm-ice) is -3.4°C; for clathrate melting it is 6.5°C. A liquid CO_2-rich phase that homogenized to vapor could be seen in only a few of the larger type C_3 inclusions. The CO_2 homogenization temperatures range between 22.7 and 28.2°C, with an average of 24.6°C. Microthermometry results are summarized in Table 6.

During heating and cooling of type C fluid inclusions, nahcolite and calcite precipitate and dissolve at various temperatures. Upon heating nahcolite dissolves and calcite precipitates; upon cooling nahcolite precipitates and calcite dissolves. The temperatures at which calcite first precipitates (the calcite-in temperature) and nahcolite finally dissolves (the nahcolite-out temperature) on a heating run could be established in some of the larger inclusions (Figure 17). In five individuals both calcite-in and nahcolite-out temperatures were found.

Since the calcite exhibits retrograde solubility, the temperature at which calcite dissolves upon cooling (the calcite-out temperature) should be more useful than the calcite-in temperature. The calcite-out temperature was found in only two of the five inclusions. The calcite-out temperatures are much lower than the calcite-in temperatures when both are located at normal heating and cooling rates. In order to obtain similar temperatures for both, heating and cooling rates of less than 0.5°C/min were used to approach the points of precipitation and final dissolution. The temperature at which calcite dissolves is strongly influenced by cooling rate. The apparent calcite-out temperature becomes higher as slower cooling rates are used over longer intervals in the cooling run. The temperature at which calcite precipitates is not as sensitive to variations in heating rate. For practical reasons, therefore, calcite-in temperatures were recorded instead of calcite-out temperatures.

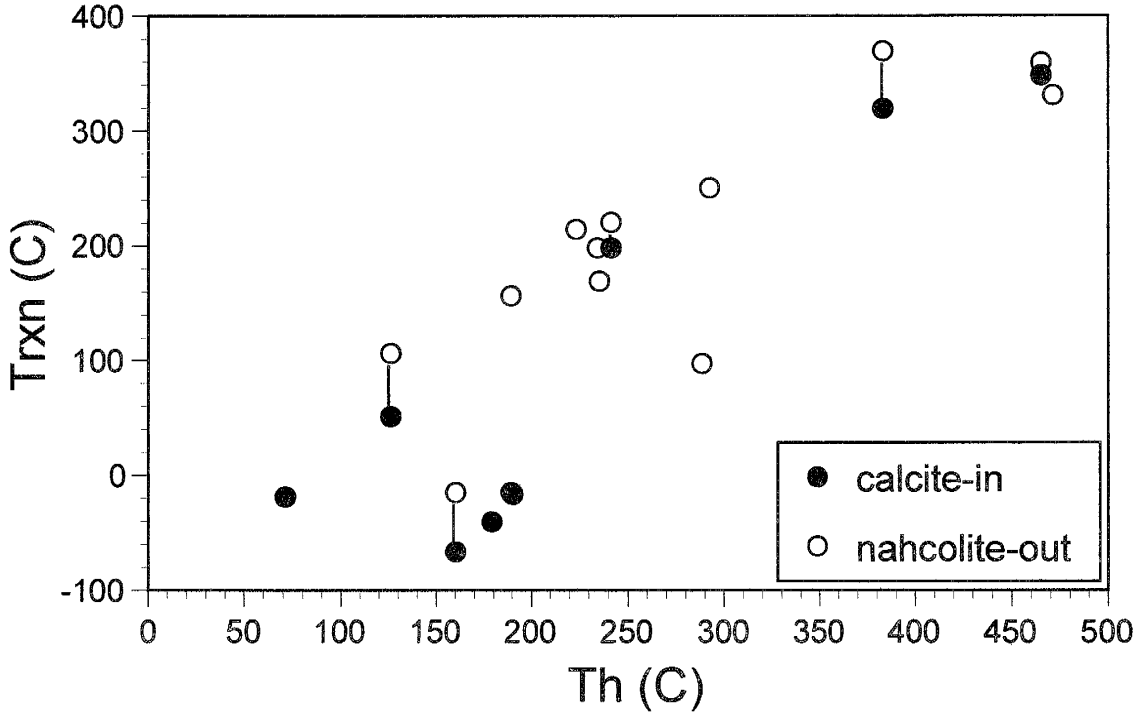

Figure 17. The temperatures (Trxn) at which calcite precipitates (●) and nahcolite finally dissolves (O) in a given fluid inclusion, as compared to final liquid phase homogenization (L+V→L).

Unusual Behavior

Type C_1 inclusions. The phase changes that occur in type C_1 fluid inclusions upon heating and cooling are illustrated in Figure 18. In type C_1 inclusions the nahcolite begins to dissolve upon heating, generally with the small vapor bubble attached to the crystal. Nahcolite is replaced by calcite in a continuous reaction that always occurs in the presence of the vapor bubble. The calcite precipitates as a tiny grain attached to the diminished nahcolite. A small mobile cluster consisting of the nahcolite, calcite and bubble is commonly formed. Final nahcolite dissolution causes a sudden and obvious change in the mode of motion of the cluster. The size of the vapor bubble appears to change only when homogenization is imminent. Homogenization of the fluid phases occurs only after the nahcolite is completely dissolved. The vapor bubble disappears while attached to the growing calcite grain. Perceptible growth of the calcite ceases at temperatures about 20 to 30 degrees higher than Th.

The dissolution of nahcolite at slow heating rates can induce the vapor bubble to detach in some cases; the bubble size does not appear to change after detachment. Slow rates of heating (less than 10°C/min) over the entire heating interval are required to keep an unattached vapor bubble from sticking to one of the carbonates.

In some type C_1 fluid inclusions, up-and-down cycling of the temperature at a point where the bubble begins to shrink can extend the life of the bubble to much higher temperatures. The Th obtained by extensive cycling may be up to 20 or 30 degrees higher than Th obtained by direct heating. In other type C_1 inclusions, a free secondary vapor bubble forms when temperatures are held slightly above Th for ten or more minutes. The second bubble exhibits Brownian motion. These inclusions recover their original degree of fill at 20°C; there is no evidence for leaking. The behavior can be repeated in another heating cycle. In one inclusion (4Z-253) Th consistently occurs at 253°C; the bubble reappears at about 270°C and disappears at about 285°C.

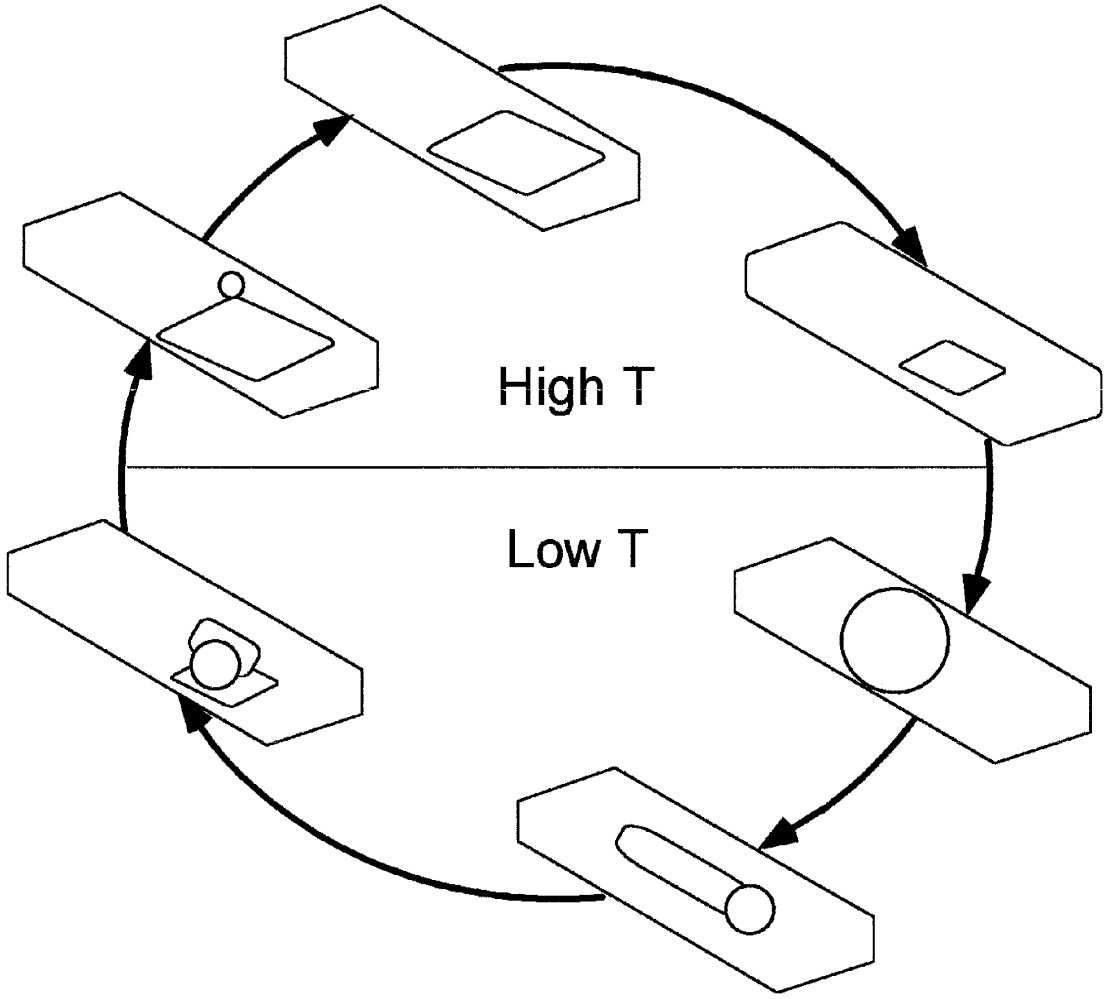

Figure 18. The phase changes that occur in a C_1 type fluid inclusion upon heating and cooling are illustrated in this cartoon. At room temperature a vapor bubble and a long slender nahcolite crystal are present. Upon heating, calcite precipitates and nahcolite eventually dissolves. The vapor bubble homogenizes to the liquid phase when nahcolite is gone. Upon cooling, the calcite persists metastably until the vapor bubble forms. At this point the calcite dissolves suddenly producing a large unstable vapor bubble. Nahcolite precipitates spontaneously.

Cooling after homogenization of the fluid phases causes the calcite to shrink and abruptly disappear, being replaced by a large bubble (20-30% by volume). The phase transition occurs so suddenly that the calcite crystal appears to explode. The large bubble spontaneously contracts to a smaller size (2-5% by volume) as nahcolite rapidly precipitates. It is impossible to stabilize the larger bubble. This spontaneous behavior is not seen during cooling prior to homogenization of the fluids. When the bubble is still present, the nahcolite crystal precipitates and grows upon cooling of the fluid inclusion, and the calcite gradually dissolves and disappears.

Type C_2 inclusions. The type C_2 fluid inclusions have freezing temperatures significantly lower than type C_1 inclusions, generally lower than -100°C. A few of the inclusions never freeze. The inclusions may freeze before or after the calcite dissolves, but calcite never dissolves after an inclusion is frozen. In some inclusions calcite dissolves before freezing, but only at slower cooling rates (less than 5°C/min). The calcite dissolves in a sudden manner, and the vapor bubble becomes much larger (20-30% by volume). As in type C_1 inclusions, the transition occurs so suddenly that the crystal appears to explode. The inclusion freezes instantaneously. In two inclusions nahcolite precipitates and the bubble shrinks when freezing occurs.

At the low point in the freezing run the inclusions may, in addition to frozen hydrous phases, contain: 1) calcite and a small vapor bubble; or 2) no minerals and a larger vapor bubble; or 3) nahcolite and a small vapor bubble. The melting behavior upon heating in the first group of inclusions is unremarkable. In the other inclusions, calcite precipitates before ice final melting occurs. In the second group of inclusions, calcite precipitates suddenly as relatively large grains and causes a noticeable reduction in vapor bubble size. In the third group of inclusions, calcite precipitation and nahcolite dissolution must occur, but the phase changes are nearly impossible to see.

Upon heating to liquid homogenization temperatures the vapor bubble generally remains attached to the calcite grain and does not show Brownian motion. There is very little change in the size of the calcite. A free vapor bubble reappears upon cooling and continues to grow. In many inclusions the bubble slowly migrates toward and attaches itself to the calcite grain.

Type C_3 inclusions. In type C_3 fluid inclusions, the vapor bubble commonly is lodged between nahcolite and calcite grains (and in some smaller inclusions it may be totally obscured), or it is attached to the calcite grain. Upon heating the nahcolite shrinks and the calcite grows. In those inclusions where the calcite is much larger than the nahcolite, the growth of calcite is not noticeable. The vapor bubble commonly remains attached to the calcite grain after nahcolite finally dissolves, shrinking and disappearing at liquid homogenization without Brownian motion.

After liquid homogenization the bubble reforms upon cooling and, in most cases, migrates to the calcite grain and becomes attached. The bubble grows with continued cooling until nahcolite is precipitated; the bubble simultaneously contracts. A gradual reduction in the size of the calcite grain may be noticed during cooling, but no abrupt size change occurs when nahcolite precipitates.

Type C_3 inclusions generally freeze at temperatures below -100°C, with both nahcolite and calcite present. The nahcolite grows and the calcite shrinks noticeably upon cooling in a few inclusions. The melting behavior upon heating is unremarkable. A few inclusions with smaller calcite grains do not freeze until after the calcite dissolves in a manner similar to the behavior in type C_2 inclusions. In these inclusions, calcite must precipitate upon heating, but it is rarely seen. In one inclusion (103-161), a small grain of calcite became noticeable upon heating at -68°C. Remarkably, the nahcolite disappeared at -16°C, even though nahcolite was seen at room temperatures prior to freezing the inclusion!

Discussion

Origin of Calcite

Type C fluid inclusions mainly occur adjacent to trails of type I and II inclusion trails, and do not form trails of their own. This observation suggests that calcite is a trapped mineral that was captured at different times in the formation of various type I and II inclusion trails. Even though type C_1 inclusions do not contain calcite at room temperatures, calcite is present when they are heated above Th, and must have been present when the inclusions were formed. Calcite does not occur in the host quartz as either isolated inclusions or as mineral veins, therefore, it probably originated in fluid inclusions that have been destroyed.

A reasonably constant ratio between inclusion volume (V) and the volume of the calcite (Vc) shown in Figure 19a suggests that calcite formed as a daughter mineral. In order to explain this, it is suggested that the microcracks which formed type I and II inclusion trails propagated along "ancestral" type C inclusion trails, destroying most of the old inclusions and dissolving many of the calcite crystals in the process. The younger fluids invaded the outlying cavities to form newer fluid inclusions; the old cavities were opened and resealed with new fluids inside. The correlation between inclusion volume and the combined volume of nahcolite and calcite (Vn+c) shown in Figure 19b is very good. This may indicate that nahcolite precipitated in place of calcite upon cooling in the type C inclusions.

No stronger evidence for the "ancestral" type C fluid inclusion trails still exists, i.e. trails containing *only* type C fluid inclusions have not been found. However, this view explains additional features in the distribution of type C fluid inclusions. They are more numerous in unrecrystallized quartz, suggesting that the "ancestral" type C inclusions formed prior to quartz recrystallization, perhaps even before peak metamorphism. Type C fluid inclusions in strain

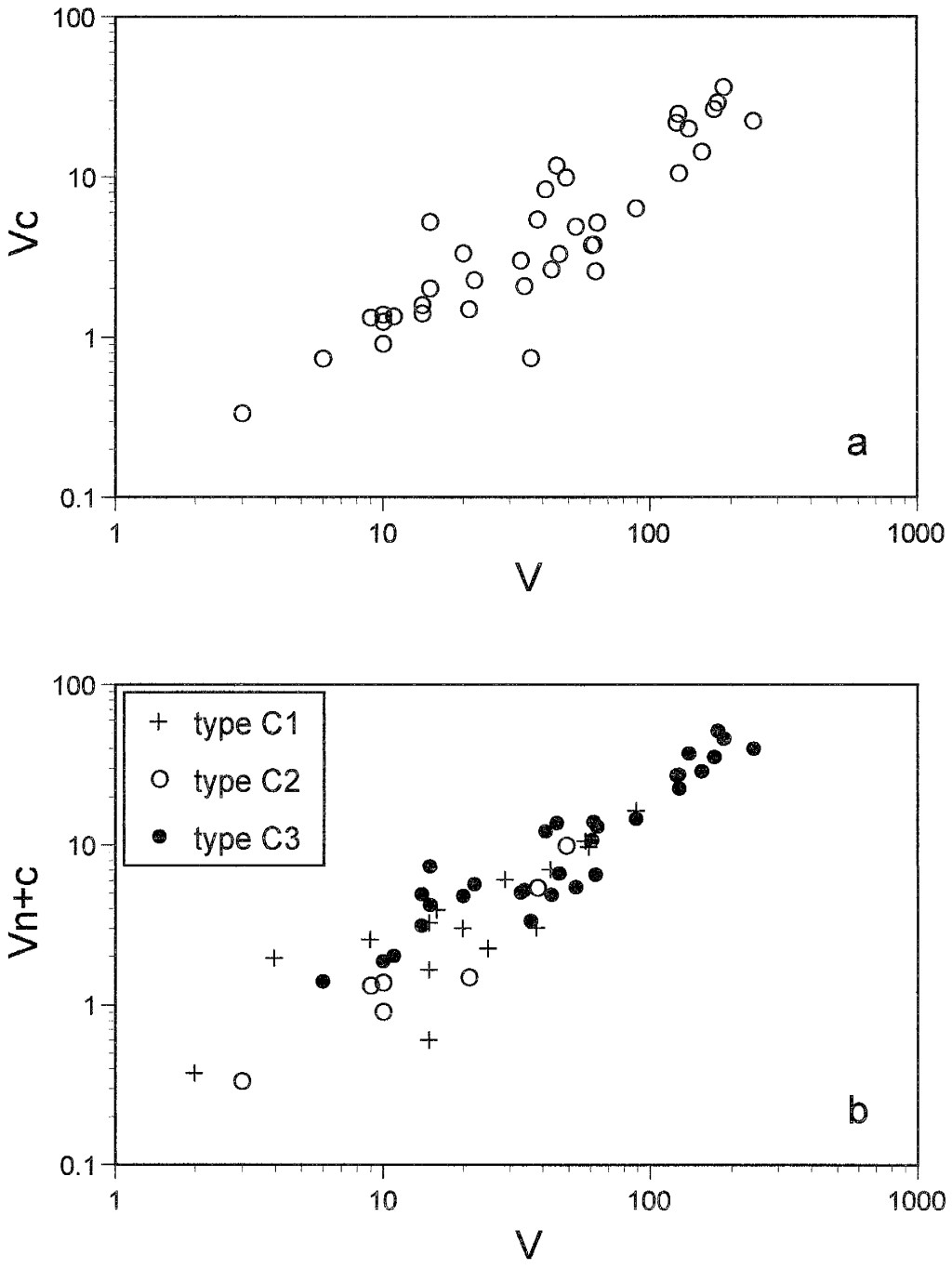

Figure 19. The relationships between inclusion and phase volumes. a) The volume of calcite (Vc) is plotted against inclusion volume (V). b) The total volume of both minerals (Vn+c) is plotted against inclusion volume. Volumes are in μm^3.

shadows developed around silicate mineral inclusions in the host quartz are evidence that some inclusions may have escaped destruction during quartz deformation. Type C inclusions on the convex side of angular bulges in new quartz grain boundaries suggest that stranded calcite was an obstacle to grain boundary migration during recrystallization. The quartz grain boundaries migrated around the calcite and new inclusions with calcite formed in the wake of the grain boundaries.

Estimating Composition

Low eutectic melting is consistent with the H_2O-NaCl-$CaCl_2$ system which exhibits a metastable eutectic at about -70°C (Davis et al., 1990). The presence of both nahcolite and calcite in all the inclusions at some point during heating or freezing indicates that $NaHCO_3$ and $CaCO_3$ are also significant components. Thus, the type C fluid inclusions belong to the system H_2O-CO_2-NaCl-$CaCl_2$-$NaHCO_3$-$CaCO_3$. This is a complex and poorly understood system, hence it is not clear how the microthermometry data should be interpreted. The approach taken here was to estimate the composition of the fluids at low temperatures from hydrohalite and ice or clathrate final melting temperatures and add or subtract solid components as dictated by volume changes in nahcolite and calcite at different temperatures. Only the ternary systems H_2O-NaCl-$CaCl_2$ and H_2O-NaCl-$NaHCO_3$ are well characterized at low temperatures (Oakes et al., 1990; Borisenko, 1974). The H_2O-NaCl-$CaCl_2$ system was used here because the Na/Ca ratios of the fluids are of particular interest, as outlined in a following section. It was assumed that aqueous $NaHCO_3$ behaves like NaCl, and aqueous $CaCO_3$ behaves like $CaCl_2$.

The salinity and mole% $CaCl_2$ (relative to NaCl) of the inclusion liquids at low temperature are listed in Table 6. Where clathrate final melting temperatures are available the salinity was obtained from them. Where hydrohalite final melting temperatures are available salinity was

obtained in the ternary system, otherwise salinity was found from ice final melting with reference to the system H_2O-NaCl. The liquids are about 5 eq. wt.% NaCl; $CaCl_2$ is about 20 mole% of the salts.

The average density of the CO_2-rich bubbles is 0.23 g/cm^3, based on an average homogenization temperature of 24°C for the CO_2. The densities of nahcolite and calcite are 2.21 and 2.71 g/cm^3 respectively. The densities of the bubble, the liquid and the solids were used to calculate the bulk composition and molar volume of the fluid inclusions, which are listed in Table 7.

For the purposes of calculating isochores for type C fluid inclusions an estimate of the total dissolved solids (TDS) for the inclusions at liquid homogenization temperatures is obtained by adding the nahcolite crystal, which completely dissolves, into the liquid phase and by removing all the $CaCl_2$ as calcite, which precipitates as a result of nahcolite dissolution. The calcite is assumed to be a trapped phase. The mass balance for calcite precipitation is:

(4.1) $$CaCl_2^a + 2\ NaHCO_3 = 2\ NaCl^a + CaCO_3 + H_2O + CO_2.$$

The molar volume is recalculated to account for the change in solid phases present in the inclusion at Th. The results of these calculations are listed in Table 7.

Trapping Conditions

The best estimate of minimum trapping conditions is made at Th since the temperature at which the last calcite precipitates cannot be determined. It must be assumed that the system H_2O-CO_2-NaCl adequately represents the composition of the fluids. Minimum trapping pressures (Pmin) calculated from the fluid properties using the Bowers and Helgeson (1983) equation of state are listed in Table 8 for those fluid inclusions that have appropriate compositions. The Pmin values are widely scattered and many are unrealistic. The problems are due to poor constraints on

Table 7. Composition of the fluid inclusions at low and high temperatures. Th = homogenization temperature.

		Mole fractions at 0°C						Mole fractions at Th				
Type	Inclusion	H_2O	CO_2	NaCl	$CaCl_2$	Nahcolite	Calcite	H_2O	CO_2	NaCl	Nahcolite	Calcite
C_1	4Z-55	0.914	0.0010	0.0039	0	0.081	0	0.914	0.0010	0.0039	0.081	0
C_1	HÖK-175	0.973	0.0049	0.0021	0	0.020	0	0.973	0.0049	0.0021	0.020	0
C_1	HÖK-183	0.886	0.0010	0.0055	0.0007	0.107	0	0.887	0.0003	0.0069	0.105	0.001
C_1	HÖK-189	0.867	0.0009	0.0302	0	0.102	0	0.867	0.0009	0.0302	0.102	0
C_1	103-194	0.827	0.0019	0.0542	0	0.117	0	0.827	0.0019	0.0542	0.117	0
C_1	DBH-223	0.905	0.0050	0.0103	0	0.080	0	0.905	0.0050	0.0103	0.080	0
C_1	DBH-234	0.912	0.0043	0.0462	0.0035	0.034	0	0.915	0.0008	0.0536	0.028	0.004
C_1	103-242	0.721	0.0022	0.0267	0	0.250	0	0.721	0.0022	0.0267	0.250	0
C_1	4Z-246	0.946	0.0018	0.0107	0	0.042	0	0.946	0.0018	0.0107	0.042	0
C_1	4Z-253	0.895	0.0051	0.0061	0.0016	0.092	0	0.896	0.0035	0.0093	0.089	0.002
C_1	DBH-278	0.884	0.0018	0.0317	0.0013	0.081	0	0.885	0.0005	0.0344	0.079	0.001
C_1	HÖK-292	0.937	0.0029	0.0066	0	0.054	0	0.937	0.0029	0.0066	0.054	0
C_1	4Z-296	0.920	0.0010	0.0045	0	0.075	0	0.920	0.0010	0.0045	0.075	0
C_1	103-465	0.913	0.0052	0.0030	0	0.079	0	0.913	0.0052	0.0030	0.079	0
C_1	4Z-477	0.792	0.0176	0.0188	0	0.171	0	0.792	0.0176	0.0188	0.171	0
C_2	4Z-174	0.875	0.0074	0.0071	0	0.000	0.110	0.875	0.0074	0.0071	0	0.1100
C_3	103-71	0.853	0.0011	0.0006	0.0002	0.066	0.079	0.853	0.0009	0.0010	0.066	0.0790
C_3	103-83	0.885	0.0017	0.0367	0.0098	0.026	0.041	0.886	0	0.0403	0.023	0.0430
C_3	103-91	0.912	0.0020	0.0043	0.0004	0.045	0.036	0.912	0.0016	0.0051	0.045	0.0370
C_3	103-97	0.905	0.0019	0.0081	0.0010	0.044	0.040	0.905	0.0009	0.0102	0.042	0.0410
C_3	HÖK-120	0.859	0.0018	0.0405	0	0.009	0.089	0.859	0.0018	0.0405	0.009	0.0890
C_3	DBH-126	0.836	0.0048	0.0415	0	0.024	0.094	0.836	0.0048	0.0415	0.024	0.0940
C_3	103-133	0.905	0.0009	0.0111	0.0029	0.051	0.029	0.905	0	0.0130	0.050	0.0300
C_3	103-161	0.912	0.0054	0.0000	0	0.049	0.033	0.912	0.0054	0	0.049	0.0330
C_3	DBH-162	0.928	0.0017	0.0142	0.0070	0.022	0.027	0.929	0	0.0178	0.019	0.0290
C_3	103-170	0.938	0.0049	0.0061	0	0.005	0.046	0.938	0.0049	0.0061	0.005	0.0460

Table 7. (continued)

		Mole fractions at 0°C						Mole fractions at Th				
Type	Inclusion	H_2O	CO_2	NaCl	$CaCl_2$	Nahcolite	Calcite	H_2O	CO_2	NaCl	Nahcolite	Calcite
C_3	103-179	0.951	0.0019	0.0019	0.0011	0.034	0.010	0.952	0.0008	0.0042	0.032	0.0110
C_3	103-189	0.879	0.0011	0.0012	0.0001	0.085	0.033	0.879	0.0009	0.0015	0.085	0.0330
C_3	HÖK-190	0.834	0.0011	0.0041	0	0.049	0.112	0.834	0.0011	0.0041	0.049	0.1120
C_3	4Z-193	0.839	0.0021	0.0091	0	0.063	0.087	0.839	0.0021	0.0091	0.063	0.0870
C_3	DBH-200	0.870	0.0022	0.0014	0	0.060	0.067	0.870	0.0022	0.0014	0.060	0.0670
C_3	DBH-202	0.888	0.0020	0.0072	0	0.061	0.042	0.888	0.0020	0.0072	0.061	0.0420
C_3	DBH-288	0.892	0.0018	0.0144	0.0085	0.041	0.042	0.893	0	0.0181	0.038	0.0443
C_3	DBH-328	0.876	0.0021	0.0057	0	0.062	0.053	0.876	0.0021	0.0057	0.062	0.0534
C_3	4Z-358	0.675	0.0025	0.0015	0	0.090	0.231	0.675	0.0025	0.0015	0.090	0.2311
C_3	4Z-363	0.875	0.0051	0.0081	0.0022	0.020	0.089	0.877	0.0029	0.0125	0.016	0.0919
C_3	HÖK-371a	0.941	0.0019	0.0092	0	0.028	0.019	0.941	0.0019	0.0092	0.028	0.0194
C_3	HÖK-371b	0.848	0.0010	0.0129	0	0.071	0.068	0.848	0.0010	0.0129	0.071	0.0677
C_3	DBH-390	0.884	0.0075	0.0275	0.0041	0.033	0.044	0.887	0.0035	0.0360	0.025	0.0485
C_3	4Z-434	0.829	0.0011	0.0051	0.0011	0.021	0.143	0.829	0	0.0072	0.019	0.1441
C_3	HÖK-436	0.898	0.0009	0.0131	0	0.029	0.059	0.898	0.0009	0.0131	0.029	0.0590

Table 8. Molar volume and minimum trapping pressures for the fluid inclusions. Th = homogenization temperature, X_w = mole fraction with respect to water, eq. wt. $\%_w$ = equivalent weight percent with respect to water, V/n = molar volume, Pmin= minimum trapping pressure.

Type	Inclusion	V/n (cm^3)	NaCl (eq. wt. $\%_w$)	X_w CO_2	Th (°C)	Pmin (bars)
C_1	4Z-55	19.17	23.08	0.0011	55	1987
C_1	HÖK-175	18.92	6.85	0.0051	175	
C_1	HÖK-183	19.26	29.08	0.0019	183	364
C_1	HÖK-189	17.56	33.02	0.0011	189	2012
C_1	103-194	17.77	40.15	0.0022	194	1855
C_1	DBH-223	19.04	24.48	0.0055	223	696
C_1	DBH-234	16.14	22.22	0.0084	234	8289
C_1	103-242	21.15	55.51	0.0031	242	
C_1	4Z-246	17.67	15.27	0.0019	246	3355
C_1	4Z-253	19.36	26.21	0.0074	253	799
C_1	DBH-278	17.10	29.28	0.0035	278	4091
C_1	HÖK-292	18.57	17.29	0.0031	292	2584
C_1	4Z-296	18.96	21.86	0.0011	296	1825
C_1	103-465	20.01	22.56	0.0057	465	3701
C_1	4Z-477	22.46	43.78	0.0217	477	1662
C_2	4Z-174	18.26	2.57	0.0084	174	892
C_3	103-71	19.50	20.18	0.0015	71	298
C_3	103-83	15.28	18.60	0.0127	83	
C_3	103-91	18.46	15.00	0.0027	91	
C_3	103-97	17.77	15.74	0.0032	97	449
C_3	HÖK-120	15.40	15.77	0.0021	120	
C_3	DBH-126	16.33	20.27	0.0057	126	4893
C_3	103-133	17.06	18.28	0.0042	133	2445
C_3	103-161	20.04	14.78	0.0059	161	
C_3	DBH-162	15.79	11.16	0.0093	162	
C_3	103-170	18.01	3.69	0.0052	170	1125
C_3	103-179	18.33	10.97	0.0032	179	715
C_3	103-189	19.72	24.23	0.0014	189	
C_3	HÖK-190	18.58	17.07	0.0013	190	612
C_3	4Z-193	18.38	21.81	0.0025	193	940
C_3	DBH-200	19.45	18.56	0.0025	200	
C_3	DBH-202	18.51	19.92	0.0023	202	898
C_3	DBH-288	16.05	16.69	0.0113	288	
C_3	DBH-328	18.77	20.11	0.0023	328	2794
C_3	4Z-358	20.61	30.49	0.0038	358	1181
C_3	4Z-363	17.57	9.54	0.0082	363	8191
C_3	HÖK-371a	17.56	11.44	0.0020	371	7748
C_3	HÖK-371b	17.94	24.25	0.0012	371	4681
C_3	DBH-390	16.96	18.16	0.0130	390	
C_3	4Z-434	17.43	9.36	0.0026	434	
C_3	HÖK-436	16.98	13.10	0.0011	436	

the molar volume and composition of the inclusion fluids and metastable homogenization of the vapor bubbles.

The results are plotted in Figure 20. Peak metamorphic conditions and the aluminum silicate phase diagram of Holdaway (1971) are shown for reference. A majority of the inclusions have minimum trapping conditions in the kyanite field. Type I and II fluid inclusions in Chapter III also have minimum trapping conditions in the kyanite field. Similar trapping conditions are required if type C inclusions formed at the same time as their type I and II neighbors.

Mineral Reactions

Observations on the CO_2-rich vapor-dominated bubbles in type C fluid inclusions can be summarized as follows: 1) the bubbles are attracted to the included mineral surfaces; 2) the bubble is always present when nahcolite and calcite are dissolving and precipitating at the same time; 3) in C_1 and C_3 inclusions the bubble homogenizes at temperatures only a little bit higher than temperatures of final nahcolite dissolution; 4) precipitation of nahcolite involves a sudden reduction in bubble size if calcite is not present; and 5) dissolution of calcite involves a sudden expansion in bubble size if nahcolite is not present.

The bubble seems to be an essential part of the mineral reaction. H_2O and CO_2 are generated by dissolution of either nahcolite or calcite according to:

(4.2) $NaHCO_3 + H^+ = Na^+ + H_2O + CO_2$ and

(4.3) $Ca^{2+} + H_2O + CO_2 = CaCO_3 + 2H^+$.

The mole fraction of CO_2 in the fluid produced is 0.50 or 50 mole%. However, the amount of CO_2 dissolved in the aqueous phase of a fluid inclusion with a vapor bubble is constrained by Henry's Law to much smaller values. Consider a type C_1 fluid inclusion. The Henry's Law constant for CO_2 in a 6% NaCl solution at 25°C is 38 bars (Drummond, 1981). The density of the CO_2-rich

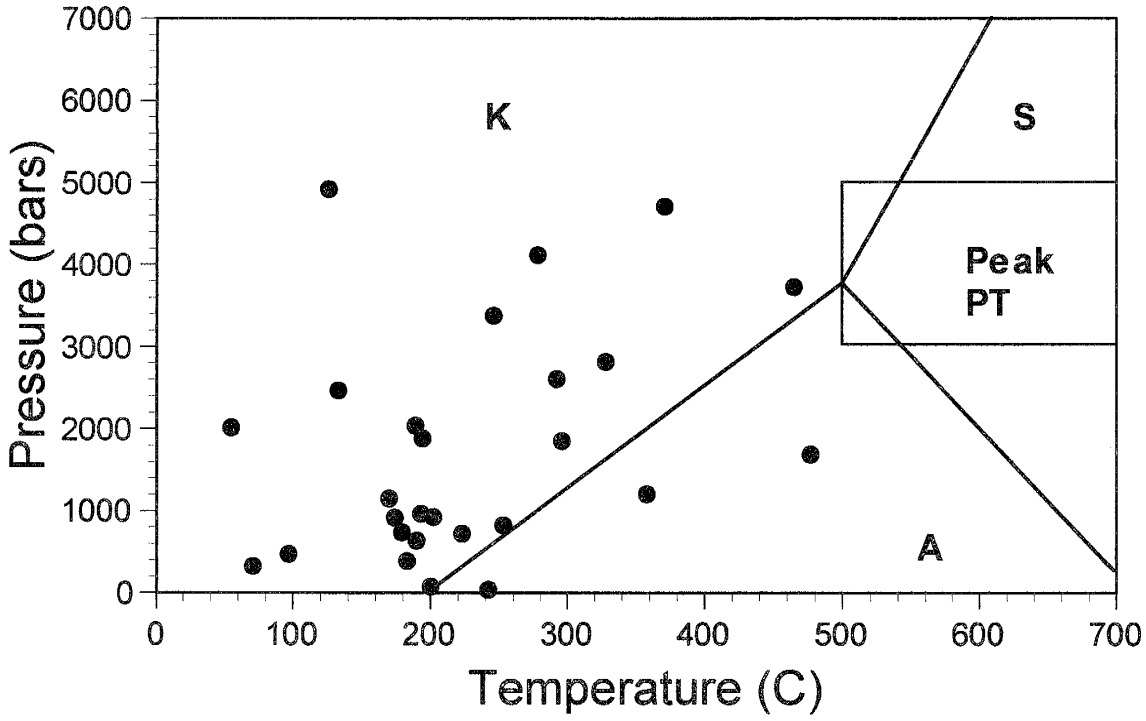

Figure 20. Minimum trapping conditions for some type C fluid inclusions. The aluminum silicate diagram of Holdaway et al. (1971) is drawn in for reference. K= kyanite. A= andalusite. S=sillimanite.

bubble in an inclusion with average characteristics is 0.23 g/cm^3 and the CO_2 partial pressure is 131 bars. The mole fraction of CO_2 in the liquid phase is then 0.035 or 3.5 mole%. When nahcolite dissolves upon heating the inclusion, the excess CO_2 generated by reaction (2) must go into the vapor bubble. Calcite precipitation eventually helps deplete the CO_2 supplied to the vapor bubble by nahcolite dissolution. The vapor bubble shrinks soon after the nahcolite completely dissolves, its supply of CO_2 having been cut off.

When calcite dissolves upon cooling in a type C_1 inclusion there is no vapor bubble in which the excess CO_2 generated by reaction (3) can be accommodated. As a result the calcite persists metastably, to temperatures much below that at which it precipitated, until a vapor bubble can nucleate. When the bubble nucleates, the calcite spontaneously and completely dissolves, releasing large amounts of CO_2 into the bubble. The bubble "explodes" to a large size. When nahcolite precipitates it consumes the excess CO_2 and the bubble shrinks to a more normal size. Nahcolite precipitation is held up until the calcite releases CO_2. In contrast to this behavior, if the vapor bubble is not homogenized and is still present upon cooling, the calcite dissolves readily and nahcolite precipitates quickly. It seems, therefore, that the bubble is critical for rapid transfer of CO_2 between nahcolite and calcite.

The behavior of C_2 fluid inclusions upon cooling below 25°C is different: the vapor bubble is always present and yet calcite is not readily dissolved and nahcolite may never precipitate. It is as if the vapor bubble were not there. The formation of clathrate may be responsible. As the temperature drops, any CO_2 liberated by calcite dissolution is trapped in the aqueous phase as clathrate. Perhaps the calcite persists metastably until its dissolution creates enough CO_2 to exceed the capacity of the aqueous phase to trap the CO_2 as clathrate. The calcite then dissolves and the bubble enlarges. The excess water freezes spontaneously. Nahcolite cannot precipitate if the water is locked up in ice and clathrate.

The molar amounts of nahcolite and calcite in the fluid inclusions should vary inversely whenever both solids are present. The mole fractions of nahcolite, calcite and water in the fluid inclusions at room temperature were calculated and the results for nahcolite and calcite are plotted in Figure 21. The amounts of the two minerals are inversely related, with a slope of about -2/3 for the type C_3 inclusion data (-0.67 with 0.09 standard error). This suggests that the net reaction for the dissolution and precipitation is:

(4.4) $3NaHCO_3 + 2Ca^{+2} = 2CaCO_3 + 3Na^+ + H^+ + CO_2 + H_2O.$

The scatter in the data indicates that the sum of the mole fractions of calcite and nahcolite is not the same in all inclusions, which might be expected since the inclusions formed at different times. The scatter is probably due mainly to small variations in the V/Vc ratios at trapping, compounded by various trapping fluids with different salinities and densities.

Estimation of Fluid pH

The pH of fluid inclusions is not usually determined from mineral equilibria simply because the mineral assemblages that constrain pH do not occur together within a single fluid inclusion. Instead, pH is deduced from P_{CO2} and carbonic acid dissociation. The fortuitous coexistence of nahcolite and calcite in type C_3 fluid inclusions facilitates the estimation of pH for the coexisting fluid phase.

An estimate of the pH of the inclusion fluids at Tm-ice may be calculated using the molalities (m) of Na^+ and Ca^{+2} and the chemical equilibrium constant (K) for:

(4.5) $NaHCO^3 + Ca^{+2} = CaCO_3 + Na^+ + H^+.$

At 0°C and 131 bars log K_5 is -3.008 and the calculation is simply:

(4.6) $pH = \log mNa^+ - \log mCa^{+2} + 3.008.$

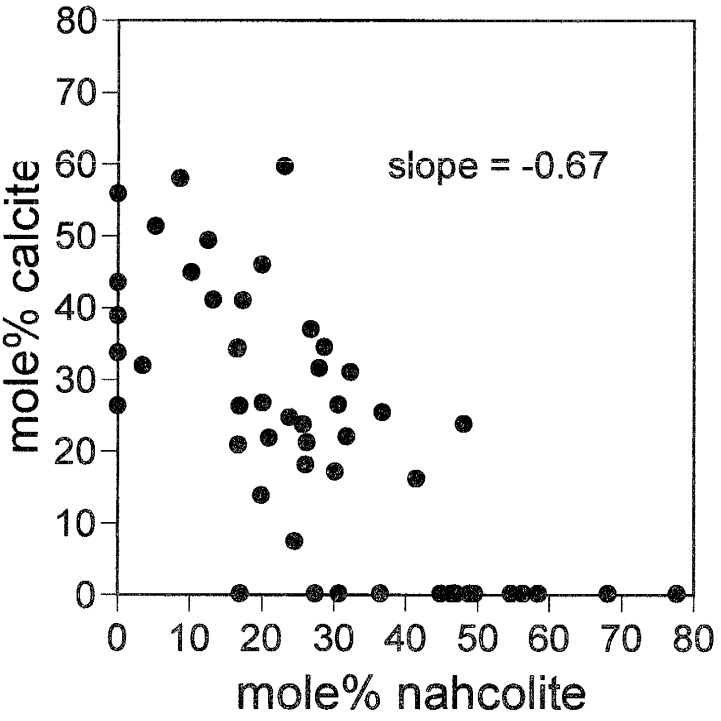

Figure 21. Mole% nahcolite versus calcite in the fluid inclusions at 25°C shows that the amounts of nahcolite and calcite are inversely related. Type C_1 inclusions plot along the bottom margin, type C_2 inclusions plot along the left margin. The distribution of points for type C_3 inclusions is linear with a slope of -0.67 (standard error of 0.09).

The concentration of Na^+ and Ca^{+2} can be determined from the hydrohalite and ice or clathrate final melting temperatures. Using activity coefficients is not warranted since the relative amounts of Na and Ca are not very accurately known.

The values for log K_5 at 0.1°C and 131 bar were obtained using the thermodynamic modeling program SUPCRT92 (Johnson et al., 1992). Thermodynamic data for nahcolite listed in Knacke et al. (1991) was added to the SUPCRT92 database. With these data, SUPCRT92 produces a reasonable solubility product for nahcolite (K_{SP} = 0.423 at 25°C and 1 bar) as compared with several determinations of nahcolite solubility reviewed in Monnin and Schott (1984).

The resulting pH for twelve fluid inclusions for which hydrohalite final melting temperatures are available are presented in Table 9. The pH of the fluids ranges between 3 and 4 at low temperature. The fluid pH at low temperature is not very useful, so fluid pH must be recalculated at trapping conditions.

Fluid pH at Trapping Conditions

Minimum trapping pressures were approximated using the Ideal Gas Law since values of Pmin obtained using the Bowers and Helgeson (1983) equation of state are not reliable. The phase volume ratios inside the fluid inclusions and the number of moles of fluid components at Th were used to calculate the pressures. All the Ca was assumed to be precipitated as calcite according to reaction (1).

An iterative technique was used to calculate pH at trapping conditions since nahcolite is no longer present in the fluid inclusions. The approach taken here was to calculate the concentration of total CO_2 using an assumed pH value and making guesses for pH until the calculated CO_2 agreed with the total CO_2 in the bulk composition of the fluid.

Table 9. Calculation of pH at 0°C and 131 bars. m = concentration in moles/kg H_2O.

Inclusion	mCa	mNa	pH
103-71	0.013	0.036	3.46
103-83	0.612	2.302	3.58
103-91	0.026	0.260	4.01
103-97	0.062	0.499	3.92
103-133	0.180	0.679	3.58
DBH-162	0.419	0.850	3.32
103-179	0.066	0.112	3.24
103-189	0.009	0.078	3.96
DBH-288	0.528	0.899	3.24
4Z-363	0.137	0.514	3.58
DBH-390	0.258	1.725	3.83
4Z-434	0.075	0.340	3.67

First, $m H^+$ and $m OH^-$ were calculated from the assumed pH. The concentration of H^+ was obtained directly from the pH. A charge balance equation involving the ions was written as:

(4.7) $$m HCO_3^- + 2\, m CO_3^{-2} = m Na^+ + m H^+ - m Cl^- - m OH^-$$

where the quantities on the right hand side are known. Since $m HCO_3^-$ and $m CO_3^{-2}$ are related by the dissociation reaction:

(4.8) $$HCO_3^- = H^+ + CO_3^{-2}$$

and $m CO_3^{-2}$ can be expressed in terms of $m HCO_3^-$ as:

(4.9) $$m CO_3^{-2} = K_8\, m HCO_3^- / m H^+,$$

substitution into equation (4.7) can be made so that:

(4.10) $$m HCO_3^- = (m Na^+ + m H^+ - m Cl^- - m OH^-) / (1 + 2\, K_8 / m H^+).$$

Once $m HCO_3^-$ was found, $m CO_3^{-2}$ was calculated from equation (4.9). From pH and $m HCO_3^-$ the concentration of aqueous CO_2 (CO_2^a) was found from the mass action constant for the dissociation reaction:

(4.11) $H_2O + CO_2^a = H^+ + HCO_3^-$.

Finally, the total CO_2 for an assumed pH was found by adding up the three CO_2 species. All of the mass action constants for the reactions at various temperatures and pressures were calculated using SUPCRT92.

Nearly all the pH values for the inclusion fluids range between 6 and 8 as shown in Table 10. Type I and II fluid inclusions discussed in Chapter III have a similar range in pH over a similar range in trapping conditions, as compared with type C inclusions. Similar fluid pH at trapping conditions is required if type C inclusions formed at the same time as their type I and II neighbors.

Association with Type I and II Fluid Inclusions

Type I and II inclusions described in Chapter III record a protracted history of trapping bicarbonate-rich fluids in the metavolcanic rocks. The fluids were mainly derived from devolatilization reactions occurring in skarn bands in the metatuffs. In particular, the production of anorthite and zoisite from calcite and albite produced Na^+ and HCO_3^-. These fluids would have been nearly saturated with calcite. Not all of the calcite occurring in type C fluid inclusions would have been dissolved when the inclusions were reopened by microcracks filled with type I or II fluids.

If the origin of the type C inclusions proposed here is correct, then the composition of the fluids at trappping conditions in both type C and type I and II inclusions must have been similar. The compositional range of type I and II inclusions is 83-86 mole% H_2O, 6-9 mole% CO_2, 3-8 mole% $NaHCO_3$ and 0.9-2.2 mole% NaCl. The average composition of fluids in type C inclusions is 92 mole% H_2O, 0.4 mole% CO_2, 6 mole% $NaHCO_3$ and 1.6 mole% NaCl. The amounts of NaCl and $NaHCO_3$ are similar in both inclusion types. Type C fluids have less CO_2, which is

Table 10. Calculation of pH at minimum trapping conditions. Th= homogenization temperature, Pmin = estimated minimum trapping pressure, mCO_2^T = concentration of all CO_2 species, mNa = concentration of Na, mCl = concentration of Cl in moles/kg H_2O.

Inclusion	Th (oC)	P (bars)	mCO_2^T (mol/kg H_2O)	mNa (mol/kg H_2O)	mCl (mol/kg H_2O)	pH
103-71	71	1468	0.0461	0.0458	0.0007	7.30
103-83	83	1937	0.0011	0.0039	0.0035	5.41
103-91	91	1640	0.0166	0.0175	0.0018	6.98
103-97	97	1732	0.0352	0.0408	0.0079	6.89
103-133	133	1979	0.0096	0.0122	0.0033	6.93
DBH-162	162	2291	0.0019	0.0041	0.0032	6.01
103-179	179	2050	0.0023	0.0024	0.0003	6.98
103-189	189	1948	0.0127	0.0127	0.0002	7.50
DBH-288	288	2907	0.0453	0.0729	0.0412	7.37
4Z-363	363	3011	0.0156	0.0190	0.0083	7.58
DBH-390	390	3251	0.1060	0.1753	0.1030	8.06
4Z-434	434	3373	0.0015	0.0019	0.0005	6.86

attributed to smaller vapor bubbles in many of the inclusions. Estimates of CO_2, however, are not very reliable since all the bubbles were assumed to have the same density.

The most perplexing difference between the fluid inclusion types is that Th in type C inclusions generally are not similar to those in neighboring type I or II inclusions. The differences are attributed to metastable behavior of the various phases during nahcolite dissolution and calcite precipitation in type C inclusions. The reappearance of vapor bubbles at higher temperatures after they have been homogenized to the liquid phase once already is an indication that Th values in type C inclusions may not indicate equilibrium between the vapor, the liquid and calcite.

Finally, the fluid that originally precipitated the calcite in "ancestral" type C fluid inclusions is gone. It is likely that it also was derived from devolatilization reactions in the skarn bands, and was similar to type I and II fluids. The "ancestral" type C fluid inclusions must have been trapped

under conditions that favored calcite over nahcolite precipitation. Calcite precipitation is expected at higher temperatures, higher P_{CO2} and lower pH. The "ancestral" type C inclusions could have formed at peak metamorphic conditions when the fluids were richer in CO_2.

Conclusions

Calcite in type C fluid inclusions is a trapped mineral that was captured at different times in the formation of various type I and II inclusion trails. The microcracks which formed type I and II inclusion trails propagated along "ancestral" type C inclusion trails, destroying most of the old inclusions. The old cavities of some "ancestral" type C inclusions were opened and resealed with new fluids and old calcite crystals inside. Type C inclusions as a group have compositions, trapping conditions and fluid pHs similar to those in type I and II inclusions.

Upon heating type C fluid inclusions, nahcolite dissolves and calcite precipitates, liberating carbon dioxide and water. A vapor bubble is always present during heating. The reverse reaction cannot take place if a vapor bubble is absent during cooling. The precipitation and dissolution of calcite are more sluggish than that of nahcolite. These features create unusual phenomena resulting from metastability during heating and cooling runs in type C fluid inclusions.

Chapter V

Fluid Inclusion Planes in Recrystallized Quartz Phenocrysts, Zinkgruvan Basin, South-Central Sweden

Introduction

Fluid inclusion parageneses are usually established using a number of textural criteria for relative dating of inclusion generations, including crosscutting relations between fluid inclusion planes (FIP) and host mineral grain boundaries, inclusion morphology and progressive migration of inclusions away from their plane of origin (Roedder, 1984, p. 343). Associating the variation in orientations of FIP with macroscopic structures of different ages is another technique for establishing the relative ages of inclusions in deformed rocks (e.g. Pêcher et al., 1985; Lespinasse and Pêcher, 1986; Cathelineau et al., 1990; Lespinasse and Cathelineau, 1990). The method addresses only those FIP that have a preferred orientation on the scale of a thin section or larger, and can be related to known phases of regional deformation. The FIP are assumed to have formed as mode I, pure extension microcracks.

Many metamorphic fluid inclusions cannot be placed into a paragenetic sequence because they do not occur in FIP with preferred orientations, nor do they exhibit features that could be used to distinguish different generations from one another. The goal of this study is to examine FIP that exhibit no preferred orientation to see if there are any other means by which different inclusion generations can be discriminated. The subjects of this study are relic quartz phenocrysts in metaporphyries, and a quartz veinlet, whose fluid inclusion parageneses are difficult to determine by microstructural criteria. Details of the fluid inclusion geochemistry are presented in Chapter III.

Geologic Setting

The relic quartz phenocrysts are found in rhyodacitic metaporphyries of Early Proterozoic age in the Zinkgruvan basin of south-central Sweden. The basin is named after the Zinkgruvan massive sulfide deposit and is part of the old mining province of Bergslagen. At roughly 1.90-187 Ga, Bergslagen developed as an extensional basin on continental crust (Allen et al., 1996). The basin was filled with volcanic rocks and sediments that were intruded by granitoids. The Svecofennian orogeny commenced about 1.85 Ga with westward-verging isoclinal folding and thrusting related to east-west shortening (e.g. Magnusson, 1936; Gaal and Gorbatschev, 1987). Many structural basins like Zinkgruvan formed between massifs of deformed granitoids. The Swedish tradition is to call the massif rocks "early orogenic" granitoids, even though it is now known that the granitoids intruded the basin rocks *before* deformation. Major folding was followed by the intrusion of "late orogenic" granitoids around 1.80-1.78 Ga. The intrusion of late orogenic granitoids is associated with the development of later local folding phases in the Zinkgruvan area (Wikström and Karis, 1991). Peak metamorphism outlasted the major folding phases (Allen et al., 1996) and was once thought to be the result of the late orogenic granitoid intrusions (Magnusson, 1936).

The Zinkgruvan basin (Figure 22) consists of an overturned west trending syncline developed in a sequence of volcanic and clastic strata (Wikström and Karis, 1991). The axial plane of the syncline generally dips steeply to the north and the hinge is located in the vicinity of a major east-west striking dike. The generally north-dipping strata in the mine are overturned. The sequence is divided into a thicker lower formation of metaporphyries and a thinner upper formation of metagreywackes, although each rock type is mixed in with the other in subordinate amounts. Skarn or marble layers and metapelites are present throughout the sequence, and exhalative strata

Figure 22. Geology of the Zinkgruvan basin after Wikström and Karis (1991). Outcrop locations for samples HÖK, SINS, 98 and 103 are indicated with a ■. The eastern shaft of Zinkgruvan is located with a ◥. Samples 4Z and DBH are from sites underground in the mine.

The Zinkgruvan basin is an early Proterozoic aged, west trending synform with younger metasedimentary rocks (white) forming the core and older metavolcanic rocks (light grey) forming the flanks. A middle Proterozoic aged basic dike (black) approximately marks the hinge of the synform. Early orogenic granitoids (medium grey) intruded both metavolcanic and metasedimentary rocks prior to formation of the synform. Late and post-orogenic granitoids are shown in dark grey. The N- to NE-striking faults are late Proterozoic in age.

The andalusite-sillimanite isograd (dotted line) outlines the area of lower amphibolite facies metamorphism. The upper amphibolite facies is limited to the northern end of the northeast fault block, in the region of sample 103. The remaining areas were generally metamorphosed to middle amphibolite grade.

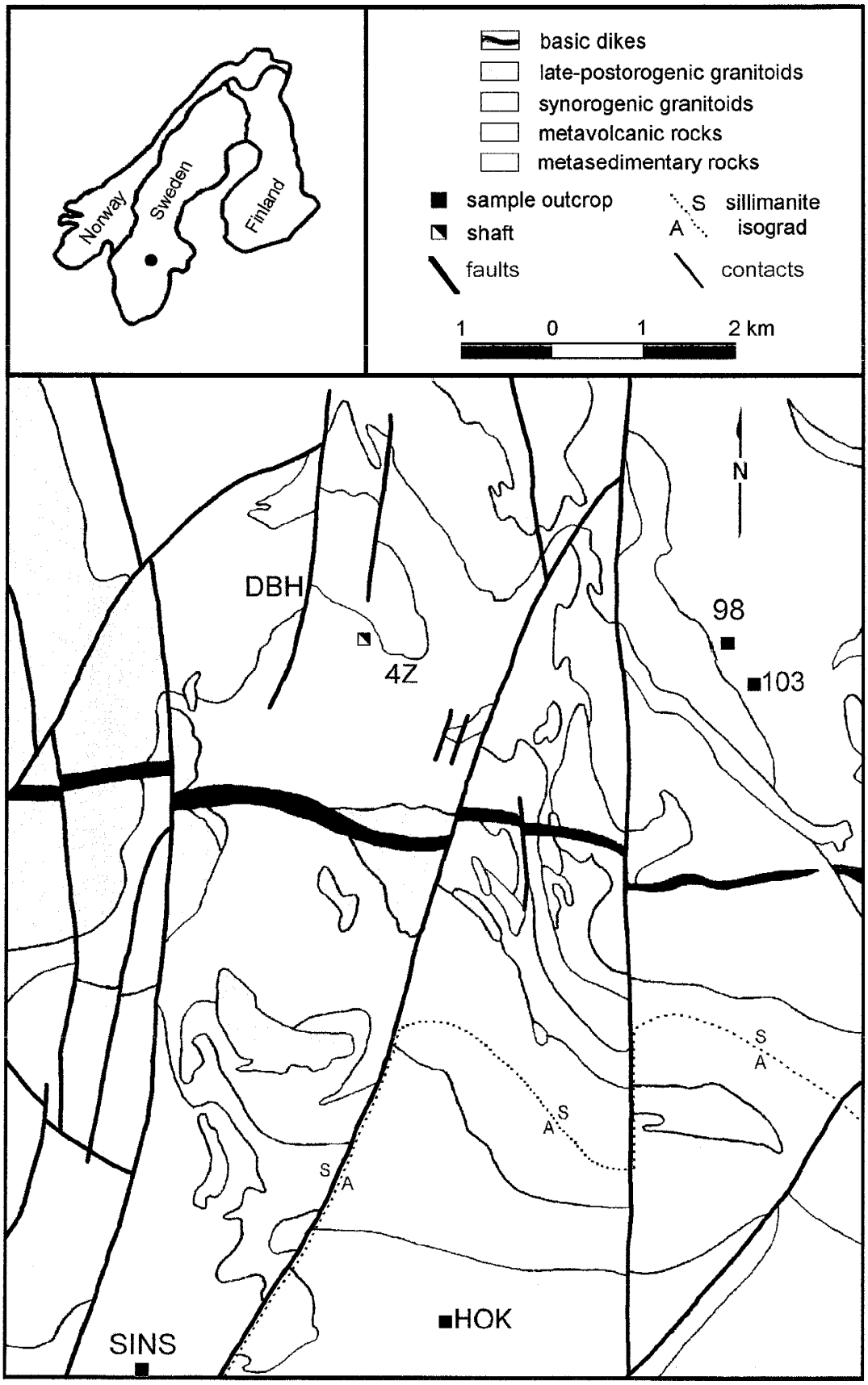
Norway
Sweden
Finland
basic dikes
late-postorogenic granitoids
synorogenic granitoids
metavolcanic rocks
metasedimentary rocks
sample outcrop
shaft
faults
S sillimanite
A isograd
contacts
1 0 1 2 km
N
DBH
4Z
98
103
S
A
SINS
HOK

and mineralized horizons, including the Zinkgruvan deposit, occur in the top of the metavolcanic unit and in the metasedimentary rocks above.

The metaporphyries have undergone extensive shearing so that the primary layering and foliation are nearly parallel and are difficult to distinguish. Structures thought to be veins and breccias within the metavolcanic unit have been transposed into elongate lenses subparallel to the layering and foliation. Contacts between metasedimentary and metavolcanic layers typically exhibit tectonic interfingering.

Four generations of mesoscopic folds have been identified in the Zinkgruvan mine (Hedström and Wikström, 1986; Hedström et al., 1989). Two sets of early isoclinal folds plunge gently to the east or west, and two sets of later open cross folds plunge steeply to the north or northeast, and east. The two earlier sets represent the major fold phases seen elsewhere in Bergslagen; the two later sets probably formed locally as a result of late orogenic granitoid intrusion. In contrast to the terminology used at the mine, the folding phases are designated F_1, F_2, F_3 and F_4 in this study.

The basin rocks have been metamorphosed to amphibolite grade. Peak temperatures at Zinkgruvan may have exceeded 700°C (Henriques, 1964). Peak pressures are constrained only by the sillimanite-kyanite phase transition, and are assumed to be 3-5 kbar (Rickard, 1988). The andalusite-sillimanite isograd is used to divide the region into lower and upper amphibolite facies areas to the south and north respectively. The upper amphibolite facies area, which includes the mine, can be subdivided further. Incipient migmatitization and pegmatite veining is seen in the eastern upper amphibolite facies area but not in the western middle amphibolite facies area (Wasström, 1995). It is unknown what controls the distribution of the metamorphic facies. Peak metamorphism is associated with the late orogenic intrusions (Wikström and Karis, 1991) but not with a specific folding phase.

Samples and Related Work

Representative metaporphyry samples were collected from the three metamorphic facies in the basin: lower amphibolite (HÖK and SINS), middle amphibolite (DBH and 4Z) and upper amphibolite (98 and 103). One sample, 4Z, consists of a boudinaged quartz veinlet and a single relic phenocryst. Quartz, chlorite-altered biotite and sericite-altered microcline are the major minerals in the metaporphyries.

All the relic phenocrysts contain sodium bicarbonate-rich fluid inclusions. Microthermometry work on these inclusions is described in Chapter III and summarized here. Three major types of fluid inclusions were identified on the basis of their maximum size and shape. Up to 2/3 of the inclusions on a given trail contain nahcolite ($NaHCO_3$) daughter minerals. The oldest, type I inclusions are small (<10 μm) and oblong or shaped like negative quartz crystals. Type II inclusions are medium sized (<20 μm) and have irregular rounded forms. Many of the youngest type III inclusions are large (>20 μm) and all have flat pinched forms with digitations.

The inclusion fluids homogenize at temperatures ranging between 94 and 555°C. The homogenization temperatures for inclusions along a single FIP are similar, with a maximum range of about 60 degrees. The mean homogenization temperature for inclusions is lower on younger FIP.

Methods

Doubly polished, unoriented fluid inclusion sections 200 μm thick were used in this study. The sections were cut perpendicular to foliation with no special reference to lineations, which are not seen in hand samples and difficult to find in metaporphyry outcrops. As a result of the poor control on orientation, the fabric elements may be misleading. The shape of a relic phenocryst

viewed in the plane of the section is described by an aspect ratio of length to width. The length of each phenocryst was measured along its longest dimension, and the width was measured along the widest dimension perpendicular to the length. The angle between the long direction of the phenocryst and the average trend of the foliation in the section describes the orientation of a phenocryst. Possible values, therefore, range between -90 and +90 degrees. Quartz grain sizes within a phenocryst were measured along the longest dimension in each grain. The differences in extinction angle between the largest grain and each of the smaller ones were also measured. Possible values range between 0 and 45 degrees.

FIP orientations were found using the method of Boullier and Robert (1992). Orientations of FIP in the relic phenocrysts in each section were measured relative to a single reference direction, i.e. one edge of the petrographic section. Horizontal displacement of a FIP between the upper and lower surfaces of the section was measured with an optical micrometer. The "dip" of the FIP was found from the ratio between section thickness and displacement; the ratio is the tangent of the dip. Most of the error in measurement is associated with shallow dips since the edges of FIP are more difficult to judge in nearly flat planes. The "strike" was determined in a straightforward manner by rotating the microscope stage.

A few relic phenocrysts were examined on a universal stage to determine the orientation of the quartz c axis with respect to the FIP and other microstructures. The software StereoNett 2.20 (Duyster, 1998) was used to plot the orientation data in lower hemisphere stereographic projections.

Terminology

Fluid Inclusions

Several fluid inclusion types occur in unique microstructural settings. These problematic inclusion types are not discussed in fluid inclusion studies, because their significance and importance is unknown, and they generally are much too small for microthermometry studies. These problematic inclusions can be, however, volumetrically significant. The terms "transposed fluid inclusions" and "exsolution inclusions" are in current use in the fluid inclusion literature. The terms "migration inclusions", "satellite inclusions" and "ghost trails" are introduced here.

Transposed fluid inclusions are linear clusters of inclusions that are assumed to form by stretching and segmentation of typical fluid inclusions. The mobilization process can be due to plastic deformation (Swanenberg, 1980) or migration along the quartz c axis (Roedder, 1984, p 66). The linear clusters are tens of μm in length and are composed of about ten inclusions whose sizes range up to 3 or 4 μm in length. Each cluster represents one former fluid inclusion. Linear clusters are organized into bands in which all the clusters are subparallel. Each band represents one former FIP.

Exsolution inclusions are micron-sized one-phase fluid inclusions that are associated with deformation bands or lamellae. The dark inclusions occur in short linear groups with few individuals. All the exsolution inclusion clusters in a single quartz grain are oriented in the same direction. Exsolution inclusions may form from mobilized structural water that migrates during plastic deformation (Wilkins and Barkas, 1978).

Migration inclusions are micron-sized one-phase fluid inclusions that congregate mostly around bulging grain boundaries, forming swarms in recrystallized phenocrysts. The inclusions also may be contained within individual grains which exhibit anomalous or no birefringence. None of the inclusions exhibit the distinctive linear clusters typical of exsolution inclusions.

Satellite inclusions are randomly dispersed fluid inclusions decorating minerals included in the recrystallized quartz phenocrysts. Individual inclusions are generally less than 3 or 4 μm in size. They form partial or complete haloes, up to tens of micrometers in radius, around the mineral inclusions. The haloes of satellite inclusions tend to be asymmetrically developed, with more fluid inclusions occupying a strain shadow on one side of the mineral inclusion.

Ghost trails consist of several short FIP that occupy a single plane. They appear to have once been continuous. The largest fluid inclusions are 6 to 8 μm in length, but most are smaller. Individual segments do not exceed 100 μm in length, and do not extend the full depth of the petrographic section. Most of the segments are rootless, i.e. the tips do not intersect any other microstructures. Some segments are ray-like structures which emanate from a recrystallized quartz grain boundary or the rim of a phenocryst. Other segments are rooted in grain boundaries of included minerals and are accompanied by smaller satellite inclusions.

Plastic Deformation Microstructures

Three types of planar deformation microstructures are recognized. Since the sections are 200 μm thick, the microstructures are not easily compared with those seen in thinner sections in other studies. The terms "birefringent deformation bands" and "birefringent deformation lamellae" are introduced here.

Birefringent deformation bands are parallel planar domains many tens of microns in thickness that extend across an entire phenocryst. They can be seen in plain light because the band boundaries are decorated with exsolution inclusions (Figure 23). Under crossed nichols, the bands in a given phenocryst exhibit extinction at a similar angle upon rotation of the microscope stage. The birefringence colors within the bands are generally higher order reds and greens whereas the band boundaries are isotropic.

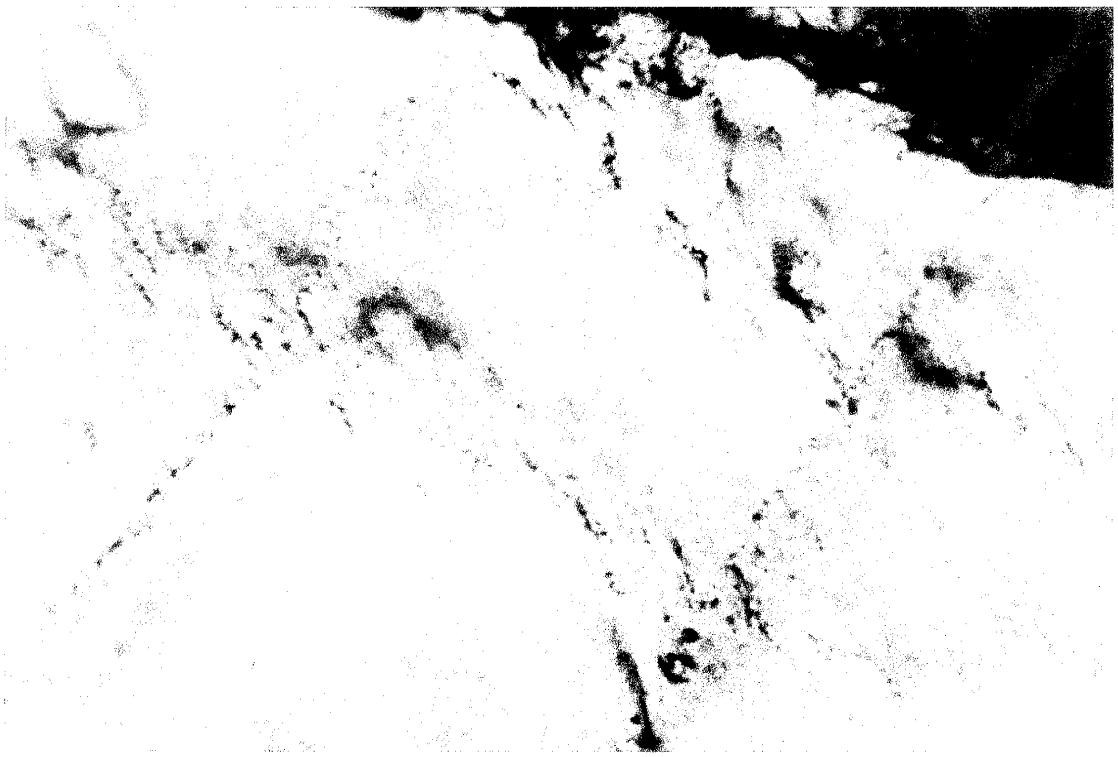

Figure 23. A photomicrograph of birefringent deformation bands in plane polarized light; field of view 600 μm. The bands extend from the SW to NE corner of the image and dip toward the SE corner. Two younger FIP extend subparallel to the bands. Two older transposed FIP intersect the bands at high angles.

Deformation lamellae are delicate planar microstructures, about a micron in thickness and tens of microns in length, that are best observed in plain light with the substage diaphragm nearly closed (Figure 24). The lamellae do not penetrate the entire 200 μm thick section. Deformation lamellae occur in parallel groups of tens, and may or may not terminate in grain boundaries.

Birefringent deformation lamellae are subparallel planar domains that have variable length and thickness. The lamellae can only be seen by rotating the stage under crossed nichols (Figure 25). Most lamellae are flame-shaped and appear black or white against a grey background. The lamellae disappear when they are oriented parallel to the N-S or E-W axis of the microscope. The grains containing lamellae do not exhibit complete extinction. The lamellae may be intragranular or they may emanate from grain boundaries. Many lamellae resemble feldspar twins, so care must be used to distinguish feldspar inclusions from quartz by their sericite alteration.

Observations and Results

General Features

There is evidence for primary layering in the metaporphyries, except in the highest grade sample, 103. Flattened lithic fragments, concentration of relic phenocrysts into bands and biotite-rich and biotite-poor domains contribute to the definition of the layering. There are two foliations expressed as preferred orientations of biotite in all the samples. The better developed foliation is subparallel to layering; the poorly developed foliation intersects the layering at a moderate angle. Clots and mats of oriented biotite in all samples contribute to the layer-parallel foliation. Only in sample 98 do the biotite mats wrap around a few of the phenocrysts. In samples DBH and 98

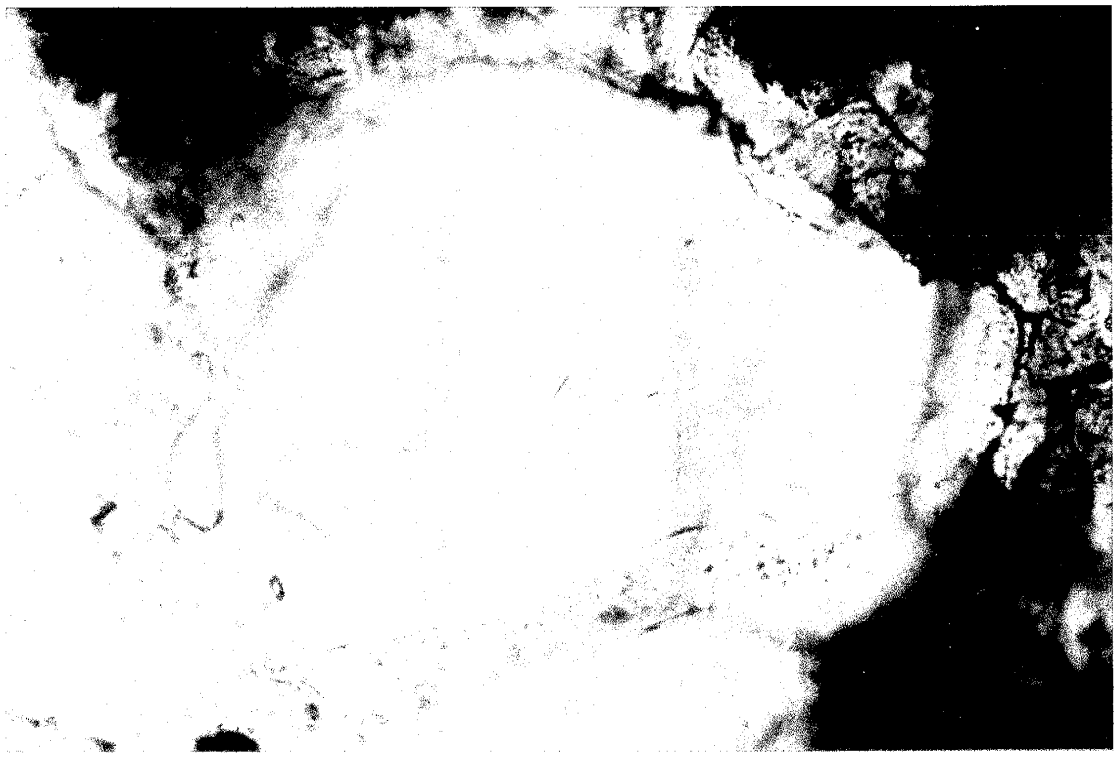

Figure 24. A photomicrograph of deformation lamellae in plane polarized light with the substage diaphragm nearly closed; field of view 600 μm. The lamellae extend from top to bottom and dip to the left hand side of the image.

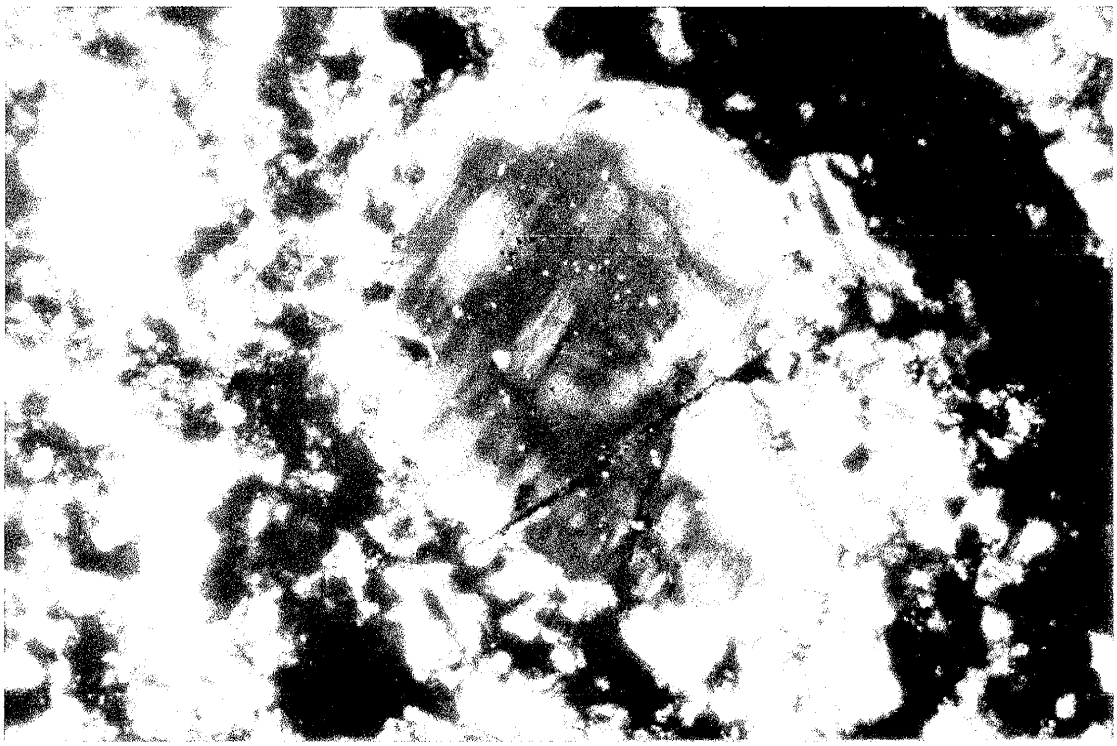

Figure 25. A photomicrograph of birefringent deformation lamellae under crossed nichols. The phenocryst is about 1 mm in length. The lamellae are oriented approximately 45° to the N-S and E-W axes of the microscope.

there are biotite stringers which crosscut layering. The biotite within the stringers, however, is oriented along the layer-parallel foliation.

The matrix grain size in all the metaporphyries is similar, with a typical grain size of about 50 μm. The matrix material is mostly quartz with variable amounts of biotite, and little microcline. The quartz grains are polygonal to interlobate with no obvious shape fabric. Undulose extinction in the quartz is common. The biotite grains are not bent or kinked.

The relic quartz phenocrysts do not have tails like porphyroclast systems. There is no convincing evidence for strain shadows developed around the phenocrysts and shear sense indicators are lacking. There is a continuum in phenocryst sizes from several millimeters on down to the matrix grain size. The largest phenocrysts occur in the lower amphibolite facies samples. Sample 4Z has the fewest and smallest phenocrysts (and the least matrix biotite) of all the samples. Phenocrysts in the other five samples exhibit a shape-preferred orientation. Phenocrysts with small aspect ratios have much weaker shape-preferred orientations than do phenocrysts with high aspect ratios. The phenocrysts are aligned either with the layering-parallel foliation (SINS, DBH and 103) or at a small angle to the layer-parallel foliation (HÖK and 98). All of the samples, except 4Z, have variably deformed phenocrysts. There is no significant difference in size between more and less deformed phenocrysts. More details can be found in Appendix B.

Recrystallization Textures

Sketches of representative relic phenocrysts illustrating recrystallized grains and dominant FIP orientations are presented in Figure 26. The scale of the sketches is uniform between frames. The phenocrysts have been oriented such that the principle foliation in each frame extends left-right. Recrystallization microstructures are very different in lower and upper amphibolite facies phenocrysts. Phenocrysts from the middle facies share features with both.

Figure 26. Sketches of representative quartz phenocrysts from the lower (HÖK, SINS), middle (DBH) and upper (98, 103) amphibolite facies samples. Both mildly and highly deformed examples are shown. The largest phenocryst in each frame is also the largest phenocryst in the petrographic section. The scale bar applies to all phenocrysts. White regions are recrystallized quartz. Grey regions are unrecrystallized "igneous" quartz. Black regions are either biotite or feldspar mineral inclusions. Short straight lines are FIP. Feathery bands are transposed FIP. Dotted regions represent concentrations of mobilized fluid inclusions. All the phenocrysts are oriented such that the layer-parallel foliation in the matrix, defined by biotite preferred orientation, extends left-right.

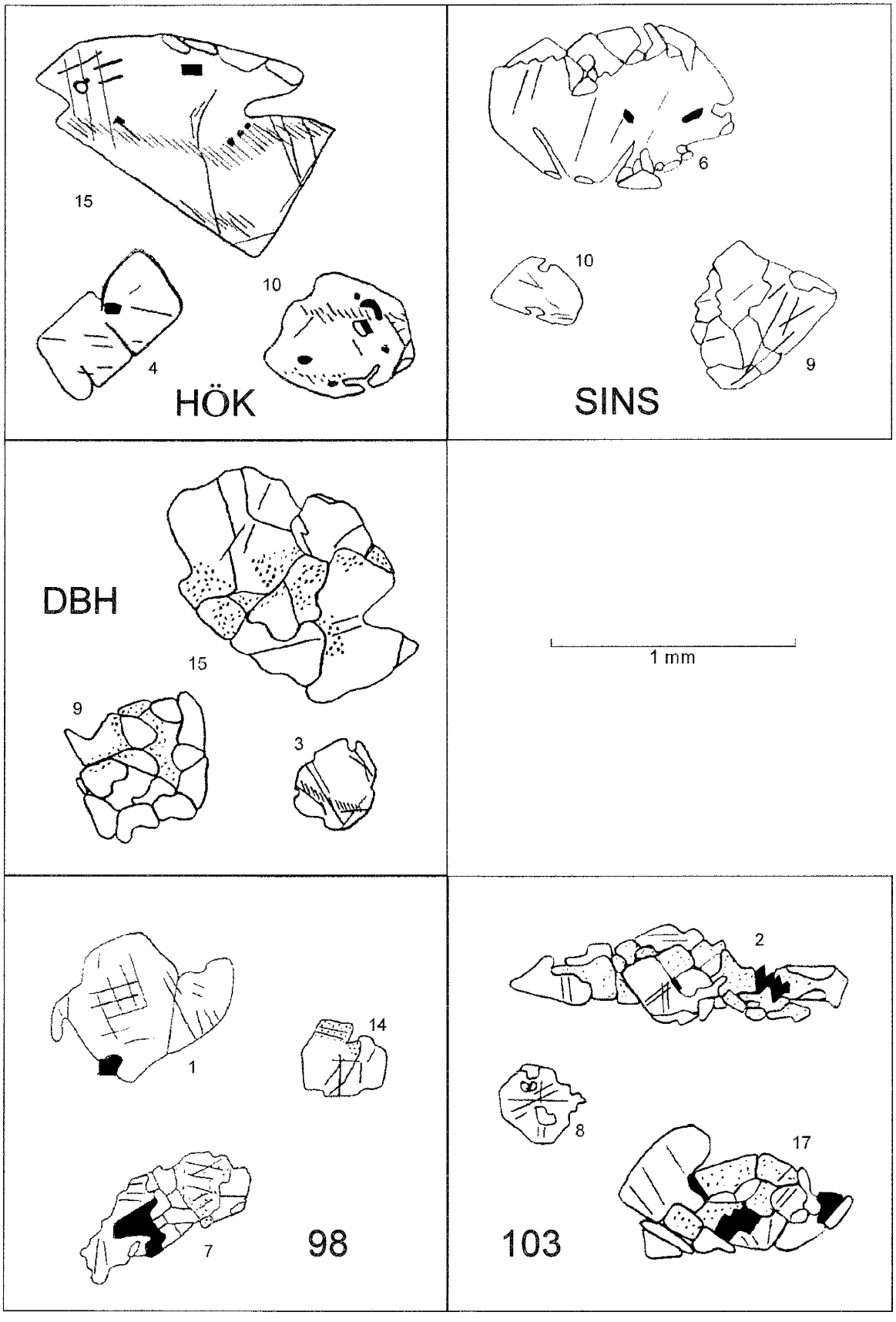
15
4
10
HÖK
6
10
9
SINS
DBH
15
9
3
1 mm
1
14
7
98
2
8
17
103

Lower amphibolite facies (HÖK and SINS). Unrecrystallized quartz is preserved in the cores of many lower amphibolite facies relic phenocrysts. Exsolution inclusions are useful for discriminating between recrystallized (new) and unrecrystallized (old) grains, since they have been eliminated from all of the new grains. Phenocrysts with minor recrystallization exhibit distinctive wriggly embayments or resorption structures, and many of them have crystallographically controlled outlines. Core-and-mantle structures are developed where new grains have formed on the margins of the phenocrysts. In some phenocrysts, recrystallized grains occupy only a single corner or one face. In others, the new grains occupy multiple faces, and sometimes they rim the entire phenocryst. Grain boundaries, viewed under high magnification, are interlocking.

Using a universal stage, it was determined that the quartz c axis orientations of new grains in sample HÖK relic phenocrysts are close to those in unrecrystallized quartz. The differences between the extinction angles of the new grains and that of the unrecrystallized quartz are mostly between 0 and 10 degrees. Many of the new grains, therefore, are subgrains. The largest of the recrystallized grains is about 600 μm in length.

Middle amphibolite facies (DBH and 4Z). Only two of the relic phenocrysts of the middle amphibolite facies have escaped complete recrystallization. Crystallographically controlled outlines are still seen in some phenocrysts, but wriggly embayments are generally obliterated. The recrystallized grains vary in size and shape. Some of the phenocrysts are recrystallized into one or two new grains which are an order of magnitude larger than all the other new grains within the same phenocryst. The smaller grains tend to be on the margins of a given phenocryst. The texture resembles "leftover grains" described by Passchier and Trouw (1996, p. 37). In other phenocrysts, all the recrystallized quartz grains may be roughly the same size. Domains of finely crystalline quartz are found inside a few of the largest phenocrysts. Many of the new grain boundaries are distinctly bulging, and some of them are "pinned" by mineral inclusions. The grain boundaries,

viewed under high magnification, are interlocking. Ghost trails are common in the "leftover grains". Migration inclusions occur in swarms along many new grain boundaries, and are particularly dense on the convex sides of bulging grain boundaries. Mineral inclusions, and some of the smaller quartz grains, are decorated with satellite inclusions. Some of the larger satellite inclusions are type I fluid inclusions.

The differences between extinction angles of the recrystallized grains and that of the biggest "leftover grain" are evenly distributed across the range of possible values. The largest of the new grains is about 300 μm in length.

The quartz veinlet in sample 4Z is boudinaged into 1 to 5 mm long, slightly curved segments, more-or-less aligned with the foliation in the metaporphyry matrix. Several anomalously large grains may have been phenocrysts; however, they lack the swarms of migration inclusions seen in the relic phenocrysts of sample DBH. Veinlets linking phenocrysts also occur in sample SINS and DBH. The variety of grain sizes and shapes in veinlets are similar to those seen in the phenocrysts.

Upper amphibolite facies (98 and 103). Only two relic phenocrysts of the upper amphibolite facies retain a crystallographically controlled outline. All of the phenocrysts are completely recrystallized. Microstructural evidence for nucleation of new grains inside the phenocrysts, rather than along the grain margins, is more common than in phenocrysts of lower grades. The new grains form polygonal aggregates, sometimes in distinctive rectilinear patterns. The blocky textures develop in phenocrysts with high aspect ratios lying parallel to the foliation of the metaporphyry. Many of the phenocrysts exhibit the "leftover grains" microstructure. Most new quartz grains have less complex boundaries than the grains in phenocrysts of lower facies. In most of the phenocrysts, migration inclusions are restricted to a few smaller grains which may be choked with the inclusions. Swarms are less common than in the lower facies phenocrysts, and tend to be associated with mineral inclusions. Satellite inclusions and ghost trails are also less common.

The differences between extinction angles of the new grains and that of the largest "leftover grain" are mostly between 20 and 30 degrees in sample 98, and between 10 and 20 degrees in sample 103. The largest of the recrystallized grains is about 300 μm in length.

Plastic Deformation Microstructures

Lower amphibolite facies (HÖK and SINS). An outstanding feature of the relic phenocrysts of the lower amphibolite facies is the birefringent deformation bands which occur in the unrecrystallized cores. The bands are decorated with exsolution inclusions. In sample HÖK, the bands have a preferred orientation throughout the petrographic section. There may be two intersecting sets of birefringent deformation bands, one more sharply defined than the other. Using a universal stage to examine several phenocrysts, it was determined that the sharply defined bands are in a sub-basal orientation. Deformation lamellae, in contrast, occur in the relatively undeformed, recrystallized quartz grains. These recrystallized grains have undulose extinction, and their c axes are oriented much like that in the unrecrystallized quartz. The deformation lamellae in several phenocrysts approximately intersect the quartz c axes; these are prism deformation lamellae. The orientations of the linear clusters in transposed fluid inclusion trails and the orientations of linear clusters of exsolution inclusions are the same in a given phenocryst. They both correspond to the intersection of the sub-basal birefringent deformation bands and the deformation lamellae. The relationships in two phenocrysts are shown in Figure 27.

Middle amphibolite facies (DBH and 4Z). Only two relic phenocrysts of the middle amphibolite facies have unrecrystallized quartz, and they have the same features seen in lower amphibolite facies phenocrysts. Most of the recrystallized quartz grains exhibit undulose extinction, and many grains also have simple deformation lamellae. Birefringent deformation lamellae rarely occur in the recrystallized grains.

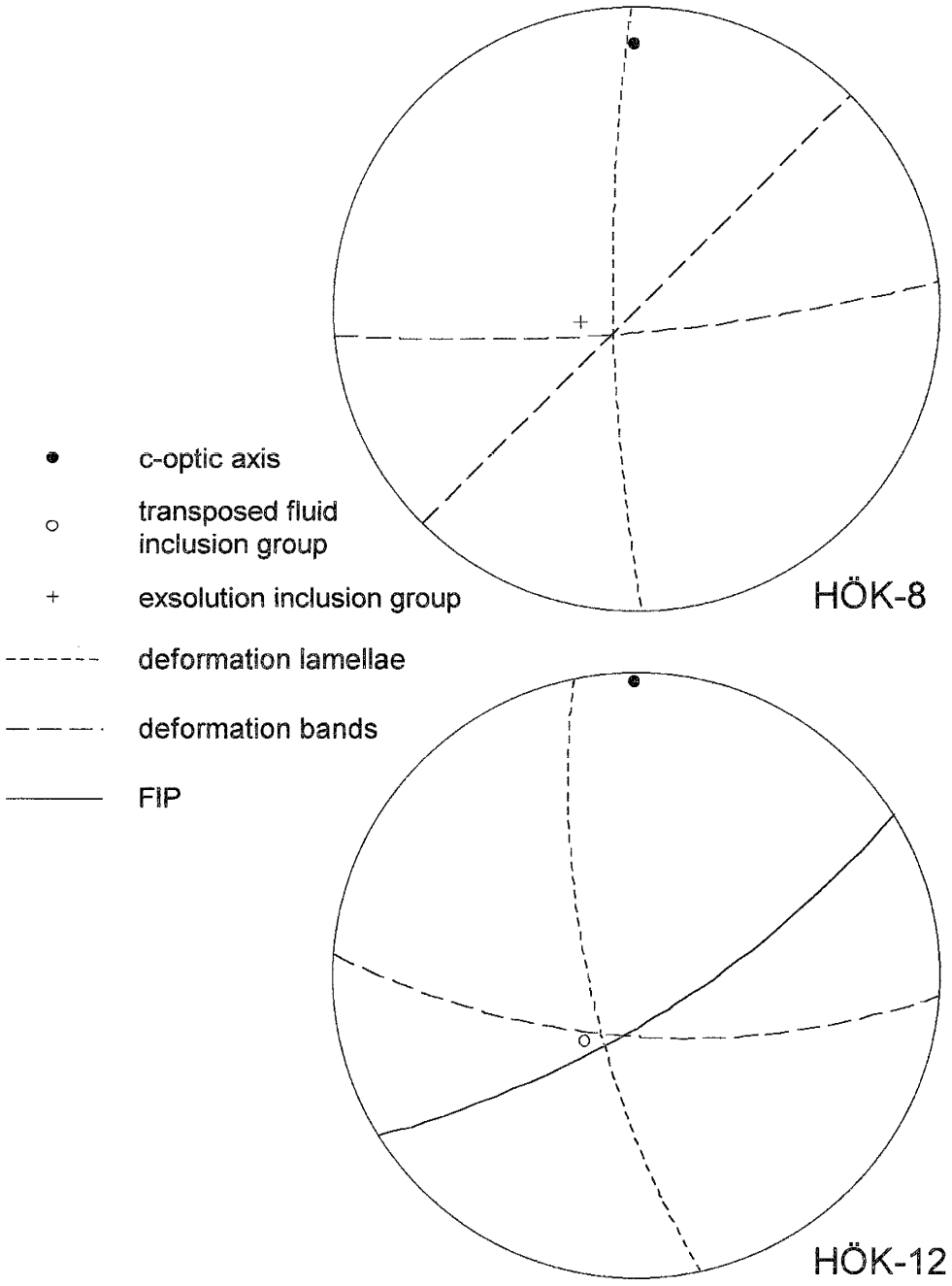

Figure 27. Deformation bands and lamellae, and exsolution and transposed fluid inclusions, occur in special orientations with respect to the quartz c axis, as seen on lower hemisphere stereographic projections. Lines are traces of planar structures. Symbols are poles to linear structures.

Upper amphibolite facies (98 and 103). Recrystallized quartz grains in the relic phenocrysts of the upper amphibolite facies generally exhibit undulose extinction. Many grains contain either simple deformation lamellae or birefringent deformation lamellae. Some "leftover grains" contain two sets of birefringent deformation lamellae that intersect at nearly right angles (Figure 25). One set of lamellae is much more strongly developed that the other.

Fluid Inclusion Planes (FIP)

There are three broad categories into which the FIP can easily be assigned. They are FIP that clearly predate or postdate recrystallization, and those FIP that originated during dynamic recrystallization. The principal criterion for dating the FIP with respect to recrystallization is the crosscutting relations between FIP and grain boundaries. Pre-recrystallization FIP are truncated by all the grain boundaries that they intersect. Post-recrystallization FIP crosscut all the grain boundaries that they intersect. Synrecrystallization FIP crosscut some grain boundaries but not others. All the synrecrystallization FIP are occupied by type I fluid inclusions. Post-recrystallization FIP are populated with either type II or type III fluid inclusions.

Transposed FIP are the only ones that unambiguously predate recrystallization. They are seen only in relic phenocrysts of the lower amphibolite facies (HÖK and SINS). Most of the transposed inclusions are small and dark. Rare individuals are as large as 3 μm, and some contain two fluid phases. They are aqueous inclusions that neither homogenize nor decrepitate at the highest temperature attainable on the fluid inclusion stage (600°C). The larger inclusions tend to be more rectilinear in outline and occur in the center of linear clusters up to 60 μm long. Transposed FIP crosscut the birefringent deformation bands. Transposed FIP generally are crosscut by new grain boundaries, but important exceptions occur. In two instances transposed FIP are refracted as they cross grain boundaries into recrystallized quartz grains. In both cases the c axis of the

recrystallized quartz grain is subparallel to the c axis of the older quartz grain, suggesting that these FIP extend across subgrain boundaries.

The crosscutting relations between type I FIP and quartz grain boundaries are confusing since some FIP appear to have formed before recrystallization, some during, and some after. Four different subtypes, illustrated in Figure 28, are recognized:

Type IA fluid inclusion planes extend along the boundaries between birefringent deformation bands in unrecrystallized quartz grains. They are crosscut by all grain boundaries.

Type IB fluid inclusion planes also are crosscut by all grain boundaries. Some line up with ghost trails in adjacent grains. Ghost trails are, therefore, considered to be in this group.

Type IC fluid inclusion planes crosscut some grain boundaries and are crosscut by others.

Type ID fluid inclusion planes crosscut all grain boundaries.

Types IA and IB are sparsely populated with fluid inclusions whereas types IC and ID have closely spaced inclusions. The inclusions usually are arranged en echelon with their longest dimensions at an angle to the strike of their FIP.

Type II and III FIP clearly postdate recrystallization. Type II and III inclusions have distinctive shapes that facilitate identification of their FIP. Many type III inclusions are naturally decrepitated. Type III FIP exhibit a preferred orientation on the scale of a thin section. They may curve toward local grain boundaries and mineral inclusions, and extend along grain boundaries and older FIP. Optical discontinuities along the FIP indicate that the microcracks which trapped the fluids are not completely healed.

When type I and II FIP orientations are plotted on stereograms, the traces in any given sample tend to intersect in one or more "hubs". Examples of this are shown in Figure 29. A single FIP trace may intersect two hubs. The trace of an open microcrack, or a type III FIP, or a transposed FIP, may intersect a hub. The hubs in some samples exhibit a preferred orientation, in others the

Figure 28. Cartoons of various fluid inclusion types discussed in the text are shown for the lower amphibolite facies (a) and the upper amphibolite facies (b).

In (a) the fluid inclusion types include transposed fluid inclusions (T) and exsolution inclusions (E). Type IA fluid inclusions occur along deformation band boundaries (horizontal) which are decorated with exsolution inclusions. The unrecrystallized quartz has birefringent deformation bands whereas the recrystallized quartz has neither deformation bands nor exsolution inclusions.

In (b) the relationships between quartz grain boundaries and fluid inclusion planes for type I fluid inclusions are shown. The upper left grain is interpreted to be growing at the expense of its neighbors. Type IB and IC fluid inclusions are removed in the process. Rootless fluid inclusion planes, and those radiating out from the biotite inclusion in the upper left grain, are interpreted to be relic type IB inclusions. Type III inclusion planes are deflected along grain boundaries, but otherwise exhibit a preferred orientation in thin section.

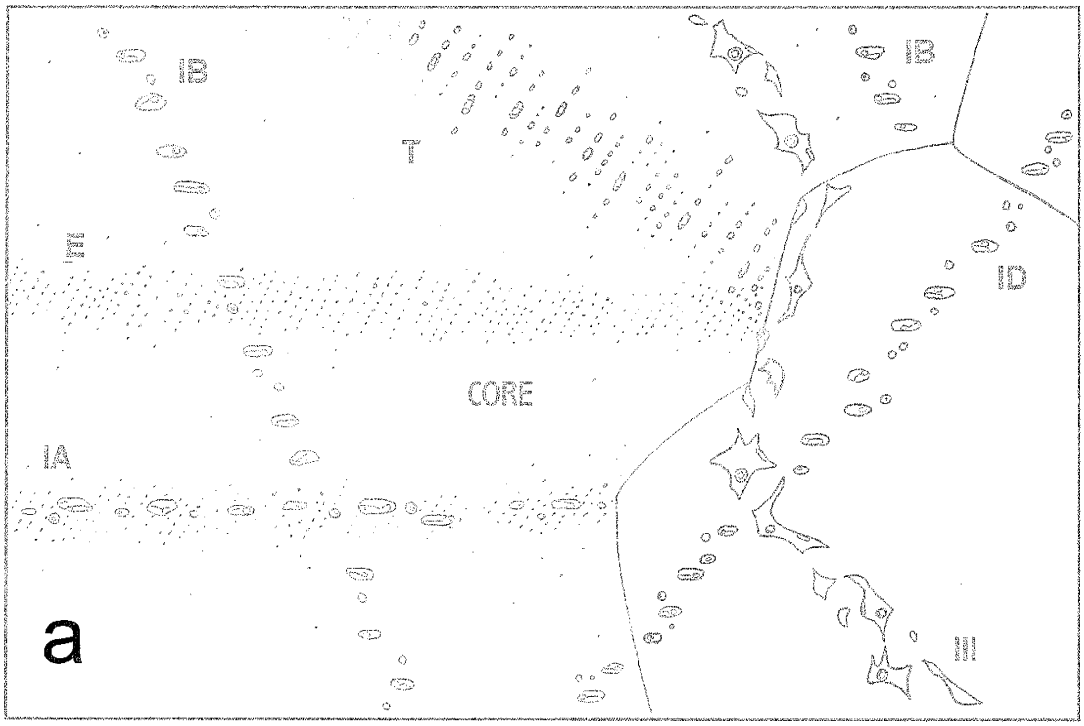
IB
T
IB
E
ID
CORE
IA
a
III

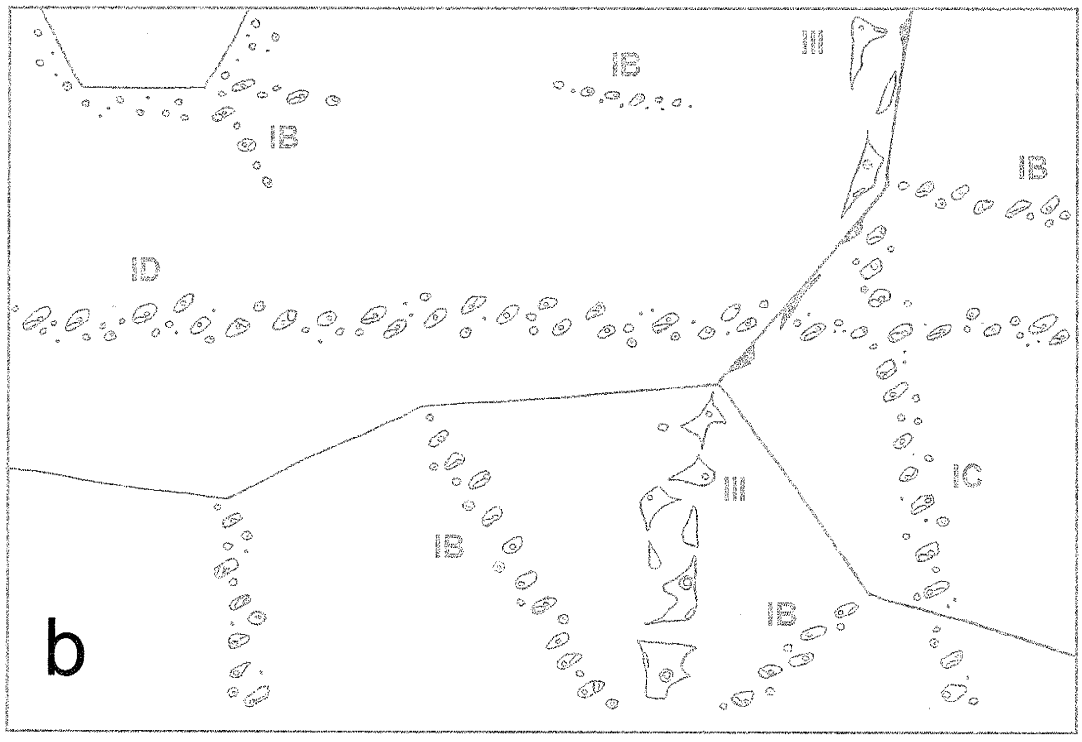
III
IB
IB
IB
ID
IC
III
IB
IB
b

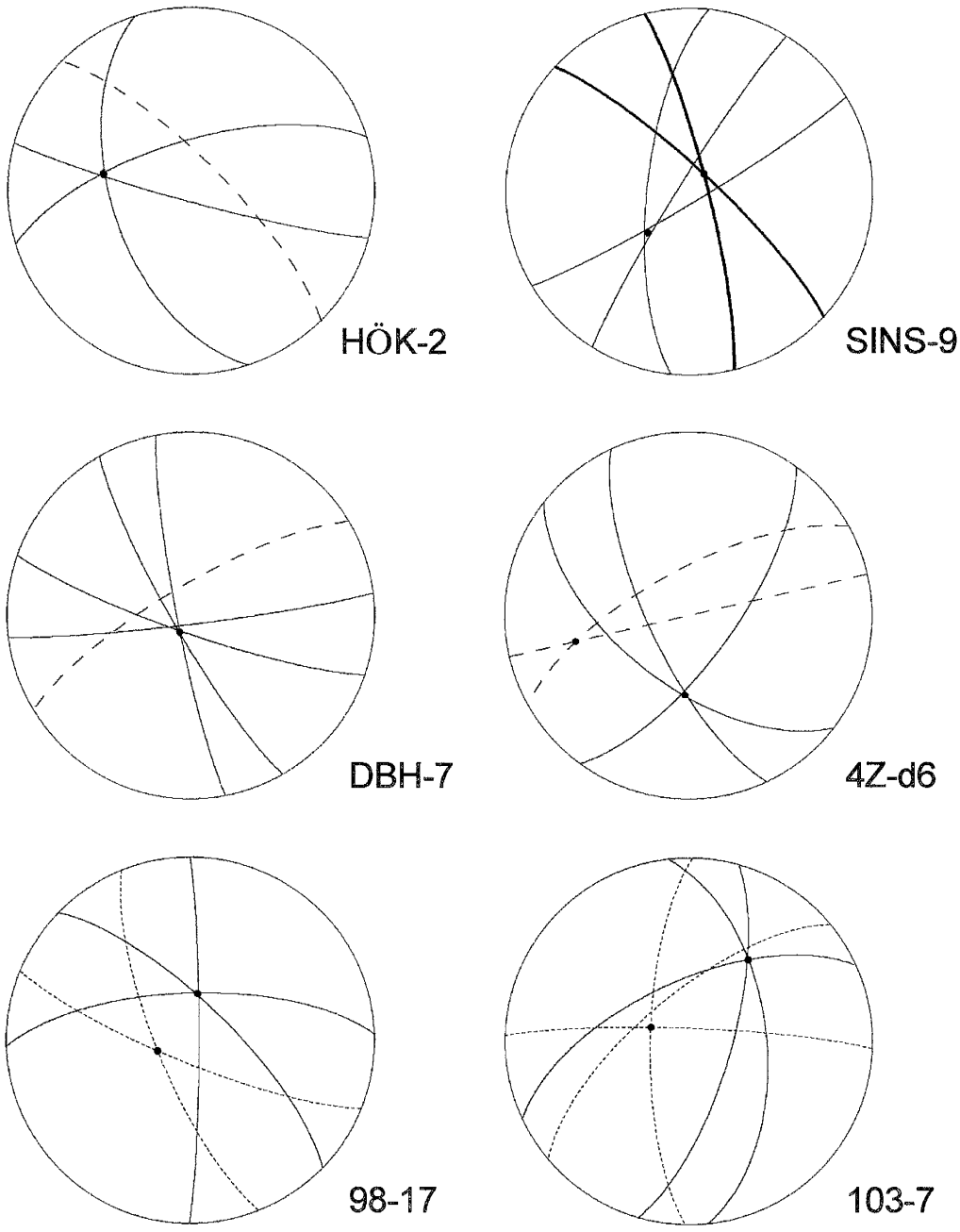

Figure 29. The orientation of FIP in selected relic phenocrysts, and a veinlet segment (4Z), on stereograms. Different traces represent different generations of FIP. Solid lines= type ID, dotted lines= type II, dashed lines= type III. Heavy lines= transposed fluid inclusion trails.

hubs are distributed along one or two great-circle girdles on the stereogram (Figure 30). The same arc described by the distribution of hubs is also a preferred orientation of the FIP in several samples (Figure 31). The angles between every two sets of FIP in each phenocryst, and in each segment of the quartz veinlet, were measured on the stereogram, and the results are illustrated on the histogram in Figure 32. The inter-FIP angles are not random; the modes in the data are at 24, 44, 62, 69 and 83 degrees.

Remarkably, the homogenization temperatures of the fluid inclusions along FIP associated with a particular hub are usually similar. Homogenization temperatures of inclusions along FIP associated with different hubs are usually different. This points to a common origin for FIP on the same hub. Figure 33 illustrates the relationship between FIP orientation and the range in homogenization temperatures in two phenocrysts.

Discussion

Plastic Deformation and Recrystallization

The Zinkgruvan metaporphyries resemble the Early Proterozoic quartz crystal rhyolites of the southwestern U.S.A. examined by Williams and Burr (1994). In the latter rocks, strained and unstrained quartz phenocrysts occur together in the same petrographic section. Variations in the crystallographic orientations of the phenocrysts are responsible for this feature, since some phenocrysts were more favorably oriented for deformation than others. Preservation of the phenocrysts was possible by strain partitioning into an extremely fine grained quartz and muscovite matrix. A similar explanation for strained and unstrained quartz grains in a quartzite mylonite was proposed by Law et al. (1986). The relic phenocrysts in the rhyolites resemble the "globular grains" found in the mylonite.

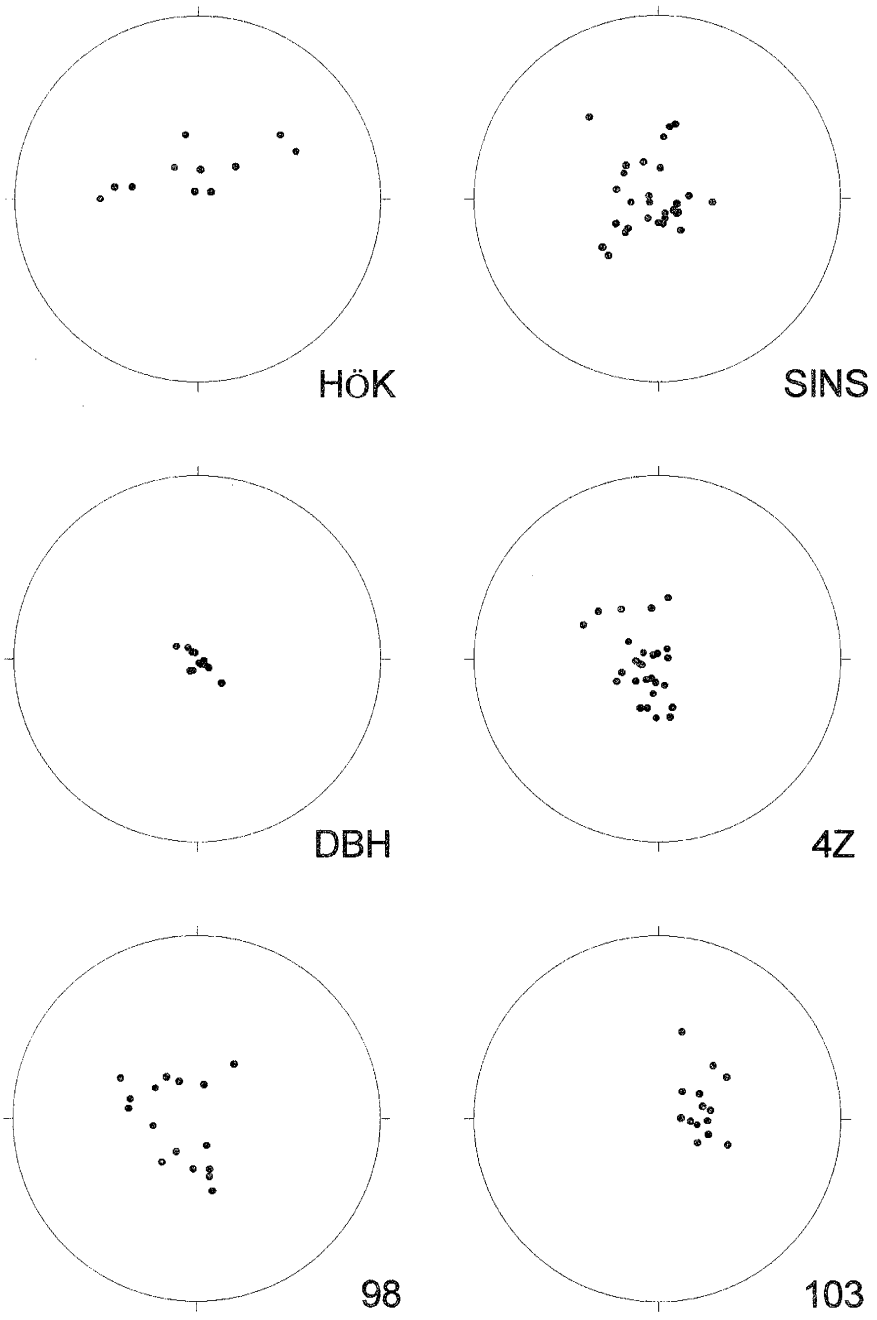

Figure 30. Lower hemisphere stereograms showing the position of "hubs" in each thin section, created by type ID FIP intersections in single phenocrysts. Most of the FIP in the relic phenocrysts are type ID.

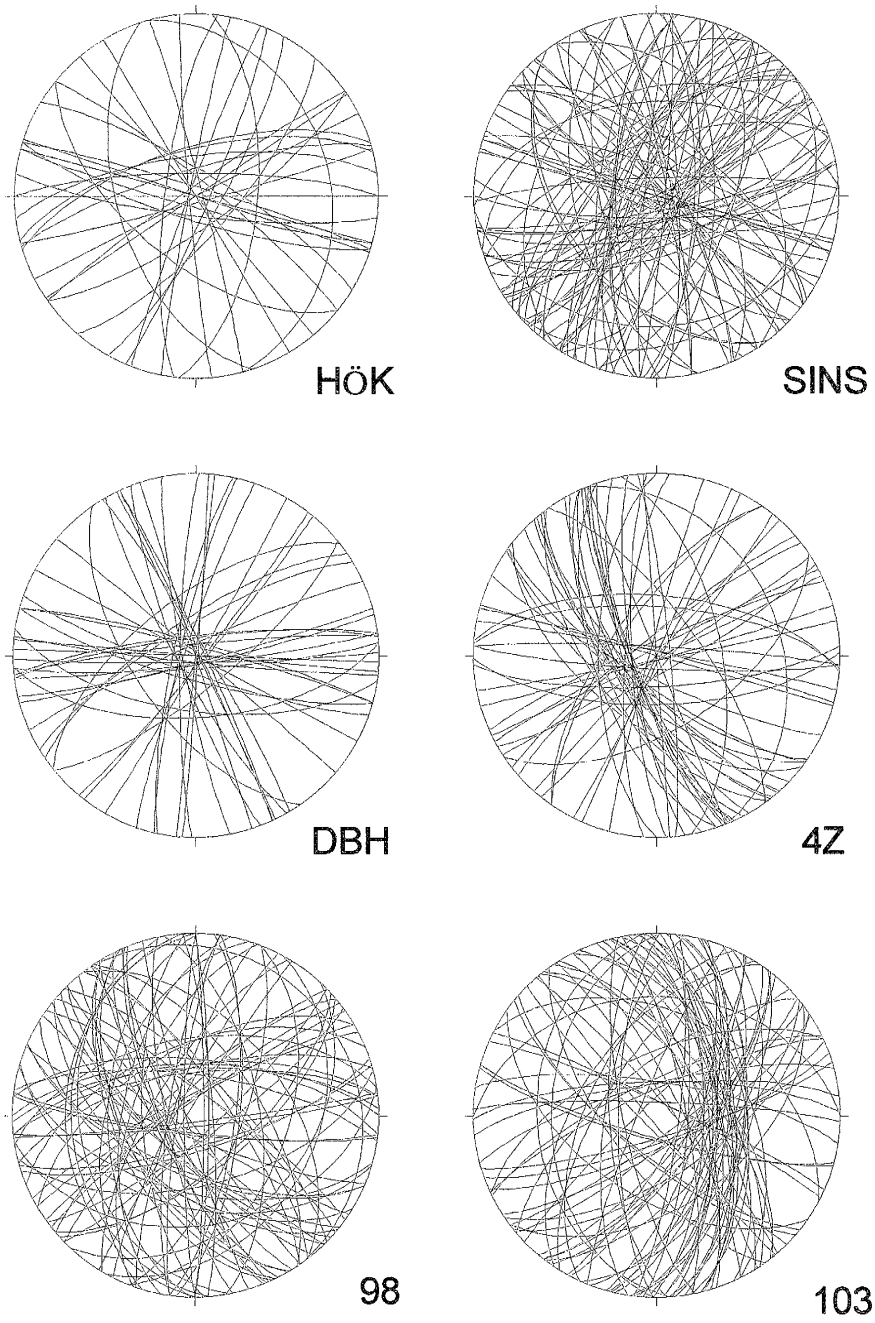

Figure 31. The FIP traces in each sample exhibit a discernable preferred orientation. Most of the FIP in each sample are type ID. The distribution of type ID hubs coincides with the traces in preferred orientation.

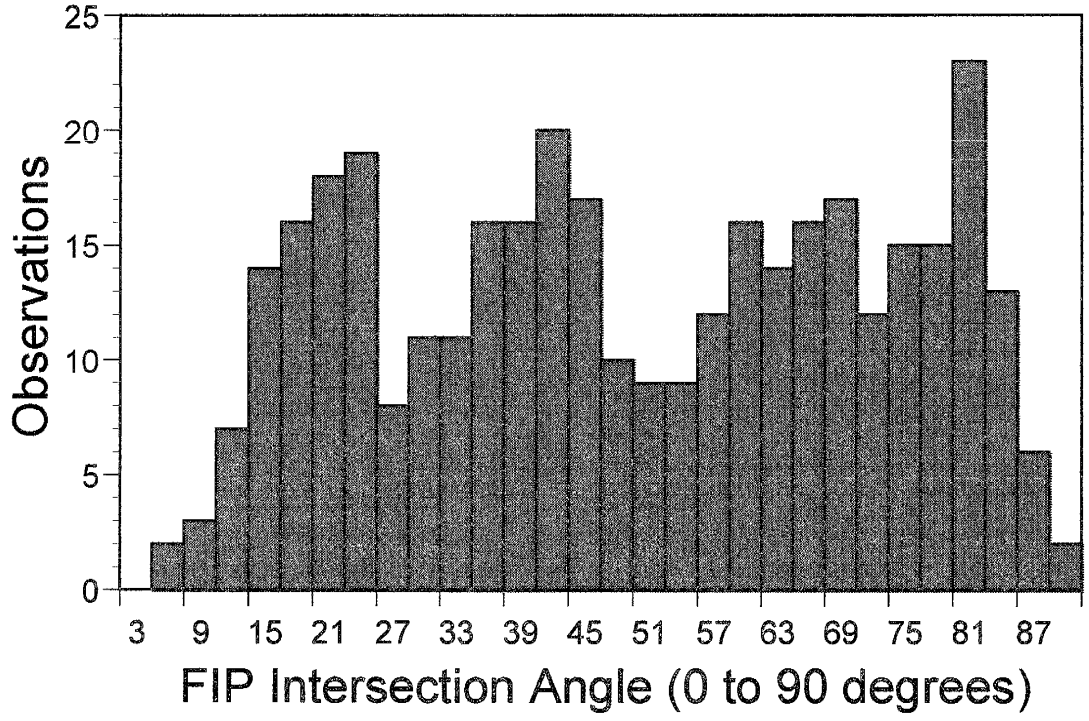

Figure 32. The distribution of inter-FIP angles is not random. This is the principal evidence for crystallographic control of the FIP.

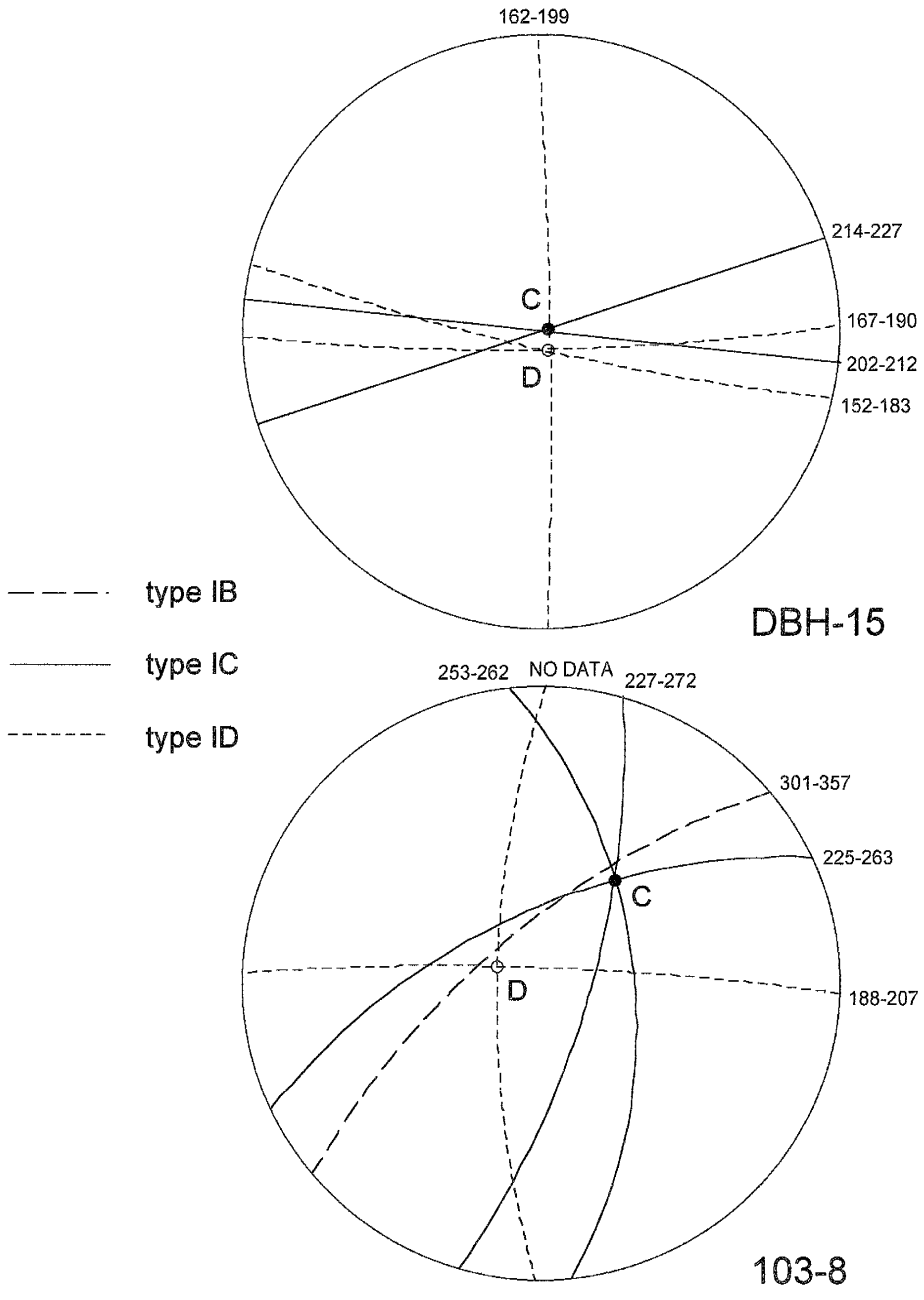

Figure 33. The relationship between Th and FIP orientations in two different phenocrysts.

The Zinkgruvan metaporphyries differ from the rhyolites studied by Williams and Burr in being coarser grained and having matrix biotite rather than muscovite. Biotite, which can deform by a process known as segmentation, is weaker than muscovite (Bell and Wilson, 1981). Biotite also persists at higher metamorphic grades where muscovite has broken down. Biotite in the matrix should, therefore, have maintained the ductility of the matrix in the metaporphyries by inhibiting quartz grain growth and promoting hydrous conditions (Williams and Burr, 1994). The preservation of a few unrecrystallized phenocrysts in amphibolite grade metaporphyries at Zinkgruvan is, therefore, assumed to be due to strain partitioning into the finer grained matrix. The mixture of strongly and weakly deformed phenocrysts is also assumed to be due to different crystallographic orientations of the phenocrysts.

The relic phenocrysts exhibit different degrees of recrystallization, both within a given sample and between samples from different metamorphic facies. Most of the phenocrysts from a given facies look similar to one another and different from phenocrysts from another facies. This is because different mechanisms of deformation and recrystallization were dominant in the various facies.

Relic phenocrysts that are not completely recrystallized (mainly in the lower amphibolite facies samples) have core-and-mantle structure, which White (1976) associated with rotation recrystallization. Similar orientations for the majority of quartz grain c axes in these phenocrysts are evidence that the dominant mechanism for new grain growth was rotation recrystallization. Many of the mantle grains are subgrains. It is remarkable that the subgrains have been swept clear of exsolution inclusions. Drury and Urai (1990) recognize a stage in rotation recrystallization where dislocations are cleared out of the subgrains leaving the subgrains relatively strain free. It occurs when the subgrains are misoriented at 5-10°. Perhaps the exsolution inclusions in the mantle subgrains were removed by mobile dislocations during this stage of rotation recrystallization.

Sub-basal birefringent deformation bands in the unrecrystallized cores indicate that plastic deformation was initially accommodated by (c)<a> slip at relatively low temperatures, perhaps less than 400°C (e.g. Hobbs, 1968; Blacic, 1975). Linear clusters of transposed and exsolution inclusions are oriented in the same direction as the intersection of deformation bands with prism lamellae in subgrains; this suggests that the linear clusters are oriented in the <a> direction of the quartz grains. Transposition of the fluid inclusions in the <a> direction is consistent with (c)<a> slip. Deformation lamellae in prism orientations indicate that later plastic deformation was accommodated by {m}<a> slip in the mantle grains. This slip system is typical of plastic deformation at temperatures above 400°C (e.g. McLaren et al., 1970; Hobbs et al., 1972; Blacic, 1975; Linker and Kirby, 1981). The lack of prism lamellae in the cores may be due to strain hardening of the unrecrystallized quartz. Strain hardening was probably augmented by the removal of structural water (which weakens the quartz) upon formation of the exsolution inclusions.

Migration recrystallization was an important mechanism for recrystallization in completely recrystallized phenocrysts (mainly in the middle and upper amphibolite facies samples). The presence of bulging grain boundaries, "pinning" microstructures and "leftover grains" (Passchier and Trouw, 1996, p. 37) identify migration recrystallization.

The occurrence of two sets of subperpendicular birefringent deformation lamellae in some grains indicates that two quartz slip systems were active in the recrystallized phenocrysts. The birefringent deformation lamellae are interpreted to be in prism and basal orientations because the quartz grains go to extinction when the lamellae are aligned with the axes of the microscope. One of the quartz slip systems is probably {m}<a>, and the other (c)<a>. The (c)<a> slip system requires greater stress for activation than {m}<a> at high temperatures (Hobbs, 1985). Activation of two slip systems may indicate that less strain was partitioned into the matrix of these samples than in the lower amphibolite facies samples.

Several relic phenocrysts from the upper amphibolite facies are flattened and have grains that are rectilinear in outline with relatively straight grain boundaries. Typical quartz annealing textures have triple junctions with grain boundaries intersecting at about 120 degrees, not 90 degrees as seen in these phenocrysts. The origin of the blocky grains is unknown. They resemble "chessboard" textures found in other high grade metamorphic rocks (Kruhl, 1996). Chessboard textures originate as elongate subgrains developed in two directions with walls in approximate basal and prism orientations. They develop only in high quartz. The geometry of the birefringent deformation lamellae and the high temperature metamorphism in the upper amphibolite facies samples are consistent with chessboard textures. The implication is that some of the new quartz grains in the phenocrysts may have formed during metamorphism in the high quartz field.

In summary, slip on (c)<a> and rotation recrystallization are important in the deformation and recovery of relic quartz phenocryst grains in the lower amphibolite facies. The recrystallized quartz includes a significant number of subgrains. Slip on both {m}<a> and (c)<a>, and migration recrystallization are important processes in the middle and upper amphibolite facies. Relic phenocrysts of different sizes and crystallographic orientations have accumulated different amounts of strain, hence there is overlap in the microstructures of recrystallized phenocrysts from different metamorphic facies. Some microstructures suggest deformation in the high quartz field, which is consistent with peak metamorphic temperatures for the upper amphibolite facies.

Preservation of Fluid Inclusions

Interesting occurrences of fluid inclusions in the relic phenocrysts raise provocative questions about the preservation of fluid inclusions during plastic deformation and recrystallization of quartz. It is generally accepted that fluid inclusions are removed by recrystallization (e.g. Kerrich, 1976; Wilkins and Barkas, 1978). Transposed fluid inclusions are an important example of the

modifications that can occur in fluid inclusions when the quartz is plastically deformed (Swanenberg, 1980). Inclusions that are deformed during dislocation creep are subject to changes in fluid density and composition that compromise their usefulness in geochemical studies (e.g. Kerrich, 1976; Hollister, 1990; Audédat and Günther, 1999).

Most of the transposed FIP in this study occupy the unrecrystallized cores of relic phenocrysts and terminate at grain and subgrain boundaries. This is consistent with the removal of inclusions by quartz recrystallization. In one instance, however, a transposed FIP crosses into a subgrain and is refracted at the subgrain boundary. It suggests that fluid inclusions can survive rotation recrystallization.

Satellite inclusions occur in asymmetrical haloes around large mineral inclusions. The haloes are interpreted to be strain shadows where inclusions were sheltered from dislocation creep by climb of dislocations around the larger mineral inclusion. Satellite inclusions are potentially good subjects for geochemical study.

Ghost trails in some "leftover grains" are lined up along a single plane as if they were once continuous. Because this is not a likely geometry for microcracks (e.g. Simmons and Richter, 1976; Kranz, 1983) the ghost trails are interpreted to be remnants of transgranular FIP that have been partly destroyed by deformation. The development of more and less deformed subgrains could account for the ghost trails. Ghost trail inclusions could have been removed from more intensely deformed subgrains by dislocation creep, but preserved in less deformed subgrains.

These problematic fluid inclusions are useful in interpreting the recrystallization history of a relic phenocryst. Some of them are amenable to geochemical study, even if the composition and density information reflects the conditions of deformation or recrystallization rather than the original conditions of fluid entrapment (e.g. Hollister, 1990; Johnson and Hollister, 1995). These fluid

inclusion types are often ignored. However, they have the potential to open more windows on fluid evolution in metamorphic rocks.

FIP Geometry

The observation that type I and II FIP traces tend to intersect in "hubs" suggests that the generation of microcracks and FIP in the quartz phenocrysts were crystallographically controlled. Bloss (1957) and Bloss and Gibbs (1963) demonstrated that cleavage in quartz forms mainly on rhombohedral (r, z and ξ), prism (m) and basal (c) planes. Quartz cleavage geometry, with likely intercrack angles determined, is illustrated on the stereogram in Figure 34. The modes in the inter-FIP angle data at 24, 44, 62, 69 and 83 degrees correlate well with the angles expected from quartz cleavage.

The distribution of inter-FIP angles in the upper amphibolite facies is different from that in the lower and middle amphibolite facies (Figure 35). There is a marked preference for FIP to develop along ξ-ξ' planes in quartz from the higher metamorphic facies, and the most frequently used hub lies in the basal plane. Both the r-z and ξ-ξ' planes are utilized by FIP in quartz from the lower metamorphic facies, and the most frequently used hub lies in a prism plane. Bloss (1957) demonstrated that cleavage on the prism plane is well developed in low quartz but not in high quartz. This helps explain why hubs on the prism plane are favored in the lower facies samples. These relationships are a potential geothermometer which might find application in fluid inclusion studies where FIP orientations are examined. Numerous inter-FIP angles at 23 and 46 degrees suggest that the FIP formed in the low quartz field, whereas inter-FIP angles at 84 and 69 degrees suggest that the FIP formed in the high quartz field.

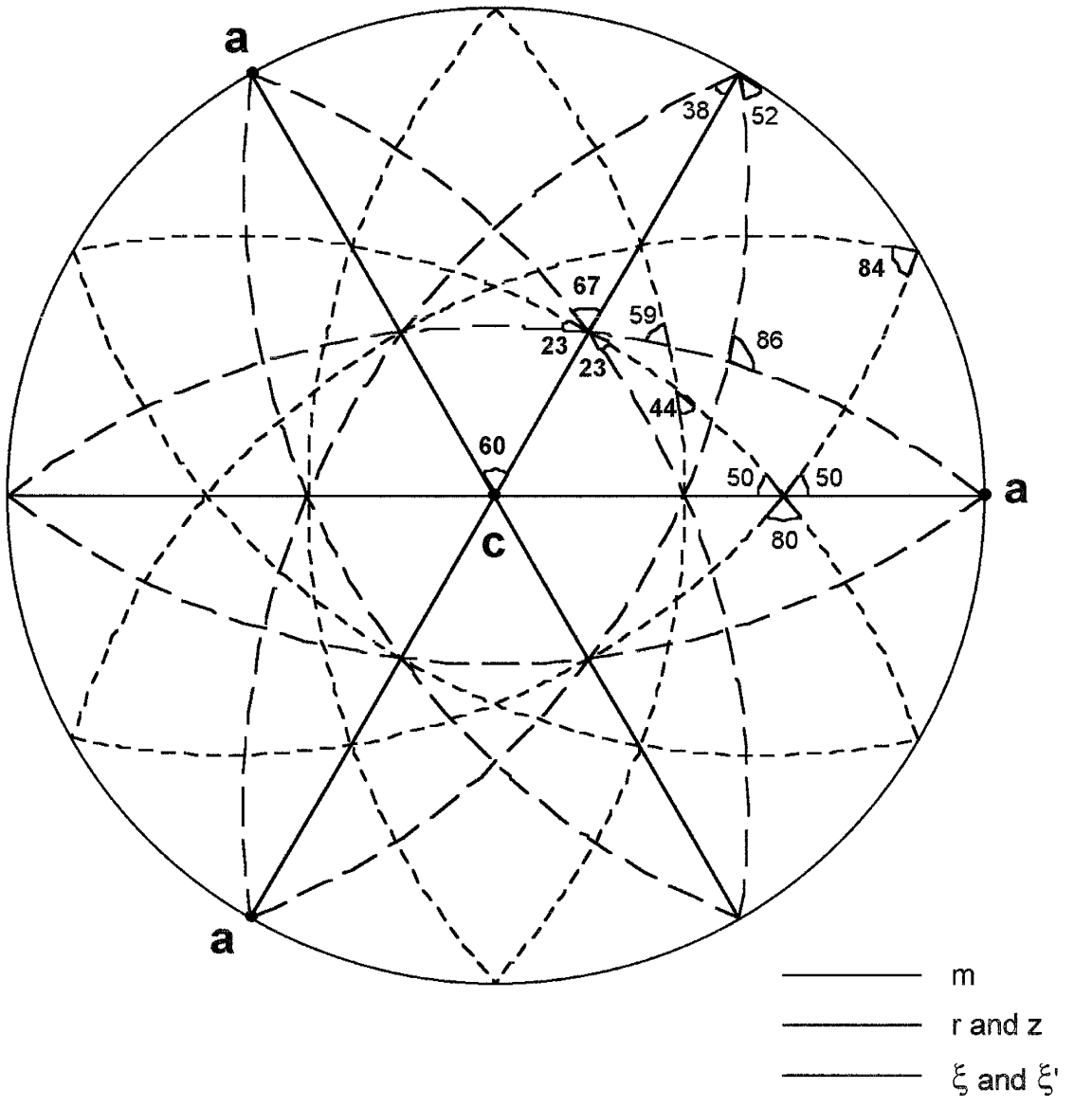

Figure 34. Quartz cleavage systems illustrated on stereogram. Point X indicates the crystallographic orientation of the most frequently found hub in lower and middle amphibolite facies samples. Point Y indicates the one for the upper amphibolite facies samples.

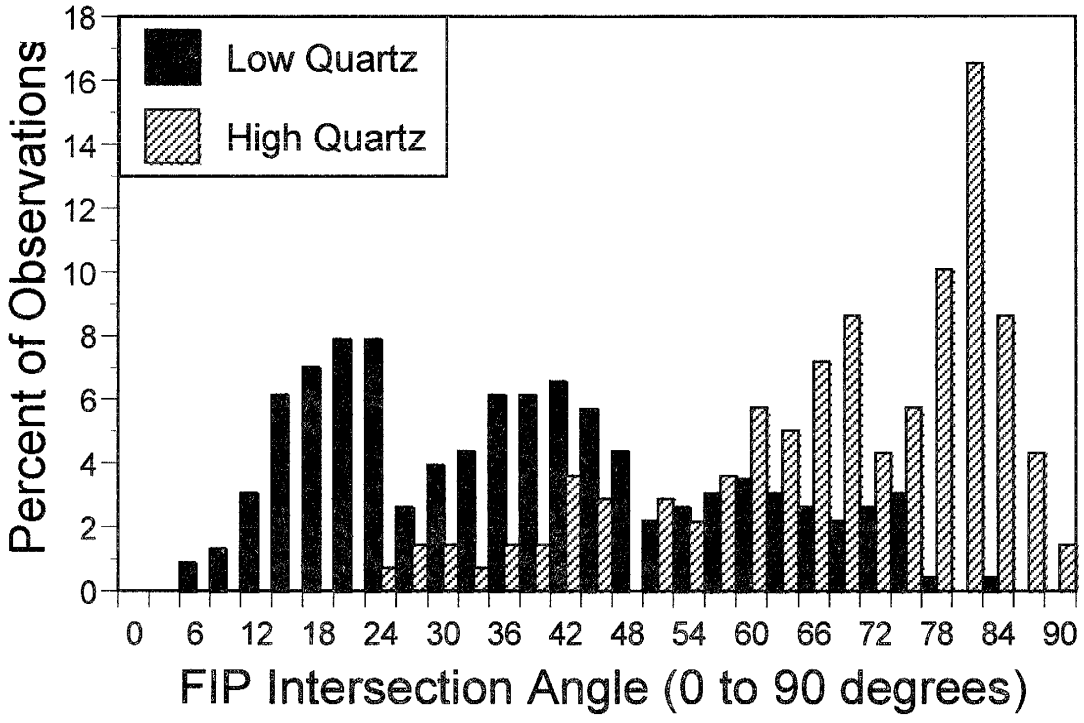

Figure 35. The differences in distribution of inter-FIP angles between lower-middle (low quartz) and upper (high quartz) amphibolite facies are distinct.

Type III FIP have a preferred orientation throughout a given petrographic section; where two sets of FIP are present they are subperpendicular. The FIP formed as intergranular microcracks and are not crystallographically controlled. They are, however, commonly deflected into type I and II FIP. The few type III FIP traces on the stereograms that are not in preferred orientation generally intersect hubs formed by type I and II FIP traces. They represent FIP that reopened the older healed cleavage cracks.

In Chapter III, the minimum pH of the fluids inside the inclusions at metamorphic pressures and temperatures was calculated to be between 6 and 8. These alkaline fluids may have been responsible for stress corrosion cracking in the quartz phenocrysts. Studies conducted at low temperature have shown that crack propagation in quartz at low stress is faster in alkaline fluids than in neutral or basic fluids (Atkinson and Meredith, 1981). The mechanism for crack propagation is the breaking of Si-O-Si bonds to form Si-O || OH-Si bonds. The rate at which OH- is supplied to the crack tip by diffusion controls the velocity of crack propagation (e.g. Martin and Durham, 1975; Atkinson, 1982). Thus, the combination of high temperature and high fluid pH favored stress corrosion cracking in the relic phenocrysts.

Hub Geometry

The FIP that define a given hub developed at the same general time. The same type of fluid inclusions are present on these FIP, and the inclusions homogenize at about the same temperature, which indicates they formed at similar metamorphic conditions. FIP related to one hub have the same cross cutting relationships with quartz grain boundaries. FIP related to different hubs in a given relic phenocryst are different ages. These relationships are helpful for constructing fluid inclusion parageneses. A method for relating hub geometry to tectonic events would also be very useful.

A number of studies have used the preferred orientations of FIP to date fluid inclusions relative to tectonic events (e.g. Pêcher et al., 1985; Lespinasse and Pêcher, 1986; Cathelineau et al., 1990; Lespinasse and Cathelineau, 1990). In these studies, it is generally accepted that the FIP originate as extensional (mode I) microcracks oriented normal to the minimum principal stress axis, σ_3. The FIP orientations are consistent with paleostress fields inferred from nearby joints, veins, fault zones and other structures. Generally, only the intergranular FIP are examined in order to ensure that FIP orientations are not crystallographically controlled. In this study, however, the crystallographically controlled FIP are of greater interest.

Hubs represent a limited number of crystallographic directions in the relic quartz phenocrysts. The crystallographic directions of hubs of the same age differ between phenocrysts. Poles to hubs in a given section tend to occur in one or two great circle girdles when plotted on a stereogram (Figure 30). A significant number of the traces of FIP that make up the hubs are correlated with the great circle girdles (Figure 31). If the processes which created the patterns of hubs and FIP were fully understood, then maybe the hub orientations could be used to establish the ages of the FIP in terms of tectonic events.

Two important questions need to be addressed by future research:

Firstly, how is a hub related to the local stress field? Studying the orientations of microcracks generated in an experimentally deformed quartz porphyry might provide the needed information. Such an experiment could even be done in a sodium bicarbonate saturated fluid to create an alkaline environment for crack propagation similar to the one in which the fluid inclusions in this study formed. FIP are generally considered to form as extensional microcracks, thus, the probable orientation for hubs is near the maximum principal stress axis, σ_1. Because the hubs occur only in special crystallographic directions, however, a small angle between each hub and the σ_1 axis is expected.

Secondly, what is the significance of the great circle girdles? An explanation for the girdles is hard to come by, particularly because it is not known if the hubs are in their original orientation, or if they have been moved relative to one another by subsequent deformation. Of practical note, however, the numerous FIP traces that coincide with the girdles may be in a preferred orientation, in which case both FIP traces and girdle orientations could be interpreted as the σ_1-σ_2 plane. The correlation between girdles and FIP traces suggests that hub girdles could be used to find the orientation of σ_3 in situations where preferred orientations of FIP are not easily discerned.

Relation to the Fluid Inclusion Study

The FIP cannot be related to tectonic events in the Zinkgruvan basin without properly oriented petrographic sections and a method for interpreting the patterns of hubs and girdles found on the stereograms. Information derived from the geochemistry of the fluid inclusions, however, can help.

In Chapter III, isochores for the various fluid inclusion types were calculated and plotted on a pressure-temperature (PT) grid. An isochore is a line on a PT grid that represents the conditions under which a given fluid inclusion could have been trapped; the location of the isochore depends upon the composition and density of the fluid inside the inclusion. The isochores, none of which intersects the conditions of peak metamorphism, can be used to constrain the retrograde metamorphic PT-time path as shown in Figure 36. Isochores for type IA and IB inclusions overlap on the PT grid, thus, the inclusions developed under similar conditions and formed close in time. Similarly, isochores for type IC, ID and II inclusions are closely spaced and form a separate group. The two groups of inclusions are interpreted to have formed during two different tectonic events.

There are four folding phases recognized in the Zinkgruvan basin; the two groups of inclusions are most likely to be associated with F_3 and F_4 folds. Peak metamorphism followed the intense deformation related to the isoclinal folding phases, F_1 and F_2 (Allen et al., 1996) and is

Figure 36. Fluid inclusion isochores constrain the retrograde metamorphic PT-time path and suggest PT regimes where various mechanisms of deformation and recrystallization occurred. The age correlation between F_3 and F_4 folding phases and formation of the various fluid inclusions is only a model for future research.

The thick black arrows labelled "lower", "middle" and "upper" are the retrograde PT time path for the three metamorphic facies. The thick dashed arrow represents the prograde metamorphic path, whose location on the grid is not constrained by isochores. The grey lines and long narrow region labelled "IA+IB", "IC+ID+II" and "III" contain isochores for the various fluid inclusion types.

Rotation recrystallization and migration recrystallization (RR+MR) and {m}<a> and (c)<a> slip were important processes in the upper amphibolite facies at the time when type I and II fluid inclusions were formed. Rotation recrystallization (RR) and {m}<a> slip were dominant mechanisms in the lower amphibolite facies. (c)<a> slip was dominant in the lower amphibolite facies prior to recrystallization of the phenocrysts.

The aluminum silicate phase diagram is from Holdaway (1971) and the high-low quartz transition is from Shen et al. (1993). K= kyanite; S= sillimanite; A= andalusite; α= low quartz; β= high quartz.

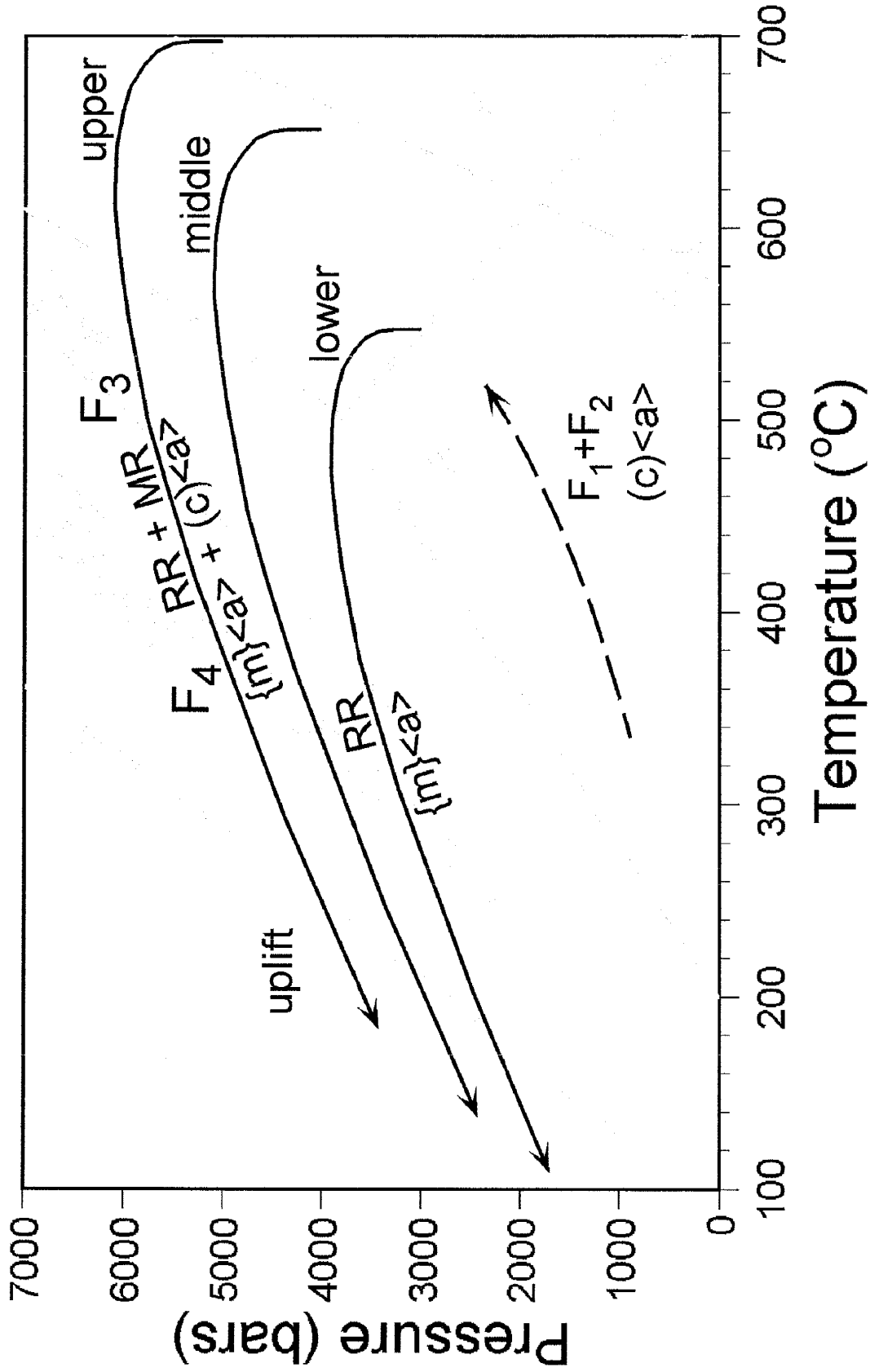
Pressure (bars)
Temperature (°C)
7000
6000
5000
4000
3000
2000
1000
0
100
200
300
400
500
600
700
upper
middle
lower
F3
F4 RR + MR {m}<a> + (c)<a>
RR {m}<a>
F1+F2 (c)<a>
uplift

associated with the intrusion of late orogenic granitoids that produced F_3 and F_4 folds (Wikström and Karis, 1991). Type III inclusions can probably be related to tectonic events during uplift. The transposed inclusions might be related to either F_1 or F_2 folds. This is a working model for future study.

The PT grid with isochores and retrograde PT-time paths for the three facies can be used to locate the conditions under which recrystallization and deformation occurred (Figure 36). The prograde metamorphic path is not constrained by isochores, but would be if microthermometry on the transposed fluid inclusions were possible. An isochore for the transposed inclusions would also indicate the conditions under which (c)<a> slip formed the birefringent deformation bands.

The PT grid highlights an interesting problem. Features in the upper amphibolite facies samples, such as chessboard texture and large inter-FIP angles, are interpreted to have formed in the high quartz field. However, the isochores and cross cutting relations between FIP and grain boundaries indicate that most of the crack propagation and recrystallization occurred in the low quartz field. These two points are difficult to reconcile unless quartz has a "memory" of the high quartz structures that guides the development of structures in the low quartz. Another possibility is that these distinctive features formed in low quartz under PT conditions where a unique combination of deformation and recrystallization mechanisms were dominant.

As shown above, the mutual study of microstructures and fluid inclusions works two ways: the microstructures can be used to help establish the fluid inclusion parageneses and the inclusions can be used to constrain the PT conditions under which the microstructures form.

Conclusions

The relic quartz phenocrysts from the Zinkgruvan basin exhibit a variety of microstructures which reflect deformation and recrystallization at different metamorphic grades. (c)<a> slip and rotation recrystallization were important in the deformation and recovery of quartz phenocryst grains in the lower amphibolite facies. {m}<a> and (c)<a> slip, and both rotation recrystallization and migration recrystalliztion, were important processes in the middle and upper amphibolite facies. It is possible for fluid inclusions to survive recrystallization of the quartz if the dominant mechanism is rotation recrystallization.

The traces of FIP tend to intersect in hubs and this geometry is interpreted to be an expression of quartz cleavage. The differences between common inter-FIP angles in lower and upper amphibolite facies is a potential geothermometer. The large number of FIP in the relic phenocrysts is likely due to the alkalinity of the fluids recorded in the inclusions, which promotes crack propagation in quartz through stress corrosion cracking.

The mechanisms that control the orientation of FIP hubs on a stereogram are unknown. However, since fluid inclusion homogenization temperatures are similar in most FIP on the same hub, and differ significantly between hubs, these relationships may prove useful for establishing fluid inclusion parageneses. Further research is required before the hub patterns can be related to tectonic events.

Chapter VI

Overview

Summary

Fluid Inclusions

Fluid inclusions in relic quartz phenocrysts from the Zinkgruvan Basin in south-central Sweden were studied. The phenocrysts occur in porphyries metamorphosed to the lower, middle and upper amphibolite facies in different areas of the basin. The majority of inclusions in samples from all the facies are $NaHCO_3$-rich and contain nahcolite daughter minerals.

Only 2/3 of the inclusions contain nahcolite crystals. Both nahcolite-bearing and solid-free inclusions on a given trail have similar liquid-vapor homogenization temperatures (Th). The explanation for this is that nahcolite precipitated in the microcracks that formed the trails before the microcracks were healed, and the bubbles formed only after the microcracks were healed. As a result, the nahcolite in the inclusions does not completely dissolve before the inclusions decrepitate. Since the nahcolite never fully dissolves the composition of the fluids cannot be easily determined.

There is microstructural evidence for different ages of the inclusions, mainly the crosscutting relations between fluid inclusion planes (FIP) and recrystallized quartz grain boundaries. Different Th are obtained from inclusions on FIP of different ages. Any given FIP has inclusions with Th that fall within about a 60 degree range. Thus, the wide range in observed Th (about 100-550°C) is due to the different ages of the FIP that record fluids trapped under different conditions. Older FIP generally contain inclusions that homogenize at higher temperatures than do those in younger FIP. The $NaHCO_3$-rich inclusions record conditions of retrograde metamorphism.

The family of bicarbonate-rich fluid inclusions is subdivided into three major types labelled in sequence from oldest to youngest: type I inclusions are small and commonly shaped like negative quartz crystals; type II inclusions are larger and have complex rounded forms; type III inclusions are larger and pinched or digitate in form. The incompletely healed FIP of type III inclusions are deflected toward the older FIP. The nahcolite in type III inclusions is probably a trapped mineral rather than a daughter mineral. Type I inclusions are further subdivided into four groups based on microstructural relationships of the FIP. Type IA FIP follow deformation bands in unrecrystallized quartz grains. Type IB FIP are typically discontinuous trails that are truncated by all grain boundaries. Type IC FIP are crosscut by some grain boundaries, but crosscut others. Type ID FIP crosscut all the quartz grain boundaries.

The minimum trapping conditions for the type I, II and III inclusions plot in the kyanite field on a pressure-temperature (PT) grid. Six isochores calculated for the bulk composition of each fluid inclusion type occur on the low temperature side of peak metamorphic conditions (3-5 kbar, 550-700°C), suggesting an anticlockwise retrograde PT-time path. Isochores tend to occur in overlapping groups: 1) types IA and IB; 2) types IC, ID and II; and 3) type III.

Various calculations of fluid pH around trapping conditions were made for each type I and II fluid inclusion bulk composition, assuming that the phase assemblages were L, L+S, L+V and L+S+V (L= liquid, S= solid, V= vapor). The fluid pH varies between about 6 and 8 depending upon composition, P and T, and the phase assemblage. In general it is not possible to precipitate a bubble unless nahcolite is present, and the precipitation of nahcolite creates a drop in pH sufficient to reduce SiO_2 solubility up to 50 percent. These calculations support the idea that nahcolite precipitated in open microcracks and induced microcrack healing through a drop in SiO_2 solubility before vapor bubbles formed.

A few of the fluid inclusions associated with a given type I FIP are peculiar in that they homogenize at different temperatures than their neighbors, and calcite is present instead of or in addition to nahcolite. In most of these type C inclusions, calcite precipitates in place of nahcolite on heating runs and nahcolite precipitates in place of calcite on cooling runs on the microthermometry stage. The amounts of nahcolite and calcite present in the inclusions are inversely related. The relative amounts of the two minerals suggest that the net reaction between the two minerals is:

(6.1) $3NaHCO_3 + 2Ca^{+2} = 2CaCO_3 + 3Na^+ + H^+ + CO_2 + H_2O.$

Type C fluid inclusions exhibit unusual behavior when heated and cooled on the stage. Upon heating a type C_1 inclusion, which has only nahcolite present at 25°C, calcite precipitates before the nahcolite is fully dissolved and liquid-vapor homogenization takes place only after the nahcolite is gone. Upon subsequent cooling the calcite persists metastably (below its precipitation temperature) and does not completely dissolve until a vapor bubble forms. Final calcite dissolution is sudden and results in the immediate precipitation of nahcolite. An unstable intermediate state consists of a large CO_2-rich bubble that exists for less than a second when neither mineral is present. Type C_2 inclusions, which have only calcite present at 25°C, and type C_3 inclusions, which have both nahcolite and calcite present at 25°C, exhibit similar phenomena but in different temperature ranges.

Type C inclusions are interpreted to be the equivalent of type I inclusions that have trapped calcite. The calcite probably precipitated in older FIP whose inclusions were destroyed when the trails were reused by type I FIP. The calculated pH of the fluids and the minimum trapping conditions for type C inclusions are broadly similar to those found for type I inclusions.

There are a number of other interesting fluid inclusion types seen in the relic phenocrysts, most important being the transposed fluid inclusions which are preserved in unrecrystallized quartz in

the lower and middle amphibolite facies samples. Theses inclusions are linear groups that are organized into bands. Each linear group is a former fluid inclusion that has been stretched along the quartz a axis, and each band of linear groups is a former FIP. Quadrupole mass spectrometry (QMS) was used to estimate the composition of these inclusions; relic phenocrysts containing transposed inclusions and type I inclusions were crushed in a vacuum and the gases analyzed. The QMS results were subdivided into two groups with different water content. Since the water-rich analyses have an average CO_2 content of 6 mole% and correspond well to the type I inclusion composition, the transposed inclusions are assumed to be relatively CO_2-rich, with about 20 mole% CO_2.

A significant portion of the fluid evolution in the Zinkgruvan Basin is recorded in the relic phenocrysts. Early fluids were relatively CO_2-rich and precipitated calcite. Later fluids had less CO_2 and precipitated nahcolite. The last fluid recorded in type III inclusions did not precipitate daughter minerals. The trace gas species (CH_4, N_2 and Ar) in the QMS gas analyses indicate that the fluids came from the same two sources evolving in a relatively closed system. The major source was metamorphic fluid that originated with devolatilization reactions in skarn bands in the metaporphyries. Na^+ and HCO_3^- in the fluids came from the breakdown of calcite and feldspars to produce anorthite, zoisite and quartz. CO_2-rich fluids were generated initially, followed by H_2O-rich fluids. The same basic fluid precipitated calcite and nahcolite at different times under different conditions of CO_2 partial pressure and temperature.

Microstructures

The relic phenocrysts exhibit a variety of features that might be useful in understanding the environments of fluid inclusion entrapment, and preservation or destruction of the inclusions. Many of the phenocrysts in samples from the lower amphibolite facies contain cores of

unrecrystallized quartz whereas others have undergone mainly rotation recrystallization. Typical deformation structures are birefringent deformation bands decorated with exsolution inclusions in the old quartz grains, and deformation lamellae in the new quartz grains. Phenocrysts in samples from the middle and upper amphibolite facies have undergone grain boundary migration recrystallization in addition to rotation recrystallization. Deformation lamellae are seen in some quartz grains. Other grains contain birefringent deformation lamellae. Blocky quartz grains in the upper amphibolite facies samples are reminiscent of "chessboard" texture. Since "chessboard" texture forms in high quartz, it appears that in some of the phenocrysts high temperature microstuctures were not erased by lower temperature processes on the retrograde metamorphic path.

Rotation recrystallization seems to be the key to preservation of several fluid inclusion types. The transposed FIP may crosscut new grain boundaries formed by rotation recrystallization. "Satellite inclusions" occur in strain shadows where they were protected by dislocation climb around an included mineral grain. "Ghost trails" are interpreted to be the fragmentary remnants of intergranular FIP that have been partly erased by dislocation movements.

The relic phenocrysts have many sets of FIP which are not in obvious preferred orientations. When the traces to FIP are plotted on stereograms the FIP tend to intersect in "hubs". The FIP that intersect in hubs contain fluid inclusions that homogenize at similar temperatures, therefore, FIP associated with the same hub are assumed to be the same age. It is not known how a hub forms in relation to stresses acting on a phenocryst, therefore, it is impossible to know how the hubs come to be in great circle girdles on stereograms. If the process of hub formation were understood, then the hub patterns might be of potential use in dating the fluid inclusions with respect to tectonic events inferred from outcrop structures.

The FIP orientations are not random. A definite preference for quartz cleavage planes is indicated by the prevalence of specific inter-FIP angles which correlate with the intersections of m,

r, z and ξ planes in low and high quartz. FIP in quartz from the the upper amphibolite facies samples tend to intersect at larger angles than FIP in quartz from the lower amphibolite facies samples. This is interpreted to be the result of FIP formed on ξ cleavage planes that are well developed only in the high quartz field.

There is evidence that the FIP have been reused by younger generations of microcracks which have produced newer fluid inclusion trails. The traces of open microcracks typically intersect the hubs of FIP. Type III FIP are deflected from a straight path into older FIP. Where the FIP reuse older FIP, nahcolite minerals are trapped in type III inclusions. The traces of type III FIP intersect the hubs formed by type I FIP. The traces of type I FIP may interesect hubs of different ages. Furthermore, type C fluid inclusions probably formed when type I FIP trapped calcite while propagating along older FIP. The reuse of older FIP permits the interpretation that type IC and ID FIP occur on ξ cleavage planes in the quartz which originally contained FIP formed in the high quartz field.

Perspective

The Zinkgruvan Basin formed during the Svecofennian orogen about 1.9 to 1.7 Ga. Four deformation phases have been recognized that are not easy to correlate with other areas in south-central Sweden (Hedström and Wikström, 1986). Two isoclinal folding phases (F_1 and F_2) are responsible for the synform, and two phases of open cross fold development (F_3 and F_4) are responsible for outcrop patterns. The later folding phases are related to the local intrusion of granitoids late in orogenesis. Peak metamorphism probably occurred in association with the late intrusions (Wikström and Karis, 1991).

It is not possible to correlate the types of fluid inclusions seen in the relic phenocrysts with the various folding phases without oriented petrographic sections and an understanding of how hubs

form in relation to the stress field in a relic phenocryst. However, a model for future study is proposed here: transposed fluid inclusions originated and were deformed during F_1 and F_2; types IA and IB inclusions were trapped during F_3; types IC, ID and II inclusions were trapped during F_4; and type III inclusions formed during uplift. Deformation associated with F_3 and F_4 was probably complex, accompanied by local variations in temperature and pressure that resulted in multiple generations of fluid inclusions. The high pH of the fluids guaranteed that a large number of FIP would be formed by stress corrosion cracking during the deformations. In this scheme, the transposed inclusions were trapped along the prograde metamorphic path, when CO_2 content of the fluids was likely to be high from the initiation of devolatilization reactions in the skarns. Inclusions with the highest Th were trapped during retrograde metamorphism when the CO_2 content of the fluids was likely to be less. These relationships are not well established and should be the focus of future research.

Significance of This Study

Quartz phenocrysts are remarkably good subjects for fluid inclusion study that have been overlooked. The results of this study are widely applicable to terranes where quartz porphyries are prevalent. "Quartz eye" porphyries are the most common type of wall rock encountered in volcanogenic massive sulfide deposits (Vernon, 1986) and are very prominent in many other Early Proterozoic terranes (e.g. Williams and Burr, 1994). Quartz porphyries may contain a longer record of metamorphic fluids than other prominent rock types that have a more homogeneous grain size, because the phenocrysts in porphyries are sheltered from recrystallization by the partitioning of strain into fine grained matrix.

Alkaline fluids are not generally considered to be geologically important, yet there are many studies that suggest nahcolite, an indicator of alkaline fluids, is a common daughter mineral in metamorphic fluid inclusions (e.g. Coolen, 1982; Olsen, 1987; Robert and Kelly, 1987; Anderson et al. 1989, 1990; Guilhaumou et al., 1990; Ansdell and Kyser, 1991). The link between skarns and alkaline metamorphic fluids merits further examination since skarns are a significant rock type in many metamorphic terranes.

It is not widely known that quartz has good cleavage at elevated temperatures. Stress corrosion cracking in quartz under metamorphic conditions may be an important deformation mechanism, particularly when the metamorphic fluids are alkaline. The FIP in most metamorphic rocks are likely to reflect cleavage in the host quartz.

Directions for Future Inquiry

There are several important lines of investigation that would improve upon this study and be of benefit to future fluid inclusion studies on rocks from metamorphic terranes.

Fluid inclusions must not be used alone to reconstruct the retrograde PT-time path. There is a discrepancy between minimum trapping conditions in the kyanite field reported here and the generally accepted view that metamorphism occurred only in the andalusite and sillimanite fields (Rickard, 1988). The peak pressure conditions in the Zinkgruvan Basin are not well known. This could be rectified by applying McKenna and Hodges (1988) garnet-plagioclase-aluminum silicate-quartz geobarometer for amphibolite grade metapelites to the metagreywackes that are adjacent to the metaporphyries in most locations. With both metagreywackes and skarns present throughout the basin, there is great potential for constraining the PT path using metamorphic mineral equilibria. The skarns, furthermore, offer ample opportunity to study the evolution of

metamorphic fluids through devolatilization reactions. Such an investigation might confirm that the fluid evolution occurred in a closed system.

The deformation microstructures in the quartz are not well understood because they have never been studied in the thick sections that are required for microthermometric study. The microstructures are useful for understanding the preservation of fluid inclusions that would otherwise go unstudied because it is assumed that all the useful information from the inclusions has been lost or altered. Deformation microstructures in the host quartz might help constrain the conditions of metamorphism under which inclusions were trapped, since certain microstructures, like "chessboard texture", can be indicative of limited ranges in metamorphic conditions (e.g. Kruhl, 1996). Combined study of thick and thin petrographic sections cut from the same billet would be very helpful for identifying the microstructures encountered in fluid inclusion studies.

Understanding what "hub" patterns on a stereogram mean might be useful for dating the inclusions on the FIP that form the hubs. If the hubs can be related to principal stress axes, and oriented thick sections are available, it might be possible to relate the hubs to local structures and, thus, regional tectonic events. Studies relating fluid composition to deformation phases have up to now been limited to intergranular FIP which exhibit strong preferred orientations (e.g. Pêcher et al., 1985; Lespinasse and Pêcher, 1986). The analysis of hubs might make similar correlations possible using crystallographically controlled FIP, which are overlooked in this type of study.

The orientation of the FIP along quartz cleavage planes is easily studied using a universal stage. Since the FIP were developed at many stages during the deformation and recrystallization of the quartz, they might be studied as an important deformation mechanism which complemented active slip systems. The proposal that FIP are repeatedly used by later generations of FIP forming microcracks might be studied by cathodoluminescence (e.g. Boiron et al., 1992).

Finally, it seems important to study the experimental system H_2O-CO_2-$NaHCO_3$-$CaCO_3$ (-NaCl-$CaCl_2$) in order to explain the fluid inclusion microthermometry results. Investigation by synthetic fluid inclusions techniques (e.g. Bodnar and Sterner, 1985) would be ideal, not only for studying the phase relationships in this system, but also for studying the unusual properties of microcrack propagation and healing in quartz under alkaline conditions.

References

Allen, R.L., Lundström, I., Ripa, M., Simeonov, A. and Christofferson, H. (1996) Facies analysis of a 1.9 Ga, continental margin, back-arc, felsic caldera province with diverse Zn-Pb-Ag-(Cu-Au) sulfide and Fe oxide deposits, Bergslagen region, Sweden, *Economic Geology 91*, 979-1008.

Anderson, T., Austrheim, H. and Burke, E.A.J. (1990) Fluid inclusions from granulites and eclogites from the Bergen Arcs, Caledonides of W. Norway, *Mineralogical Magazine 54*, 145-158.

Anderson, T., Burke, E.A.J. and Austrheim, H. (1989) Nitrogen-bearing, aqueous fluid inclusions in some eclogites from the Western Gneiss Region of the Norwegian Caledonides, *Contributions to Mineralogy and Petrology 103*, 153-165.

Ansdell, K.M. and Kyser, T.K. (1991) The geochemistry and fluid history of the Proterozoic Laurel Lake Au-Ag deposit, Flin Flon greenstone belt, *Canadian Journal of Earth Science 28*, 155-171.

Armands, G and Xefteris, A. (1987) Swedish granitoids of S- and I-type and their lithophile element distribution, *Geologiska Föreningens i Stockholm Förhandlingar 109*, 177-195.

Atkinson, B.K. (1982) Subcritical crack propagation in rocks: theory, experimantal results and applications, *Journal of Structural Geology 4*, 41-56.

Atkinson, B.K. and Meredith, P.G. (1981) Stress corrosion cracking of quartz: a note on the influence of chemical environment, *Tectonophysics 77*, T1-T11.

Audédat, A. and Günther, D. (1999) Mobility and H_2O loss from fluid inclusions in natural quartz crystals, *Contributions to Mineralogy and Petrology 137*, 1-14.

Balzers A.G. (1983) *Partial Pressure Measurement in Vacuum Technology*, Fachbericht BG 800 169 PE, Balzers A.G., Liechtenstein, 32 pages.

Barker, C. and Smith, M.P. (1986) Mass spectrometric determination of gases in individual fluid inclusions in natural minerals, *Analytical Chemistry 58*, 1330-1333.

Beetsma, J.J. (1992) Retrograde fluid evolution of the Stollberg Pb-Zn-Fe-Mn-(Ag) ore deposit, central Bergslagen, Sweden, *Geologiska Föreningens i Förhandlingar 114*, 279-290.

Bell, I.A. and Wilson, C.J.L. (1981) Deformation of biotite and muscovite: TEM microstructure and deformation model, *Tectonophysics 78*, 201-228.

Blacic, J.D. (1975) Plastic deformation mechanisms in quartz: The effect of water, *Tectonophysics 27*, 271-294.

Blom, K.A. (1988) Subsolidus migmatization in high-grade meta-tuffs (Kurkijärvi, southwest Finland), *Lithos 21*, 263-278.

Bloss, F.D. (1957) Anisotropy of fracture in quartz, *American Journal of Science 255*, 214-225.

Bloss, F.D. and Gibbs, G.V. (1963) Cleavage in quartz, *American Mineralogist 48*, 821-838.

Bodnar, R.J. (1993) Revised equation and table for determining the freezing point depression of H_2O-NaCl solutions, *Geochimica et Cosmochimica Acta 57*, 683-684.

Bodnar, R.J. and Sterner, S.M. (1985) Synthetic fluid inclusions in natural quartz; II, Application to PVT studies, *Geochimica et Cosmochimica Acta 49*, 1855-1859.

Boiron, M.C., Essarraj, S., Sellier, E., Cathelineau, M., Lespinasse, M. and Poty, B. (1992) Identification of fluid inclusions in relation to their host microstructural domains in quartz by cathodoluminescence, *Geochimica et Cosmochimica Acta 56*, 175-185.

Borisenko, A.S. (1974) Possible determination of sodium carbonates and bicarbonates in solutions of gaseous-liquid inclusions in minerals, *Doklady Akademii Nauk SSSR 214*, 917-20. (in Russian)

Boullier, A.-M. and Robert, F. (1992) Paleoseismic events recorded in Archean gold-quartz vein networks, Val d'Or, Abitibi, Quebec, Canada, *Journal of Structural Geology 14*, 1161-1179.

Bowers, T.S. and Helgeson, H.C. (1983) Calculation of the thermodynamic and geochemical consequences of nonideal mixing in the system H_2O-CO_2-NaCl on phase relations in geologic systems: equation of state for H_2O-CO_2-NaCl fluids at high pressures and temperatures, *Geochimica et Cosmochimica Acta 47*, 1247-1275.

Burruss, R.C. (1981) Analysis of fluid inclusions: phase equilibria at constant volume, *American Journal of Science 281*, 1104-1126.

Busey, R.H. and Mesmer, R.E. (1977) Ionization equilibria of silicic acid and polysilicate formation in aqueous sodium chloride solutions to 300°C, *Inorganic Chemistry 16*, 2444-2450.

Cathelineau, M., Lespinasse, M., Bastoul, A.M., Bernard, C. and Leroy, J. (1990) Fluid migration during contact metamorphism: the use of oriented fluid inclusion trails for a time/space reconstruction, *Mineralogical Magazine 54*, 169-182.

Collins, P.L.F. (1979) Gas hydrates in CO_2-bearing fluid inclusions and the use of freezing data for estimation of salinity, *Economic Geology 74*, 1435-1444.

Coolen, J.J.M.M.M. (1982) Carbonic fluid inclusions in granulites from Tanzania - a comparison of geobarometric methods based on fluid density and mineral chemistry, *Chemical Geology 37*, 59-77.

Crawford, M.L. (1981) Fluid inclusions in metamorphic rocks - low and medium grade, *in* Crawford, M.L. and Hollister, L.S., editors, *Fluid Inclusions: Applications to Petrology, Mineralogical Association of Canada Short Course Handbook 6*, Mineralogical Association of Canada, Calgary, pages 157-181.

Crerar, D.A. and Anderson, G.M. (1971) Solubility and solvation reactions of quartz in dilute hydrothermal solutions, *Chemical Geology 8*, 107-122.

Davis, D.W., Lowenstein, T.K. and Spencer, R.J. (1990) Melting behavior of fluid inclusions in laboratory grown halite crystals in the systems NaCl-H_2O, NaCl-KCl-H_2O, NaCl-$MgCl_2$-H_2O, and NaCl-$CaCl_2$-H_2O, *Geochimica et Cosmochimica Acta 54*, 591-601.

Drummond, E.J.S. (1981) *Boiling and Mixing of Hydrothermal Fluids: Chemical Effects on Mineral Precipitation*, Ph.D. Dissertation, Pennsylvania State University, 380 pages.

Drury, M.R. and Urai, J.L. (1990) Deformation-related recrystallization processes, *Tectonophysics 172*, 235-253.

Duyster, J.P. (1998) StereoNett 2.20, *http://homepage.ruhr-uni-bochum.de/Johannes.P.Duyster/stereo/stereo1.htm.*, University of Bochum.

Ferry, J.M. (1976) P, T, f_{CO2}, and f_{H2O} during metamorphism of calcareous sediments in the Waterville-Vassalboro area, south-central Maine, *Contributions to Mineralogy and Petrology 57*, 119-143.

Freeth F.A. (1922) The system Na_2O-CO_2-NaCl-H_2O considered as two four-component systems, *Philosophical Transactions of the Royal Society (London) A 223*, 35-87.

Frietsch, R. (1982) Alkali metasomatism in the ore-bearing metavolcanics of central Sweden, *Sveriges Geologiska Undersökning C 791*, 54 pages.

Gaal, G. and Gorbatschev, R. (1987) An outline of the Precambrian evolution of the Baltic Shield, *Precambrian Research 35*, 15-52.

Garney, J.R. and Kesler, S.E. (1995) Factors affecting gas analysis of inclusion fluid by quadrupole mass spectrometry, *Geochimica et Cosmochimica Acta 59*, 3977-3986.

Giggenbach, W.F. (1986) The use of gas chemistry in delineating the origin of fluid discharges over the Taupo Volcanic Zone: a review, *Proceedings: Fifth International Volcanological Congress*, Hamilton, New Zealand, pages 47-50.

Giggenbach, W.F. (1997) The origin and evolution of fluids in magmatic-hydrothermal systems, in Barnes, H.L. editor, *Geochemistry of Hydrothermal Ore Deposits, Third Edition*, John Wiley and Sons, New York, pages 737-796.

Gorbatschev, R. and Gaal, G. (1987) The Precambrian history of the Baltic shield, *in* Kroner, A. editor, *Proterozoic Lithospheric Evolution, American Geophysical Union Geodynamics Series 17,* American Geophysical Union, Washington D.C., pages 149-159.

Guilhaumou, N., Santos, M., Touray, J.C., Beny, C. and Dardenne, M. (1990) Multiphase methane-rich fluid inclusions in gold-bearing quartz as illustrated at Pontal (Goias, Brazil), *Mineralogical Magazine 54*, 257-266.

Harley, S.L. (1989) The origins of granulites: a metamorphic perspective, *Geological Magazine 126*, 215-247.

Harvie, C.E., Møller, N. and Weare, J.H. (1984) The prediction of mineral solubilities in natural waters: The Na-K-Ca-Mg-H-Cl-SO_4-OH-HCO_3-CO_3-CO_2-H_2O system to high ionic strengths at 25°C, *Geochimica et Cosmochimica Acta 48*, 723-751.

Hedström, P. and Wikström, A. (1986) The Zinkgruvan (Åmmeberg) zinc-lead deposit, *7th IAGOD Symposium Excursion Guide 3*, 33-36.

Hedström, P., Simeonov, A. and Malmström, L. (1989) The Zinkgruvan ore deposit, south-central Sweden; a Proterozoic, proximal Zn-Pb-Ag deposit in distal volcanic facies, *Economic Geology 84*, 1235-1261.

Helgeson, H.C. and Kirkham D.H. (1974a) Theoretical prediction of the thermodynamic behavior of aqueous electrolytes at high pressures and temperatures. I. Summary of the thermodynamic and electrostatic properties of the solvent, *American Journal of Science 274*, 1089-1198.

Helgeson, H.C. and Kirkham D.H. (1974b) Theoretical prediction of the thermodynamic behavior of aqueous electrolytes at high pressures and temperatures. II. Debye-Hückel parameters for activity coefficients and relative partial molal properties, *American Journal of Science 274*, 1199-1261.

Helgeson, H.C., Kirkham, D.H. and Flowers, G.C. (1981) Theoretical prediction of the behavior of aqueous electrolytes at high pressures and temperatures: calculation of activity coefficients, osmotic coefficients, and apparent molal and standard and relative partial molal properties to 600°C and 5 kbar, *American Journal of Science 281*, 1249-1516.

Henriques, A. (1964) Geology and ores of the Åmmeberg district (Zinkgruvan) Sweden, *Arkiv för Mineralogi och Geologi 4*, 246 pages.

Hobbs, B.E. (1968) Recrystallization of single crystals of quartz, *Tectonophysics 6*, 353-401.

Hobbs, B.E. (1985) The geologic significance of microfabric, *in* Wenk, H.R., editor, *Preferred Orientation in Deformed Metals and Rocks*, Academic Press, New York, pages 463-484.

Hobbs, B.E., McLaren, A.C. and Paterson, M.S. (1972) Plasticity of single crystals of synthetic quartz, *in* Heard, H.C., editor, *Flow and Fracture of Rocks, Geophysical Monograph Series 16*, American Geophysical Union, Washington D.C., pages 29-53.

Holdaway, M.J. (1971) Stability of andalusite and the aluminum silicate phase diagram, *American Journal of Science 271*, 97-131.

Hollister, L.S. (1990) Enrichment of CO_2 in fluid inclusions in quartz by removal of H_2O during crystal-plastic deformation, *Journal of Structural Geology 12*, 895-901.

Houghton, G., McLean, A.M. and Ritchie, P.D. (1957) Compressibility, fugacity, and water-solubility of carbon dioxide in the region 0-36 atm. and 1-100°C, *Chemical Engineering Science 6*, 132-137.

Johansson, H. (1910) The Åmmeberg zinc ore field, *Geologiska Föreningens i Stockholm Förhandlingar 32*, 1051-1078.

Johnson, E.L. and Hollister, L.S. (1995) Syndeformational fluid trapping in quartz: determining the pressure-temperature conditions of deformation from fluid inclusions and the formation of pure CO_2 fluid inclusions during grain-boundary migration, *Journal of Metamorphic Geology 13*, 239-249.

Johnson, J.W., Oelkers, E.H. and Helgeson, H.C. (1992) SUPCRT92: A software package for calculating the standard molal thermodynamic properties of minerals, gases, aqueous species, and reactions from 1 to 5000 bar and 0 to 1000 degrees C, *Computers and Geosciences 18*, 899-947.

Kautsky, F. (1955) Der Bau des Westrandes der svionischen leptitzone im Gebiet der Zinkgrube von Åmmeberg, *Geologiska Föreningens i Stockholm Förhandlingar 77*, 161-184.

Keilland J. (1937) Individual activity coefficients of ions in aqueous solutions, *Journal of the American Chemical Society 59*, 1675-1678.

Kelley, K.K. (1960) Contributions to the data in theoretical metallurgy XIII: High temperature heat content, heat capacities and entropy data for the elements and inorganic compounds, *U.S. Bureau of Mines Bulletin 584*, 232 pages.

Knacke, O., Kubaschewski, O. and Hesselmann, K., editors (1991) *Thermochemical Properties of Inorganic Substances,* Springer-Verlag, New York, 2412 pages.

Kobayashi, K. (1952) The heat capacities of inorganic substances at high temperature. Part VII. The heat capacities of sodium carbonate and sodium bicarbonate, *Science Reports of Tohoku University 36*, 21.

Kranz, R.L. (1983) Microcracks in rocks: a review, *Tectonophysics 100*, 449-480.

Kruhl, J.H. (1996) Prism- and basal-plane parallel subgrain boundaries in quartz: a microstructural geothermobarometer, *Journal of Metamorphic Geology 14*, 581-589.

Lagerblad, B. (1988) Evolution and tectonic history of the Bergslagen volcano-plutonic complex, central Sweden, *Geologie en Mijnbouw 67*, 165-176.

Lagerblad, B. and Gorbatschev, R. (1985) Hydrothermal alteration as a control of regional geochemistry and ore formation in the central Baltic Shield, *Geologische Rundschau 74*, 33-49.

Law, R.D, Casey, M. and Knipe, R.J. (1986) Kinematic and tectonic significance of microstructures and crystallographic fabrics within quartz mylonites from the Assynt and Eriboll regions of the

Moine thrust zone, NW Scotland, *Transactions of the Royal Society of Edinburgh: Earth Sciences 77*, 99-125.

Lespinasse, M. and Pêcher, A. (1986) Microfracturing and regional stress field: a study of the preferred orientations of fluid-inclusion planes in a granite from the Massif Central, France, *Journal of Structural Geology 8*, 169-180.

Lespinasse, M. and Cathelineau, M. (1990) Fluid percolations in a fault zone: a study of fluid inclusion planes in the St Sylvestre granite, northwest Massif Central, France, *Tectonophysics 184*, 173-187.

Lindblom, S. and Burke, E. (1988) Raman spectrometry and microthermometry data on CO_2-CH_4-bearing fluids in late orogenic quartz from the Saxberget Zn-Pb-Cu-Ag deposit, central Sweden, *Geologie en Mijnbouw 67*, 471-476.

Linke, W.F. (1965) *Solubilities, Volume II, Inorganic and Metal-Organic Compounds*, 4th Edition, American Chemical Society, Washington D.C., 1914 pages.

Linker, M.F. and Kirby, S.H. (1981) Anisotropy in the rheology of hydrolytically weakened synthetic quartz crystals, *in* Carter, N.L., editor, *Mechanical Behavior of Crustal Rocks, Geophysical Monograph Series 24*, American Geophysical Union, Washington D.C., pages 29-48.

Loberg, B.E.H. (1980) A Proterozoic subduction zone in southern Sweden, *Earth and Planetary Science Letters 46*, 287-294.

Löfgren, C. (1979) Do leptites represent Precambrian island arc rocks?, *Lithos 12*, 159-165.

MacDonald, A.J. and Spooner, E.T.C. (1981) Calibration of a Linkam TH600 programmable heating-cooling stage for microthermometric examination of fluid inclusions, *Economic Geology 74*, 1248-1258.

Magnusson, N.H. (1936) The evolution of the lower Archean rocks in central Sweden and their iron, manganese and sulphide ores, *Quarterly Journal of The Geological Society of London 92*, 332-358.

Magnusson, N.H., Thorslund, P., Brotzen, F., Asklund, B. and Kulling, O. (1962) Beskrivning till Karta over Sveriges Bergrund, *Sveriges Geologiska Undersökning Serie Ba 16*, 290 pages.

Manning, C.E. (1994) The solubility of quartz in H_2O in the lower crust and upper mantle, *Geochimica et Cosmochimica Acta 58*, 4831-4839.

Marshall, B. and Gilligan, L.B. (1993) Remobilization, syn-tectonic processes and massive sulphide deposits, *Ore Geology Reviews 8*, 39-64.

Martin, R.J. III and Durham, W.B. (1975) Mechanisms of crack growth in quartz, *Journal of Geophysical Research 80*, 4837-4844.

McLaren, A.C., Turner, R.G., Boland, J.W. and Hobbs, B.E. (1970) Dislocation structure of the deformation lamellae in synthetic quartz: A study by electron and optical microscopy, *Contributions to Mineralogy and Petrology 29*, 104-115.

Meere, P.A. (1995) High and low density fluids in a quartz vein from the Irish Variscides, *Journal of Structural Geology 17*, 435-446.

Monnin, C. and Schott, J. (1984) Determination of the solubility products of sodium carbonate minerals and an application to trona deposition in lake Magadi (Kenya), *Geochimica et Cosmochimica Acta 48*, 571-581.

Moore, J.N., Norman, D.I. and Kennedy, B.M. (2001) Fluid inclusion gas compositions from an active magmatic-hydrothermal system: a case study of The Geysers geothermal field, USA, *Chemical Geology 173*, 3-30.

Moore, J.N., Powell, T.S., Heizler, M.T. and Norman, D.I. (2000) Mineralization and hydrothermal history of the Tiwi geothermal system, Philippines, *Economic Geology 95*, 1001-1024.

Moorman, A.C., Andriessen, P.A.M., Boelrijk, N.A.I.M., Hebeda, E.H., Oen, I.S., Priem, H.N.A., Verdurmen, E.A.T., Verschure, R.H. and Wiklander, U. (1982) K-Ar and Rb-Sr mineral ages of skarns and associated metabasites and leptites in the Hjulsjö area of the Bergslagen ore province, central Sweden, *Geologiska Föreningens i Stockholm Förhandlingar 104*, 1-9.

Neumann, B. and Domke, R. (1928) Die Gleichgewichtsverhältnisse beim Ammoniaksodaprozesse unter Druck, *Zeitschrift für Elektrochemie und Angewandte Physikalische Chemie 34*, 136-153.

Norman, D.I. and Musgrave, J.A. (1994) N_2-Ar-He compositions in fluid inclusions: indicators of fluid source, *Geochimica et Cosmochimica Acta 58*, 1119-1131.

Norman, D.I. and Sawkins, F.J. (1987) Analysis of gases in fluid inclusions by mass spectrometer, *Chemical Geology 61*, 1-10.

Norman, D.I., Moore, J.N., Yonaka, B. and Musgrave, J. (1997) Gaseous species in fluid inclusions: A tracer of fluids and indicator of fluid processes, *Proceedings: 21st Workshop on Geothermal Reservoir Engineering*, Stanford University, Stanford, California, pages 22-24.

Nyström, J.O. (1992) Post-Svecokarelian andinotype evolution in central Sweden, *Geologische Rundschau 71*, 141-157.

Oakes, C.S., Bodnar, R.J. and Simonson, J.M. (1990) The system NaCl-$CaCl_2$-H_2O: I. The ice liquidus at 1 atm total pressure, *Geochimica et Cosmochimica Acta 54*, 603-610.

Oen, I.S. (1987) Rift-related igneous activity and metallogenesis in SW Bergslagen, Sweden, *Precambrian Research 35*, 367-382.

Oen, I.S., Helmers, H., Verschure, R.H. and Wiklander, U. (1982) Ore deposition in a Proterozoic incipient rift zone environment: a tentative model for the Filipstad-Grythyttan-Hjulsjö region, Bergslagen, Sweden, *Geologische Rundschau 71*, 182-194.

Olsen, S.N. (1987) The composition and role of the fluid in migmatites: a fluid inclusion study of the Front Range rocks, *Contributions to Mineralogy and Petrology 96*, 104-120.

Palache, C., Berman, H. and Frondel, C. (1951) *Dana's System of Mineralogy, 7th Ed., Volume II*, John Wiley and Sons, New York, 1124 pages.

Passchier, C.W. and Trouw, R.A.J. (1996) *Microtectonics*, Springer-Verlag, New York, 289 pages.

Pêcher, A., Lespinasse, M. and Leroy, J. (1985) Relation between fluid inclusion trails and regional stress field: a tool for fluid chronology. The example of an intragranitic uranium ore deposit, north west Massif Central, France, *Lithos 18*, 229-237.

Peiper, J.C. and Pitzer, K.S. (1982) Thermodynamics of aqueous carbonate solutions including mixtures of sodium carbonate, bicarbonate and chloride, *Journal of Chemical Thermodynamics 14*, 613-638.

Phillips, G.N. (1980) Water activity changes across an amphibolite-granulite facies transition, Broken Hill, Australia, *Contributions to Mineralogy and Petrology 75*, 377-386.

Pitzer, K.S. (1981) Characteristics of very concentrated aqueous solutions, in Richard, D.T. and Wickman, F.E., editors, *Chemistry and Geochemistry of Solutions at High Temperatures and Pressures*, Pergamon Press, 564 pages.

Plimer, I.R. (1987) Remobilization in high-grade metamorphic environments, *Ore Geology Reviews 2*, 231-245.

Potter, R.W. and Brown, D.L. (1977) The volumetric properties of aqueous sodium chloride solutions from 0° to 500°C at pressures up to 2000 bars based on a regression of available data in the literature, *U.S. Geological Survey Bulletin 1421-C*, 36 pages.

Rankin, A.H. (1975) Fluid inclusion studies in apatite from carbonatites of the Wasaki area of western Kenya, *Lithos 8*, 123-136.

Rankin, A.H. and LeBas, M.J. (1974) Nahcolite ($NaHCO_3$) in inclusions in apatites from some E. African ijolites and carbonatites, *Mineralogical Magazine 39*, 564-570.

Rickard, D. (1988) Regional metamorphism in the Bergslagen province, south central Sweden, *Geologie en Mijnbouw 67*, 139-155.

Robert, F. and Kelly, W.C. (1987) Ore-forming fluids in Archaean gold-bearing quartz veins at the Sigma mine, Abitibi greenstone belt, Quebec, Canada, *Economic Geology 82*, 1464-1482.

Robinson, R.A. and Stokes, R.H. (1970) *Electrolyte Solutions*, Second Edition, Butterworth and Company, London, 236 pages.

Roedder, E. (1967) Metastable superheated ice in liquid-water inclusions under high negative pressure, *Science 155*, 1413-1417.

Roedder, E. (1984) *Fluid Inclusions, Reviews in Mineralogy Volume 12*, The Mineralogical Society of America, Washington, D.C., 646 pages.

Ruff, R.K. (1993) *Gas Analysis of Fluid Inclusions: Application toward Precious Metal Exploration, Steeple Rock Mining District, Grant County, New Mexico*, M.S. Thesis, New Mexico Institute of Mining and Technology, 83 pages.

Schreurs, J. (1984) The amphibolite-granulite facies transition in West Uusimaa, SW Finland. A fluid inclusion study, *Journal of Metamorphic Geology 2*, 348-357.

Schreurs, J. and Westra, J. (1985) Cordierite-orthopyroxene rocks: the granulite facies equivalents of the Orijarvi cordierite-anthophyllite rocks in West Uusimaa, southwest Finland, *Lithos 18*, 215-228.

Seward, T.M. (1974) Determination of the first ionization constant of silicic acid from quartz solubility in borate buffer solutions to 350°C, *Geochimica et Cosmochimica Acta 38*, 1651-1664.

Shen, A.H., Bassett, W.A. and Chou, I-M. (1993) The α-β quartz transition at high temperatures and pressures in a diamond-anvil cell by laser interferometry, *American Mineralogist 78*, 694-698.

Shepherd, T.J., Rankin, A.H. and Alderton, D.H.M. (1985) *A Practical Guide to Fluid Inclusion Studies*, Chapman and Hall, New York, 239 pages.

Shmulovich, K.I. and Plyasunova, N.V. (1993) Phase equilibria in ternary systems formed by H_2O and CO_2 with $CaCl_2$ or NaCl at high T and P, *Geochemistry International 30*, 53-71.

Shock, E.L. and Helgeson, H.C. (1988) Calculation of the thermodynamic and transport properties of aqueous species at high pressures and temperatures: correlation algorithms for ionic species and equation of state predictions to 5 kb and 1000°C, *Geochimica et Cosmochimica Acta 52*, 2009-2036.

Simmons, G. and Richter, D. (1976) Microcracks in rocks, *in* Strens, R.G.J., editor, *The Physics and Chemistry of Minerals and Rocks*, John Wiley & Sons, New York, pages 105-137.

Stephansson, O. (1975) Polydiapirism of granitic rocks in the Svecofennian of central Sweden, *Precambrian Research 2*, 189-214.

Stephens, M.B. and Wahlgren, C.H. (1993) Oblique-slip, right-lateral ductile deformation zones in the Svecokarelian orogen, south-central Sweden, *Rapporter och Meddelanden, Sveriges Geologiska Undersökning 76*, 18-19.

Sterner, S.M. (1992) Homogenization of fluid inclusions to the vapor phase: the apparent homogenization phenomenon, *Economic Geology 87*, 1616-1623.

Stålhös, G. (1976) Aspects of the regional tectonics of eastern central Sweden, *Geologiska Föreningens i Stockholm Förhandlingar 98*, 19-29.

Stålhös, G. (1981) A tectonic model for the Svecokarelian folding in east central Sweden, *Geologiska Föreningens i Stockholm Förhandlingar 103*, 33-46.

Stålhös, G. (1984) Svecokarelian folding and interfering macrostructures in eastern central Sweden, *in* Kröner, A. and Greiling, R., editors, *Precambrian Tectonics Illustrated*, Schweizerbartsche Verlagsbuchhandlung, Stuttgart, pages 369-379.

Stålhös, G. and Welin, E. (1984) Maximum age of the synmetamorphic Svecokarelian fold phases in south central Sweden, *Geologiska Föreningens i Stockholm Förhandlingar 108*, 31-34.

Swanenberg, H.E.C. (1980) *Fluid Inclusions in High-Grade Metamorphic Rocks from S.W. Norway*, Ph.D. Dissertation, Rijksuniversitiet te Utrecht, 147 pages.

Tanger, J.C. IV and Helgeson, H.C. (1988) Calculation of the thermodynamic and transport properties of aqueous species at high pressures and temperatures: revised equations of state for the standard partial molal properties of ions and electrolytes, *American Journal of Science 288*, 19-98.

Thiery, R., van den Kerkhof, A.M. and Dubessy, J. (1994) vX modelling of CH_4-CO_2 and CO_2-N_2 fluid inclusions (T<31°C, P<400 kbar), *European Journal of Mineralogy 6*, 753-772.

Touret, J. (1977) The significance of fluid inclusions in metamorphic rocks, *in* Fraser, D.G., editor, *Thermodynamics in Geology*, D. Reidel Publishing, Dordrecht-Holland, pages 203-227.

van den Kerkhof, A.M. (1987) The fluid evolution of the Harmsarvet ore deposit, central Sweden, *Geologiska Föreningens i Förhandlingar 109*, 1-12.

van der Velden, W., Baker, J., de Maesschalck, S. and van Meerten, T. (1982) Bimodal early Proterozoic volcanism in the Grythytte field and associated volcano-plutonic complexes, Bergslagen, central Sweden, *Geologische Rundschau 71*, 171-181.

Vanderzee, C.E. (1982) Thermodynamic relations and equilibria in (Na_2CO_3+$NaHCO_3$+H_2O): standard Gibbs energies of formation and other properties of sodium hydrogen carbonate, sodium carbonate heptahydrate, sodium carbonate decahydrate trona: ($Na_2CO_3 \cdot NaHCO_3 \cdot 2H_2O$) and Wegscheider's salt: ($Na_2CO_3 \cdot NaHCO_3$), *Journal of Chemical Thermodynamics 14*, 219-238.

Vivallo, W. and Rickard, D. (1990) Genesis of an early Proterozoic zinc deposit in high-grade metamorphic terrane, Saxberget, central Sweden, *Economic Geology 85*, 714-736.

Vokes, F.M. (1969) A review of the metamorphism of sulphide deposits, *Earth-Science Reviews 5*, 99-143.

Vokes, F.M. and Craig, J.R. (1993) Post-recystallization mobilization phenomena in metamorphosed stratabound sulfide ores, *Mineralogical Magazine 57*, 19-28.

Waldeck, W.F., Lynn, G. and Hill, A.E. (1934) Aqueous solubility of salts at high temperatures. II. The ternary system Na_2CO_3-$NaHCO_3$-H_2O from 100 to 200°, *Journal of the American Chemical Society 56*, 43-47.

Walther, J.V. and Helgeson, H.C. (1977) Calculation of the thermodynamic properties of aqueous silica and the solubility of quartz and its polymorphs at high pressures and temperatures, *American Journal of Science 277*, 1315-1351.

Walther, J.V. and Orville, P.M. (1983) The extraction-quench technique for determination of the thermodynamic properties of solute complexes: application to quartz solubility in fluid mixtures, *American Mineralogist 68*, 731-741.

Wasström, A. (1995) A petrologic study of the altered footwall rocks in Zinkgruvan and some mineralisations in the Zinkgruvan basin, *Närings- och Teknikutvecklingsverket (NUTEK) Unpublished Project Report 94-2462*, 54 pages.

Welin, E. (1992) Isotopic results of the Proterozoic crustal evolution of south-central Sweden: review and conclusions, *Geologiska Föreningens i Stockholm Förhandlingar 114*, 299-312.

Welin, E. and Stålhös, G. (1986) Maximum age of the synmetamorphic Svecokarelian fold phases in south central Sweden, *Geologiska Föreningens i Stockholm Förhandlingar 108*, 31-34.

White, S. (1976) The effects of strain on the microstructures, fabrics, and deformation mechanisms in quartzites, *Philosophical Transactions of the Royal Society of London A 283*, 69-86.

Wikström, A. (1984) A possible relationship between augen gneisses and post orogenic granites in S.E. Sweden, *Journal of Structural Geology 6*, 409-415.

Wikström, A. (1991) Structural features of some younger granitoids in central Sweden and implications for the tectonic subdivision of granitoids, *Precambrian Research 51*, 151-159.

Wikström, A. and Aaro, S. (1986) The Finspång augen-gneiss massif - geology, geophysics and relationship to postorogenic granites, *Sveriges Geologiska Undersökning Serie C 813.*

Wikström, A. and Karis, L. (1991) Beskrivning till berggrundskartorna Finspång NO, SO, NV, SV, *Sveriges Geologiska Undersökning Serie Af 162-165*, 216 pages.

Wilkins, R.W.T. and Barkas, J.P. (1978) Fluid inclusions, deformation and recrystallization in granite tectonites, *Contributions to Mineralogy and Petrology 65*, 293-299.

Williams, A.E. (1996) Mass spectrometric analysis of volatiles in fluid inclusions: aliquot calibration valve to simulate inclusion rupture, *Chemical Geology 131*, 155-165.

Williams, M.L. and Burr, J.L. (1994) Preservation and evolution of quartz phenocrysts in deformed rhyolites from the Proterozoic of southwestern North America, *Journal of Structural Geology 16*, 203-221.

Wilkins, R.W.T. and Barkas, J.P. (1978) Fluid inclusions, deformation and recrystallization in granite tectonites, *Contributions to Mineralogy and Petrology 65*, 293-299.

Wilson, M.R. (1980) Granite types in Sweden, *Geologiska Föreningens i Stockholm Förhandlingar 102*, 167-176.

Wise, D.U. (1964) Microjointing in basement, Middle Rocky Mountains of Montana and Wyoming, *Geological Society of America Bulletin 75*, 287-306.

Åberg, A. and Fallick, A.E. (1993) A fluid inclusion and light stable element isotope study of the gold-bearing quartz vein system, Falun, Sweden, *Mineralium Deposita 12*, 324-333.

Appendix A

The calculations undertaken in this appendix address three questions raised in Chapter III. How does P_{CO2} elevated above atmospheric levels affect the solubility of nahcolite? What is the pH of a typical fluid inclusion under isochoric PT conditions, and how does the precipitation of a vapor bubble or a nahcolite crystal affect this pH? How sensitive is the solubility of quartz to changes in fluid pH at high temperature and pressure, particularly pH changes of the magnitude caused by the precipitation of nahcolite or bubbles?

Solubility of Nahcolite

Experimental nahcolite solubility data is summarized in Linke (1965). It mainly comes from three sources: Freeth (1922), who examined low temperature relations in the system $NaHCO_3$-NaCl-H_2O; Waldeck et al. (1934) who studied high temperature nahcolite solubility "at the natural pressure of the system"; and Neumann and Domke (1928) who determined low temperature nahcolite solubility at 1.2 atm P_{CO2} (about 1.2 bars). The mole percent of CO_2 in air is about 0.032% which suggests that P_{CO2} in air, the conditions of Freeth's experiments, is about 0.00032 bars. Waldeck et al. calulated P_{CO2} in their 200°C experiment to be 1120 lbs/in^2 or about 77 bars. The results of all three studies were recalculated in terms of $m\mathrm{Na}^+$ and plotted in Figure 37. In addition, the low temperature data has been extrapolated (dotted lines) to 100°C using a least-squares best-fit curve method to find solubility as a second-order polynomial function of temperature. It is of particular interest to note that the solubility of nahcolite at 20, 30 and 40°C *increases* with a rise in P_{CO2} to 1.2 bars. This must be due to a drop in solution pH.

The dissolution of nahcolite involves a change in pH, and the liberation of water and carbon dioxide according to the reaction:

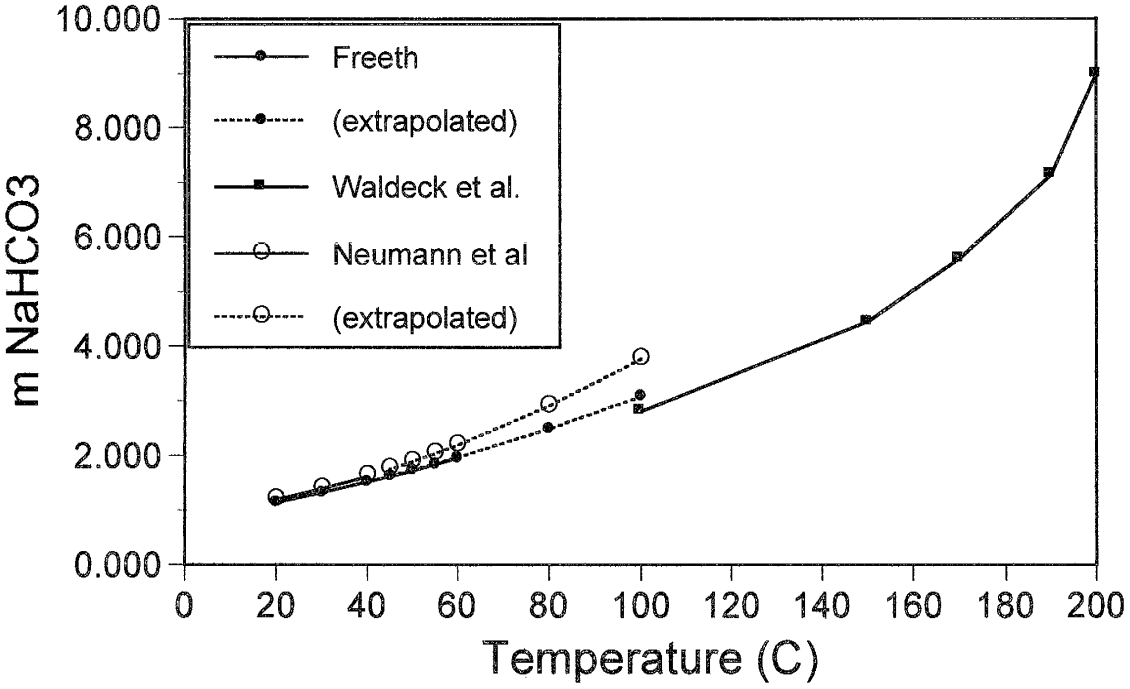

Figure 37. The nahcolite solubility data of Freeth (1922), Waldeck et al. (1934) and Neumann and Domke (1928) recalculated in M (moles/1000g H_2O) units. Dotted lines connect points extrapolated to temperatures higher than experimental conditions. The results of Waldeck et al. were obtained at "the natural pressure of the system", i.e. P_{CO2} was higher under experimental conditions than at atmospheric conditions. P_{CO2} at 200°C was estimated to be 77 bars.

(A.1) $NaHCO_3 + H^+ = Na^+ + CO_2^a + H_2O$.

For a given temperature (T) and partial pressure of carbon dioxide (P_{CO2}) the solubility of nahcolite and pH for the solution are uniquely defined using the following relations:

(A.2) $P_{CO2} = K_H X_{CO2a}$

(A.3) $H_2O + CO_2^a = H^+ + HCO_3^-$

(A.4) $HCO_3^- = H^+ + CO_3^{-2}$

(A.5) $H_2O = H^+ + OH^-$

(A.6) $m Na^+ + m H^+ = m OH^- + m HCO_3^- + 2m CO_3^{-2}$.

The Henry's Law constant (K_H) in (2) relates P_{CO2} to the mole fraction of aqueous CO_2 (X_{CO2a}) in the liquid phase of a fluid inclusion whenever a vapor bubble is present. Since K_H is a function of Na^+ molality (m) an iterative technique must be used to find mNa^+ in order to model nahcolite solubility. The method used here is to "guess" mNa^+ until the ion charge balance condition (A.6) is satisfied, using (A.2) for calculation of mCO_2^a, (A.1) for mH^+, (A.3) for $mHCO_3^-$, (A.4) for mCO_3^{-2} and (A.5) for mOH^-. The calculations were done on an electronic spreadsheet.

Calculation of K_H as a function of Na^+ molality was done using the equation of Drummond (1981) which is valid for up to 6.0 M NaCl:

(A.7) $\ln K_H = A + BT + CX + D/T + E/X + FXT + GX/T + HT/X$.

X is the molality of NaCl and T is in Kelvin. The constants A through H are as follows: A= 20.244, B= -0.016323, C= -1.0312, D= -3629.7, E= 0.4445, F= 0.0012806, G= 255.9, and H= -0.00160. It was assumed that the Drummond equation, which fits CO_2 solubility data for the H_2O-CO_2-NaCl system, would adequately predict relations in the H_2O-CO_2-$NaHCO_3$ system. At 25°C, 0.0 M NaCl, and 1 bar P_{CO2} the mole fraction of CO_2 in the aqueous phase should be about 0.00034 (Houghton et al., 1957). Drummond's equation predicts X_{CO2a} to be 0.034, in error by a factor of 100, suggesting that the X_{CO2a} units are in percent and not mole fraction. In subsequent

calculations, K_H from Drummond's equation is divided by 100% in order to avoid impossibly high solubilities of nahcolite, as constrained by the experimental nahcolite solubility data.

The mass action constants (K) for reactions (A.4), (A.5) and (A.6) were found using the computer program SUPCRT92 available from James Johnson at *johnson@s05.es.llnl.gov* and described in Johnson et al. (1992). Thermodynamic data for nahcolite had to be provided. The standard state properties for nahcolite were taken from Knacke et al. (1991). The nahcolite heat capacity data of Kobayashi (1952) determined over the 300-385°C temperature range was used. The solubility product (K_{SP}) for nahcolite described by:

(A.8) $NaHCO_3 = Na^+ + HCO_3^-$

is calculated to be 0.378 ($\log K_{SP}$ = -0.423) at 25°C. This falls between the K_{SP} estimates for nahcolite solubility of Harvie et al. (1982) and Vanderzee (1982), as listed in Monnin and Schott (1984). Monnin and Schott obtained K_{SP} = 0.407 ($\log K_{SP}$ = -0.390) using the ion-interaction model of Peiper and Pitzer (1982) for their work. The log K values generated with SUPCRT92 for reactions (A.1), (A.3) and (A.8) are acceptable, and are internally consistent.

Activity of the aqueous species at elevated pressure-temperature (PT) conditions were calculated using the Debye-Hückel equation modifications of Helgeson and Kirkham (1974a, 1974b):

(A.9) $\log \gamma = bI - Z^2 A_\gamma I^{1/2} / (1+\text{å}B_\gamma I^{1/2})$

where the activity coefficient (γ) of a given species depends upon ionic strength (I), an ion interaction factor (b), the charge (Z) and effective ionic radius (å) of the hydrated species, and the properties of water at the given PT conditions (A_γ and B_γ). An ion interaction factor of 0.055 was used, as suggested by Robinson and Stokes (1970) for strong electrolytes. The ionic radii of Na^+, H^+, OH^-, HCO_3^- and CO_3^{-2} were taken to be 4, 9, 3.5, 4 and 4.5 Å respectively (Keilland, 1937). I was initially set equal to $m Na^+$, but in subsequent iterations was calculated as:

(A.10) $I = (m Na^+ + m H^+ + m OH^- + m HCO_3^- + 4m CO_3^{-2}) / 2$.

The calculation of nahcolite solubility requires two iterative steps: 1) correct "guessing" of $m\mathrm{Na}^+$ at the given PT and assumed I conditions, and 2) correction of I and γ for all species based on the last best guess for $m\mathrm{Na}^+$. Steps 1 and 2 are repeated until the corrections of I and γ become diminishingly small. This may require up to ten repetitions of steps 1 and 2. The results of calculations for given T and P_{CO2} are listed in Table 11 and plotted in Figure 38. In all cases it was assumed that P_{CO2} was equal to the total pressure in the system.

In the model, nahcolite solubility increases with a rise in temperature and decreases with the addition of NaCl, as does the experimental data at atmospheric P_{CO2}. A direct comparison is not possible because the equations of state used in SUPCRT92 are not valid at pressures less than 1 bar. At investigated temperatures and NaCl molality, nahcolite solubility *initially decreases* with a rise in P_{CO2} above 1 bar, and *subsequently increases* with a further rise in P_{CO2} above 10 bars. At the investigated temperatures, nahcolite solubility reaches a minimum between 5 and 10 bars of CO_2 partial pressure. This is not consistent with the experimental data of Neumann and Domke (1922) which suggests that nahcolite solubility should *increase* with elevated P_{CO2} as compared with experiments done under atmospheric conditions.

The variation in nahcolite solubility with P_{CO2} can also be calculated according to the ion-interaction model of Pitzer (1981) which was developed for high ionic strength solutions. The model for $NaHCO_3$, however, is limited to temperatures close to 25°C. Peiper and Pitzer (1982) addressed the thermodynamics of aqueous $NaHCO_3$-Na_2CO_3 solutions in the 5 to 45°C range, and calculated equilibrium CO_2 vapor pressures (P_{CO2}) for pure $NaHCO_3$ solutions between 0.001 and 1.000 M. The results of their calculations are plotted in Figure 39. Their results also suggest that nahcolite solubility should *increase* with a rise in P_{CO2} at partial pressures much less than 1 bar.

Monnin and Schott (1984) used Pitzer's ion-interaction model to calculate mineral equilibria between nahcolite, trona ($Na_3HCO_3CO_3 \cdot 2H_2O$) and natron ($Na_2CO_3$) and found the minimum P_{CO2}

Table 11. Results of nahcolite solubility calculations. T= temperature, *m*= concentration in moles/kg H_2O, PCO_2= partial pressure of CO_2, wt. %= weight percent.

T (°C)	*m*Cl (mol/kg H_2O)	PCO_2 (bars)	*m*Na (mol/kg H_2O)	pH	*m*$NaHCO_3$ (mol/kg H_2O)	Na (wt. %)
100	0	1.013	1.88	8.34	1.88	13.6
100	0	5	1.84	7.66	1.84	13.4
100	0	10	1.83	7.36	1.83	13.3
100	0	50	1.84	6.64	1.84	13.4
100	0	100	1.85	6.32	1.85	13.5
100	0	200	1.87	5.98	1.87	13.6
100	0	300	1.90	5.77	1.90	13.8
100	0	400	1.92	5.60	1.92	13.9
100	0	500	1.94	5.47	1.94	14.0
100	0.01	1.013	1.88	8.34	1.87	13.6
100	0.01	5	1.84	7.66	1.83	13.3
100	0.01	10	1.84	7.36	1.83	13.3
100	0.01	50	1.84	6.64	1.83	13.3
100	0.01	100	1.86	6.32	1.85	13.4
100	0.01	200	1.88	5.98	1.87	13.6
100	0.01	300	1.90	5.77	1.89	13.7
100	0.01	400	1.93	5.60	1.92	13.9
100	0.01	500	1.95	5.47	1.94	14.0
100	0.1	1.013	1.92	8.33	1.82	13.2
100	0.1	5	1.88	7.65	1.78	13.0
100	0.1	10	1.88	7.35	1.78	12.9
100	0.1	50	1.88	6.64	1.78	13.0
100	0.1	100	1.90	6.31	1.80	13.1
100	0.1	200	1.92	5.97	1.82	13.2
100	0.1	300	1.94	5.76	1.84	13.4
100	0.1	400	1.97	5.60	1.87	13.5
100	0.1	500	1.99	5.46	1.89	13.6
100	0.5	1.013	2.11	8.30	1.61	11.7
100	0.5	5	2.07	7.62	1.57	11.5
100	0.5	10	2.07	7.32	1.57	11.4
100	0.5	50	2.07	6.61	1.57	11.5
100	0.5	100	2.09	6.29	1.59	11.6
100	0.5	200	2.11	5.95	1.61	11.7
100	0.5	300	2.13	5.73	1.63	11.9
100	0.5	400	2.16	5.57	1.66	12.0
100	0.5	500	2.18	5.43	1.68	12.1

Table 11. (continued)

T (°C)	*m*Cl (mol/kg H_2O)	PCO_2 (bars)	*m*Na (mol/kg H_2O)	pH	*m*$NaHCO_3$ (mol/kg H_2O)	Na (wt. %)
100	1	1.013	2.37	8.27	1.37	9.99
100	1	5	2.34	7.58	1.34	9.76
100	1	10	2.33	7.28	1.33	9.73
100	1	50	2.34	6.57	1.34	9.76
100	1	100	2.35	6.25	1.35	9.85
100	1	200	2.37	5.91	1.37	9.99
100	1	300	2.40	5.70	1.40	10.1
100	1	400	2.42	5.54	1.42	10.3
100	1	500	2.44	5.40	1.44	10.4
200	0	15.54	2.80	8.18	2.80	19.0
200	0	20	2.79	8.07	2.79	19.0
200	0	50	2.80	7.67	2.80	19.0
200	0	100	2.82	7.35	2.82	19.1
200	0	200	2.86	7.01	2.86	19.4
200	0	300	2.90	6.80	2.90	19.6
200	0	400	2.94	6.64	2.94	19.8
200	0	500	2.97	6.51	2.97	20.0
200	0.01	15.54	2.80	8.18	2.79	19.0
200	0.01	20	2.80	8.07	2.79	19.0
200	0.01	50	2.80	7.67	2.79	19.0
200	0.01	100	2.82	7.35	2.81	19.1
200	0.01	200	2.86	7.01	2.85	19.3
200	0.01	300	2.90	6.80	2.89	19.5
200	0.01	400	2.94	6.64	2.93	19.8
200	0.01	500	2.97	6.51	2.96	19.9
200	0.1	15.54	2.84	8.18	2.74	18.6
200	0.1	20	2.83	8.07	2.73	18.6
200	0.1	50	2.84	7.66	2.74	18.7
200	0.1	100	2.86	7.35	2.76	18.8
200	0.1	200	2.90	7.01	2.80	19.0
200	0.1	300	2.94	6.80	2.84	19.2
200	0.1	400	2.98	6.64	2.88	19.4
200	0.1	500	3.01	6.50	2.91	19.6
200	0.5	15.54	3.01	8.16	2.51	17.1
200	0.5	20	3.01	8.05	2.51	17.1
200	0.5	50	3.01	7.65	2.51	17.1
200	0.5	100	3.03	7.33	2.53	17.2

Table 11. (continued)

T (°C)	*m*Cl (mol/kg H_2O)	PCO_2 (bars)	*m*Na (mol/kg H_2O)	pH	*m*$NaHCO_3$ (mol/kg H_2O)	Na (wt. %)
200	0.5	200	3.07	6.99	2.57	17.5
200	0.5	300	3.11	6.78	2.61	17.7
200	0.5	400	3.15	6.62	2.65	17.9
200	0.5	500	3.18	6.49	2.68	18.1
200	1	15.54	3.25	8.14	2.25	15.4
200	1	20	3.24	8.03	2.24	15.3
200	1	50	3.24	7.63	2.24	15.3
200	1	100	3.26	7.31	2.26	15.4
200	1	200	3.30	6.98	2.30	15.7
200	1	300	3.34	6.77	2.34	15.9
200	1	400	3.37	6.61	2.37	16.1
200	1	500	3.40	6.48	2.40	16.2

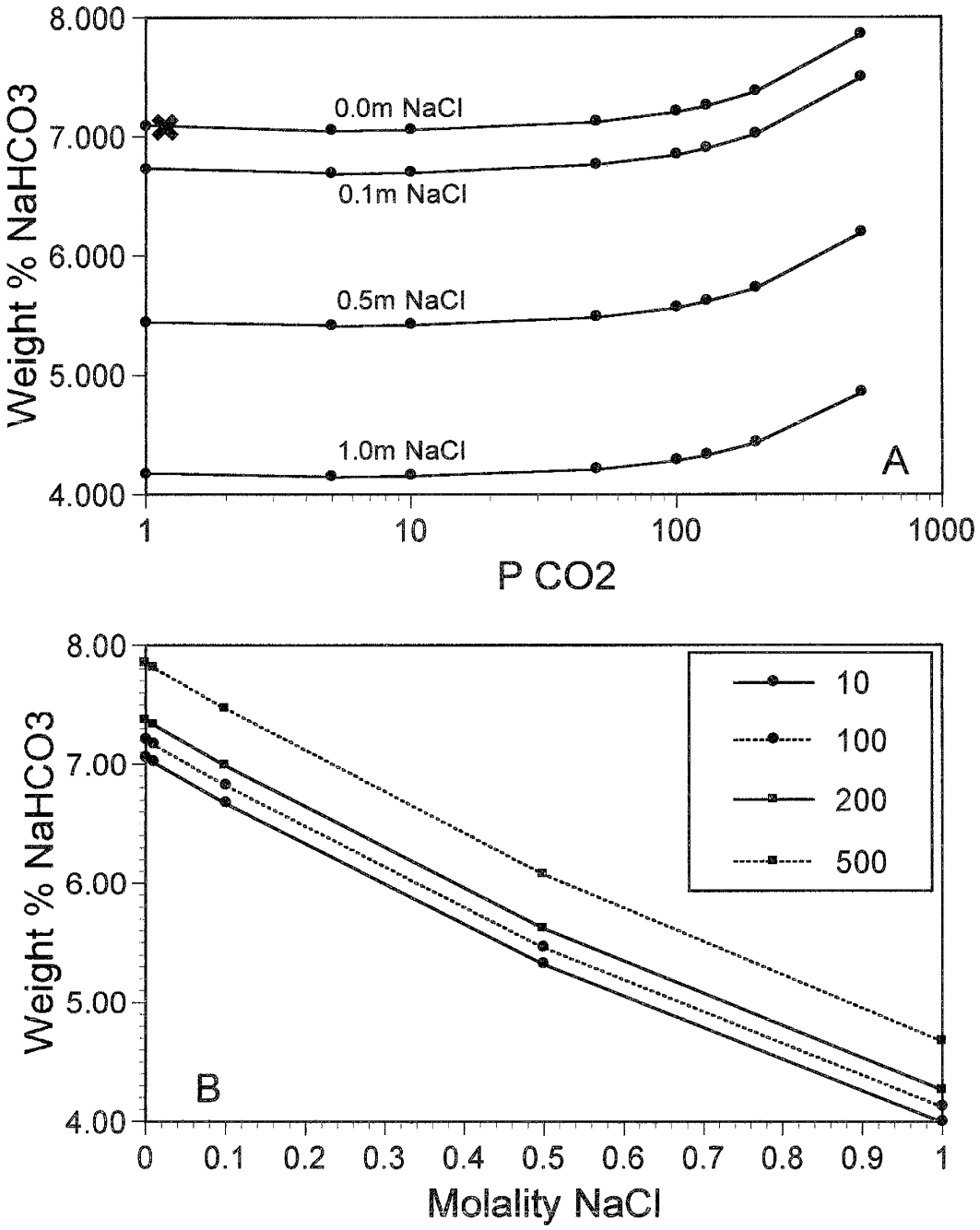

Figure 38. The solubility of nahcolite at 25°C as calculated using SUPCRT92. A) Solubility variation with P_{CO2} for a given NaCl molality. The data of Neumann and Domke (1928) interpolated to 25°C is indicated with an "x". B) Solubility variation with NaCl molality for a given P_{CO2}.

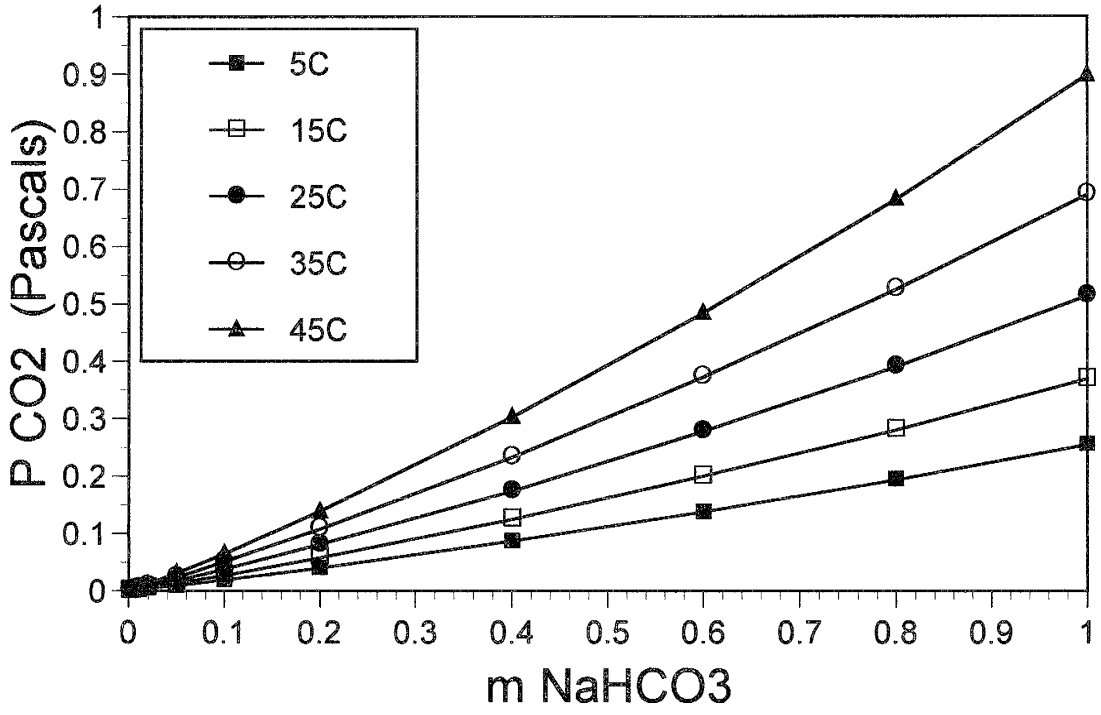

Figure 39. Relations between nahcolite solubility, CO_2 partial pressure and temperature calculated by Peiper and Pitzer (1982) using an ion-interaction model. Nahcolite solubilty is enhanced by increases in both temperature and P_{CO2}.

for nahcolite stability to be 0.0033 bars at 21°C. Their equation for nahcolite solubility in terms of reaction (A.8) is given as:

(A.11) $\ln K_8 = 7.7 - 2570/T$

with T in Kelvin. The effect of high (>0.001 bar) P_{CO2} was not considered since their study addressed mineral precipitation in alkaline lakes.

pH in the System H_2O-CO_2-$NaHCO_3$-NaCl

At least seven aqueous species are present in nahcolite-bearing fluid inclusions at elevated temperatures (T) and pressures (P), and their relative amounts are dependent upon both the PT conditions and the number of phases (fluid, vapor bubble and solid nahcolite) present inside the inclusions. In order to simplify calculation of the distribution of species in a fluid inclusion, (from which pH can be obtained) the following assumptions are made: 1) activity coefficients (γ) are all equal to 1.00; 2) fugacity coefficients are all equal to 1.00; 3) there are no density (ρ) changes in the fluid phase with changing molalities of aqueous species; 4) there are no changes in the density of solid nahcolite with variation in P and T; 5) there are no changes in the volume of the fluid inclusion due to the thermal expansion of the quartz host or dissolution of quartz on the inclusion walls; 6) fluids and aqueous species do not migrate into or out of the inclusion; 7) only CO_2 is present in the vapor bubble; and 8) changes in log K values due to small changes in pressure can be ignored. The purpose of the calculations outlined below are to demonstrate the direction of changes in pH that must occur when either a bubble or nahcolite precipitate in a fluid inclusion, and not to accurately determine the solution pH and other parameters.

The distribution of species and pH of the fluid inside an inclusion are calculated using an iterative method on electronic spreadsheet. The approach is to "guess" pH and calculate the molalities of H^+, OH^-, HCO_3^-, CO_3^{-2} and CO_2^a using the assumed pH. The nominal composition of the fluid

inclusion in terms of X_{H2O}, X_{CO2}, X_{NaHCO3} and X_{NaCl} must be known from microthermometry data, or assumed. The molalities of Cl-, Na^+ and CO_2 for the completely homogenized inclusion are obtained from the nominal composition, formulated as moles/1000 grams of water (M units). The total Na^+ molality (mNa^{+TN}) includes contributions from the $NaHCO_3$ and NaCl components. The total CO_2 molality (mCO_2^{TN}) includes a contribution from the $NaHCO_3$ component. The molalities of H^+ and OH^- are obtained from the assumed pH using log K for reaction (A.5).

In the case of one fluid phase with no bubble and no nahcolite, pH is assumed and $mHCO_3^-$ is calculated from the mass balance equation for the carbon dioxide species. This is done by noting that mCO_2^a and mCO_3^{-2} can be expressed in terms of $mHCO_3^-$ by using the mass action relations:

(A.12) $$mCO_2^a = mH^+ \, mHCO_3^- / K_3$$

(A.13) $$mCO_3^{-2} = K_4 \, mHCO_3^- / mH^+$$

which can be inserted into the mass balance equation for carbon dioxide:

(A.14) $$mCO_2^T = mCO_2^a + mHCO_3^- + mCO_3^{-2}$$

to yield the following relationship:

(A.15) $$mHCO_3^- = mCO_2^T / (mH^+/K_3 + 1 + K_4/mH^+).$$

Successive guesses for pH are made until the sum of the charges on the cations balances the sum of the charges on the anions according to:

(A.16) $$mNa^+ + mH^+ = mCl^- + mOH^- + mHCO_3^- + 2\, mCO_3^{-2}.$$

Finding the correct pH when nahcolite is present in the fluid inclusion is more complicated since "guesses" must be made for both pH and the mNa^+ remaining in solution until two conditions are met. The approach is to "guess" pH for an assumed mNa^+, and then calculate $mHCO_3^-$ using two different methods. Successive guesses for pH are made until the $mHCO_3^-$ calculated by the different methods are in agreement. One way to calculate $mHCO_3^-$ is outlined above. The second method for calculating $mHCO_3^-$ is to use the mass action relation:

(A.17) $m\mathrm{HCO_3^-} = K_8 / m\mathrm{Na^+}$.

If the sum of the charges on the cations and anions do not balance after these calculations, then another $m\mathrm{Na^+}$ is chosen (for which another pH must be found) until the ion charges do balance.

Finding the correct pH when a bubble is present in the fluid inclusion also involves two "guesses", one for pH and one for P_{CO2} in the bubble. When a bubble is present, the relationship between vapor and liquid pressures must be:

(A.18) $P_{CO2} = P_{H2O}$

where P_{CO2} is used here for the bubble and P_{H2O} is used for the liquid. Solving the problem begins with assuming P_{CO2}, and calculating $m\mathrm{CO_2^a}$ using relations (A.7) and (A.2). "Guesses" at pH are then made, and $m\mathrm{H^+}$, $m\mathrm{OH^-}$, $m\mathrm{HCO_3^-}$ and $m\mathrm{CO_3^{-2}}$ are calculated from the pH using relations (A.3) and (A.4) until the ion charge balance is satisfied. The "molality" of the CO_2 in the bubble can be calculated using:

(A.19) $m\mathrm{CO_2^V} = m\mathrm{CO_2^{TN}} - m\mathrm{CO_2^a} - m\mathrm{HCO_3^-} - m\mathrm{CO_3^{-2}}$.

Calculation of P_{H2O} is made simpler by assuming that the inclusion has a volume of 1 cm^3. The nominal composition can be recalculated in terms of numbers of moles (n) of the various components. The number of moles of CO_2 in the bubble ($n\mathrm{CO_2^V}$) is calculated from:

(A.20) $n\mathrm{CO_2^V} = n\mathrm{H_2O}\ m\mathrm{CO_2^V} / (m\mathrm{CO_2^V} + m\mathrm{CO_2^a} + m\mathrm{HCO_3^-} + m\mathrm{CO_3^{-2}})$.

From P_{CO2} and the number of moles of CO_2 in the bubble, the bubble volume is calculated using the ideal gas law:

(A.21) $V_{CO2} = n\mathrm{CO_2^V}\ R\ T / P_{CO2}$

where V_{CO2} is the volume of the bubble, R is the ideal gas constant (= 83.14241bar • cm^3/K • mole) and T is in Kelvin. The pressure of the fluid phase (P_{H2O}) is calculated from the number of moles in the liquid ($n\mathrm{H_2O}+n\mathrm{CO_2}-n\mathrm{CO_2^V}$) and the liquid volume ($1-V_{CO2}$) using the ideal gas law (A.21). If

the calculated P_{H2O} does not equal the assumed P_{CO2} another P_{CO2} is chosen and the process is repeated.

The two procedures outlined above can be combined to find the pH of a fluid inclusion which contains both a bubble and a solid, but requires guesses for P_{CO2}, pH and $m\mathrm{Na}^+$. First, a P_{CO2} is assumed, and "guesses" for pH are made until the ion charge balance is satisfied. The presence of nahcolite permits $m\mathrm{Na}^+$ to be found from the mass action equation for equilibrium (A.8). Next, P_{H2O} is calculated, and if it does not equal the assumed P_{CO2} another P_{CO2} is chosen and the process is repeated until P_{CO2} equals P_{H2O}. Successive rounds of guesses for P_{CO2} and pH are made after recalculating a new Henry's Law constant from the last best estimate of $m\mathrm{Na}^+$.

The results of pH calculations for six fluid inclusion types are presented in Table 12. One set of PT conditions is the minimum trapping conditions (Th and Pmin) for the model fluid inclusions listed in Table 4. It is important to remember that 1) the nahcolite in a real fluid inclusion does not completely dissolve at Th, therefore, the temperature at which nahcolite precipitates is likely to be greater than the listed Th, and 2) the pressure at which bubbles form is certainly less than the listed Pmin. To address these concerns a second set of PT conditions was chosen on the isochores at 50 degrees higher than Th and a third set of PT conditions was chosen at Th but with a pressure of Pmin minus 500 bars. In some cases no numerical solution is possible for the given PT conditions and phase assemblage given the composition of the fluid inclusions.

The precipitation of nahcolite is associated with a significant decrease in pH in type IB, IC, ID and II fluid inclusions. There is no numerical solution for pH in type IA inclusions, which may be due to extrapolation of the thermodynamic data for nahcolite beyond reasonable limits. There is a *rise* in pH in type III inclusions associated with nahcolite precipitation. The major difference between type III inclusions and all the others is a lower $NaHCO_3$ concentration. Lowering the

Table 12. Estimated pH and SiO_2 solubility in fluid inclusions at selected PT conditions and phase assemblages. SiO_2^T= concentration of all Si species, mol= moles, ns= no numerical solution, L= liquid, S= solid nahcolite, V= vapor bubble, PCO_2= partial pressure of carbon dioxide.

type	phases	T (oC)	P (bars)	pH	SiO_2^T (mol/kg H2O)	PCO_2 (bars)
IA	L	501	6022	8.11	0.472	
	L-S	501	6022	ns	ns	
	L-V	501	6022	ns	ns	
	L-S-V	501	6022	ns	ns	
IA	L	451	5162	7.86	0.385	
	L-S	451	5162	ns	ns	
	L-V	451	5162	ns	ns	
	L-S-V	451	5162	ns	ns	
IA	L	451	4662	8.00	0.378	
	L-S	451	4662	ns	ns	
	L-V	451	4662	ns	ns	
	L-S-V	451	4662	ns	ns	
IB	L	389	4015	7.91	0.448	
	L-S	389	4015	7.87	0.300	
	L-V	389	4015	7.54	0.332	2528
	L-S-V	389	4015	7.58	0.247	2528
IB	L	339	3069	7.64	0.181	
	L-S	339	3069	7.41	0.083	
	L-V	339	3069	7.60	0.165	2337
	L-S-V	339	3069	7.33	0.079	2337
IB	L	339	2569	7.79	0.183	
	L-S	339	2569	7.46	0.067	
	L-V	339	2569	7.74	0.167	2337
	L-S-V	339	2569	7.38	0.064	2337
IC	L	292	3280	7.08	0.074	
	L-S	292	3280	7.01	0.052	
	L-V	292	3280	7.03	0.068	2271
	L-S-V	292	3280	6.92	0.048	2271
IC	L	242	2465	6.79	0.027	
	L-S	242	2465	6.50	0.016	
	L-V	242	2465	6.81	0.028	2070
	L-S-V	242	2465	6.60	0.016	2070
IC	L	242	1965	6.94	0.025	
	L-S	242	1965	6.57	0.014	
	L-V	242	1965	6.95	0.026	2070
	L-S-V	242	1965	6.68	0.014	2070

Table 12. (continued)

type	phases	T (oC)	P (bars)	pH	SiO_2^T (mol/kg H2O)	PCO_2 (bars)
ID	L	210	1413	6.35	0.0073	
	L-S	210	1413	6.52	0.0077	
	(L-V)	210	1413	6.28	0.0072	1920
	(L-S-V)	210	1413	6.30	0.0076	1920
ID	L	160	610	6.16	0.0029	
	L-S	160	610	6.10	0.0028	
	(L-V)	160	610	6.12	0.0029	1730
	(L-S-V)	160	610	5.96	0.0028	1730
ID	L	160	110	6.36	0.0025	
	L-S	160	110	6.21	0.0024	
	(L-V)	160	110	6.32	0.0025	1730
	(L-S-V)	160	110	6.07	0.0024	1730
II	L	221	2182	6.64	0.0167	
	L-S	221	2182	6.29	0.0107	
	L-V	221	2182	6.68	0.0175	1984
	L-S-V	221	2182	6.45	0.0110	1984
II	L	171	1759	6.30	0.0064	
	L-S	171	1759	5.78	0.0046	
	(L-V)	171	1759	6.37	0.0067	1783
	(L-S-V)	171	1759	6.06	0.0047	1783
II	L	171	1259	6.45	0.0057	
	L-S	171	1259	5.87	0.0040	
	(L-V)	171	1259	6.52	0.0061	1783
	(L-S-V)	171	1259	6.18	0.0040	1783
III	L	179	2234	5.62	0.0058	
	L-S	179	2234	ns	ns	
	L-V	179	2234	ns	ns	
	L-S-V	179	2234	ns	ns	
III	L	129	1033	5.58	0.0020	
	L-S	129	1033	5.78	0.0020	
	L-V	129	1033	ns	ns	
	L-S-V	129	1033	ns	ns	
III	L	129	533	5.78	0.0017	
	L-S	129	533	5.89	0.0017	
	L-V	129	533	ns	ns	
	L-S-V	129	533	ns	ns	

$NaHCO_3$ concentrations by very small amounts in the pH calculations for the other fluid inclusion types indicates that the pH drop will indeed be smaller for less $NaHCO_3$-rich compositions.

Solubility of Quartz

The solubility of quartz in water may be described by one or the other of the "equivalent" equilibria:

(A.22) $SiO_2 = SiO_2^a$

(A.23) $SiO_2 + 2H_2O = H_4SiO_4^a$

where the neutral aqueous species $H_4SiO_4^a$ is sometimes written as $Si(OH)_4^a$. Much experimental data for quartz solubility, particularly along the L-V saturation curve for water and for H_2O-NaCl solutions, has been available for a long time (e.g. papers reviewed in Crerar and Anderson, 1971). Recently, Manning (1994) investigated quartz solubility as a function of P and T over a wide range of conditions and formulated an expression for quartz solubility incorporating his data and that in the literature. The expression:

(A.24) $$\log K_{22} = 4.2620 - 5764.2 / T + 1.7513 \times 10^6 / T^2 - 2.2869 \times 10^8 / T^3 + \log \rho_{H2O}(2.8454 - 1006.9 / T + 3.5689 \times 10^5 / T^2)$$

where T is in Kelvin and ρ_{H2O} is the density of water, should only be used when solution pH is less than 8 and SiO_2^a is the dominant aqueous species.

In contrast, the pH dependence of quartz solubility is not well understood. It is generally assumed that the hydrated (aqueous) silica species is $SiO_2 \cdot 2H_2O$, however, there are other points of view. For example, Walther and Orville (1983) argue for a hydration number of 4 not 2. Busey and Mesmer (1977) cite studies that identify polynuclear anionic species such as $Si_4(OH)_{18}^{-2}$, with hydration numbers above 2, that form in concentrated solutions.

The thermodynamic database in SUPCRT92 employs a hydration number of 1. In order to use SUPCRT92 to calculate the variation in quartz solubility with changing pH the equilibria:

(A.25) $H_2O + SiO_2^a = H^+ + HSiO_3^-$

(A.26) $NaHSiO_3^a = Na^+ + HSiO_3^-$

must be used with equilibrium (A.22). Since NaOH is used to attain high solution pH in most experimental systems, Walther and Helgeson (1977) believe that $NaHSiO_3^a$ is necessarily a significant Si species at high pH.

Seward (1974) used borax ($Na_2B_4O_7 \cdot 10H_2O$) to buffer his experiments and recognized the formation of $NaH_3O_4^a$ in his calculations of the first dissociation constant (K) of silicic acid. The K value for the equilibrium (Seward uses a hydration number of 2):

(A.27) $H_4SiO_4 = H^+ + H_3SiO_4^-$

can be calculated from Seward's equation:

(A.28) $-\log K_{27} = 6.372 + 0.054t - 4.072 \times 10^{-4} t^2 + 1.264 \times 10^{-6} t^3 - 1.293 \times 10^{-9} t^4$

where t is temperature in Celcius.

Busey and Mesmer (1977) used NaOH to buffer their experiments on silicic acid dissociation in the system H_2O-SiO_2-NaCl and found no definitive evidence for the formation of an aqueous Na-Si species. The K value for the equilibrium (they also use a hydration number of 2):

(A.29) $Si(OH)_4^a + OH^- = SiO(OH)_3^- + H_2O$

can be calculated from a complicated equation involving ionic strength, the osmotic coefficient for sodium chloride solutions and a Pitzer function. Busey and Mesmer also cite Raman evidence from other studies for the existence of a second dissociation species, $SiO_2(OH)_2^{-2}$. It must form by:

(A.30) $SiO(OH)_3^- + OH^- = SiO_2(OH)_2^{-2} + H_2O$

but was not identified in their experiments due to its extremely low concentrations, even in silica saturated solutions at the highest pH. It is useful to note that $SiO(OH)_3^-$ and $SiO_2(OH)_2^{-2}$ are equivalent to $H_3SiO_4^-$ and $H_2SiO_4^{-2}$.

It is apparent that only two aqueous Si species are generally recognized in the geochemical literature and that the solubility of quartz at high pH must take both of them into account. Seward's equation is only valid for vapor saturated systems, whereas the model in SUPCRT92 can be applied to a large range of pressure and temperature conditions. A crude comparison of the two models can be made by calculating quartz solubility with SUPCRT92 along the L-V curve for pure H_2O at various values of solution pH.

The solubility of quartz at high pH can be modeled with SUPCRT92 using relations (A.22) and (A.25). Only one of the relations is dependent upon pH so the calculation of total SiO_2 in solution is straight forward:

(A.31) $$m SiO_2^a = K_{22} ,$$

(A.32) $$m HSiO_3^- = K_{25}\, m SiO_2^a / m H^+$$

(A.33) $$m SiO_2^T = m SiO_2^a + m HSiO_3^-$$

where SiO_2^T is the total silica in solution. Similarly, the solubility of quartz can be modeled using equilibria (A.23) and (A.27) and an analogous set of equations:

(A.34) $$m H_4SiO_4^a = K_{23}$$

(A.35) $$m H_3SiO_4^- = K_{27}\ m H_4SiO_4^a / m H^+$$

(A.36) $$m SiO_2^T = m H_4SiO_4^a + m H_3SiO_4^-$$

and the results compared to those generated by SUPCRT92. There is very little difference between the two methods of calculating quartz solubility at temperatures above 125°C, as shown in Figure 40. Therefore, the SUPCRT92 model is used in further calculations.

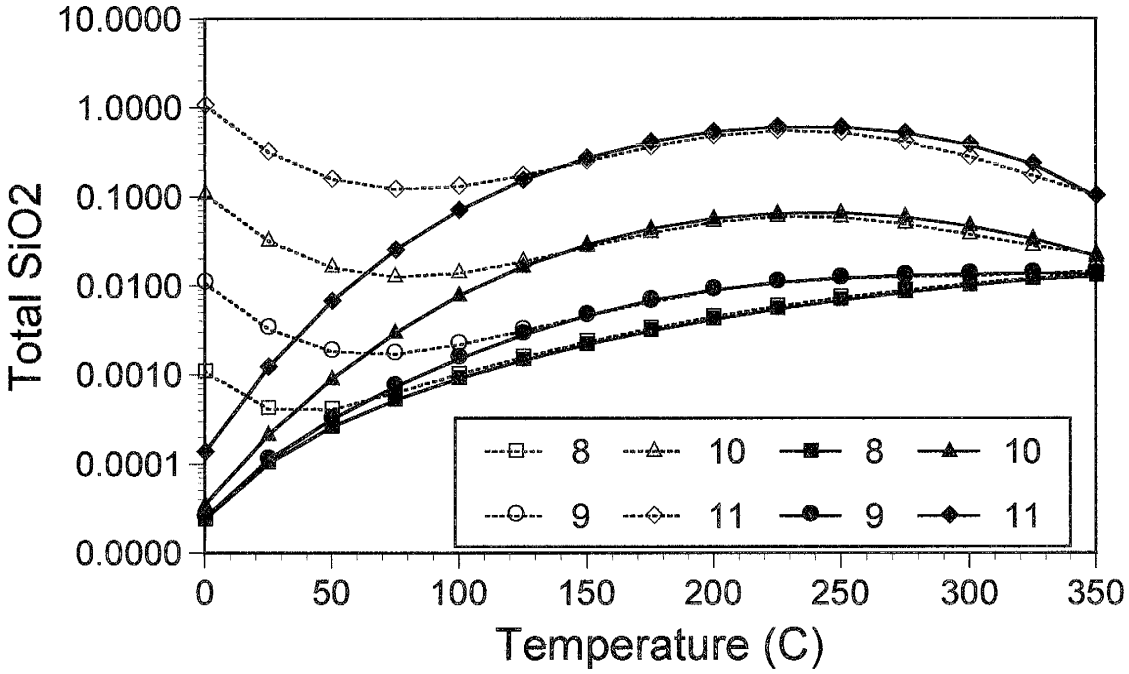

Figure 40. The solubility of quartz along the L-V curve for water at different solution pH. Data points along dotted lines were generated using the equations of Manning (1994) and Seward (1974). Data points along solid lines were generated using SUPCRT92.

The results of quartz solubility calculations at various pressures, temperatures and solution pH using SUPCRT92, made without correction for activities, are shown in Figure 41. Changes in quartz solubility with variations in solution pH are more pronounced at lower temperatures. At solution pH greater than 8 units SUPCRT92 predicts that quartz solubility *decreases* with increasing temperatures above 400°C at metamorphic pressures. Increasing pressure tends to increase quartz solubility at any given pH.

pH in the System H_2O-CO_2-$NaHCO_3$-NaCl-SiO_2

The pressures, temperatures, fluid compositions and pH conditions which were addressed previously in Table 12 were used to calculate quartz solubility in the different types of fluid inclusions. The calculations involve adding relations (A.22), (A.25) and (A.26) into the algorithm for three additional unknowns, $m SiO_2^a$, $m HSiO_3^-$ and $m NaHSiO_3^a$, and adding $m HSiO_3^-$ to the charge balance equations. The pH changes caused by nahcolite precipitation are sufficient to precipitate quartz as shown in the table.

Summary Points

The solubility of nahcolite *increases* with a rise in P_{CO2}. This is due to a drop in solution pH. The solubility of nahcolite also increases with a rise in temperature. Bubbles cannot form in the bicarbonate-rich fluid inclusions at PT conditions along an isochore. Nahcolite precipitation and falling temperatures create significant decreases in pH inside the fluid inclusions.

Quartz solubility is much higher in more alkaline (high pH) fluids. On the water L-V curve at pH greater than 9 there is a maximum in quartz solubility at 250°C. At successively higher pressures the quartz solubility maximum shifts to increasingly higher temperatures. The drop in pH caused by nahcolite precipitation is sufficient to precipitate quartz.

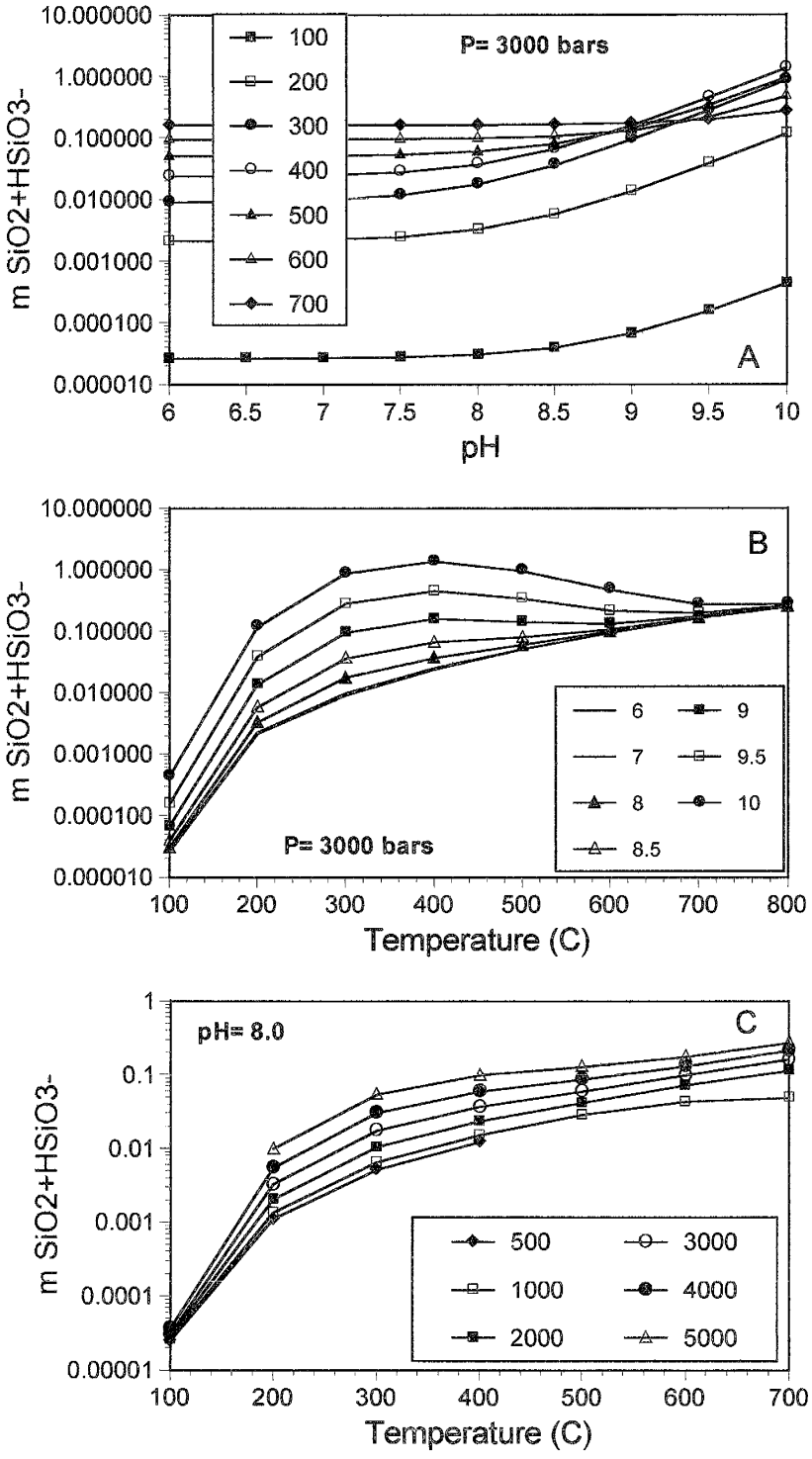

Figure 41. The solubility of quartz as calculated using SUPCRT92. A) At 3000 bars and various temperatures. B) At 3000 bars and various pH. C) At pH=8.0 and various pressures.

Appendix B

Figures 42 through 47 are photographs of the petrographic sections of the six metaporphyry samples examined in this study. The sections are about 3 by 2 cm in length and width, and 200 μm in thickness. Foliation and the shape preferred fabric of some relic phenocrysts can be seen. The foliations do not line up with the edges of the sections. "North" on the sections is pointing toward the top of the page.

Figures 48 through 52 are sketches of the relic phenocrysts. Each phenocryst was assigned a number for identification purposes. The relative spacing and position between phenocrysts is altered to fit the diagram. The orientation of each phenocryst with respect to the principal foliation (left-right) is shown. "North" in the sections does not correspond to the top of the sketches. The scale of the sketches is uniform between frames.

Figure 53 provides evidence for the shape preferred fabric of relic phenocrysts in the various samples. Figures 54 through 56 illustrate features developed by recrystallization of the phenocrysts. The preferred orientation of transposed FIP and type III FIP are shown in Figures 57 and 58.

Figures 59 through 64 are the orienation data for FIP addressed in this study. All the stereograms are equal angle, lower hemisphere projections. "North" on the stereograms corresponds to "north" in the petrographic sections. FIP traces are color coded as follows: purple= transposed FIP; green= type IB or IC; black= type ID; blue= type II; red= type III. Dotted black lines are traces of open microcracks.

Figure 42. Photograph of the petrographic section for sample HÖK from the lower amphibolite facies area. The field of view is 3 cm.

Figure 43. Photograph of the petrographic section for sample SINS from the lower amphibolite facies area. The field of view is 3 cm.

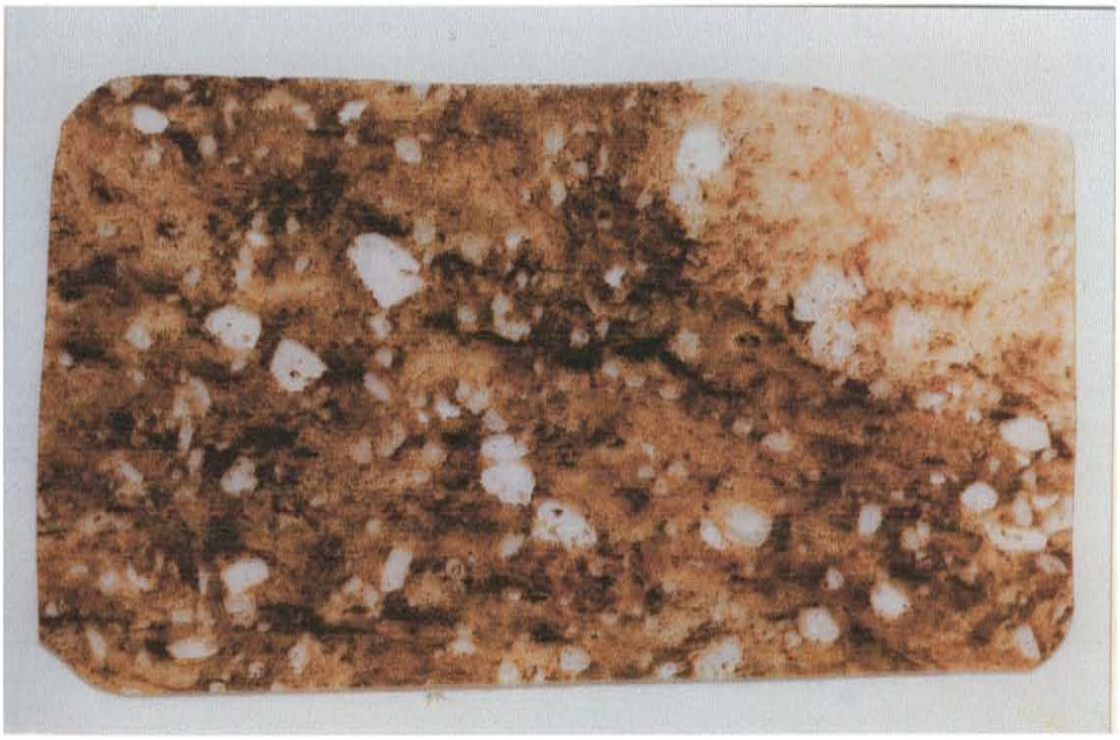

Figure 44. Photograph of the petrographic section for sample DBH from the middle amphibolite facies area. The field of view is 3 cm.

Figure 45. Photograph of the petrographic section for sample 4Z from the middle amphibolite facies area. The field of view is 3 cm.

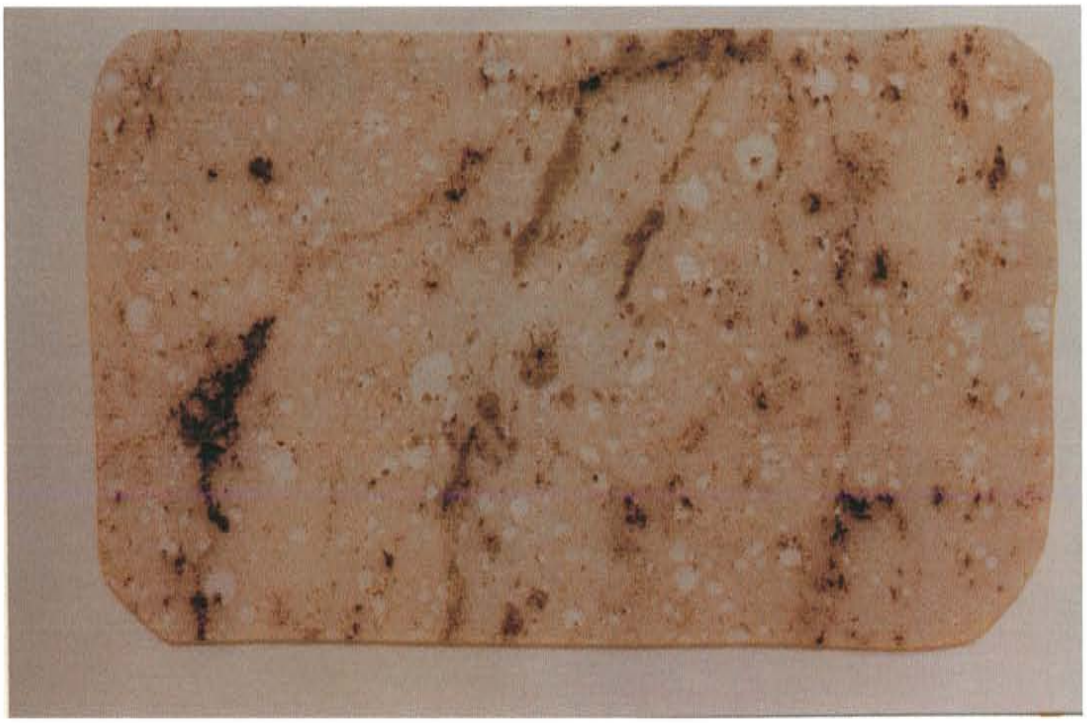

Figure 46. Photograph of the petrographic section for sample 98 from the upper amphibolite facies area. The field of view is 3 cm.

Figure 47. Photograph of the petrographic section for sample 103 from the upper amphibolite facies area. The field of view is 3 cm.

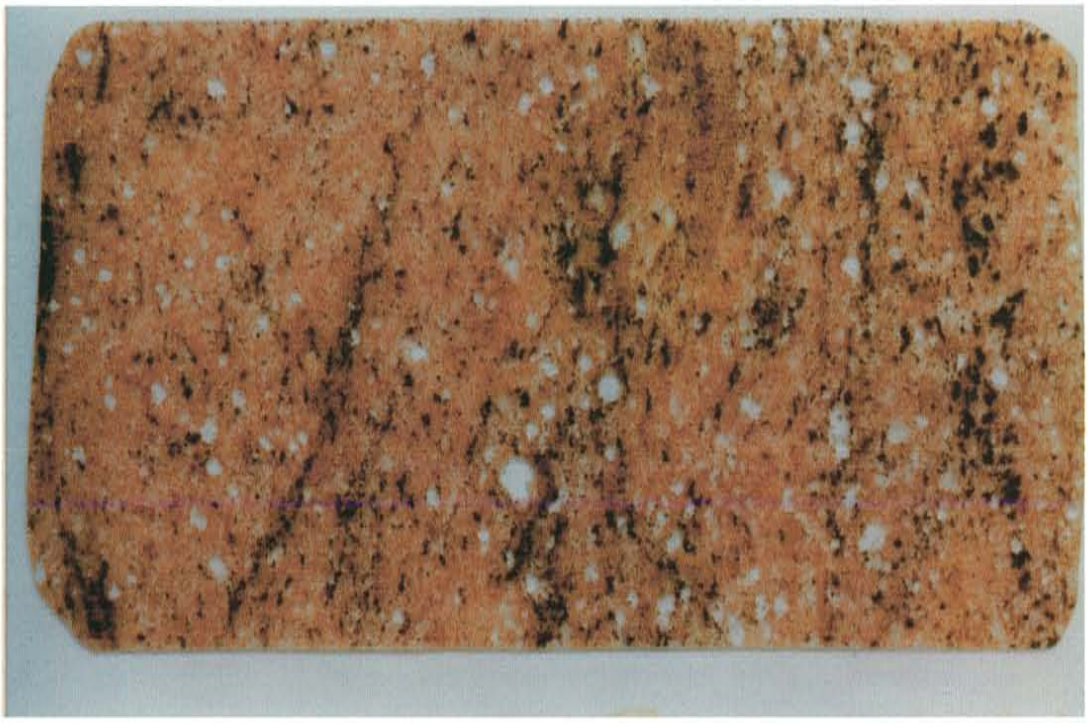

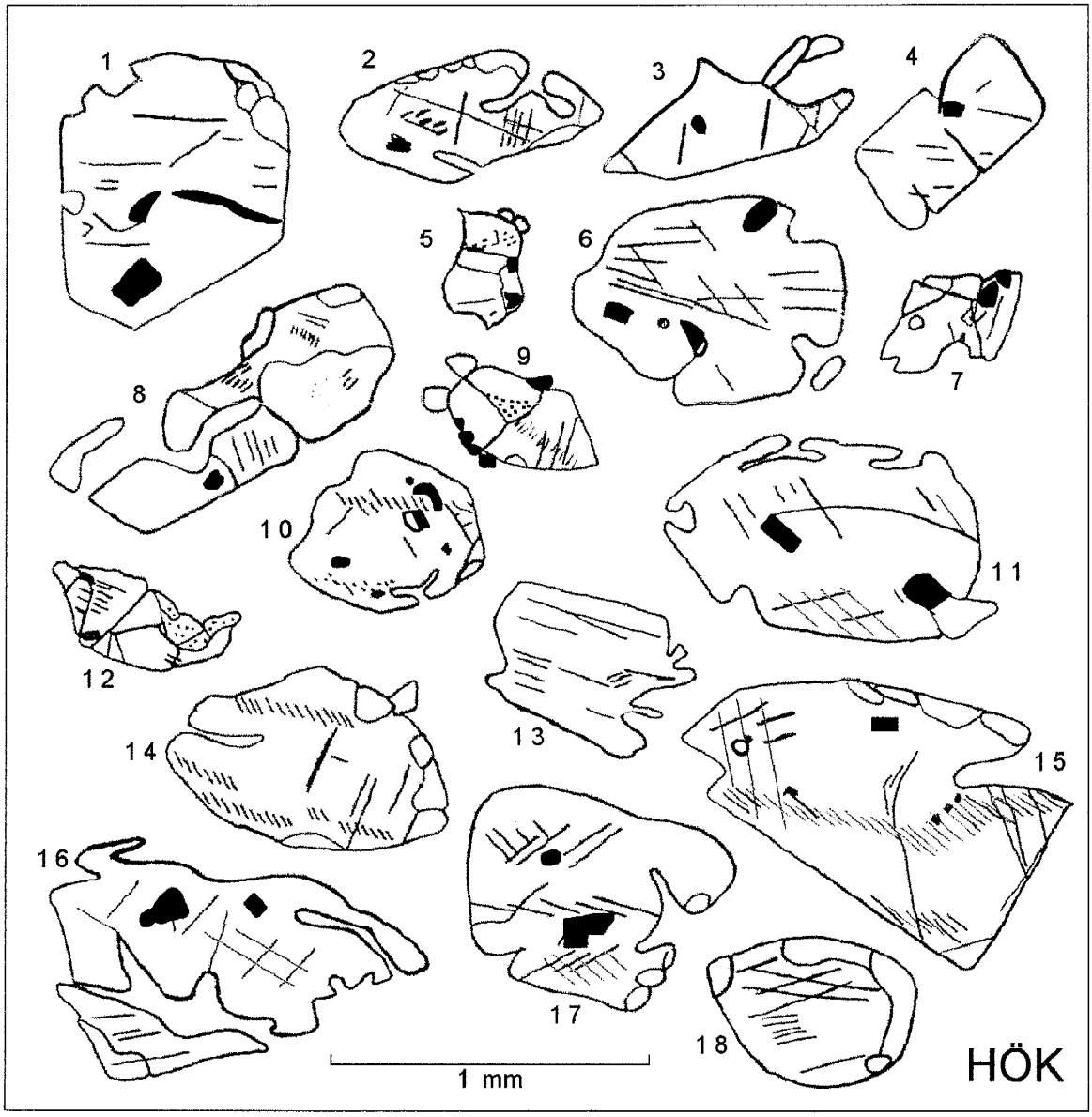

Figure 48. Recrystallization of phenocrysts in the lower amphibolite grade sample HÖK. Shaded areas are unrecrystallized quartz. White areas are recrystallized quartz grains. Solid areas are mineral inclusions. Short straight lines are FIP. Feathery bands are transposed FIP. Dots indicate the distribution of mobilized fluid inclusions.

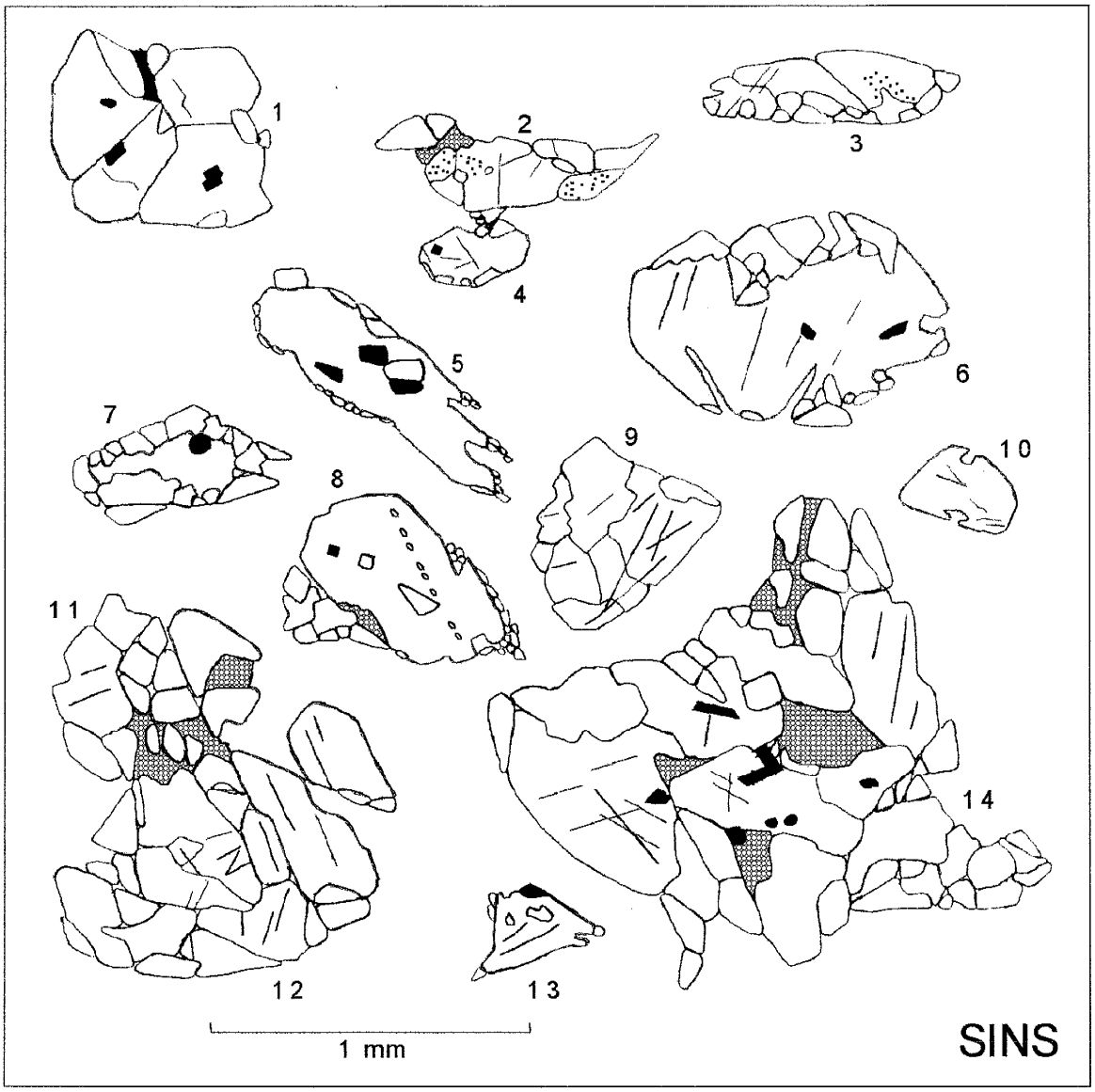

Figure 49. Recrystallization of phenocrysts in the lower amphibolite grade sample SINS. Shaded areas are unrecrystallized quartz. White areas are recrystallized quartz grains. Patterned areas are finely recrystallized quartz. Solid areas are mineral inclusions. Short straight lines are FIP. Dots indicate the distribution of mobilized fluid inclusions.

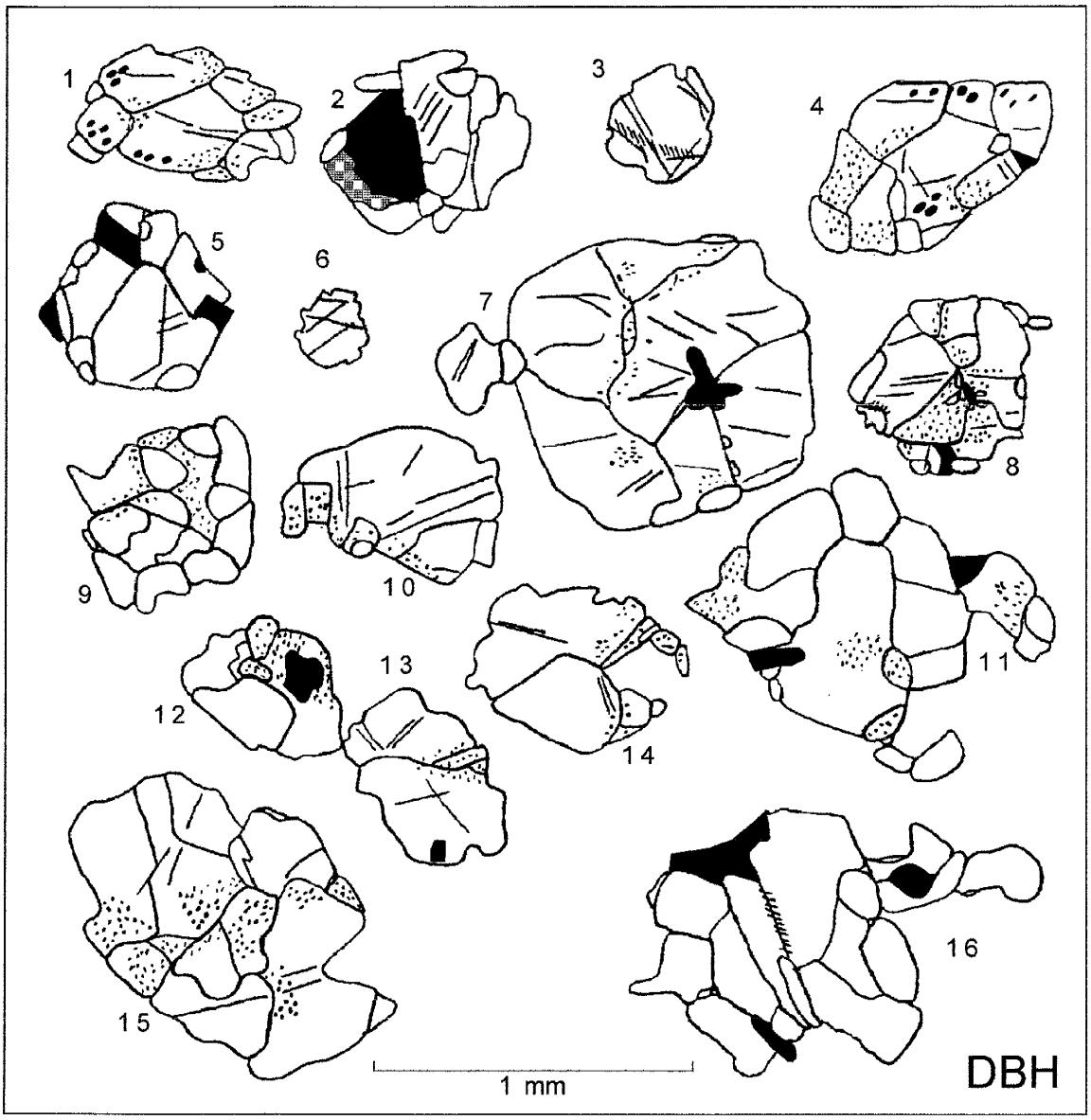

Figure 50. Recrystallization of phenocrysts in the middle amphibolite grade sample DBH. Shaded areas are unrecrystallized quartz. White areas are recrystallized quartz grains. Patterned areas are finely recrystallized quartz. Solid areas are mineral inclusions. Short straight lines are FIP. Feathery bands are transposed FIP. Dots indicate the distribution of mobilized fluid inclusions.

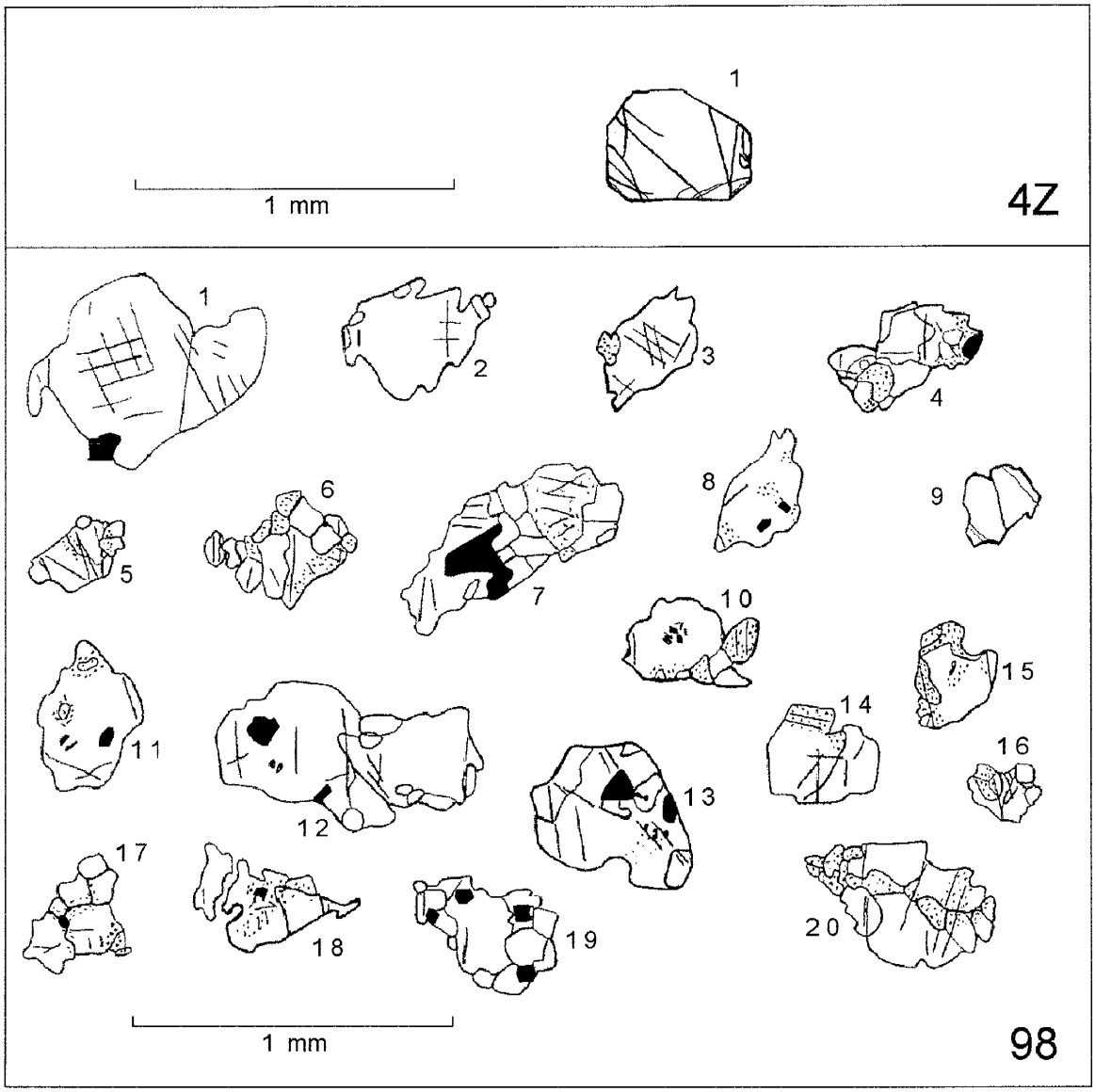

Figure 51. Recrystallization of phenocrysts in the upper amphibolite grade sample 98. Shaded areas are unrecrystallized quartz. White areas are recrystallized quartz grains. Solid areas are mineral inclusions. Short straight lines are FIP. Dots indicate the distribution of mobilized fluid inclusions. Middle amphibolite grade sample 4Z has only one phenocryst, included here.

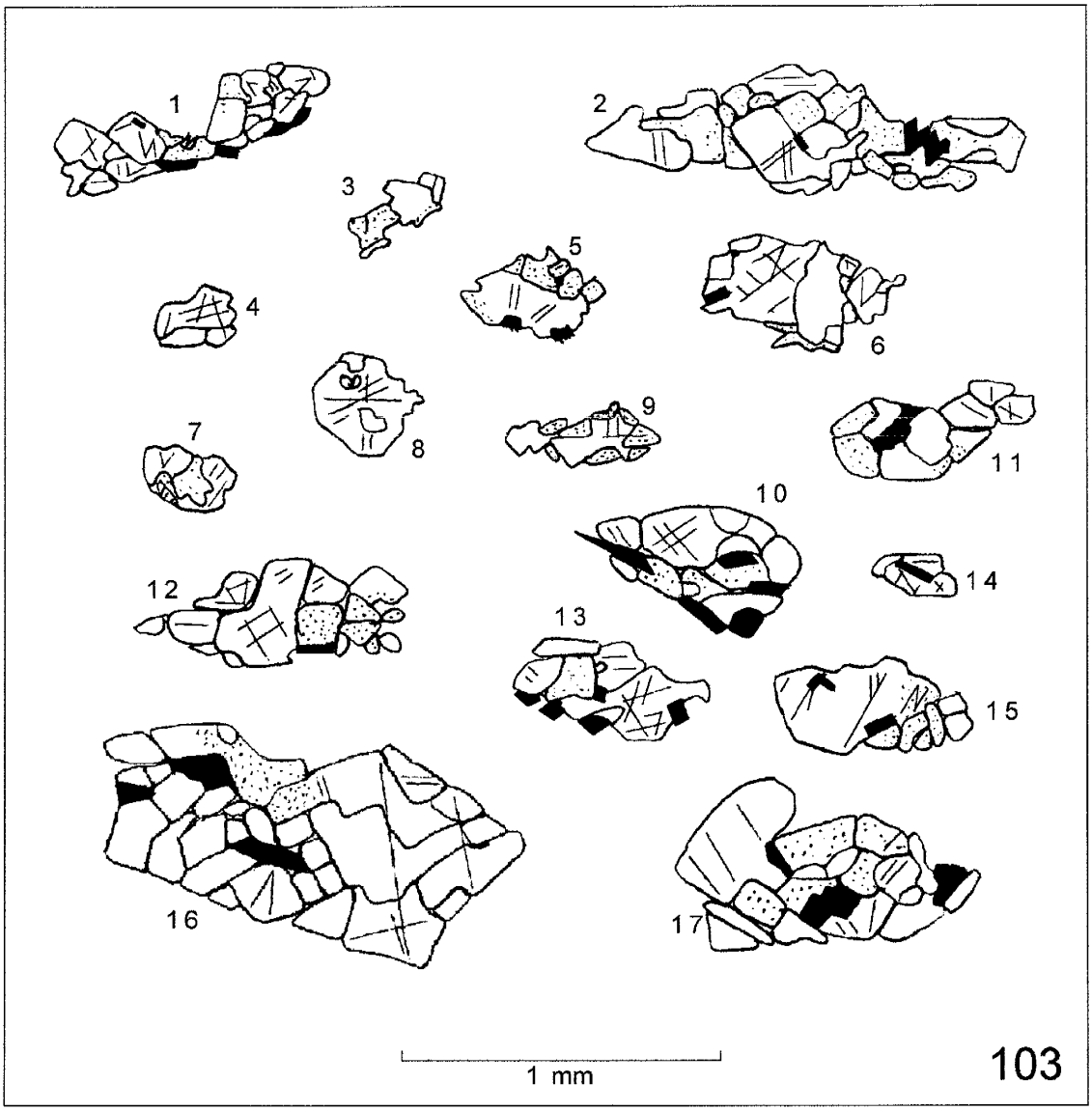

Figure 52. Recrystallization of phenocrysts in the upper amphibolite grade sample 103. Shaded areas are unrecrystallized quartz. White areas are recrystallized quartz grains. Solid areas are mineral inclusions. Short straight lines are FIP. Dots indicate the distribution of mobilized fluid inclusions.

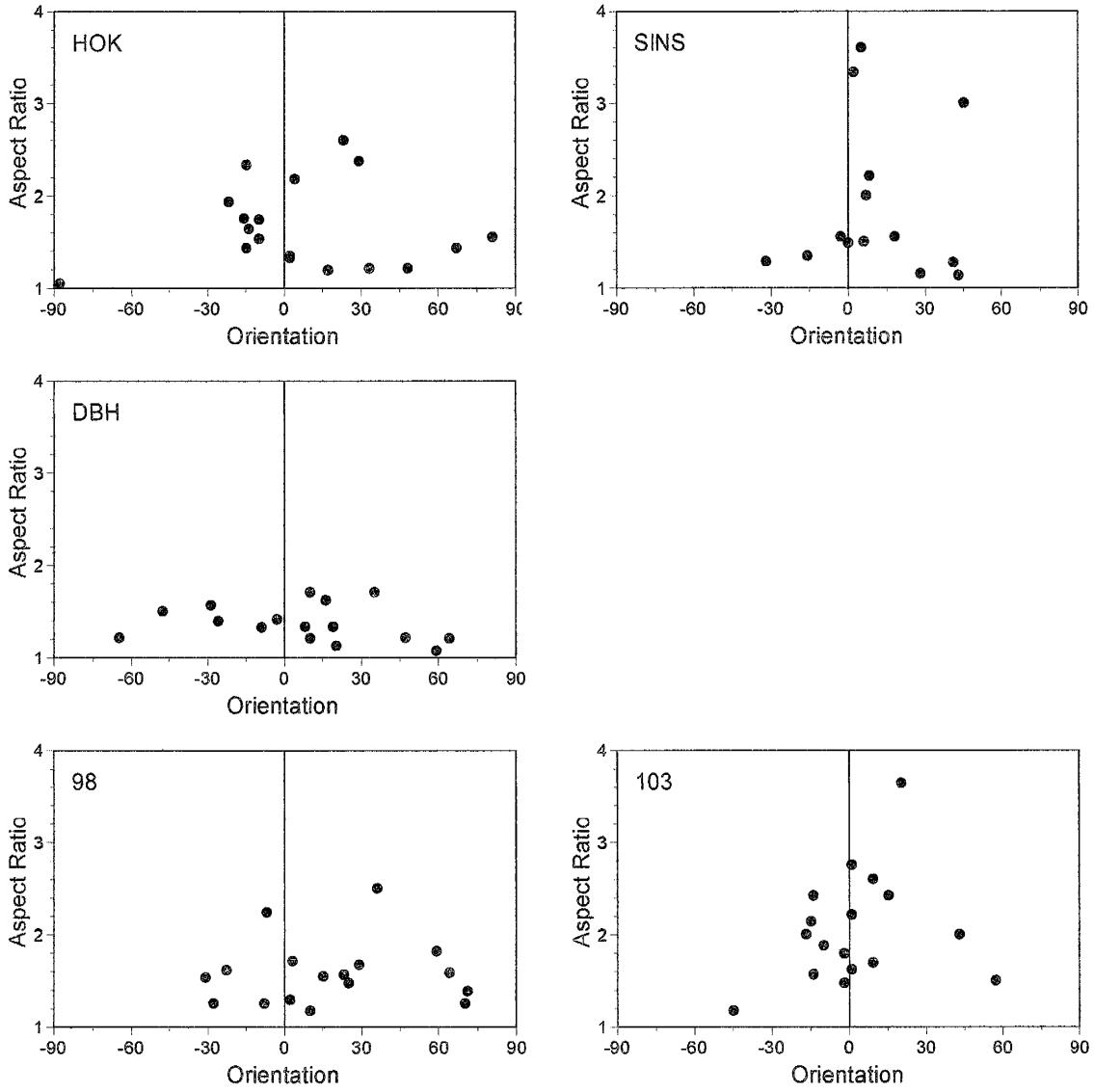

Figure 53. Plots of phenocryst aspect ratio (length/width) versus phenocryst orientation suggest that longer, narrower phenocrysts are more likely to be aligned with the foliation in the matrix (e.g. 103) than are shorter, fatter phenocrysts (e.g. DBH).

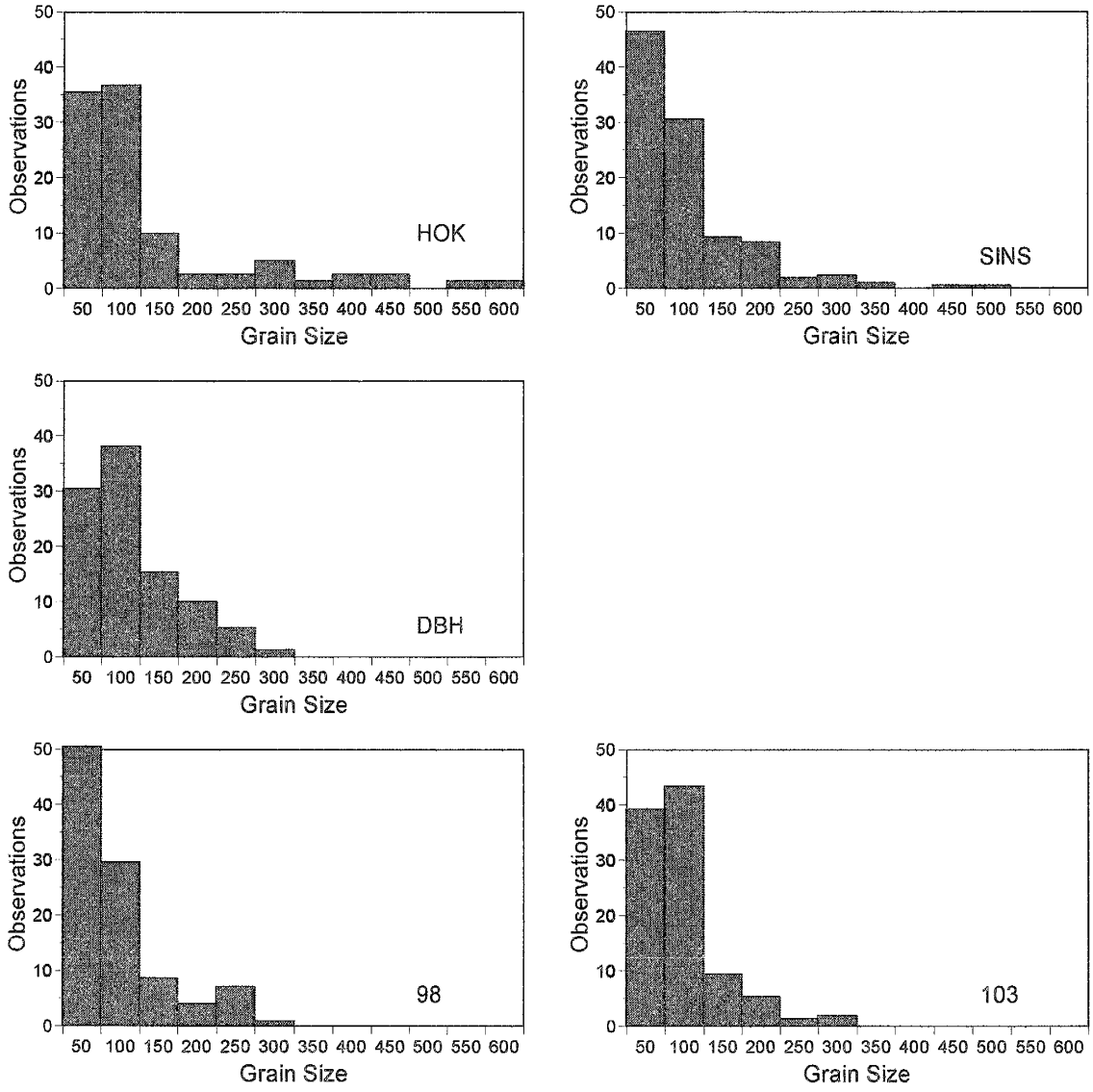

Figure 54. Size distribution of quartz grains in phenocrysts at various metamorphic grades. Lower amphibolite grade, HÖK and SINS; middle amphibolite grade, DBH; upper amphibolite grade, 98 and 103. Grain size is in μm.

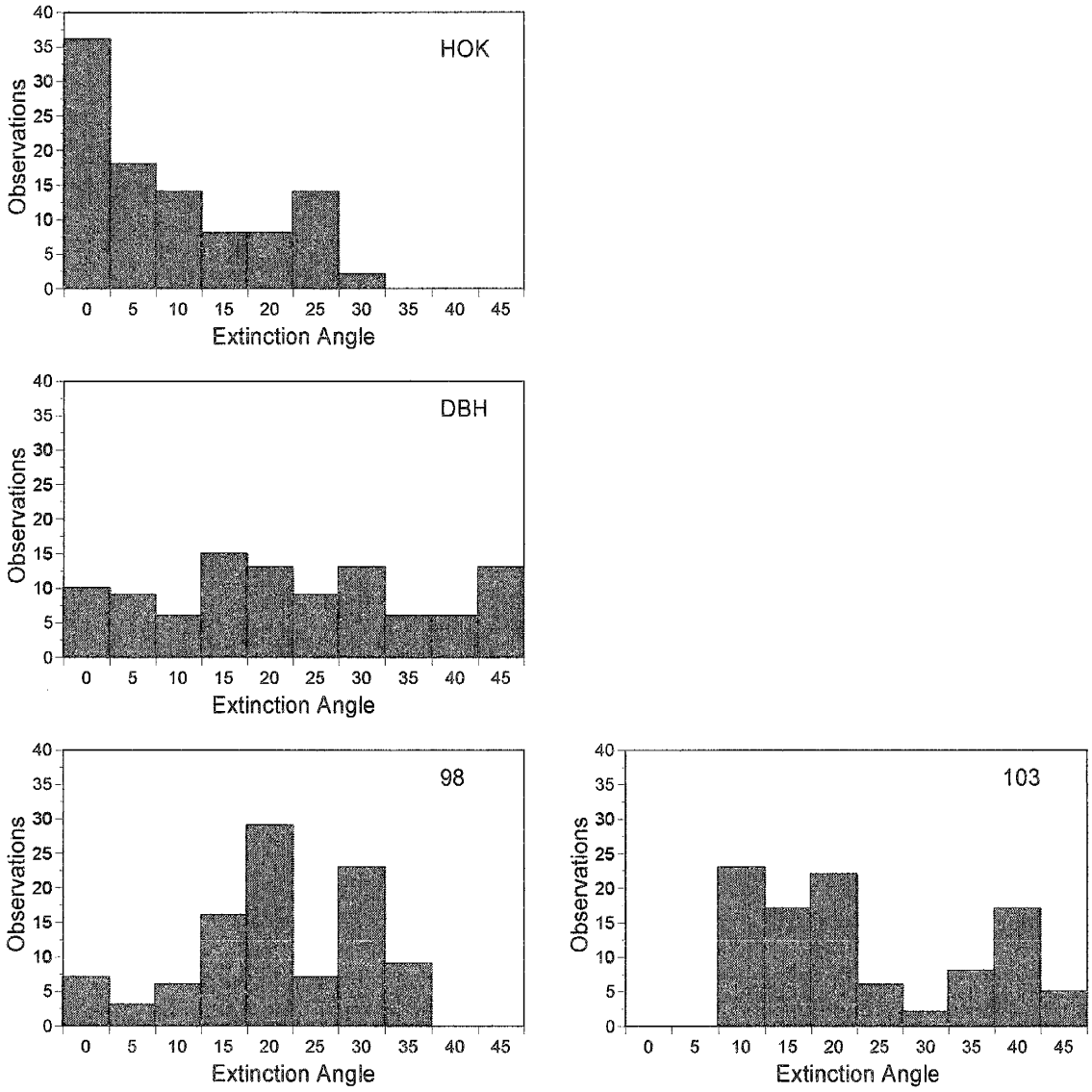

Figure 55. Differences in grain orientation are approximated by differences in extinction angle observed upon rotation of the microscope stage. Measurements in degrees are made relative to the orientation of extinction in the largest quartz grain in a given phenocryst.

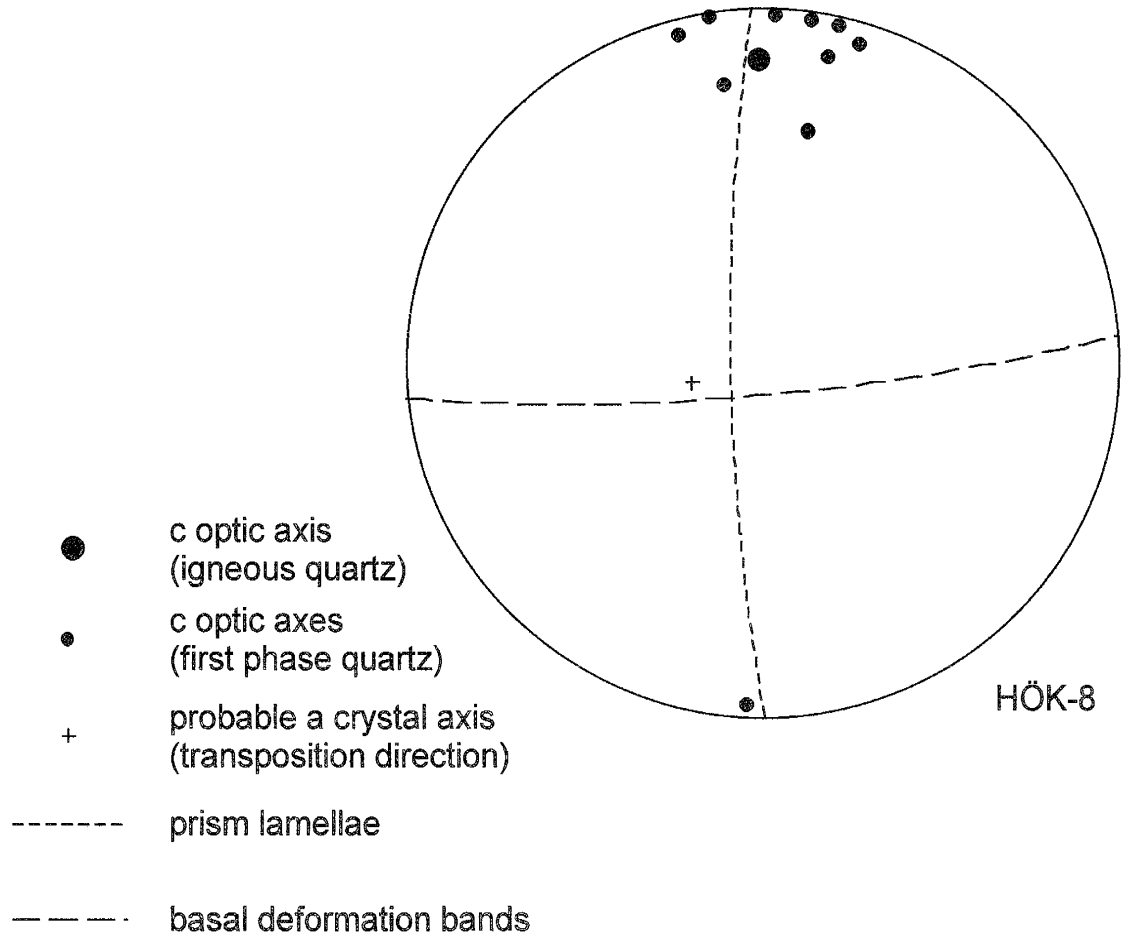

Figure 56. Preferred orientation of quartz c axes in newly recrystallized grains of one phenocryst from the lower amphibolite sample, HÖK. The diagram is a lower hemisphere stereographic projection. Lines are traces of lamellae and deformation bands. Symbols are poles to optic axes.

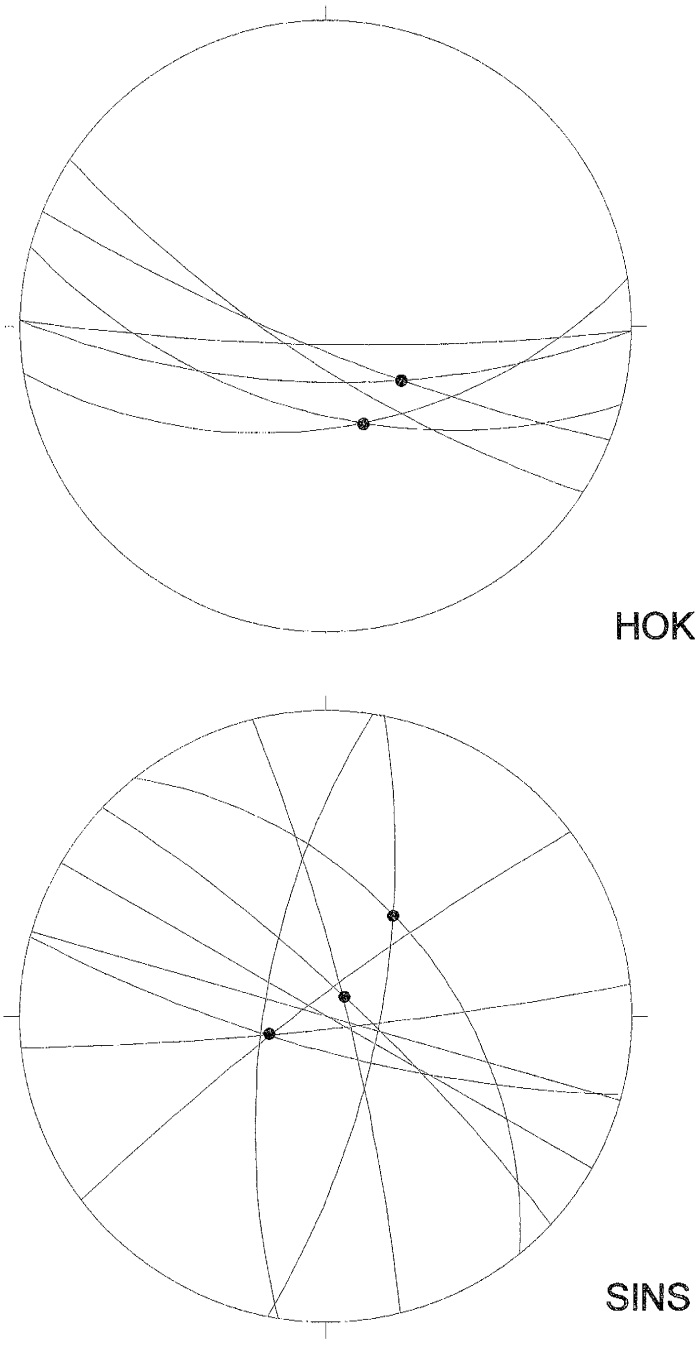

Figure 57. Preferred orientation of deformation bands is seen only in the lowest metamorphic grade sample, HÖK. The diagrams are lower hemisphere stereographic projections. Lines are traces of deformation band boundary planes. Dots are poles to linear groups of transposed fluid inclusions.

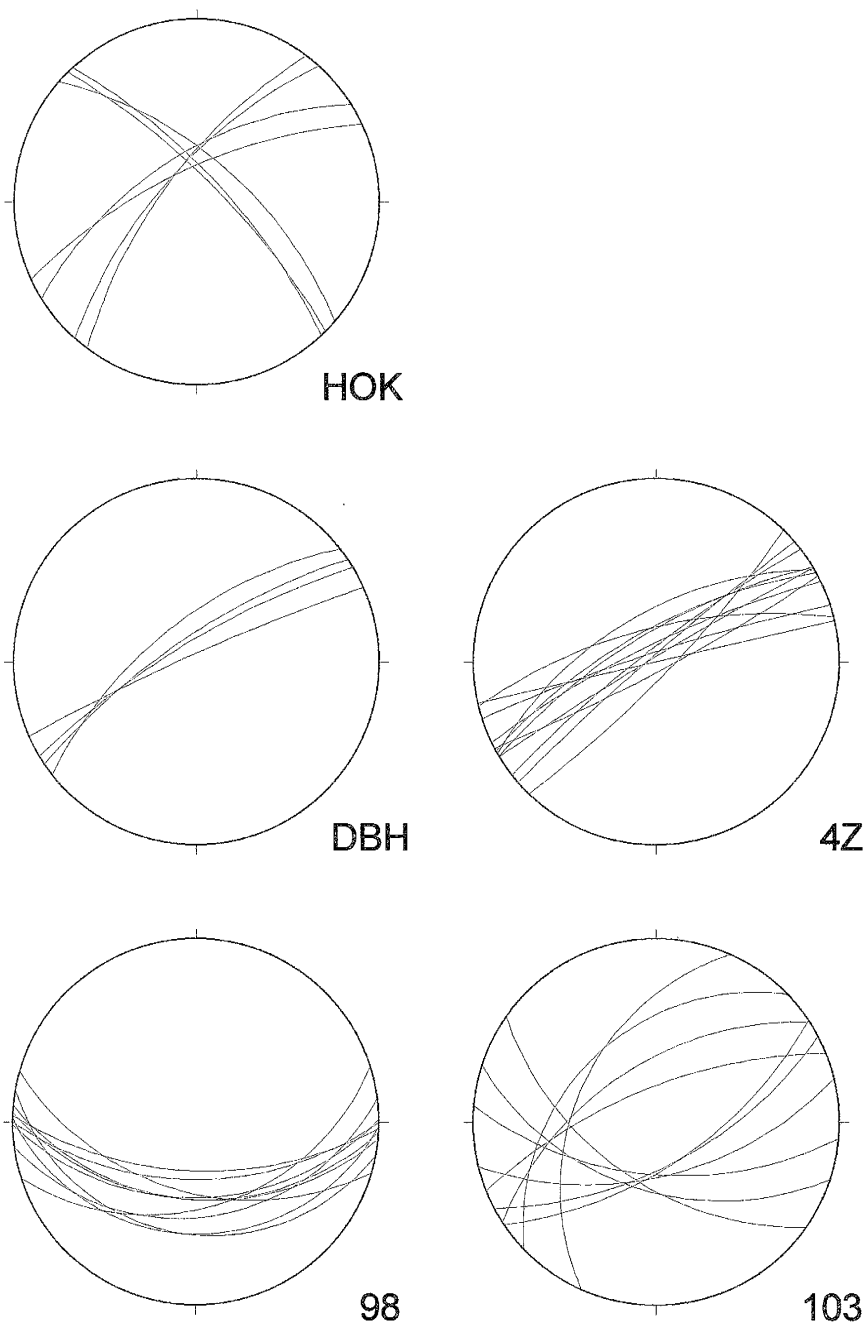

Figure 58. The preferred orientation of type III FIP in various samples.

Figure 59. The traces of FIP from sample HÖK are plotted on lower hemisphere equal area stereograms. Purple traces are transposed FIP, black traces are postrecrystalliztion FIP (type ID), and red traces are type III postrecrystallization FIP. Dotted black lines are open microcracks.

a) HÖK-1, b) HÖK-2, c) HÖK-3, d) HÖK-4, e) HÖK-5, f) HÖK-6, g) HÖK-7, h) HÖK-8, i) HÖK-9, j) HÖK-10, k) HÖK-11, l) HÖK-12, m) HÖK-13.

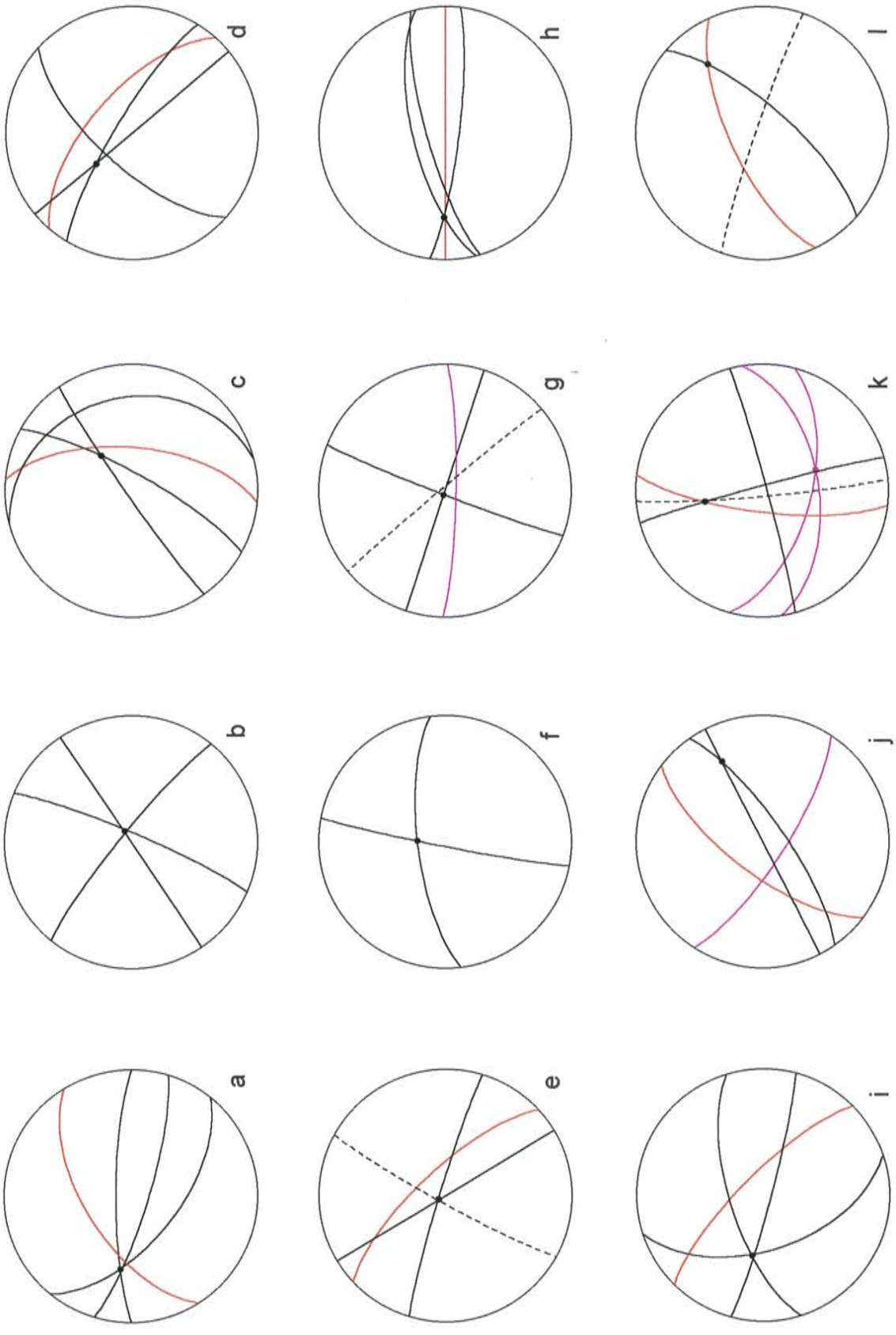
d
h
l
c
g
k
b
f
j
a
e
i

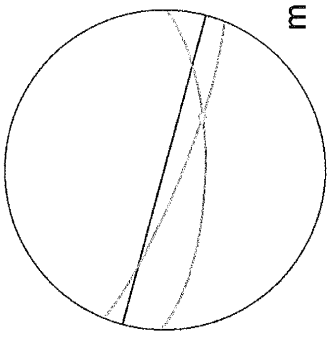
m

Figure 60. The traces of FIP from sample SINS are plotted on lower hemisphere equal area stereograms. Purple traces are transposed FIP, blue traces are type IB FIP, green traces are type IC FIP, black traces are type ID FIP, and red traces are type III FIP. Dotted black lines are open microcracks.

a) SINS-1, b) SINS-2, c) SINS-3, d) SINS-4, e) SINS-5, f) SINS-6, g) SINS-7, h) SINS-8, i) SINS-9, j) SINS-10, k) SINS-11, l) SINS-12a, m) SINS-12b, n) SINS-13, o) SINS-14a, p) SINS-14b.

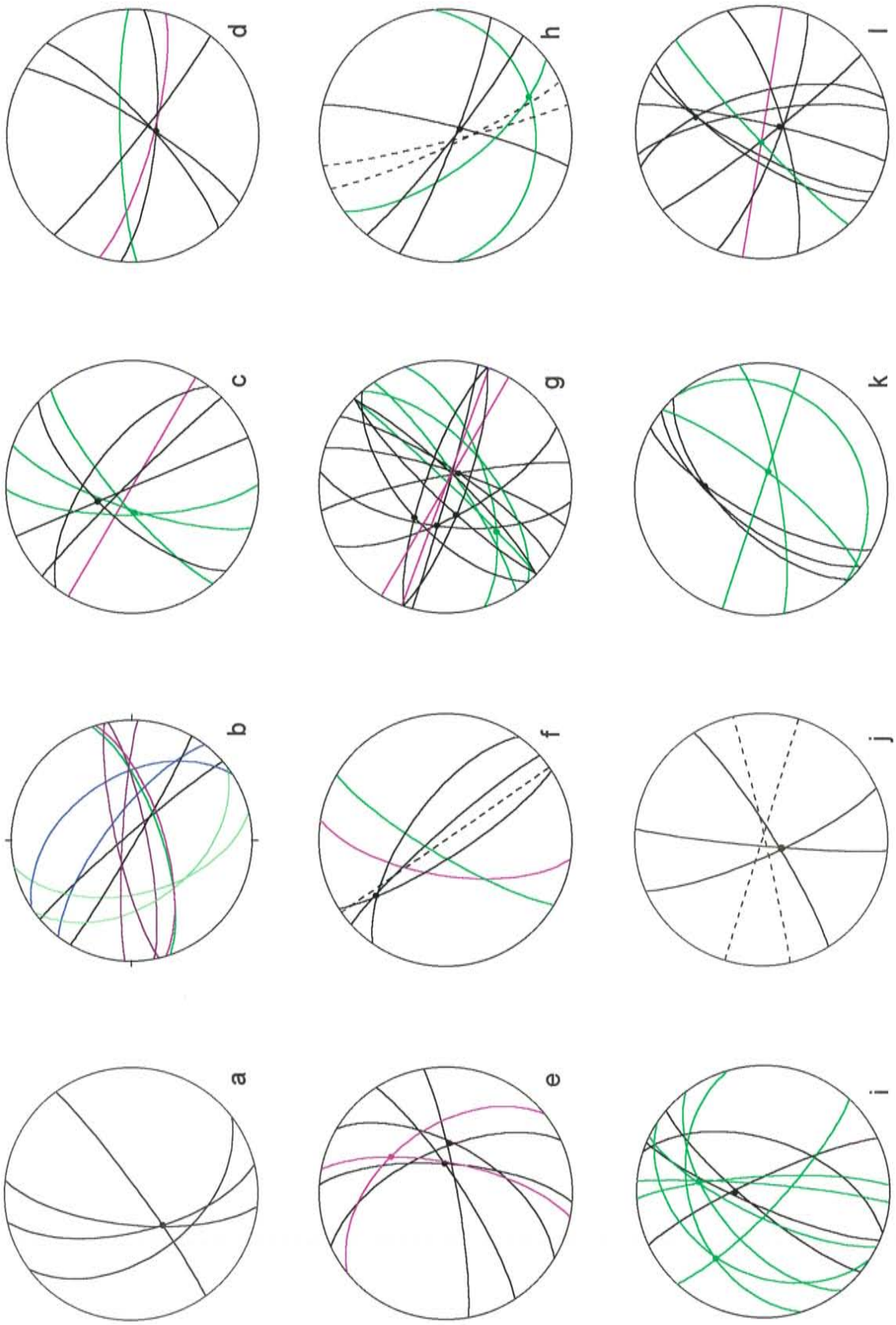
a
b
c
d
e
f
g
h
i
j
k
l

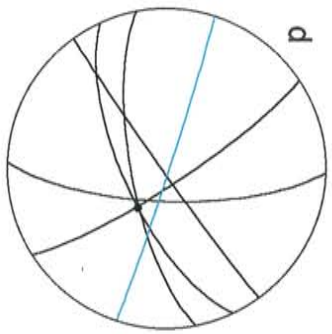
p

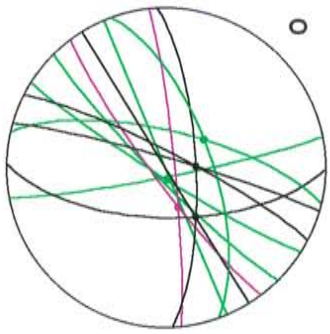
o

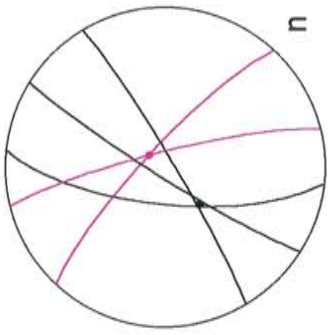
n

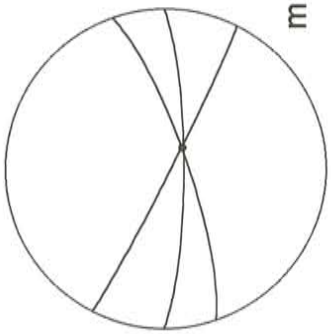
m

Figure 61. The traces of FIP from sample DBH are plotted on lower hemisphere equal area stereograms. Blue traces are type IB FIP, green traces are type IC FIP, black traces are type ID and II FIP, and red traces are type III FIP. Dotted black lines are open microcracks.

a) DBH-1, b) DBH-2, c) DBH-3, d) DBH-4, e) DBH-5, f) DBH-7, g) DBH-8, h) DBH-10, i) DBH-12, j) DBH-13, k) DBH-14, l) DBH-15, m) DBH-16.

d
h
l
c
g
k
b
f
j
a
e
i

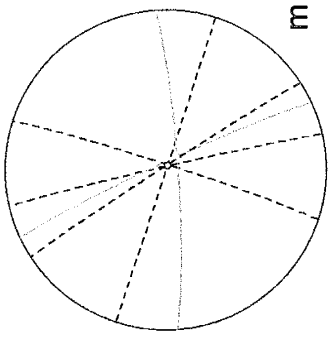
m

Figure 62. The traces of FIP from sample 4Z are plotted on lower hemisphere equal area stereograms. The vein has four segments labelled a, b, c and d. Each segment was subdivided into numbered domains consisting of 5-10 quartz grains. Blue traces are type IB FIP, green traces are type IC FIP, black traces are type ID and II FIP, and red traces are type III FIP. Dotted black lines are open microcracks.

a) 4Z-a1, b) 4Z-a2, c) 4Z-a3, d) 4Z-a4, e) 4Z-b1, f) 4Z-b2, g) 4Z-b3, h) 4Z-b4, i) 4Z-c1, j) 4Z-c2, k) 4Z-c3, l) 4Z-c4, m) 4Z-d1, n) 4Z-d2, o) 4Z-d3, p) 4Z-d4, q) 4Z-d5, r) 4Z-d6.

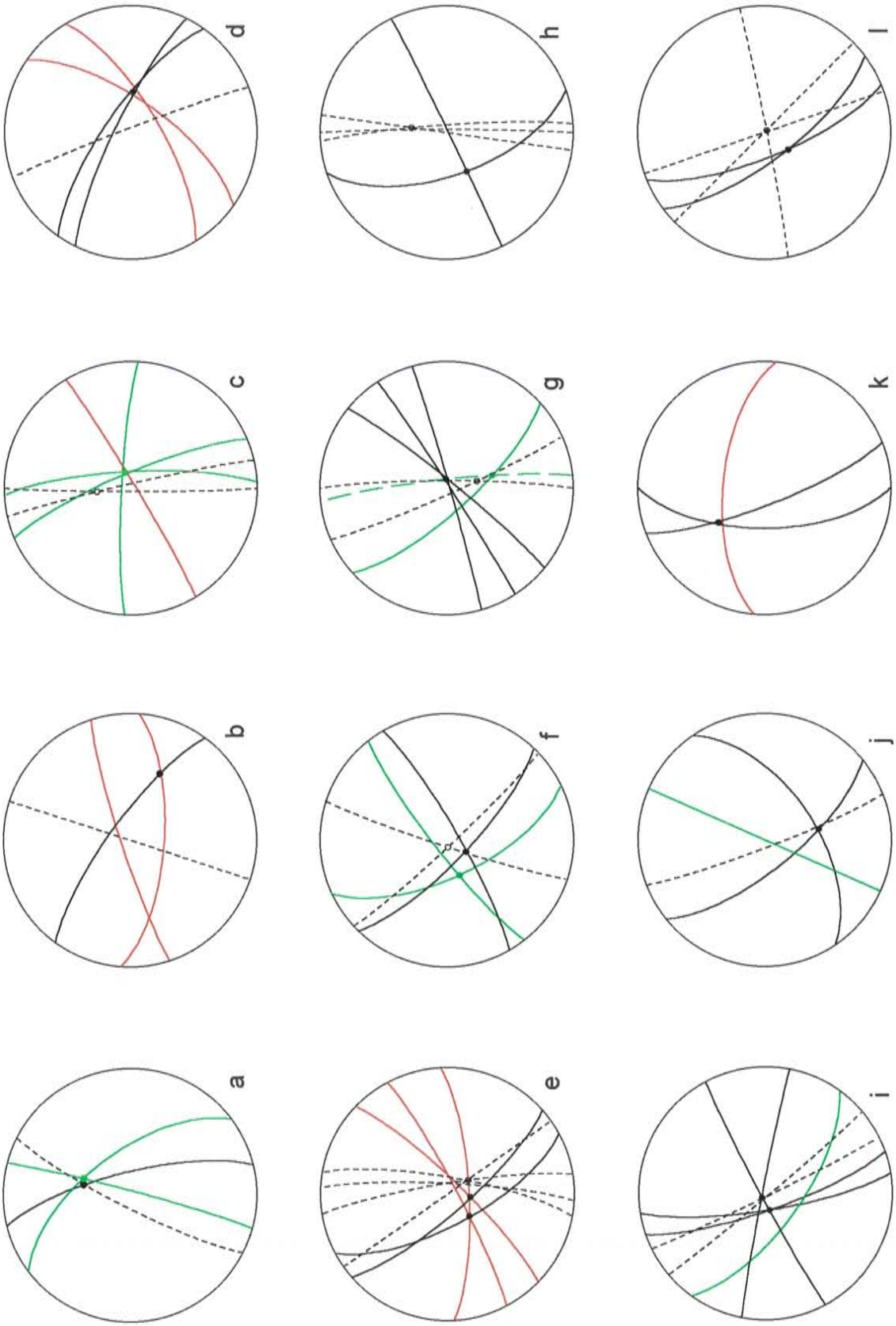
d
h
l
c
g
k
b
f
j
a
e
i

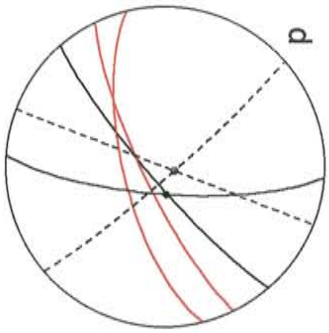
p

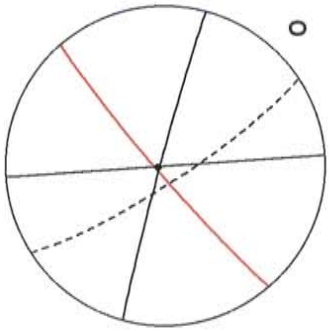
o

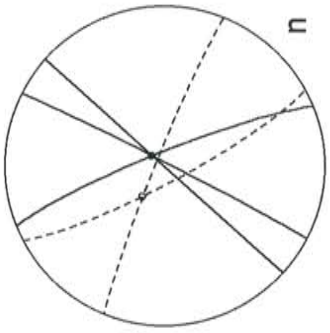
n

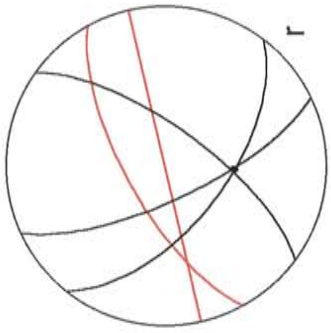
r

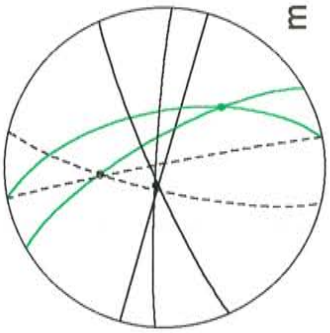
m

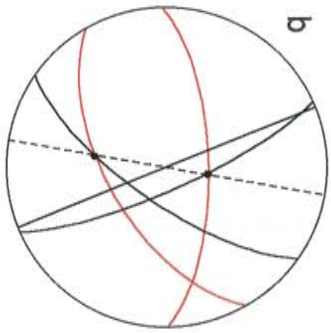
q

Figure 63. The traces of FIP from sample 98 are plotted on lower hemisphere equal area stereograms. Blue traces are type IB FIP, green traces are type IC FIP, black traces are type ID FIP, and red traces are type III FIP. Dotted black lines are open microcracks.

a) 98-1, b) 98-2, c) 98-3, d) 98-4, e) 98-5, f) 98-6, g) 98-7, h) 98-8, i) 98-9, j) 98-10, k) 98-11, l) 98-12, m) 98-13, n) 98-14, o) 98-15, p) 98-16, q) 98-18, r) 98-20.

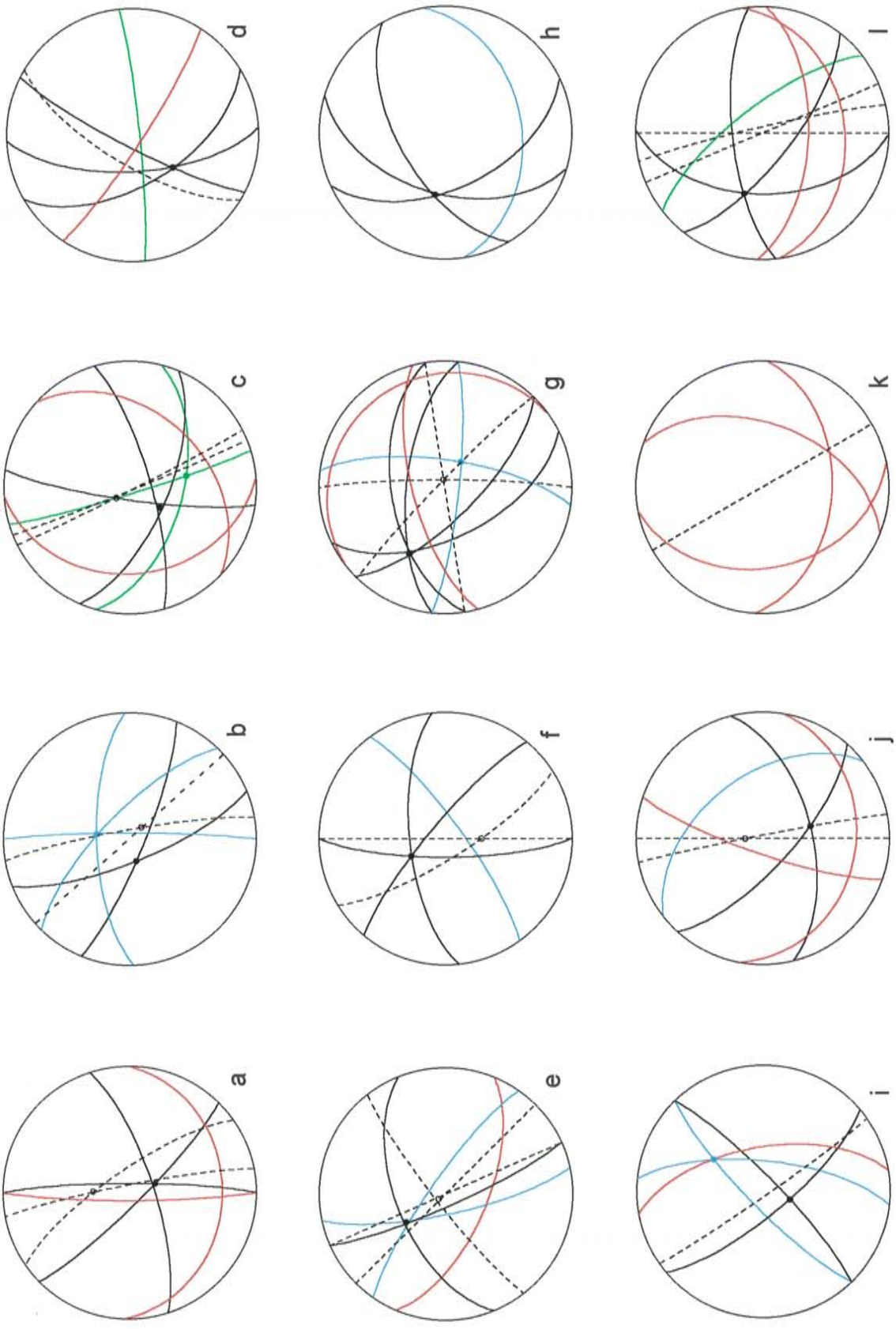
d
h
l
c
g
k
b
f
j
a
e
i

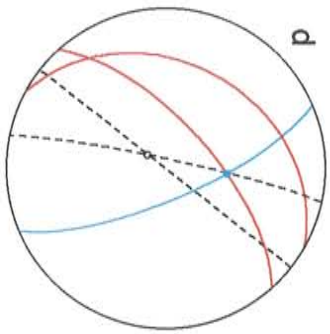
p

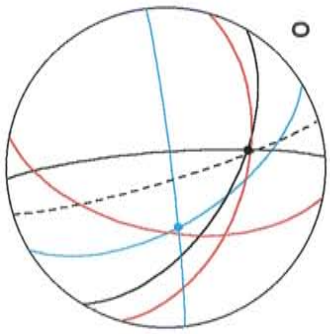
o

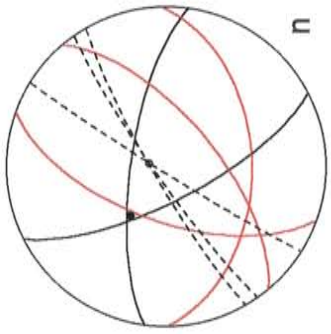
n

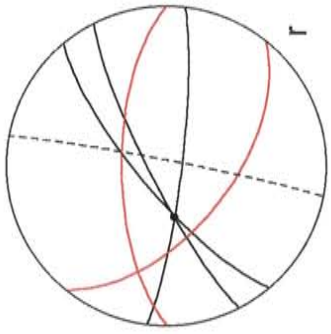
r

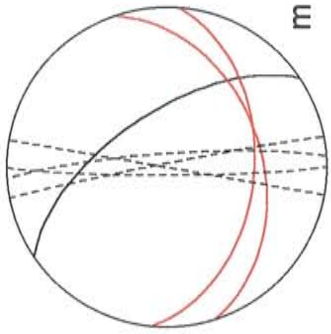
m

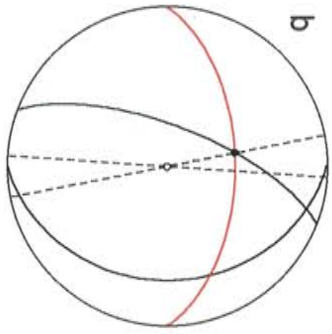
q

Figure 64. The traces of FIP from sample 103 are plotted on lower hemisphere equal area stereograms. Blue traces are type IB FIP, green traces are type IC FIP, black traces are type ID and II FIP, and red traces are type III FIP. Dotted black lines are open microcracks.

a) 103-1, b) 103-2, c) 103-3, d) 103-4, e) 103-5, f) 103-6, g) 103-7, h) 103-8, i) 103-9, j) 103-10, k) 103-11, l) 103-12, m) 103-13, n) 103-14, o) 103-15, p) 103-16, q) 103-17.

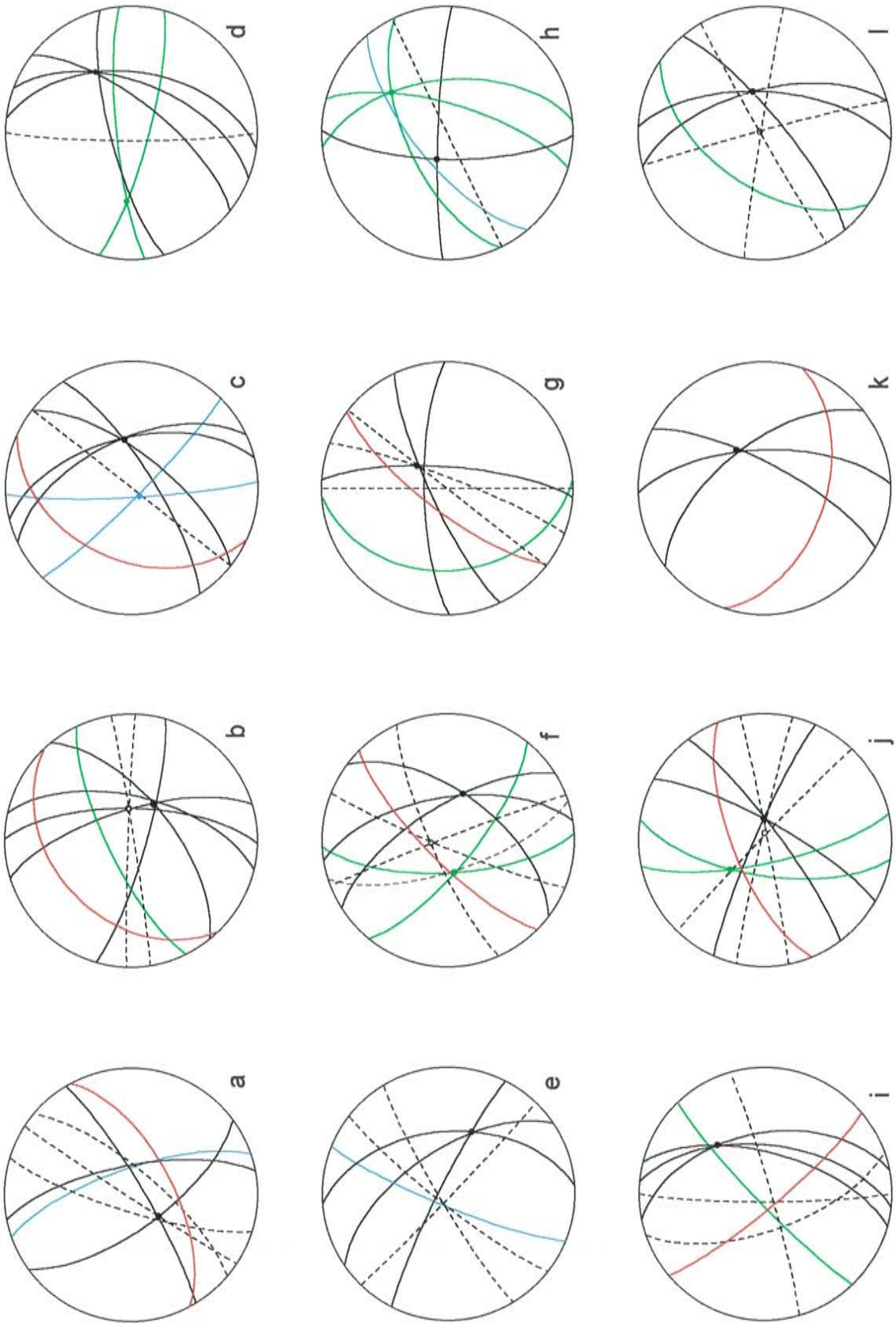
d
h
l
c
g
k
b
f
j
a
e
i

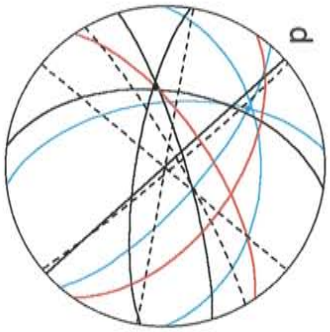
p

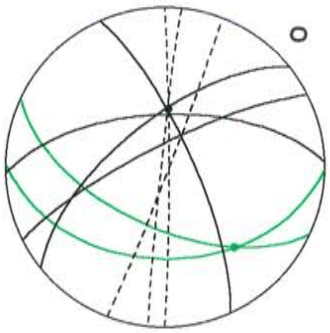
o

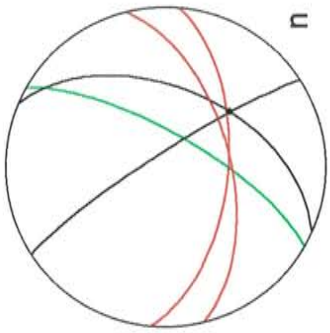
n

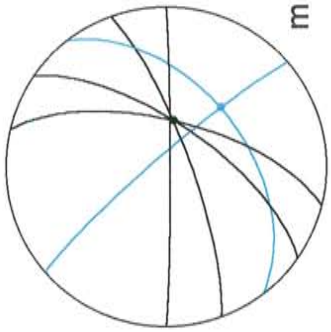
m

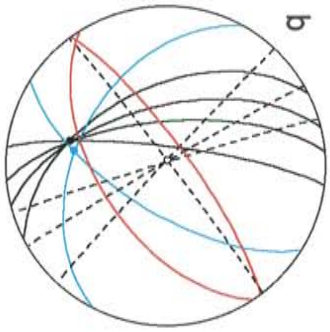
q